Carbon Fibers

Edited by

Jonathan Phillips

Printed Edition of the Special Issue Published in *Materials*

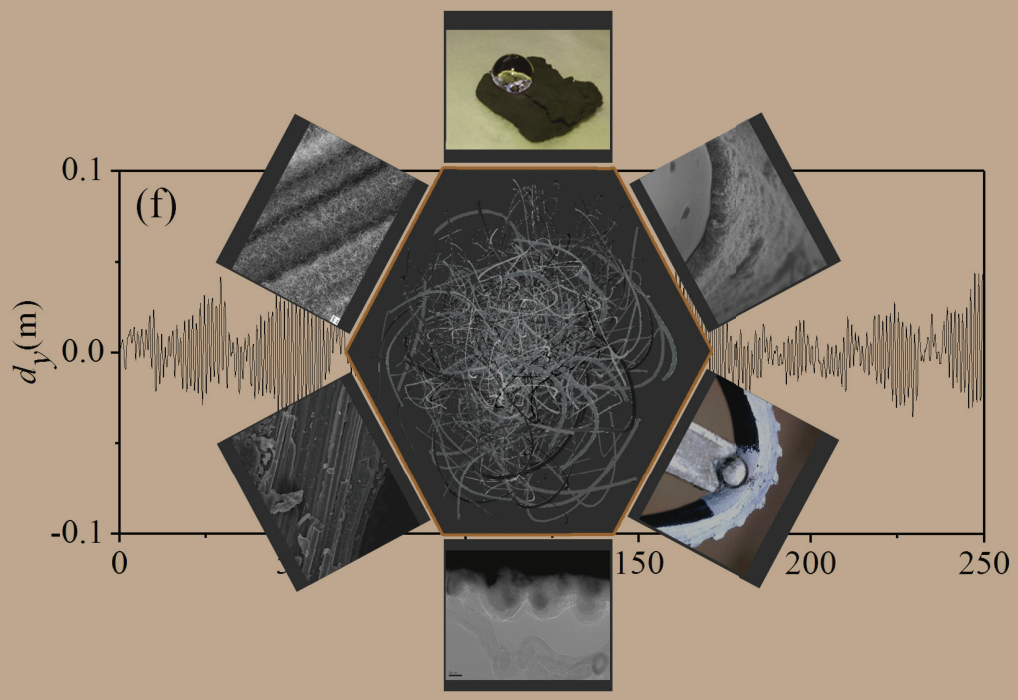

www.mdpi.com/journal/materials

Jonathan Phillips (Ed.)

Carbon Fibers

MDPI

This book is a reprint of the Special Issue that appeared in the online, open access journal, *Materials* (ISSN 1996-1944) in 2014 (available at: http://www.mdpi.com/journal/materials/special_issues/carbon-fibers).

Guest Editor
Jonathan Phillips
Naval Postgraduate School
Department of Physics
Monterey, CA 93943-5216
USA

Editorial Office
MDPI AG
Klybeckstrasse 64
4057 Basel
Switzerland

Publisher
Shu-Kun Lin

Production Editor
Martyn Rittman

1. Edition 2015

MDPI • Basel • Beijing • Wuhan • Barcelona

ISBN 978-3-906980-70-6 (PDF)
ISBN 978-3-906980-69-0 (Hbk)

Table of Contents

List of Contributors

Victor Hugo C. de Albuquerque: Programa de Pós-Graduação em Informática Aplicada (PPGIA), Universidade de Fortaleza (UNIFOR), Av. Washington Soares, 1321, Sala J30, CEP 60.811-905, Edson Queiroz, Fortaleza, Brazil.

Antonio Díaz-Álvarez: Department of Mechanical Engineering, Universidad Carlos III de Madrid, Avda. Universidad 30, Leganés, Madrid 28911, Spain.

José Díaz-Álvarez : Department of Bioengineering and Aerospace Engineering, Universidad Carlos III de Madrid, Avda. Universidad 30, Leganés, Madrid 28911, Spain.

Oscar N.G. Andrade: ISEP/CIDEM, School of Engineering-Polytechnic of Porto, Rua Doutor António Bernardino de Almeida, 431, Porto 4200-072, Portugal.

Mark A. Atwater: Applied Engineering, Millersville University, Millersville, PA 17551 USA.

Ayoub Yari Boroujeni: Department of Engineering Science and Mechanics, Virginia Tech, Blacksburg, VA 24061, USA.

José Luis Cantero: Department of Mechanical Engineering, Universidad Carlos III de Madrid, Avda. Universidad 30, Leganés, Madrid 28911, Spain.

Ho-Hwan Chun: Department of Naval Architecture and Ocean Engineering, Pusan National University,Busan 609-735, Korea.

D. Chris Daskam: Mechanical and Aerospace Engineering Department, Naval Postgraduate School, 700 Dyer Rd., Monterey, CA 93943, USA.

Luis Miguel Pereira Durão: ISEP/CIDEM, School of Engineering-Polytechnic of Porto, Rua Doutor António Bernardino de Almeida, 431, Porto 4200-072, Portugal.

Norberto Feito: Department of Mechanical Engineering, Universidad Carlos III de Madrid, Avda. Universidad 30, Leganés, Madrid 28911, Spain.

Edwin Gonzalez: Hartnell College, Salinas, CA—Naval Postgraduate School, Monterey, CA 93943, USA.

Marwan S. Al-Haik: Department of Engineering Science and Mechanics, Virginia Tech, Blacksburg, VA 24061, USA.

Mohammad Jalalpour: Civil Engineering Department, University of New Mexico, Albuquerque, NM 87131, USA.

Wan-Kuen Jo: Department of Environmental Engineering, Kyungpook National University, Daegu, Korea.

Usama Kandil: Polymer Nanocomposites Center, Egyptian Petroleum Research Institute, 1 Ahmed El-Zomor Street, Nasr City, Cairo 11727, Egypt.

Joon Yeob Lee: Department of Environmental Engineering, Kyungpook National University, Daegu 702-701, Korea.

Zayd C. Leseman: Mechanical Engineering Department, University of New Mexico, Albuquerque, NM 87131, USA.

Xiaozhang Li: Department of Civil Engineering, Zhejiang University, Hangzhou 310058, Zhejiang, China.
Xinyan Liu: College of Packaging & Printing Engineering, Tianjin University of Science & Technology, Tianjin, China.
Claudia C. Luhrs: Mechanical and Aerospace Engineering Department, Naval Postgraduate School, 700 Dyer Rd, Monterey, CA 93943, USA.
Xiaojun Ma: College of Packaging & Printing Engineering, Tianjin University of Science & Technology, Tianjin, China.
Jorge Filipe S. Marques: ISEP/CIDEM, School of Engineering-Polytechnic of Porto, Rua Doutor António Bernardino de Almeida, 431, Porto 4200-072, Portugal.
Carosena Meola: Department of Industrial Engineering—Aerospace Division, University of Naples Federico II, Via Claudio 21, Napoli, Italy**.**
María Henar Miguélez: Department of Mechanical Engineering, Universidad Carlos III de Madrid, Avda. Universidad 30, Leganés, Madrid 28911, Spain.
Arash K. Mousavi: Mechanical Engineering Department, University of New Mexico, Albuquerque, NM 87131, USA.
Behnam K. Mousavi: Electrical & Computer Engineering Department, University of New Mexico, Albuquerque, NM 87131, USA.
Alvaro Olmedo: Department of Continuum Media and Structural Analysis, Universidad Carlos III de Madrid, Avda. Universidad 30, Leganés, Madrid 28911, Spain.
Jonathan Phillips: Department of Physics, Naval Postgraduate School, 833 Dyer Rd Monterey, CA 93943, USA.
Carlos Santiuste: Department of Continuum Media and Structural Analysis, Universidad Carlos III de Madrid, Avda. Universidad 30, Leganés, Madrid 28911, Spain.
Yonggang Shen: Department of Civil Engineering, Zhejiang University, Hangzhou 310058, Zhejiang, China.
Eslam Soliman: Department of Civil Engineering, Assiut University, Assiut 71515, Egypt.
Mahmoud Reda Taha: Department of Civil Engineering, University of New Mexico, MSC01 1070, Albuquerque, NM 87131, USA.
João Manuel R.S. Tavares: Instituto de Engenharia Mecânica e Gestão Industrial (INEGI), Departamento de Engenharia Mecânica (DEMec), Faculdade de Engenharia, Universidade do Porto (FEUP), Rua Doutor Roberto Frias, s/n, 4200-465 Porto, Portugal.
Mehran Tehrani: Department of Mechanical Engineering, University of New Mexico, Albuquerque, NM 87131, USA.
Cinzia Toscano: C.I.R.A.—Italian Aerospace Research Centre, via Maiorise sn, Capua (CE), Italy.
Xu Xie: Department of Civil Engineering, Zhejiang University, Hangzhou 310058, Zhejiang, China.
Cheng Yuan: College of Packaging & Printing Engineering, Tianjin University of Science & Technology, Tianjin, China.

Preface

Remarkably, truly novel structures are still being found for materials made of a single element: carbon. Perhaps there is a ‘revolution’ in carbon-only materials. Indeed, recently, two Nobel prizes were awarded for new forms of carbon: for fullerenes in 1996, and for graphene in 2010. And the magic and beauty of carbon nanotubes has held the attention of the scientific world for more than a decade. Yet, there is still more to discover and to explain. In this Special Issue, the focus is on just one area of carbon research: fibers. Even given this relatively narrow focus there is a diversity of research that is both compelling and frustrating. Compelling as it demonstrates the vitality of the subject, and frustrating as it makes it difficult to organize. The topics covered include new fiber fabrication protocols, the mechanical behavior of fiber reinforced polymers, new techniques to study the microstructure of fiber containing composites, new uses of fiber structures, the use of carbon fibers as catalyst supports, and studies regarding the difficulties of machining fiber structures for inclusion in complex structures.

After some deliberation the following order was determined. The first articles consider the mechanical properties and uses of fiber reinforced composites. These articles lead because these materials have made the jump to broad commercial use, hence probably have the largest audience. Indeed, these materials are employed everywhere, increasingly in aircraft, race cars, luxury cars, oil pipelines, chemical processing structures, bridge decks, windmill turbine blades, sports equipment, etc. Next, is an article regarding methods to better characterize these widely employed composites. The next group of articles includes new methods of fabrication of raw fibers, electrical and mechanical properties of raw fiber macro structures and even novel applications. The final article group drilling fibers, a process necessary for many applications.

Mechanical properties of composites all are concerned with changes to the fibers that might make them interact more strongly with the polymer component of the composites, hence reducing problems with ‘pullout’ and perhaps permitting the formation of composites with higher fiber loadings. The Taha group (1) shows that changing the surface functionalization of fibers added in low concentrations to epoxy structures can significantly change some mechanical properties. The Al-Haik group (2) focused on the potential value of fiber-on-fiber growth as a means to promote physical interaction between the polymer host matrix and carbon fiber reinforcements. Moreover, the Al-Haik group uses the graphitic structure by design (GSD) method to grow more fiber. This is an approach to fiber formation that this Special Issue clearly demonstrates is finding a wider audience. Next, the Shen team (3) explores the possibility that fiber reinforced structures could replace steel cable in major infrastructure such as suspension bridges. Fiber reinforced polymer cables not only have appropriate physical parameters, but are lighter and more resistance to corrosion than the metal cables presently in use. The final paper on fiber reinforced composites regards one of

the major difficulties: Certifying that the manufactured material has minimal void content, as voids are detrimental to mechanical properties. Meola and Toscano (4) review the state of the art of non-destructive testing methods, particularly flash tomography and ultrasonic.

New methods for making carbon fibers are always under exploration to see if even stronger and less expensive fibers can be produced. Ma et al. (5) describe the characteristics of carbon fibers generated from inexpensive cellulose. As carbonization fraction is increased strength increases, but yield length decreases. Both the Leseman (6) and the Luhrs group (7) report on the mechanical and electrical properties of solid, pure, 'fiber foams' grown catalytically in a mold, using the GSD technique, from fuel rich ethylene oxygen mixtures at relatively low (ca. 550 C) temperatures. Both demonstrate this method can create solid fiber foams of virtually any shape. The Leseman group points out that the study of anisotropic fiber based materials is in its infancy relative to the behavior of 1-dimensional fibers. They successfully model the mechanical behavior as typical for non-woven fiber composites. The Luhrs group focused on two aspects of the behavior: i) after limited mechanical aging the fiber foams show perfect viscoelastic behavior, and ii) the electrical conductivity is a function only of foam thickness, thus the material can be used as a strain gauge.

The next paper illustrates the breadth of applications found for foam. Jo *et al*. (8) demonstrate that carbon fibers can be employed in a chemical application. In particular, they found that titania fibers grown on larger diameter carbon fibers (essentially catalyst supports) had excellent activity for some common air pollutants (BTEX). They also showed that the shape of the titania structure on the carbon, spheres vs. fibers, had a dramatic impact on activity.

The final section of the Special Edition features three articles on the special character of drilling a fibrous material (9-11).

Prof. Jonathan Phillips
Guest Editor

Improved Strength and Toughness of Carbon Woven Fabric Composites with Functionalized MWCNTs

Eslam Soliman, Usama Kandil and Mahmoud Reda Taha

Abstract: This investigation examines the role of carboxyl functionalized multi-walled carbon nanotubes (COOH-MWCNTs) in the on- and off-axis flexure and the shear responses of thin carbon woven fabric composite plates. The chemically functionalized COOH-MWCNTs were used to fabricate epoxy nanocomposites and, subsequently, carbon woven fabric plates to be tested on flexure and shear. In addition to the neat epoxy, three loadings of COOH-MWCNTs were examined: 0.5 wt%, 1.0 wt% and 1.5 wt% of epoxy. While no significant statistical difference in the flexure response of the on-axis specimens was observed, significant increases in the flexure strength, modulus and toughness of the off-axis specimens were observed. The average increase in flexure strength and flexure modulus with the addition of 1.5 wt% COOH-MWCNTs improved by 28% and 19%, respectively. Finite element modeling is used to demonstrate fiber domination in on-axis flexure behavior and matrix domination in off-axis flexure behavior. Furthermore, the 1.5 wt% COOH-MWCNTs increased the toughness of carbon woven composites tested on shear by 33%. Microstructural investigation using Fourier Transform Infrared Spectroscopy (FTIR) proves the existence of chemical bonds between the COOH-MWCNTs and the epoxy matrix.

Reprinted from *Materials*. Cite as: Soliman, E.; Kandil, U.; Taha, M.R. Improved Strength and Toughness of Carbon Woven Fabric Composites with Functionalized MWCNTs. *Materials* **2014**, *7*, 4640ï 4657.

1. Introduction

The use of fiber-reinforced polymer (FRP) composites has grown very rapidly over the last few decades, due to their attractive physical, mechanical and thermal properties [1]. Some of their common applications include civil infrastructure, composite bridge decks, oil and gas pipelines and turbine blades in windmills. The woven fabric composite, in particular, has attracted the interest of engineers and researchers, due to its relatively high delamination and impact resistance. However, the failure of FRPs is complex, especially when multi-layer laminates are examined. The failure behavior depends on many factors, such as the loading nature and direction with respect to the fibers, the fabrication quality and the structure of the composite fabric. Typical failure modes of FRPs include fiber fracture, matrix fracture, fiber-matrix interface debonding and interlaminar delamination [2,3]. One of the recent promising techniques to overcome the premature failure of composites due to delamination/debonding is to reinforce the composites with nanoparticles.

Carbon nanotubes (CNTs), nano-clay, graphene nanoparticles (GNPs), and nano-silica are common non-metallic nanoparticles used to fabricate nanocomposites [4,5]. Discovered by Ijima in 1991 [6], CNTs have attracted many scientists worldwide, because of their distinguished mechanical properties compared with conventional structural materials. Therefore, many researchers have focused on using the CNTs in polymer nanocomposites. Over the last two decades, various techniques have been

developed to ensure a good dispersion of CNTs in polymeric matrices, such as non-covalent [7–9] and covalent [10–12] functionalization. The covalent functionalization involves impregnating functional groups on the surface of nanotubes. The functional groups are expected to react with the polymer matrix and increase the interfacial bond significantly. A review for the use of functionalized CNTs in polymeric matrices can be found elsewhere [13–15].

Several studies reported good improvement in FRP mechanical properties when CNTs were used in polymer nanocomposites. The mechanism of CNTs in composite is expected to resist the inter-fiber fracture and enhance their respective mechanical properties. The improvements of FRP composites include the tensile and shear property of glass fiber-reinforced polymer (GFRP) composites [16] and Mode I and Mode II fracture toughness [17,18]. For instance, Qiu *et al.* [16] examined the tensile and shear behavior of (GFRP) composites. With 1.0% by weight functionalized multi-walled carbon nanotubes (MWCNTs), they reported a 14% and 5% increase in on-axis tensile and shear strengths, respectively. They also reported a 20% and 8% increase in tensile Young's and short beam shear moduli. In addition, Garcia *et al.* [18] examined the fracture toughness of carbon fiber-reinforced polymer (CFRP) with nanotubes joining the prepregs, and they found a 250% increase in Mode I and a 300% increase in Mode II fracture toughness. Furthermore, compression shear tests were performed to determine the interlaminar shear strength (ILSS) of glass woven fabric composites with different dispersion techniques and showed no variation in ILSS due to the addition of 0.5 wt% MWCNTs [19].

Few studies examined using nanoparticles to improve the flexure behavior of FRP composites, such as increasing the ultimate strength, the flexural modulus or the energy absorption under flexural loads. Hossain *et al.* [20] reported a 49% and 31% increase in the flexural strength and modulus of on-axis woven E-glass/polyester composites reinforced by 0.1–0.4 wt% carbon nanofibers (CNF). In addition, 1.5 wt% aligned MWCNTs are used to improve on-axis flexure strength and modulus for (CFRP) composites by 74% and 75%, respectively [21]. To date, the effect of using functionalized MWCNTs on the flexure behavior of carbon woven fabric composites has not yet been reported. In this investigation, a carboxyl functionalized multi-walled carbon nanotube (COOH-MWCNTs) epoxy nanocomposite is used to improve the on- and off-axis flexural behavior of woven carbon fiber composites.

2. Experimental Methods

2.1. Materials

The carbon fiber and the epoxy were supplied by U.S. Composites, Inc., Florida, FL, USA. The fabric is FG-CARB5750, a balanced plain bidirectional (0°–90°) weave, PAN-based fiber, a 3 k tow size and 254 μm-thick. The tensile strength of the raw carbon fibers is 4.48 GPa and the tensile modulus is 231 GPa. The bi-directional plain weave fabric was selected over the other types of weaves (*i.e.*, twill or satin), because it provides the largest number of interlaces between the warp and filling threads. Such a large number of interlaces maintains the geometry of the woven fabric cloth and minimizes any weaving of the fiber bundles that might occur due to rolling the epoxy during the fabrication process of the FRP composites.

The epoxy used in fabrication is the commercially available EPOTUF® 37–127 epoxy system. The epoxy resin is a diluted liquid based on bisphenol-A and contains diglycidyl ether (DGEBPA), while the hardener is an aliphatic amine. The resin to hardener mixing ratio was 2:1; the pot life was 30–45 min at 80 °F (26.7 °C); the set time was 5–6 h, and the curing time was 24–28 h at room temperature. This type of epoxy has relatively low viscosity, which facilitates the impregnation of the carbon fibers during the fabrication process. Furthermore, the epoxy pot life is relatively long to allow adequate time for the impregnation and the application of the vacuum environment before the epoxy hardens partially. The tensile strength and tensile elongation for the epoxy are 65 MPa and 25%, respectively.

Carboxyl functionalized COOH-MWCNTs were supplied by Cheap Tubes, Inc., VT, USA. According to the manufacturer's data, the outer diameter of the CNTs is 20–30 nm, the inner diameter is 5–10 nm and the length is 10–30 μm with an aspect ratio ranging from 500 to 1000. The nanotubes were manufactured using the catalytic chemical vapor deposition technique with the purity being greater than 95 wt%. The functionalization was performed by the manufacturers using a mixture of non-organic acids. According to the manufacturer, the functionalized MWCNTs had (COOH) functional groups of 1.23 wt%.

2.2. COOH-MWCNTs/Epoxy Nanocomposite Fabrication

Two different types of treated epoxies were produced to fabricate the carbon woven composites in this study. The first type was a neat epoxy prepared by mixing the resin with the hardener and applying the mixture directly to the carbon fabric during the impregnation process. The second type was prepared by reinforcing the epoxy with functionalized COOH-MWCNTs. The COOH-MWCNTs were added first to the resin, and the mixture was sonicated for 1.0 h at 40 °C, as shown in Figure 1a. In order to ensure the chemical reaction between the functional groups on the surface of the nanotubes and the resin chains, the dispersed mixture was stirred for 2.0 h at 80 °C. The hardener was added after cooling the resin, and the COOH-MWCNTs/epoxy nanocomposite was further homogenized by mechanical mixing for 10 min and then used in the composite fabrication. Figure 2a shows the Scanning Electron Microscope (SEM) images for well-dispersed 1.0 wt% COOH-MWCNTs in the epoxy matrix. The image shows the absence of aggregates/agglomeration of MWCNTs as an indication of the effectiveness of the dispersion process using sonication and mechanical stirring. A close view is shown in Figure 2b confirming the diameter and their good dispersion of the MWCNTs.

2.3. Fabrication of the Multi-Scale Woven Fabric Epoxy Composite

Fabrication of the woven fabric composite plates was performed in accordance with ASTM D5687 [22]. The vacuum-assisted hand lay-up technique was implemented to fabricate the composite plates. Ten layers of fabric were used to fabricate the specimens. The average dimensions of the composite specimens were 40 mm-long, 19 mm-wide and 2.7 mm-thick. Peel plies, non-porous and porous release films, breather plies and an aluminum plate were used to ensure straight and compacted composite sheets and to facilitate the peeling off of the composite after curing. Adequate epoxy impregnation was achieved using a roller, and a breather ply was placed to form the uniform

air paths once the vacuum was applied. The same epoxy/carbon fabric weight ratio was used during the fabrication of all composite specimens in order to maintain the same epoxy weight fraction. The epoxy weight fractions were obtained by measuring the change in weight between the original carbon fabric before and after epoxy impregnation and ranged between 30% and 33%. It is important to note that the addition of COOH-MWCNTs increased the viscosity of the epoxy during the fabrication; therefore, the limitation on the upper bound of the COOH-MWCNTs content was set as 1.5 wt% of epoxy. The vacuum bag contents were maintained at a vacuum level of 2.3×10^{-2} Torr for 24 h. This relatively high level of vacuum applied for long time period ensures the elimination of all air bubbles. Furthermore, to ensure the consistent production of the composite with different levels of nanomaterials, ASTM D3171 was used for determining the fiber weight fraction, and the fiber volume fractions for the different composite materials were found to be 54.3%, 55.5%, 53% and 52.4% for the neat, 0.5%, 1.0% and 1.5% COOH-MWCNTs epoxy woven fabric composites, respectively, confirming the acceptable consistency in production [23]. Relatively high void contents of 2%, 2.3%, 1.5% and 3% were observed in 0, 0.5 wt%, 1.0 wt% and 1.5 wt% COOH-MWCNTs, respectively, due to the use of the vacuum-assisted hand layup technique in the fabrication process. The variation in void content is ±0.8%, and the variation in the fiber fraction is ±1.7%. Such variation in void and fiber fractions within ±2.0% was reported in the literature to have an insignificant effect on the mechanical properties of composites [24–26]. Therefore, the above variations would not affect our ability to examine the significance of COOH-MWCNTs on the strength and toughness of carbon fiber composites.

Figure 1. Fabrication of multi-scale epoxy/carbon woven fabric composite specimens: (**a**) sonication of COOH-MWCNTs in the epoxy resin; (**b**) stirring of the COOH-MWCNTs in the epoxy resin; and (**c**) the vacuum environment applied to the composite specimens during the curing of the epoxy.

(**a**) (**b**) (**c**)

2.4. Mechanical Testing

Three-point bending tests were conducted to examine the on- and off-axis flexure behavior of the composite specimens. The flexure test setup and geometry of the specimens are shown in Figure 3a,b. In the on-axis test, the orientation of the fibers was in the span direction, while the fibers were oriented at a 45° angle with respect to the span direction in the off-axis test. On the other hand, the short-span shear test was conducted on the on-axis composite plates via four-point bending. The shear test setup is shown in Figure 3c. The flexure and shear tests were performed on the composite

plates using an MTS® Bionix servo hydraulic system. The machine has a load cell with a capacity of 25 kN and a maximum stroke of 130 mm. The sampling rate for all of the experiments was 50 Hz, and the data was collected by the FlexStar MTS® 793 data acquisition system. In each test, the load and displacement were measured and recorded.

Figure 2. SEM image showing the dispersion of 1.0 wt% COOH-MWCNTs in the epoxy matrix. (**a**) The general view with the marked area shown at high resolution in (**b**); (**b**) the high resolution view of COOH-MWCNTs in epoxy showing individual carbon nanotubes.

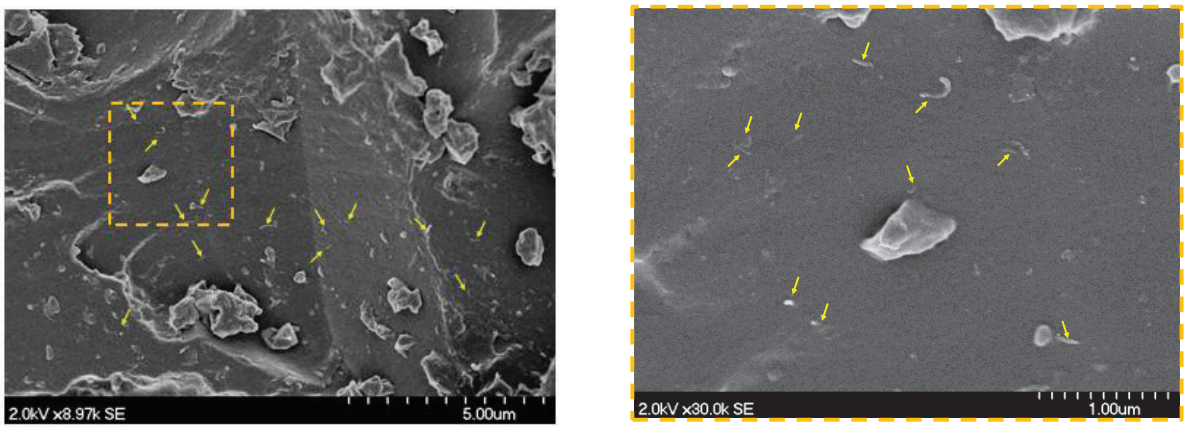

(**a**) (**b**)

Figure 3. on- and off-axis arrangements for a flexure test: (**a**) on-axis flexure test; (**b**) off-axis flexure test; (**c**) on-axis shear test.

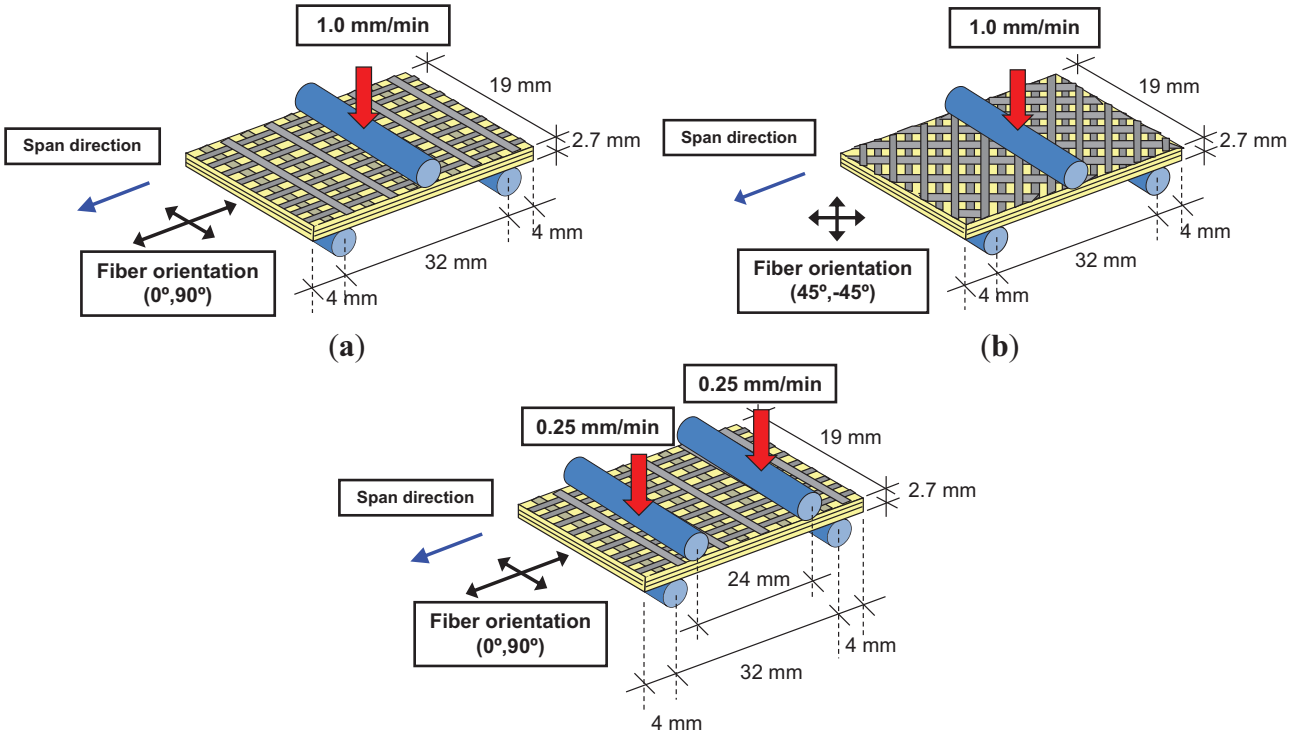

(**a**) (**b**)

(**c**)

The flexure stress-strains $\sigma_f - \varepsilon_f$ were then obtained using Equations (1) and (2) following ASTM D790-10 [27].

$$\sigma_f = \frac{3PL}{2bd^2} \tag{1}$$

$$\varepsilon_f = \frac{6Dd}{L^2} \tag{2}$$

where P is the applied load, L is the span length, b is the width of the specimen, d is the depth of the specimen and D is the deflection of the mid-span. On the other hand, the average shear stress-strains $\tau - \gamma$ were obtained according to Equations (3) and (4).

$$\tau = \frac{P}{2bd} \tag{3}$$

$$\gamma = \frac{D}{a} \tag{4}$$

where a is the shear span. In addition to the neat epoxy, three loadings of COOH-MWCNTs were examined. They are 0.5, 1.0 and 1.5 wt% of epoxy. Three specimens were tested for each COOH-MWCNTs loading. The flexure and shear strength, modulus and toughness were then evaluated and compared. Statistical analyses were performed on the test results and the statistical significance of the difference between the specimens was evaluated using the Student's *t*-test assuming a 95% level of significance.

2.5. Microstructural Investigation

To explain the role of functionalized COOH-MWCNTs on the behavior of carbon fibers, Fourier Transform Infrared Spectroscopy (FTIR) measurements were conducted on 25.4 mm × 25.4 mm samples cut from CFRP specimens. Three types of samples were compared: neat CFRP samples, CFRP samples incorporating 0.5 wt% COOH-MWCNTs and CFRP samples incorporating 1 wt% COOH-MWCNTs. Furthermore, COOH-MWCNTs powder was separately measured. All of the samples were analyzed with biconical reflectance Nicolet Nexus 670 micro-Fourier Transform Infrared Spectroscopy (Micro-FTIR) (Thermo Fisher Scientific, Waltham, MA, USA). The FTIR has a continuum microscope with a Globar source, an XT-KBr beam splitter and a MCT-A detector over a 100 × 100 micron area with a 4 cm-1 resolution. Spectra were background corrected using a reflective gold slide and converted to absorbance using the Kramers-Kronig equation, as per the standard FTIR analysis method after Stefanie *et al.* [28].

2.6. Micromechanical Modeling

In order to understand the failure mode of the on- and off-axis flexure tests, a micromechanical finite element model is developed under ANSYS® APDL modeling environment (Pennsylvania, PA, USA) coupled with micromechanical Autodesk® composite simulation analysis (California, CA, USA). The micromechanical model is based on multi-continuum theory (MCT) for composite analysis. In MCT, continuum-based (phase-averaged) stresses and strains can be predicted for each constituent (e.g., fibers or matrix) in finite element (FE) analysis. In addition, the failure criterion for each constituent of the composite is predicted and displayed separately, allowing a progressive failure

to take place. Previous research proved the failure analysis by MCT to be fairly close to experimental observations, since it takes into account matrix damage and the associated reduction in stiffness [29–31]. Two 3D FE models for flexure test specimens were constructed. The two models consist of 10 layers of woven fabric composite with an equal fill and wrap fiber volume fraction and a thickness of 0.27 mm. In the first model, the fill fibers were set in the span direction, while in the second model, the fill fibers were set at a 45° angle with respect to the span direction. 3D SOLSH190 elements are used to model the laminated composite. Table 1 lists all material properties used in the FE simulations. The material properties of the constituent materials are obtained experimentally [32], from the manufacturer's data or using classical lamination theory (CLT).

Table 1. The material properties of woven fabric composite laminates used in FE simulation.

Designation	E_{11}, GPa	E_{22}, GPa	G_{12}, GPa	$+S_{11}$, MPa	$-S_{11}$, MPa	S_{12}, MPa	υ_{12}
Lamina	40 *	40 *	3.9 *	555 *	−310 †	70 *	0.20 †
Fibers	230 †	50 †	–	–	–	–	–
Matrix	2.0 *		0.74 ‡	–	–	–	0.35 †

* The material properties obtained experimentally from [32]; † the material properties obtained from the manufacturer's specifications and other sources; ‡ the material properties computed using classical lamination theory (CLT); E_{11}: elastic modulus in the fill fiber direction; E_{22}: elastic modulus in the wrap fiber direction; G_{12}: in-plane shear modulus; $+S_{11}$: ultimate tensile strength in the fill or wrap fiber directions; $-S_{11}$: ultimate compressive strength in the fill or wrap fiber directions; S_{12}: in-plane shear strength.

3. Results and Discussion

Figure 4a,b shows the deformed shape of the on- and off-axis flexure tests, respectively. As expected, the off-axis specimens exhibited higher deflection and less strength than the on-axis specimens. Close views for the failed on-axis specimens show that failure occurred due to kink/breakage of the fibers in the compression side (Figure 4c,e). This is expected, since FRP composites are stronger in tension than they are in compression. In addition, high resolution microscopic images in Figure 4g,h show the kink and rupture of fibers in the top and bottom surfaces of the on-axis test specimens, respectively. On the other hand, failure of the off-axis specimens was due to shear-off of the fibers at a 45° angle in the compression zone, as shown in (Figure 4d,f). This shear-off is attributed to the weak shear strength of the epoxy matrix.

The flexure stress-strain curves for the on- and off-axis flexure tests are depicted in Figure 5a,b up to the 5% and 10% strain levels, respectively. For all COOH-MWCNTs loadings, the on-axis flexure stress-strain curves were linear up to a maximum value corresponding to the flexure strength of the composite specimens, where the failure in the compression side occurred (Figure 5a). Once compression failure occurred, the flexure stress was reduced as the fiber breakage propagated through the thickness. The linearity in the on-axis stress strain curve before failure proves the fiber domination of the on-axis flexure behavior. On the contrary, a non-linear stress-strain curve associated with a yield-like plateau was observed in the off-axis flexural behavior (Figure 5b). The significant non-linearity in the off-axis stress-strain curves is attributed to the matrix domination on the off-axis flexural behavior. In addition, the post-peak loss in flexure stress occurred in a more gradual fashion in the off-axis behavior than it occurred in the on-axis direction.

Figure 4. Deformation and failure of on- and off-axis flexure composite specimens. (**a**) deformation of on-axis flexure specimens; (**b**) deformation of off-axis flexure specimens; (**c**) failure of on-axis flexure specimens; (**d**) failure of off-axis flexure specimens; (**e**) kink/breakage of fibers at the top surface; (**f**) shear-off of the fibers at the top surface; (**g**) high resolution microscopic image for the kink of fibers at the top surface of the on-axis test; (**h**) high resolution microscopic image for the rupture of fibers at the bottom surface of the on-axis test.

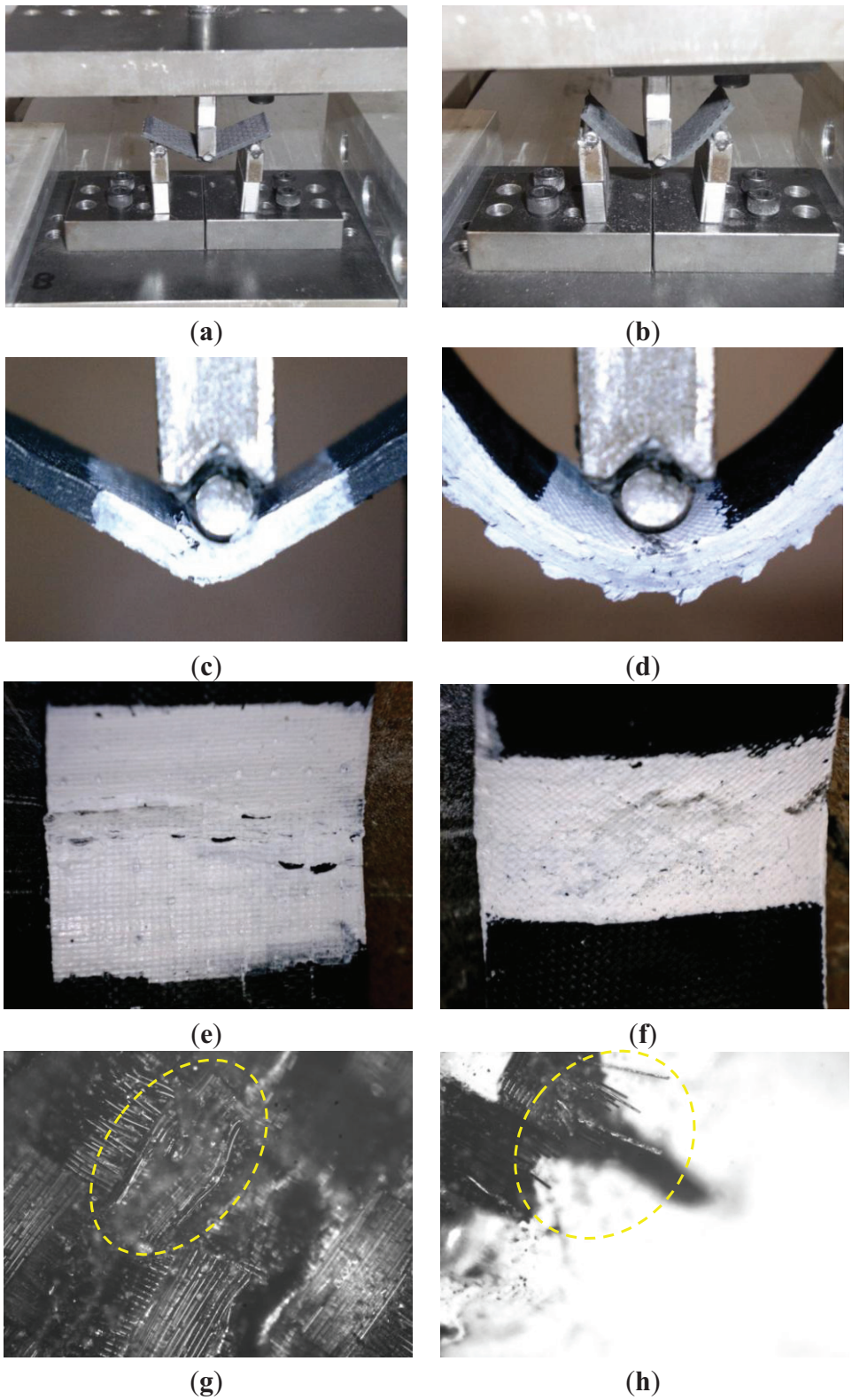

Figure 5. Flexure stress-strain curves for composite plates. (**a**) on-axis; (**b**) off-axis.

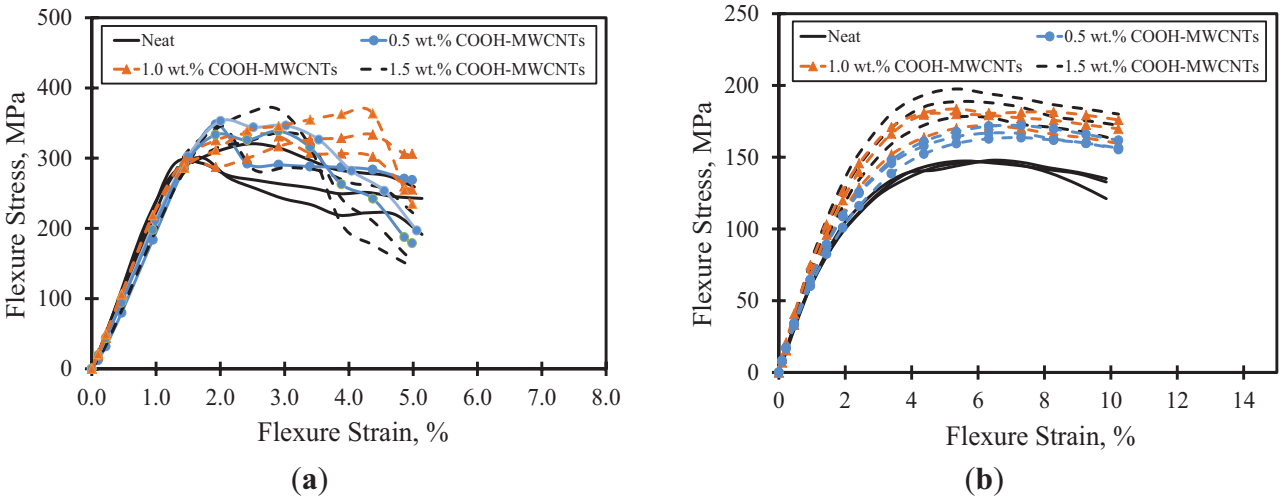

Tables 2 and 3 show the statistical analyses for the mechanical properties of on- and off-axis composite specimens with various COOH-MWCNTs loadings. The flexure toughness for the on-axis test specimens were computed from the area under the stress-strain curves up to the 3.0% flexure strain level; the limit sufficiently extends beyond the fiber breakage first observed at the end of the proportional limit. On the other hand, the flexure toughness for the off-axis specimens were computed from the area under the stress-strain curves up to the 5.0% strain level, The proposed limits meet the recommendations of ASTM D790 [27]. From both tables, it can be observed that the flexure strength (~150–180 MPa) and modulus (~6–8 GPa) of the off-axis flexure test specimens were about one-half and one-third of that of the on-axis flexure test specimens, respectively. This is a typical observation supported by composite theory, where the behavior in the on-axis direction dominated by the strong fibers is much stronger than off-axis direction dominated by the matrix. The coefficients of variation for all specimens were below 10%, and therefore, all cases of COOH-MWCNTs loadings showed valid results.

Based on the Student's *t*-test, no significant statistical difference was observed in the on-axis flexure strength, modulus and toughness between composite specimens with various COOH-MWCNTs loadings and the neat material. This observation confirms that the on-axis flexural behavior of the composite plates is dominated by the strong carbon fibers oriented in the span direction, and the change/modification in the epoxy matrix produces minimal to no effect on the on-axis behavior.

A similar observation, related to the fiber domination on the behavior of woven fabric composites subjected to on-axis tension was reported earlier by Naik *et al.* [33] and recently by Soliman *et al.* [32]. In this case, the composite coupons exhibit fiber breakage associated with limited damage in the matrix. On the other hand, significant statistical differences in the flexure strength, modulus and toughness associated with the off-axis flexural test were observed especially with the addition of large contents of COOH-MWCNTs. For instance, improvements in flexure strength, modulus and toughness with the addition of 1.5 wt% COOH-MWCNTs reached 19%, 28% and 20.7%, respectively (Table 3).

Table 2. Statistical analyses for the on-axis flexure test with various COOH-MWCNTs loadings: flexure modulus of elasticity (*E*), flexure strength (σ_u) and flexure toughness at the 3% strain level (*T*-3%).

COOH-MWCNTs	Criterion	*E* (GPa)	σ_u (MPa)	*T*-3% (MPa.mm/mm)
0 wt% (neat)	Mean	21.70	320	6.70
	STD	0.7	11.93	0.25
0.5 wt%	Mean (% increase)	20.40 (−6%)	348 (8%)	6.96 (3.9%)
	STD	0.61	6.24	0.52
1.0 wt%	Mean (% increase)	19.33 (−10%)	340 (6%)	6.77 (1.04%)
	STD	0.85	23.90	0.45
1.5 wt%	Mean (% increase)	20.40 (−6%)	344 (7%)	6.94 (3.48%)
	STD	0.82	29.28	0.36

Table 3. Statistical analyses for the off-axis flexure test with various MWCNTs loadings: flexure modulus of elasticity (*E*), flexure strength (σ_u), and flexure toughness at 5% strain level (*T*-5%).

COOH-MWCNTs	Criterion	*E* (GPa)	σ_u (MPa)	*T*-5% (MPa.mm/mm)
0 wt% (neat)	Mean	6.73	147.7	5.85
	STD	0.29	0.58	0.03
0.5 wt%	Mean (% increase)	7.00 (4%)	167.7 (13%)	6.05 (3.53%)
	STD	0.26	4.04	0.21
1.0 wt%	Mean (% increase)	7.60 (13%)	179 (21%)	6.74 (15.28%)
	STD	0.78	6.08	0.4
1.5 wt%	Mean (% increase)	8.00 (19%)	189 (28%)	7.06 (20.70%)
	STD	0.46	9.54	0.42

Previous research reported that significant damage in the matrix occurs prior to fiber reorientation and breakage when carbon woven fabric composites are loaded off-axis [32,33]. In this case, the damage in the matrix is gradual, causing significant nonlinearity in the load-displacement response. Similarly, the failure behavior of the off-axis flexure test can be therefore attributed to the damage of the epoxy matrix; thus, the effect of the multi-wall carbon nanotubes is evident. Similar findings on the significance of carbon nanotubes on the on- and off-axis tension test of composite coupons with carbon nanotubes were reported elsewhere by the authors [32]. It can be argued that the improvement in the off-axis behavior is attributed to a strong bond between the COOH functional groups attached to the MWCNTs and the epoxy groups. This bond seems to significantly improve the matrix behavior and, thus, to improve the flexure strength and modulus of the composite.

Figure 6 shows a comparison between the stress-strain curves for the on- and off-axis flexure test obtained experimentally and numerically. In general, the figure shows fair agreement between the experiments and FE simulations. However, the FE simulation fails to predict the on-axis post-peak behavior. This can be attributed to the fact that MCT is a class of FE simulation that uses a representative volume element (RVE) based on idealizing the microstructure of woven composites to develop a unit cell. The unit cell is used in the analysis and the average stress for each constituent is checked. Therefore, the FE model does not capture severe damage associated with large deformations and any change in

geometry due to fiber breakage in compression. In order to capture these effects, the complete non-linear stress-strain curves for the constituents would help in improving the prediction of the post-peak behavior. This might be outside the scope of this effort, which is concerned with identifying the composite constituent responsible for failure. Furthermore, the numerical off-axis simulation exhibited multiple drops and subsequent increases of load in a "saw-tooth"-like behavior in the stress-strain, as reported elsewhere [29]. Such behavior depends on the FE mesh size and could be attributed to matrix damage in some elements and subsequent stress redistribution to undamaged elements.

Figure 6. Comparison between experiment and FE simulation for on- and off-axis flexure behavior.

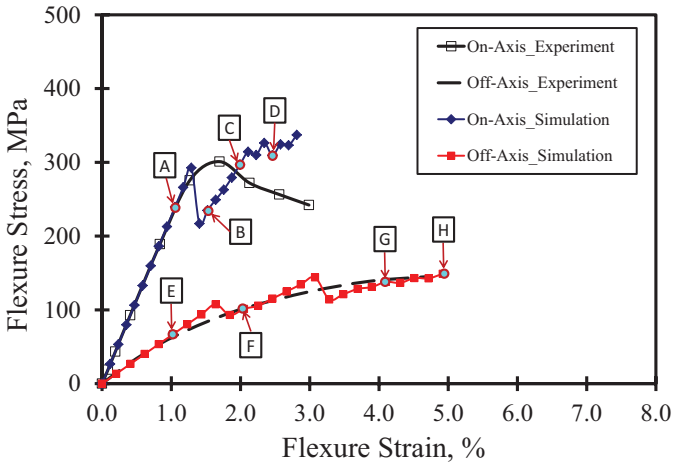

On the other hand, the FE simulation is capable of predicting the off-axis flexure behavior to a great extent. Snapshots for the undamaged and damaged regions at different strain levels are shown in Figure 7. The images from A–E correspond to the on-axis test results, while the images from F–J correspond to the off-axis test results. For the on-axis test, it is observed that significant fiber damage occurs at the 1.5% strain level in the compression zone only. As the strain increases, the fiber and matrix damage propagate. On the other hand, significant matrix damage is observed in the off-axis test at the 3% strain level prior to any fiber damage. The onset of fiber damage is observed at a relatively high strain level (4.0%) in the compression zone. The fiber damage extends through the depth at the 5.0% strain level. The FE simulation confirms the fiber domination in the on-axis flexure behavior and the matrix domination in the off-axis flexure behavior, as shown in Figure 7.

The shear stress-strain response of FRP composite plates with various contents of MWCNTs is also shown in Figure 8. The figure also displays *in situ* microscopic images of the deformation at the loaded part. The images show that no cracks were observed, as the stress was within the linear elastic zone. As the stress increased passing the linear zone, delamination between the CFRP laminates took place.

In the stress-strain curve, it can be noted that the neat epoxy CFRP composites undergo a strain softening plateau after passing the linear elastic zone. This is contrary to the majority of the COOH-MWCNT-reinforced epoxy CFRP composites, where a clear trend of the straining hardening plateau occurred after passing the linear elastic zone. We attribute the difference in the shear behavior to the improvements in the interlaminar shear strength of the epoxy matrix in the composites. Such an improvement might be explained by the chemical reaction of the functionalized

COOH-MWCNTs and the base resin. To further quantify the improvement associated with the addition of COOH-MWCNTs on the shear response, the shear toughness up to the 25% strain level is computed and compared in Figure 9. The average shear toughness was calculated for the neat, 0.5 wt%, 1.0 wt% and 1.5 wt% COOH-MWCNT cases as 2.89, 3.30, 3.86 and 3.39 MPa.mm/mm respectively. A noticeable 33% increase in the shear toughness is associated with the addition of 1.5 wt% COOH-MWCNTs compared to neat composite. This increase might be attributed to the significant increase in the inelastic energy absorption due to the strain hardening plateau associated with the addition of COOH-MWCNTs, as is apparent in Figure 8.

Figure 7. Contour plots for undamaged/damaged matrix and fibers for on- and off-axis flexure test at different strain level. (**A**) ~1.0%; (**B**) ~1.5%; (**C**) ~2.0%; (**D**) ~2.5%; (**E**) ~1.0%; (**F**) ~2.0%; (**G**) ~4.0%; (**H**) ~5.0%.

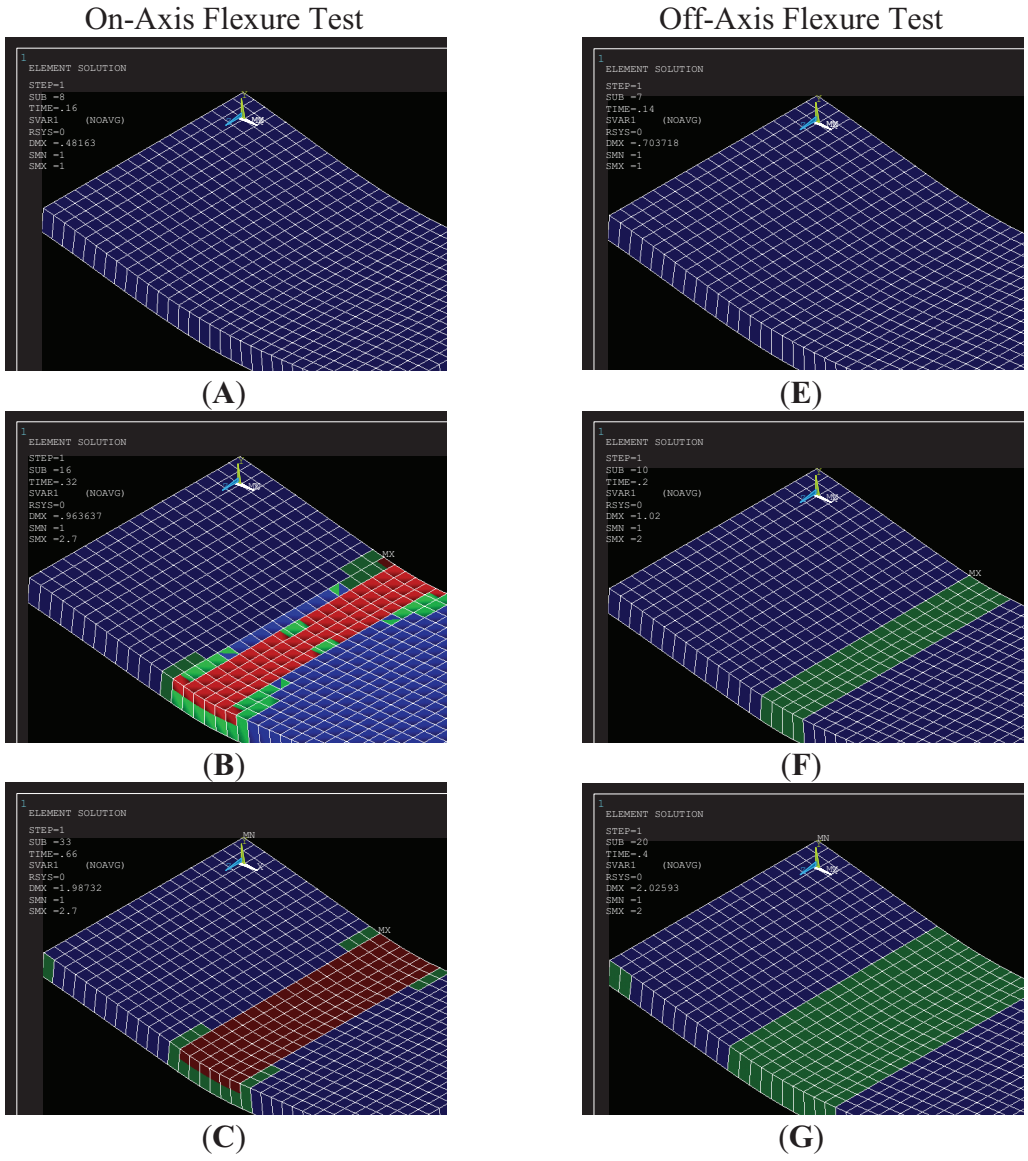

Figure 7. *Cont.*

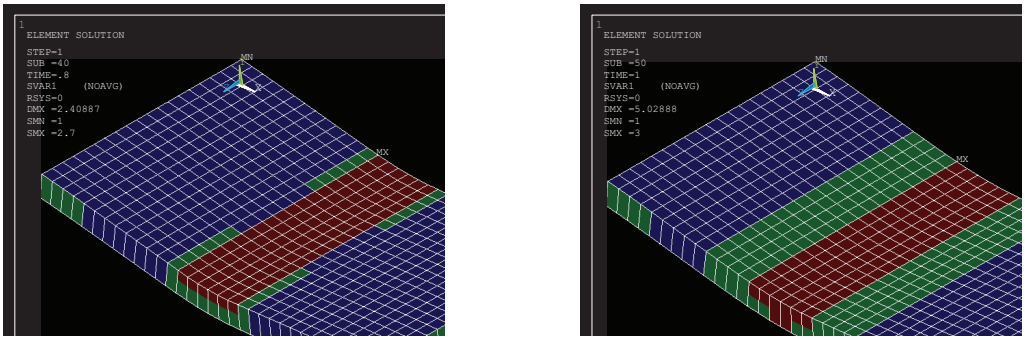

(D) **(H)**

Notes: — Undamaged matrix and undamaged fiber; — Failed matrix and undamaged fiber; — Failed matrix and failed fiber.

Figure 8. Shear stress-strain curves for composite plates with *in situ* microscopic images.

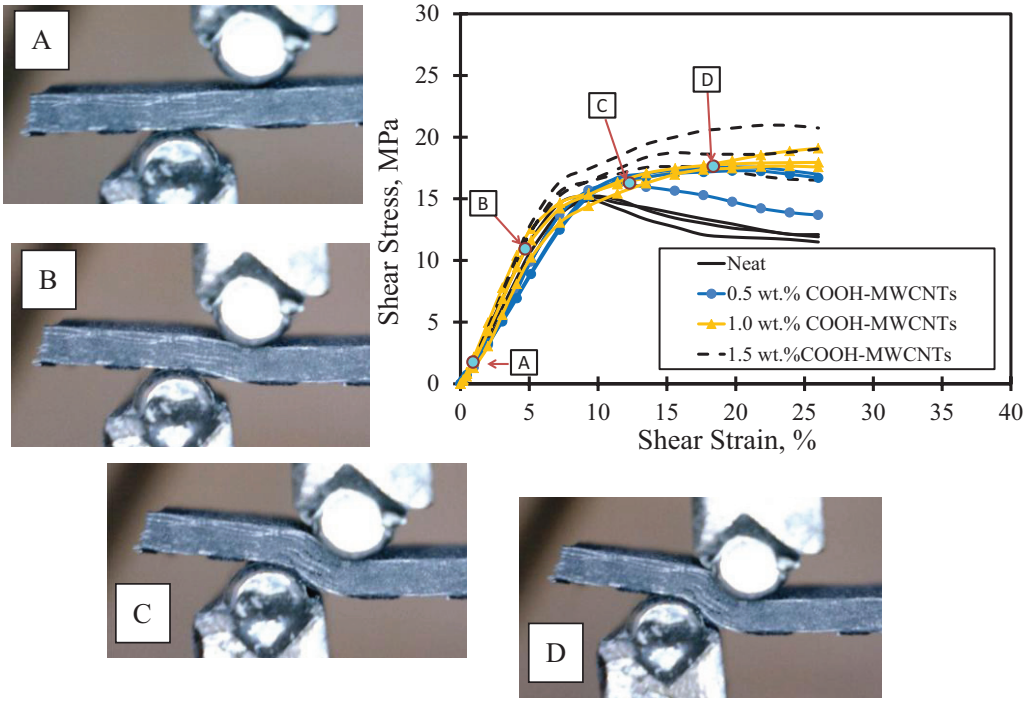

Analysis of the FTIR measurements shown in Figure 10 was performed. In Figure 10a, the characteristic vibrational modes of the carbonyl group (1710 cm^{-1}) and the hydroxyl group (3415 cm^{-1}) were observed in the spectrum of the powder-functionalized COOH-MWCNTs. We look at three cases in Figure 10b: neat epoxy, epoxy with 0.5 wt% COOH-MWCNTs and epoxy with 1 wt% COOH-MWCNTs. For the COOH-MWCNTs/epoxy, C=O stretching vibration peak (red) of the ester groups is observed at 1735 cm^{-1}, while the C=O stretching vibration peak (green) of the amide groups is at 1660 cm^{-1}, formed by the reaction of the carboxylic group in COOH-MWCNTs with the amine-based hardener. The amide groups peak at 1660 cm^{-1} and the ester group peak at 1735 cm^{-1}

are weakly apparent in 0.5 wt% COOH-MWCNTs and strongly apparent in 1 wt% COOH-MWCNTs, and are all missing in the neat epoxy.

Figure 9. Comparison of shear toughness at the 25% strain level for various wt% of COOH-MWCNTs.

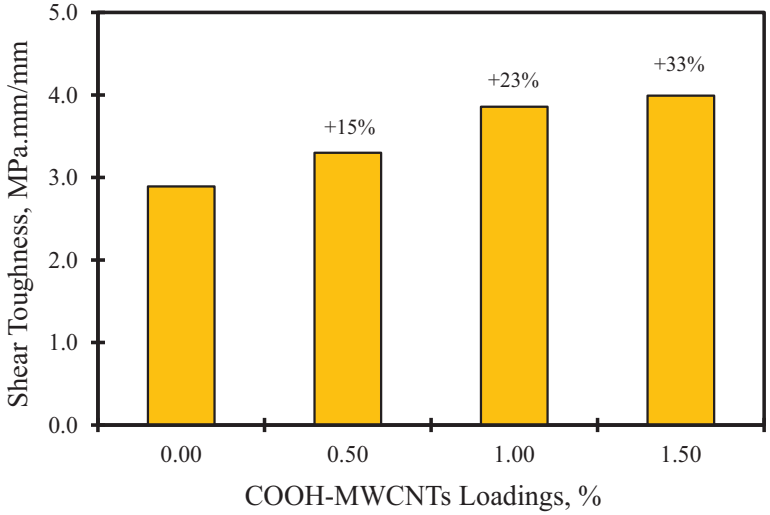

Figure 10. FTIR transmission curves of (**a**) COOH-MWCNTs powder and (**b**) COOH-MWCNTs/epoxy nanocomposites.

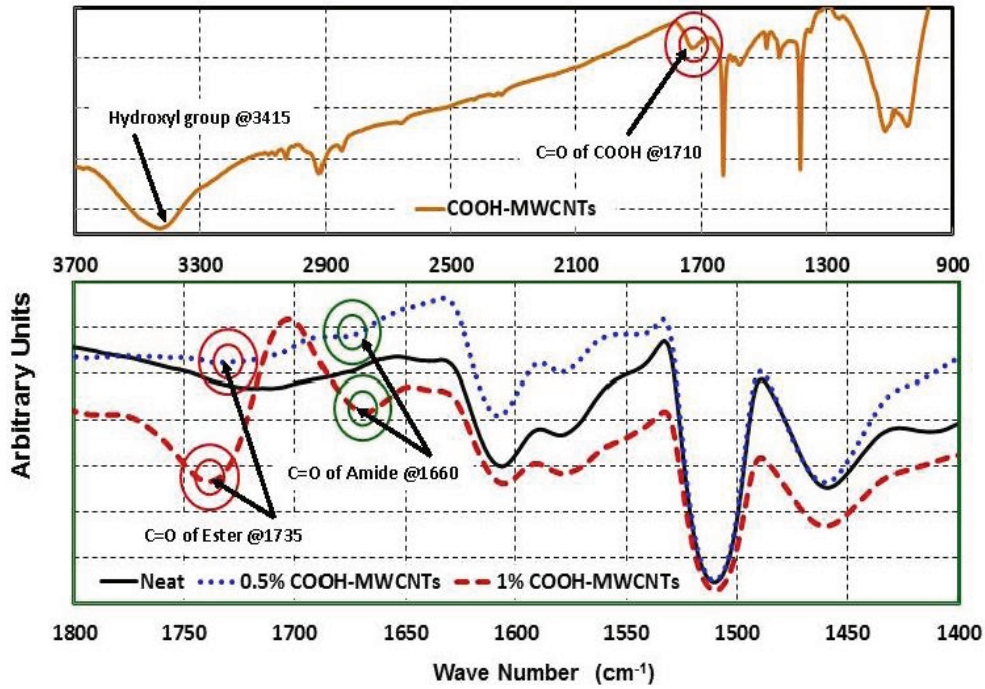

The above peaks can be explained by the fact that in neat epoxy, the carbonyl group peak is missing, due to the absence of the COOH group and the complete reaction of epoxy. In the presence of COOH-MWCNTs, part of the carboxyl groups reacted with the epoxy base in the first step of fabrication and produced ester showing the C=O red peak, which is shifted to be at 1735 cm^{-1}. This shift in the C=O peak due to COOH has been reported in the literature by Zou *et al.* [34] and Kim *et al.* [35]. This reaction might have happened via direct coupling between carboxylic group

COOH of the COOH-MWCNTs and the hydroxyl groups of the epoxy resin. The potential for such a direct reaction has been reported by Kim *et al.* [36] and can be attributed to the fact that ester formation is feasible when the stoichiometric ratio is shifted to let one component of the reactants to present in a large excess. Since the epoxy resin is in a very large excess compared with COOH, this enhances the chances of the reversible esterification reaction in the forward direction according to Le Chatelier's principle. It is also believed that the conditions of mixing COOH-MWCNTs with the epoxy resin under relatively high temperature, 40 °C for one hour then 80 °C for 2 h, would enable the removal of the small amount of water formed during esterification, which would further favor the forward esterification reaction.

In the second step of nanocomposite fabrication, the amine-based hardener was added to the epoxy base/COOH-MWCNTs dispersion. Therefore, all of the remaining carboxyl groups reacted with the hardener during the curing reaction of the epoxy and formed amide groups, which showed their C=O blue peak at 1660 cm^{-1}, as reported previously by Zhang *et al.* [37]. The FTIR observations prove our argument that the COOH functional group resulted in the reaction between the MWCNTs and the epoxy and, thus, improved the shear strength of the epoxy matrix and the bond strength of the COOH-MWCNTs/epoxy nanocomposite matrix and carbon fibers. These improvements, in turn, resulted in the observed strength, modulus and ductility improvements of the flexural and shear off-axis behavior of CFRP.

Finally, it is evident from this study that improvements of 20%–30% can be achieved in the flexure properties of woven fabric composites by incorporating 1.5 wt% COOH-MWCNTs in epoxy. Moreover, improvements reaching 45% in the post peak energy of composites can be achieved with the addition of COOH-MWCNTs. These improvements in strength and toughness can be of significant value for woven fabric composite applications governed by the shear strength of the polymer matrix. Examples include composite pipelines, armored vehicles, aircrafts/aerospace shuttles and offshore structures. Delamination and debonding in these structures due to blasts, environmental condition or cyclic loading are critical parameters in design.

4. Conclusions

In this experimental investigation, the flexure and shear behavior of the multi-scale on-axis and off-axis functionalized COOH-MWCNTs/epoxy woven carbon fabric composite plates were examined. The results showed that the flexure behavior of such thin woven fabric composite plates depends significantly on the fiber orientation. Statistically-significant improvements in the mechanical properties were observed in the off-axis flexure behavior of CFRP incorporating COOH-MWCNTs, while no significant statistical difference was observed when the flexure composite plates are loaded on-axis. By using the 1.5 wt% COOH-MWCNTs/epoxy nanocomposite, flexure strength, modulus and toughness improvements of 28%, 19% and 20.7% were achieved. FE simulation showed that the fiber dominates the on-axis flexure behavior, while the matrix dominates the off-axis flexure behavior. Furthermore, this investigation also showed that more ductile woven carbon composite plates can be obtained by incorporating COOH-MWCNTs. The improvement in the toughness can reach 33% with the addition of 1.5 wt% COOH-MWCNTs. Microstructural investigations using FTIR showed that the mechanical improvements observed might be attributed to the chemical reaction of the MWCNTs with epoxy through the COOH functional group. Such a reaction resulted

in the improved shear strength of the polymer matrix and the improved bond strength between the matrix and the carbon fibers. The above improvement in mechanical properties using COOH-MWNCTs can benefit several composite applications.

Acknowledgments

The authors greatly acknowledge funding by the U.S. National Science Foundation (NSF) to the University of New Mexico, Award No. OISE-1103601. The authors also greatly acknowledge funding by the Science and Technology Development Fund (STDF) for the U.S.-Egypt (STDF/NSF) Program, Award No. 3713, and the (STDF-CSE) Program (ID 5213) to Polymer Nanocomposites Center, EPRI, Cairo, Egypt.

Author Contributions

Usama Kandil and Eslam Soliman conducted the synthesis of COOH-MWCNTs epoxy nanocomposites. Mahmoud Reda Taha and Eslam Soliman carried out macro-scale flexure experiments and the micromechanical modeling. Mahmoud Reda Taha and Usama Kandil conducted microstructural investigation with SEM and high resolution microscope images. The three authors participated in writing the manuscripts and responding to the reviewer's comments.

Conflicts of Interest

The authors declare no conflict of interest.

References

1. American Concrete Institute. *Guide for the Design and Construction of Concrete Reinforced with FRP Bars*; American Concrete Institute: Detroit, MI, USA, 2006.
2. Hyer, M.W. *Stress Analysis of Fiber-Reinforced Composite Materials*; McGraw-Hill: New York, NY, USA, 1997; pp. 349–357.
3. Knops, M. *Analysis of Failure of Fiber Reinforced Polymer Laminates*; Springer: New York, NY, USA, 2008; pp. 2–12.
4. Agubra, V.; Owuor, P.; Hosur, M. Influence of nanoclay dispersion methods on the mechanical behavior of E-Glass/Epoxy nanocomposites. *Nanomaterials* **2013**, *2*, 550–563.
5. King, J.A.; Klimek, D.R.; Miskioglu, I.; Odegard, G.M. Mechanical properties of graphene nanoplatelet epoxy composites. *J. Appl. Polym. Sci.* **2013**, *128*, 4217–4223.
6. Iijima, S. Helical microtubules of graphitic carbon. *Nature* **1991**, *354*, 56–58.
7. Gong, X.; Liu, J.; Baskaran, S.; Voise, R.D.; Young, J.S. Surfactant-assisted processing of carbon nanotube/polymer composites. *Chem. Mater.* **2000**, *12*, 1049–1052.
8. Islam, M.F.; Rojas, E.; Bergey, D.M.; Johnson, A.T.; Yodh, A.G. High weight fraction surfactant solubilization of single-wall carbon nanotubes in water. *Nano Lett.* **2003**, *3*, 269–273.
9. Geng, Y.; Liu, M.Y.; Li, J.; Shi, X.M.; Kim, J.K. Effects of surfactant treatment on mechanical and electrical properties of CNT/epoxy nanocomposites. *Compos. Part A* **2008**, *39*, 1876–1883.

10. Zhu, J.; Kim, J.D.; Peng, H.; Margrave, J.L.; Khabashesku, V.N.; Barrera, E.V. Improving the dispersion and integration of single-walled carbon nanotubes in epoxy composites through functionalization. *Nano Lett.* **2003**, *3*, 1107–1113.
11. Breton, Y.; Desarmot, G.; Salvetat, J.P.; Delpeux, S.; Sinturel, C.; Beguin, F.; Bonnamy, S. Mechanical properties of MWNT/epoxy composites: Influence of network morphology. *Carbon* **2004**, *42*, 1027–1030.
12. Gojny, F.H.; Wichmann, M.; Fiedler, B.; Schulte, K. Influence of different carbon nanotubes on the mechanical properties of epoxy matrix composites—A comparative study. *Compos. Sci. Technol.* **2005**, *65*, 2300–2313.
13. Ma, P.C.; Siddiqui, N.A.; Marom, G.; Kim, J.K. Dispersion and functionalization of carbon nanotubes for polymer-based nanocomposites: A review. *Compos. Part A* **2010**, *41*, 1345–1367.
14. Sahoo, N.G.; Rana, S.; Cho, J.W.; Li, L.; Chana, S.W. Polymer nanocomposites based on functionalized carbon nanotubes. *Prog. Polym. Sci.* **2010**, *35*, 837–867.
15. Spitalsky, Z.; Tasisb, D.; Papagelis, K.; Galiotis, C. Carbon nanotube-polymer composites: Chemistry, processing, mechanical and electrical properties. *Prog. Polym. Sci.* **2010**, *35*, 357–401.
16. Qiu, J.; Zhang, C.; Wang, B.; Liang, R. Carbon nanotube integrated multifunctional multiscale composites. *Nanotechnology* **2007**, *18*, 1–11.
17. Seyhan, A.T.; Tanoglu, M.; Schulte, K. Mode I and mode II fracture toughness of E-glass non-crimp fabric/carbon nanotube (CNT) modified polymer based composites. *Eng. Fract. Mech.* **2008**, *75*, 5151–5162.
18. Garcia, E.J.; Wardle, B.L.; Hart, A.J. Joining prepreg composite interfaces with aligned carbon nanotubes. *Compos. Part A* **2008**, *39*, 1065–1070.
19. Chandrasekaran, V.C.S.; Advani, S.G.; Santare, M.H. Role of processing on interlaminar shear strength enhancement of epoxy/glass fiber/multi-walled carbon nanotube hybrid composites. *Carbon* **2010**, *48*, 3692–3699.
20. Hossain, M.K.; Hossain, M.E.; Hosur, M.V.; Jeelani, S. Flexural and compression response of woven E-glass/polyester-CNF nanophased composites. *Compos. Part A* **2011**, *42*, 1774–1782.
21. Aldajah, S.; Haik, Y. Transverse strength enhancement of carbon fiber reinforced polymer composites by means of magnetically aligned carbon nanotubes. *Mater. Des.* **2012**, *34*, 379–383.
22. ASTM D5687/D5687M–95. *Standard Guide for Preparation of Flat Composite Panels with Processing Guidelines for Specimen Preparation*; ASTM International: West Conshohocken, PA, USA, 2007.
23. ASTM D3171–06. *Standard Test Methods for Constituent Content of Composite Materials*; ASTM International: West Conshohocken, PA, USA, 2006.
24. De Almeida, S.F.M. Effect of void content on the strength of composite laminates. *Compos. Struct.* **1994**, *28*, 139–148.
25. Zhu, H.Y.; Li, D.H.; Zhang, D.X.; Wu, B.C.; Chen, Y.Y. Influence of voids on interlaminar shear strength of carbon/epoxy fabric laminates. *Trans. Nonferr. Met. Soc. China* **2009**, *19*, S470–S475.

26. Madsen, B.; Lilholt, H. Physical and mechanical properties of unidirectional plant fibre composites—An evaluation of the influence of porosity. *Compos. Sci. Technol.* **2003**, *63*, 1265–1272.
27. *ASTM D790–10 Standard Test Methods for Flexural Properties of Unreinforced and Reinforced Plastics and Electrical Insulating Materials*; ASTM International: West Conshohocken, PA, USA, 2010.
28. Stefanie, A.S.; Jae-Hwang, L.; Joseph, J.W.; Edwin, L.T.; Timothy, M.S. Epoxy functionalized multi-walled carbon nanotubes for improved adhesives. *Carbon* **2013**, *59*, 109–120.
29. Mayes, J.; Hansen, A. Multicontinuum failure analysis of composite structural laminates. *Mech. Compos. Mater. Struct.* **2001**, *8*, 249–262.
30. Key, C.T.; Six, R.W.; Hansen, A.C. A three-constituent multicontinuum theory for woven fabric composite materials. *Compos. Sci. Technol.* **2003**, *63*, 1857–1864.
31. Mayes, J.; Hansen, A. A Comparison of multicontinuum theory based failure simulation with experimental results. *Compos. Sci. Technol.* **2004**, *64*, 517–527.
32. Soliman, E.; al-Haik, M.; Reda Taha, M. On and off-axis tension behavior of fiber reinforced polymer composites incorporating multi-walled carbon nanotubes. *J. Compos. Mater.* **2012**, *47*, 1–15.
33. Naik, N.K.; Shembekar, P.S.; Hosur, M.V. Failure behavior of woven fabric composites. *J. Compos. Technol. Res.* **1991**, *13*, 107–116.
34. Zou, W.; Du, Z.; Liu, Y.; Yang, X.; Li, H.; Zhang, C. Functionalization of MWNTs using polyacryloyl chloride and the properties of CNT-epoxy matrix nanocomposites. *Compos. Sci. Technol.* **2008**, *68*, 3259–3264.
35. Kim, W.-J.; Kang, S.-O.; Ah, C.S.; Lee, Y.-W.; Ha, D.H.; Choi, I.S.; Yun, W.S. Functionalization of Shortened SWCNTs using esterification. *Bull. Korean Chem. Soc.* **2004**, *25*, 1301–1302.
36. Kim, S.W.; Kim, T.; Kim, Y.S.; Choi, H.S.; Lim, H.J.; Yang, S.J.; Park, C.R. Surface modifications for the effective dispersion of carbon nanotubes in solvents and polymers. *Carbon* **2012**, *50*, 3–33.
37. Zhang, T.; Xu, M.; He, L.; Xi, K.; Gu, M.; Jiang, Z. Synthesis, characterization and cytotoxicity of phosphoryl choline-grafted water-soluble carbon nanotubes. *Carbon* **2008**, *46*, 1782–1791.

Hybrid Composites Based on Carbon Fiber/Carbon Nanofilament Reinforcement

Mehran Tehrani, Ayoub Yari Boroujeni, Claudia Luhrs, Jonathan Phillips and Marwan S. Al-Haik

Abstract: Carbon nanofilament and nanotubes (CNTs) have shown promise for enhancing the mechanical properties of fiber-reinforced composites (FRPs) and imparting multi-functionalities to them. While direct mixing of carbon nanofilaments with the polymer matrix in FRPs has several drawbacks, a high volume of uniform nanofilaments can be directly grown on fiber surfaces prior to composite fabrication. This study demonstrates the ability to create carbon nanofilaments on the surface of carbon fibers employing a synthesis method, graphitic structures by design (GSD), in which carbon structures are grown from fuel mixtures using nickel particles as the catalyst. The synthesis technique is proven feasible to grow nanofilament structures—from ethylene mixtures at 550 °C—on commercial polyacrylonitrile (PAN)-based carbon fibers. Raman spectroscopy and electron microscopy were employed to characterize the surface-grown carbon species. For comparison purposes, a catalytic chemical vapor deposition (CCVD) technique was also utilized to grow multiwall CNTs (MWCNTs) on carbon fiber yarns. The mechanical characterization showed that composites using the GSD-grown carbon nanofilaments outperform those using the CCVD-grown CNTs in terms of stiffness and tensile strength. The results suggest that further optimization of the GSD growth time, patterning and thermal shield coating of the carbon fibers is required to fully materialize the potential benefits of the GSD technique.

Reprinted from *Materials*. Cite as: Tehrani, M.; Boroujeni, A.Y.; Luhrs, C.; Phillips, J.; al-Haik, M.S. Hybrid Composites Based on Carbon Fiber/Carbon Nanofilament Reinforcement. *Materials* **2014**, *7*, 4182ï 4195.

1. Introduction

Fiber-reinforced polymer plastics (FRPs) possess superior specific strengths and stiffness in comparison to other structural composites, such as metal or ceramic-reinforced composites. The relative ease of manufacturing, light weight, wide range of physical properties and high corrosion resistance make FRPs very desirable for several applications [1,2].

Compared to other structural fibers, carbon fibers are utilized when fatigue resistance, moderate strength and electrical conductivity are needed and when weight savings are crucial. Recently, nanofilament forms of carbon reinforcement, such as carbon nanotubes (CNTs) and carbon nanofibers [3], have gained growing interest in the composites community, due to their attractive mechanical properties. However, researchers have attempted to incorporate CNTs in polymer matrices and have met limited success, due to the extreme difficulty in uniformly dispersing CNTs in polymeric matrices, because of the large surface area of CNTs [4]. The high-aspect ratio CNTs tend to entangle and form agglomerates when dispersed into a viscous polymeric matrix. Sonication [3] and calendaring [5] have been employed extensively to mitigate this problem, but both techniques are not

feasible beyond ~3.0 wt% CNT, due to the formation of aggregates [6]. A combination of dispersion and extrusion techniques have been reported in the literature for producing CNT composites [6] with a tailored microstructure, e.g., aligned CNTs. However, in both dispersion and extrusion techniques, producing uniform and well-dispersed CNT composites is difficult, due to the phase separation stemming from the stronger van der Waals interactions amongst the CNTs bundles compared with that between the CNTs and the polymer matrix [7]. Furthermore, excessive sonication of CNTs toward better dispersion might result in breaking them into shorter tubes, thus reducing their aspect ratios [8] and, consequently, negatively affecting their derived composite mechanical performance.

One viable alternative to prevent nanofilaments agglomeration is to anchor one end of the nanofilament to the substrate, thereby creating a stable multiscale structure. This approach can be implemented by physically growing the nanofilaments directly on the surface of the substrate (in this study, the substrate is micro-scale carbon fiber bundles). Carbon nanotubes have been grown on most substrates, such as silicon, silica and alumina [9]. However, there are fewer reports discussing CNT growth on carbon materials; in particular, yarns and fabrics [10]. Two challenges face CNT growth on carbon substrates, namely: (i) the transition metals that catalyze the CNTs growth can easily diffuse into the carbon substrates and; (ii) different phases of carbon materials are able to form on the graphite substrates, because the CNT growth conditions are identical to the graphite or diamond-like carbon growth [11].

Recently, carbon nanofilaments were grown on carbon fibers, both polyacrylonitrile- (PAN) and pitch-based, by hot filament chemical vapor deposition (HFCVD) using H_2 and CH_4 as precursors [12]. Nickel clusters were electrodeposited on the fiber surfaces to catalyze the growth, and uniform CNT coatings were obtained on both the PAN and pitch-based carbon fibers. Multi-walled CNTs with smooth walls and low impurity content were also grown on a carbon fiber cloth using plasma-enhanced chemical vapor deposition (PECVD) from a mixture of acetylene and ammonia [13]. In this case, a cobalt colloid was utilized to achieve the good coverage of nanofibers on the carbon cloth. The main draw back to CNT growth via CVD is the damage induced on the carbon fiber surface due to the high-temperature synthesis (>750 °C) [11,12]. Qu *et al.* [14] reported a new method for the uniform deposition of CNTs on carbon fibers. However, this method requires processing at 1100 °C in the presence of oxygen, and such a high temperature is anticipated to severely damage the carbon fibers. One approach to circumvent the thermal damage due to the synthesis at elevated temperature environments is to utilize ceramic-based thermal barrier coatings, such as SiC or SiO_2.

In this study, carbon nano-filaments were grown utilizing a moderate temperature (*i.e.*, 550 °C) under atmospheric pressure. This atmospheric pressure process, derived from the process, graphitic structures by design (GSD) [15,16], is rapid, and the temperature is low enough (*i.e.*, 550 °C) to avoid severe structural damage to the substrate macroscale carbon fibers; and, the process is inexpensive and readily scalable. The GSD process does not utilize any toxic hydrocarbons or catalysts (e.g., xylene and metallocene) unlike CCVD [17]. Finally, GSD could offer the opportunity to place CNTs in pre-designated locations where the catalyst is pre-deposited. In contrast, utilizing the CCVD technique, CNTs grow everywhere. This investigation sheds some light on the effect of

the growth technique on the quasistatic mechanical properties of FRPs made out of a hybrid reinforcement that utilizes carbon nanofilaments grown on the surface of carbon fibers.

2. Results and Discussion

Based on previous experiences, the nickel film should be fragmented into particles to grow carbon nanofilaments via GSD; otherwise, it might lead to the growth of either graphene of graphite [18]. A reduction step at 550 °C under a N_2-H_2 environment was carried out for 2 h under atmospheric pressure to fragment the nickel film into nanometer-sized particles and to remove any nickel oxides (Figure 1a). These particles are retained on the tips of the nanofilaments grown via GSD, as shown in Figure 1b.

Figure 1. SEM micrographs for (**a**) nickel particles formed after the reduction process under N_2-H_2 at 550 °C; (**b**) nanofilaments grown utilizing the graphitic structures by design (GSD) technique with nickel particles attached to their tips.

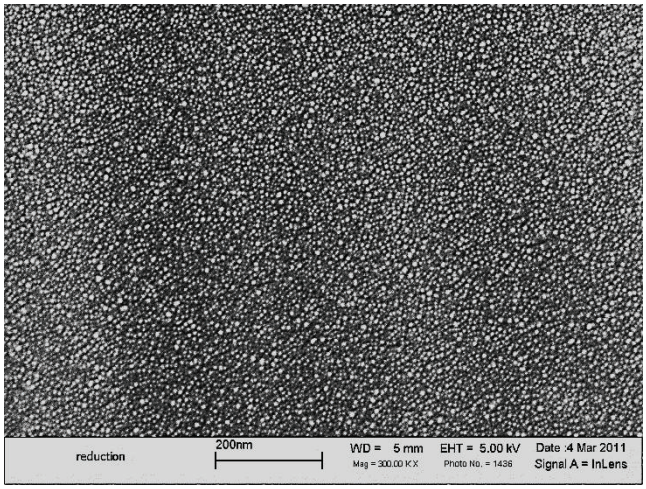

(**a**)

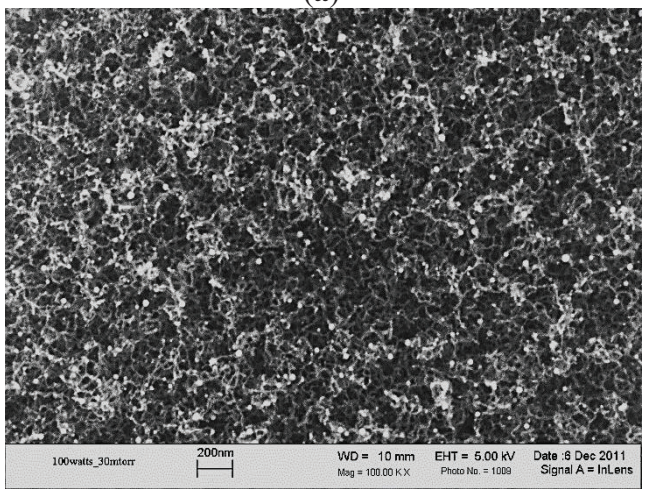

(**b**)

The SEM micrographs in Figure 2a,b exhibit a uniform growth of CNTs utilizing GSD and CCVD techniques, respectively, on the surface of PAN-based carbon fibers, where the nickel catalytic particles were deposited (for the case of GSD). Both fibers were precoated with 75 nm-thick films of SiO_2, in anticipation of better thermal shielding against the synthesis temperature. The

morphologies of the grown nanofilaments are shown in the TEM micrographs (Figure 2c,d). The GSD-synthesized nanofilament does not exhibit well-defined walls and possesses a diameter of less than 20 nm, whereas the CCVD yielded better defined multiwall CNTs (MWCNTs) with variable diameters.

Figure 2. The SEM micrograph of nanofilaments grown via (**a**) GSD and (**b**) chemical vapor deposition (CCVD); The TEM micrograph of the morphologies of nanofilaments grown via (**c**) GSD and (**d**) CCVD.

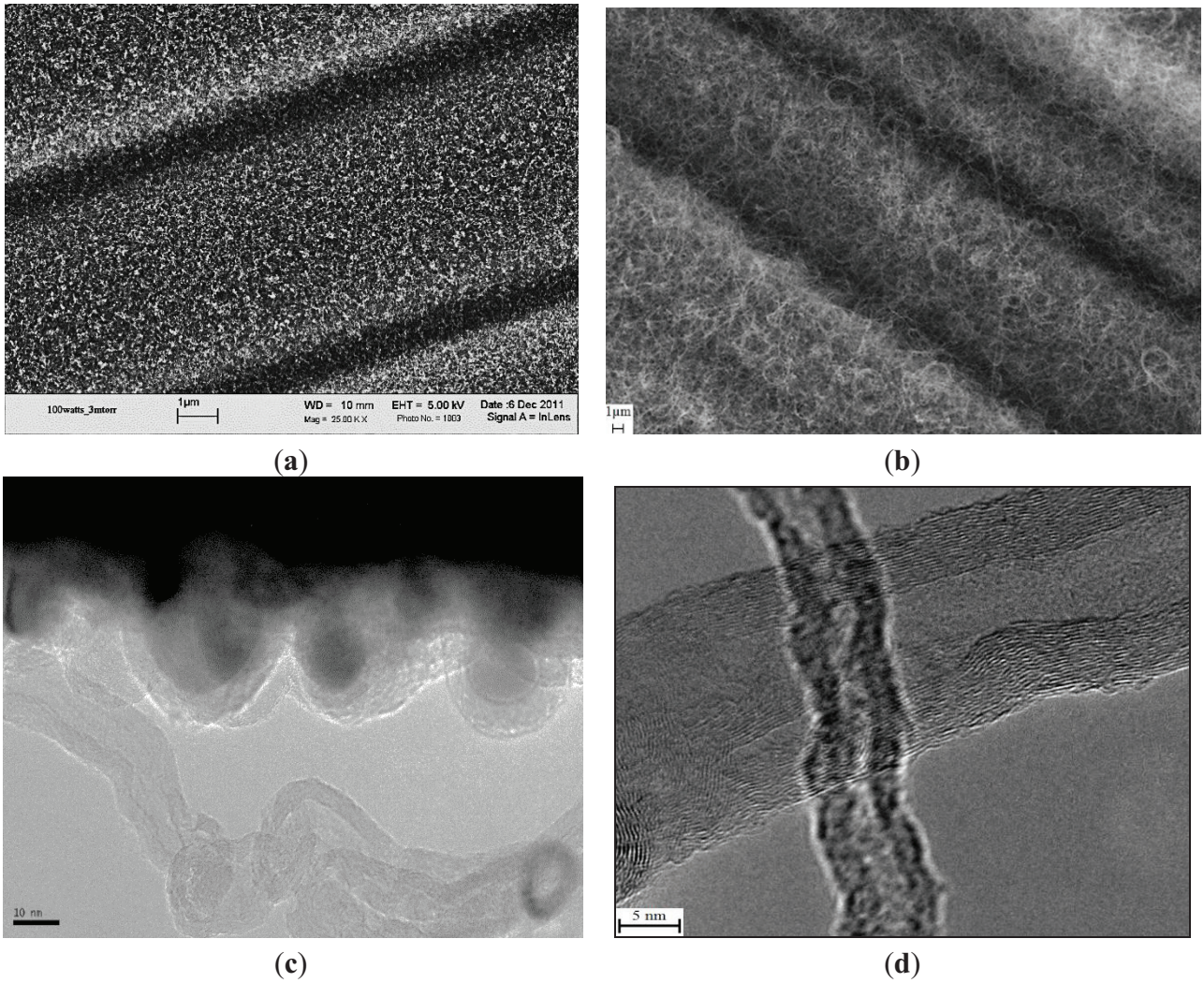

(**a**) (**b**)

(**c**) (**d**)

Since the samples comprising the surface-grown nanofilaments were exposed to elevated temperatures (*i.e.*, 550–680 °C), reference samples of raw fabric and SiO_2 sputter-coated fabric were exposed to an identical thermal environment similar to GSD (except for prohibiting the growth without the flowing of hydrocarbon gas) for later comparison. These samples are referred to as "heat treated" throughout this study. The Raman spectra were measured for the raw PAN-based carbon fabric, SiO_2 sputter-coated fabric, heat-treated fabric, heat-treated SiO_2 sputter-coated fabric and samples with CNTs grown on their surfaces via the GSD and CCVD techniques. While the as-sputtered nickel thin film is amorphous, evidenced by the ordered fringe patterns of Figure 3, upon fragmentation and reduction, the nickel particles become crystalline.

For carbonaceous materials, the Raman spectra exhibit two distinct bands. The disorder induced D band at 1354.7 cm^{-1} in the MWCNT spectra and between 1330 and 1390 cm^{-1} in single wall carbon nanotubes (SWCNT) The tangential mode G band, related to the ordered graphitic structure, appears at 1581.2 cm^{-1} for the MWCNT and between 1595 and 1605 cm^{-1} for the SWCNT [19].

Figure 3. The TEM micrograph of a nickel particle from which a carbon nanofilament was grown.

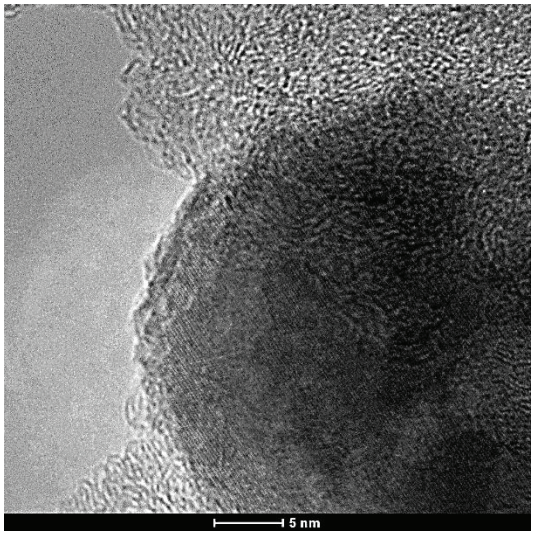

Raman peaks (Figure 4) for all of the samples without nanofilament growth are very weak, regardless of the prior surface treatment, and do not exhibit the presence of a crystalline form of carbon. The raw carbon fibers did not display significant peaks. It is well known that PAN-based carbon fibers do not exhibit the G band (unlike graphitic pitch-based fibers); rather, they exhibit the turbostratic appearance of the D line, which corresponds to the structural disorder caused by the existence of the sp^3 bonds [20].

Figure 4. Raman spectra of the surfaces of different processed carbon fibers. Specimens are based on raw polyacrylonitrile (PAN)-based carbon fabric (Raw), SiO_2 sputter-coated fabric (Sp), heat-treated fabric (HT), SiO_2 sputter-coated then heat-treated fabric (Sp + HT), and with CNTs grown on their surfaces via graphitic structures by design (GSD) and catalytic chemical vapor deposition (CCVD).

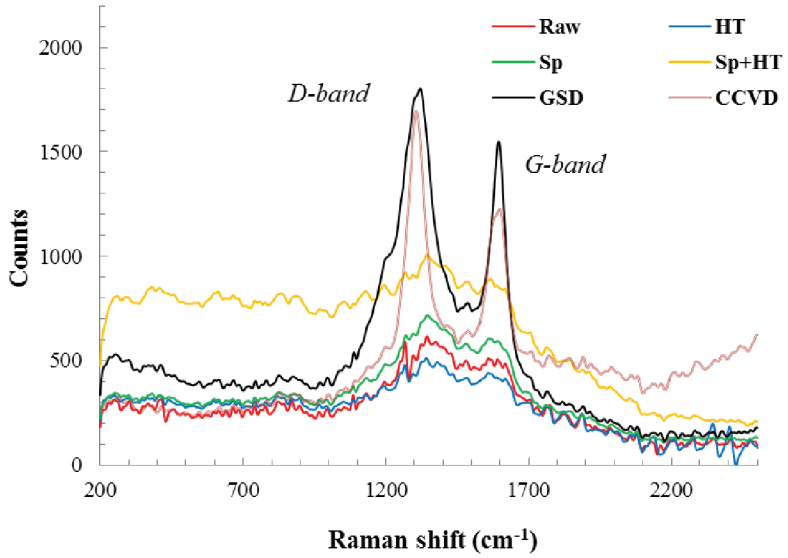

Sputtering the fibers with nickel and SiO_2 films assisted in contrasting the G band for the fibers. Furthermore, heat treating of the samples with the deposited films made the D and G bands more pronounced. The CNTs grown on the surfaces of the PAN-based carbon fiber fabric via GSD or CCVD demonstrate the D-band center value at 1350 cm^{-1} and the G-band at 1580 cm^{-1}, respectively; in good agreement with those of the Raman spectra of MWCNTs. Although these peaks are also observed for graphite [21], it is evident from the SEM and TEM micrographs of the nanofilaments that the Raman peaks cannot be from graphite.

The intensity ratio of the two bands (I_D/I_G) can be conceded as a quantitative measure of the amount of structurally-ordered graphite crystallite in the carbonaceous material. From Figure 4, the decrease in the intensity ratio (I_D/I_G) was more noticeable for the carbon fibers with MWCNTs grown by CCVD. This reveals that the degree of crystallinity of the MWCNTs grown using CCVD is higher than that for the nanofilaments grown via GSD. Moreover, the width of the D peak for the CCVD sample is narrower than that for the sample prepared via GSD. This is indicative of a higher degree of order in the MWCNTs prepared via CCVD compared to the nanofilaments grown via GSD, which was confirmed by the TEM images, Figure 2c,d.

The stiffness of the two-lamina composites is governed by the carbon fiber's core and, hence, is less likely to be affected by the elevated temperatures of CCVD and GSD if an inert atmosphere is employed. However, the tensile strength is highly influenced by the quality of the surface of the carbon fibers and the strength of the adhesion (uniform stress transfer) between the matrix and the fibers. Therefore, the ultimate tensile strength is expected to be affected by the surface coating, heat treatment and the growth time.

The morphology, length and density of the grown CNTs or nanofilaments are postulated to affect the polymer matrix infusion into the CNT or nanofilament layer and, subsequently, the

interfacial bonding at the fiber/epoxy interface. Figure 5 shows SEM micrograph of a cross-sectional view of carbon fiber covered with a dense layer of GSD-grown nanofilament. The thickness of the layer (1 h growth time) is almost 0.5 microns. The length of the grown CNTs can be controlled by the initial thickness of the nickel layer and the growth time. The filament layer seems to be coherent and connected to the surface of the PAN carbon fibers. However, to attain a good adhesion between the polymer/fiber, it is imperative that the polymer matrix infuses into the dense CNT forest.

The carbon monofilaments only grew on the exposed fiber bundles on the upper and lower surfaces of the woven carbon fabrics (*i.e.*, what will be the ply interfaces in a composite lamina). However, they did not influence the polymer matrix penetration to the regions adjacent to the grown nanofilaments (see Figure 6). As observed from the SEM micrographs of the cross-sections of different samples (Figure 7), the overall penetration of the matrix seems to be identical for all the samples. However, while grafting of CNTs was achieved with a minimal weight penalty, it affected the volume fractions of the composite panels. The volume fractions for different composite configurations are summarized in Table 1.

The tensile test results were, therefore, normalized with respect to the corresponding volume fractions according to the composites rule of mixture. Although the rule of mixture does not provide the most accurate prediction of tensile properties, it is employed here to justify the comparison between the different samples and to provide a better contrast of the effects of the different surface treatments on the tensile properties. The results of the tension tests are summarized in Table 2.

Figure 5. Cross-sectional SEM micrograph of a carbon fiber grafted with surface-grown carbon nanofilament utilizing the GSD technique.

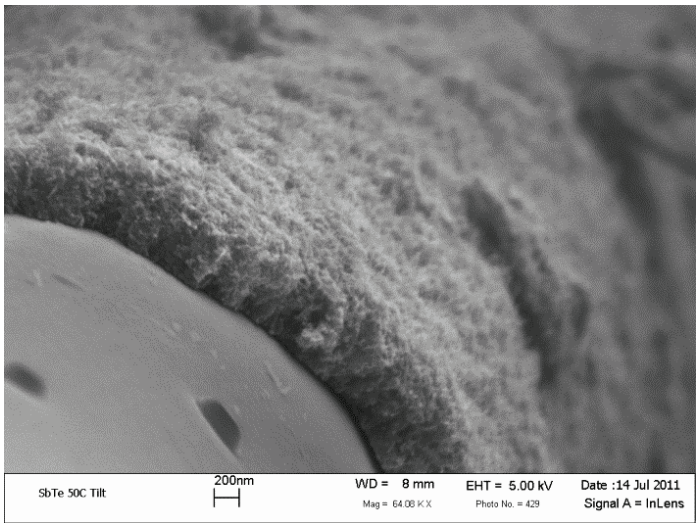

Figure 6. Polymer matrix penetration of the region adjacent to the nanofilaments for the composites based on the (**a**) CCVD and (**b**) GSD methods.

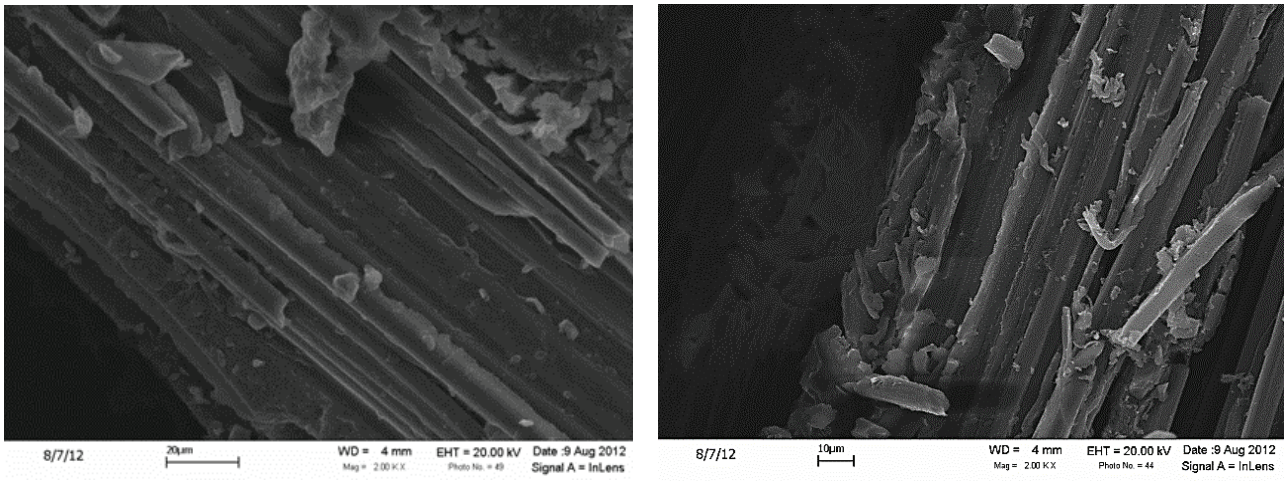

(**a**) (**b**)

The normalized mechanical properties (Table 2) indicate that the stiffness of the composite was retained upon exposure to moderate temperatures (*i.e.*, 550 °C in N_2 atmosphere). This observation is manifested by the heat-treated fabric (HT) and the HT and SiO_2 sputter-coated fabric (HT + Sp) samples. The surface alteration via coating with SiO_2 and the heat treatment or the presence of GSD-CNTs on the surface resulted in an increase in the stiffness (see Table 2). However, the sample with CCVD-grown CNTs on the SiO_2 layer exhibited a slight degradation of almost 4% in the stiffness of the corresponding composite. This degradation can be attributed to the higher temperature of the CCVD reaction that accelerates carbon diffusions and partially deteriorates the carbon fiber and, to a lesser extent, to the poor adhesion between the epoxy/fibers and CNT/fiber.

Figure 7. The cross-sections of all fabricated composite samples were investigated under scanning electron microscopy (SEM). The cross-sectional images of all samples, as well as the magnified images for the GSD and CCVD samples are shown below. The SEM micrographs show the same level of matrix penetration for all samples. (**a**) R; (**b**) R + HT; (**c**) Sp + HT; (**d**) GSD; (**e**) CCVD.

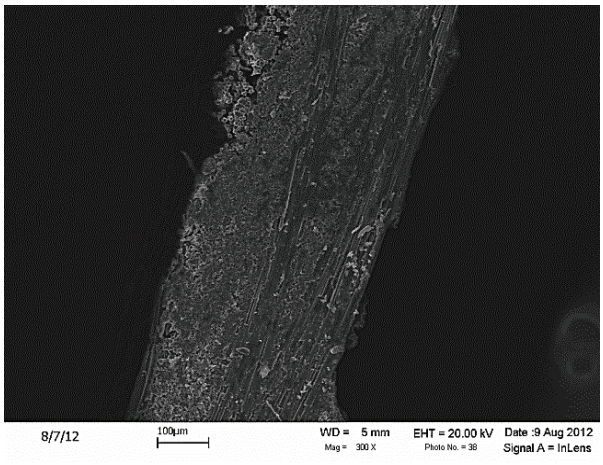

(**a**)

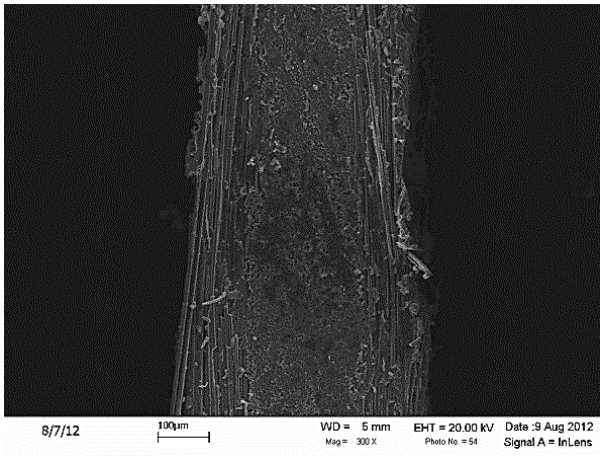

(**b**)

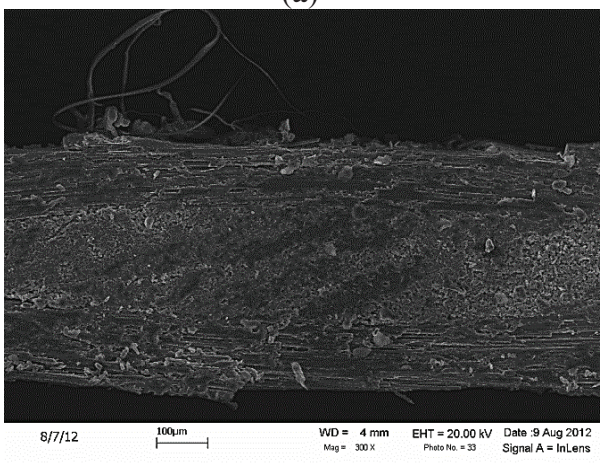

(**c**)

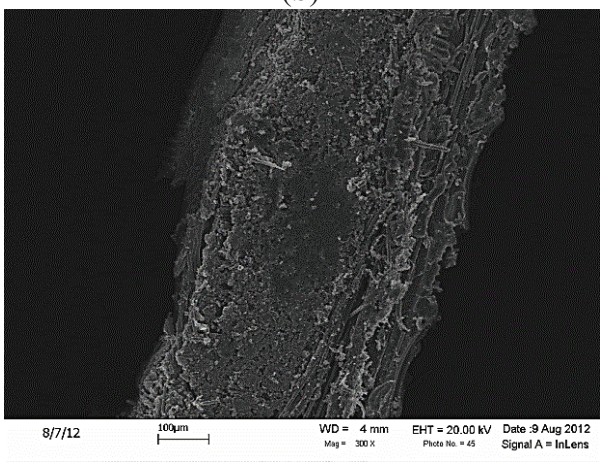

(**d**)

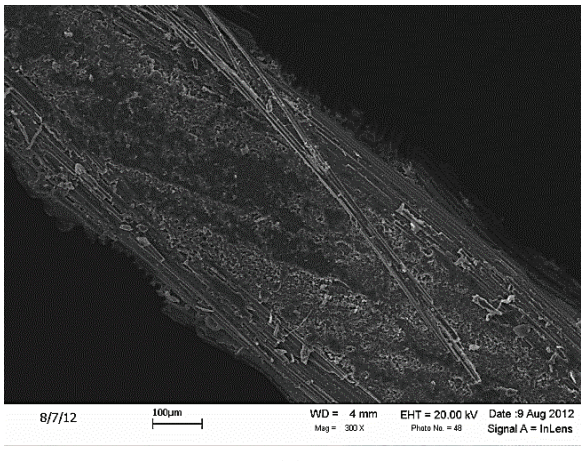

(**e**)

Table 1. Fiber volume fractions for the specimens based on raw PAN-based carbon fabric (Raw), SiO_2 sputter-coated fabric (Sp), heat-treated fabric (HT), SiO_2 sputter-coated then heat-treated fabric (Sp + HT) and with CNTs grown on their surfaces via graphitic structures by design (GSD) and catalytic chemical vapor deposition (CCVD).

Composite Sample	Label	V_f (%)
Raw	R	56
Heat treated	HT	57
SiO_2 sputter-coated	Sp	55
SiO_2 sputter-coated then heat treated	Sp + HT	54
CNT grown with GSD	GSD	49
CNT grown with CCVD	CCVD	49

Table 2. Tensile mechanical properties for the specimens based on raw PAN-based carbon fabric (Raw), SiO_2 sputter-coated fabric (Sp), heat-treated fabric (HT), SiO_2 sputter-coated then heat-treated fabric (Sp + HT) and with CNTs grown on their surfaces via GSD and CCVD.

Fiber's configuration	Young's modulus (GPa)	Tensile strength (MPa)
Raw	40.4 ± 1.2	606 ± 31
HT	41.4 ± 0.9	556 ± 44
Sp	40.6 ± 3.6	547 ± 42
Sp + HT	44.1 ± 1.4	557 ± 27
GSD	43.7 ± 2.6	585 ± 37
CCVD	38.9 ± 4.8	184 ± 10

Heat treatment of the carbon fabric also leads to the removal of the sizing and, thus, alteration of the surface of the fibers. Removing the sizing through heat treatment resulted in an 8% reduction in the strength of the composite compared to the reference composite with the sizing intact (Table 2). The introduction of the SiO_2 layer (Sp sample) lessens the bonding between the epoxy and fibers and, thus, induces a slight reduction in the strength of the composite. The heat treatment of the sputter-coated fabrics (see the Sp + HT sample) does not appear to influence the adhesion of fiber/matrix and the strength of the composites; the strength of the Sp and the Sp + HT composites were virtually identical.

Grafting the nanofilaments directly onto the fibers allows for the placement of high volume fractions of un-agglomerated nanofillers. This volume fraction is far larger than what can be effectively achieved when CNTs are pre-mixed with the epoxy matrix (typically within 3% for proper dispersion). It is speculated that the highly viscous matrix (viscosity of 950 cps) might not be efficient in fully impregnating the dense surface-grown nanofilament forests. Conversely, the enhanced fiber/matrix adhesion due to the interactions between the surface grown CNTs and the polymer matrix yielded an improved stress transfer to the fibers compared to all other samples with modified surfaces (*i.e.*, Sp, Sp + HT and HT).

The composite based on the GSD grown nanofilaments counterbalanced some of the undesired effects from the presence of the SiO_2 layer and heat treatment on the strength. While the strength of the GSD samples improved by 5% compared to the Sp + Ht ones, it was still 3.5% lower than the

strength of the reference samples. Nevertheless, the harsh thermal environment of CCVD (*i.e.*, exposure to the temperature of 680 °C) causes drastic degradation of the fibers due to temperature-accelerated diffusion and oxidation of carbon, which deteriorates the carbon fiber core and surface. Moreover, the surface of the fibers is malformed due to the presence of nanofilaments (possibly not fully attached to the fiber) on the surface of the SiO_2-coated carbon fibers. Test coupons based on FRPs with CCVD surface-grown CNTs ruptured in a very brittle manner. A 70% decrease in the strength of the composites based on CCVD-CNTs can be primarily attributed to the severe degradation of the fiber surfaces, due to the elevated synthesis temperatures. Among the tested samples, only the SiO_2-coated (Sp) and SiO_2-coated/heat-treated (Sp + HT) samples exhibited delamination during the tension tests.

The carbon fiber samples were weighed pre- and post-processing in the synthesis reactor. The measurements were repeated for the samples with SiO_2 coating only (the Sp + HT sample was considered as the reference for calculating the weight of CNTs) and for the samples with SiO_2 coating and nickel catalyst (the ones that CNTs grow on later). Utilizing a digital scale with an accuracy of ±0.0001 g, we conclude that for both samples processed via GSD and CCVD, the weight fractions of the CNTs in the composite is less than 0.05 wt%.

The hand layup process that was used for the fabrication of the panels does not effectively control the volume fractions of composites. However, the normalized tensile test results confirmed the hypothesis that the core of the fibers is unaffected by the elevated reaction temperatures of both GSD and CCVD.

Among all the samples, the tensile strength of the panels fabricated from the CCVD-processed fabrics degraded significantly. Thermally-induced surface damage to the fiber surface and the weak interaction between the surface CNTs and polymer matrix are the main reasons for the mechanical weakening of the CCVD composite samples. The conclusion that can be drawn is that the CCVD technique allows for the placement of high-quality crystalline CNTs (compared to the nanofilaments grown via GSD) at the price of significantly degrading the mechanical properties, due to the severe substrate fiber damage.

The reduction of tensile properties of the GSD samples (Table 2) is at worst 3.5% for the strength. The CCVD yielded even more significant reductions of 4% and 70% for the modulus and the strength, respectively. The degradation of the composites properties due to thermal annealing of the base carbon fibers during CCVD was observed by several other groups. For example, when utilizing CCVD for growing CNTs on the surface of IM7 carbon fibers (much stronger and denser than the AS4 fibers) at 750 °C for 1 h, Qian *et al.* [22] reported a 15%–25% reduction on the tensile strength. Zhang *et al.* [17] performed a CCVD to grow CNTs over T650 and IM7 carbon fibers and observed that the strength of the corresponding composite based on T650 fibers with grafted CNTs compared to composite based on the raw fibers drops by 46% when the growth temperatures was 800 °C. In contrast, under the same growth conditions, the composites based on IM7 carbon fibers with grafted CNTs exhibited a reduction of 70% of the original strength.

3. Experimental Section

3.1. Growing Carbon Nanofilament Using GSD

Commercial PAN-based plain-woven carbon fabric (AS4 supplied by HEXCEL Inc., Stamford, CT, USA) was utilized as the substrate to grow carbon nanofilaments. Samples of 13 × 13 cm^2 were cut from the raw fabric, some of which were reserved intact for the next step as reference samples. In anticipation of shielding the carbon yarn against the elevated temperatures encountered during the growth procedures and to prevent undesired carbon diffusion, thin films of thermal coating (75 nm thick SiO_2) were sputtered on the fabric top and bottom surfaces [23]. The catalyst in the form of a 2 nm-thick film of nickel was sputtered on top of the SiO_2 layers. A magnetron sputtering system (ATC Orion high vacuum sputtering system, AJA International Inc., Scituate, MA, USA) was employed to sputter both the SiO_2 and nickel films on the PAN-based carbon fiber fabrics. The sputtering process was carried out with an argon gas flow at 300 Watts power from a radio frequency (RF) source (to deposit the 75-nm SiO_2 film on the surface of the carbon fibers) and a DC source (to deposit the 2-nm nickel film on top of the SiO_2 film,) both at 3 millitorr vacuum.

In order to grow carbon nanofilaments on the fabrics coated with SiO_2 and nickel films, a tube furnace reactor was utilized. The furnace was comprised of a 7.62-cm diameter quartz tube and a 45.72-cm heating zone. The first step of the growth process involves flushing the tube with nitrogen and vacuuming it with a mechanical pump while the nitrogen was flowing. This step ensures the elimination of oxygen inside the reaction tube.

The CNT growth was initiated as a mixture of $N_2/H_2/C_2H_4$ and was introduced while maintaining the temperature at 550 °C. The growth time was set to one hour. The hydrocarbon (ethylene) undergoes a homogeneous reaction over the nickel catalyst in the presence of H_2, and the carbon radicals get deposited in the form of nanotubes [18,24,25]. The furnace was cooled down to ambient temperature under an inert nitrogen environment.

To provide better insight into the effect of the nanofilament growth condition and synthesis method, MWCNTs were also synthesized on separate yarns by catalytic chemical vapor deposition (CCVD) in a simple hot-wall reactor at ambient pressure. In this process, the catalyst, ferrocene, was dissolved in a liquid hydrocarbon, xylene, to form a feed solution. This solution was delivered by a syringe pump to an injection tube and dispersed into a flow stream of hydrogen and helium. This vapor was transported to a hot quartz tube reactor. Carbon nanotubes were grown on SiO_2-coated woven carbon fabric at 680 °C for 1 h.

3.2. Microstructural and Mechanical Characterization

A 5200 Hitachi SEM (Tokyo, Japan) and a Titan 300 TEM (FEI, Inc., Hillsboro, OR, USA) operated at 5 and 300 keV, respectively, were utilized to examine the synthesized MWCNTs. Raman spectra were obtained utilizing a ProSeek Raman system from Raman System, Inc. (Woburn, MA, USA) These spectra were obtained with a confocal Raman microscope, using a 5-mW, 785-nm

excitation wavelength laser beam focused on the sample with a 50× objective. Spectra were obtained as the sum of 30-s integration time.

For the purpose of mechanical testing, a set of flat, two-layer composite lamina of 12.5 × 12.5 cm^2 were manufactured using vacuum and a press-assisted hand lay-up process. The lay-up stack comprised a vacuum bag, peel ply release fabric, stacked carbon fabrics impregnated with the epoxy, another peel ply film, perforated release film and breather cloth, sequentially. The lay-up set was vacuum bagged, while a pressure of 5 kN via a dead weight was applied to it. Simultaneous use of the vacuum and dead weight assured the degassing and curing of the resin, while the carbon fabric stack was kept intact under high pressure. The composite was left to cure under room temperature for 24 h. The matrix material was Aeropoxy™ manufactured by PTM&W Industries, Inc. (Santa Fe Springs, CA, USA) This epoxy system was used to manufacture both FRPs [26,27] and composites based on SWCNT [7] and MWCNT [28]. Abraded G-10 tabs were attached utilizing the Aeropoxy to the ends of the tensile specimen. Tensile test coupons of 12.5 × 1.25 cm^2 were cut using a table saw. The ultimate tensile strength and Young's modulus for the specimens were measured from tension tests utilizing an Instron® 4400R frame (Instron, Inc. Norwood, MA, USA). The tensile tests were performed according to the ASTM standard D3039/D3039M-08 [29] under a constant cross-head speed of 2 mm/min until failure occurred.

The strain was measured using an extensometer (MTS Testing Systems, Inc., Eden Prairie, MN, USA). A total of eight samples for each configuration were tested to determine the tensile properties.

4. Conclusions

The surface modification of the carbon fiber through heat treatment, coating with SiO_2 film in an attempt to prevent the fibers' thermal degradation and growing carbon nanofilaments via GSD and CCVD on the surface influence the mechanical properties of the composites based on these different fiber configurations. The mechanical testing showed that composites using the GSD-grown nanofilaments outperform those using the CCVD-grown CNTs in terms of stiffness and tensile strength. The conclusion that can be drawn is that the CCVD technique allows for the placement of higher quality CNTs (compared to GSD) at the compromise of significantly degraded mechanical properties. The tensile results indicated that the SiO_2 thin film protected the PAN-based carbon fiber against undesired diffusions and the temperatures utilized in GSD technique (550 °C), but were not capable of shielding the fibers at higher temperatures used in the CCVD method. The reduction in the strength encountered by the fibers via the GSD growth is not desirable and, yet, are minimal (only a 3.5% reduction in strength compared to the reference samples). This trend was observed by the different groups who have utilized CCVD to grow CNTs on the surface of carbon fibers. Therefore, it is believed that the GSD still needs further optimization in terms of the growth temperature and the shielding of the base fibers.

Acknowledgments

This work has been supported by the Office of Naval Research (ONR), Grant No. 10960991, and the National Science Foundation (NSF), awards CMMI-0846589 and CMMI-1200506. The authors gratefully acknowledge this support.

Author Contributions

Mehran Tehrani and Ayoub Yari Boroujeni carried out the experimental work under the supervision of Marwan al-Haik. Jonathan Phillips and Claudia Luhrs supervised the early development of the GSD process. All the authors participated in writing the manuscript.

Conflicts of Interest

The authors declare no conflict of interest.

References

1. Hyer, M.W. *Stress Analysis of Fiber-reinforced Composite Materials*; McGraw-Hill Companies, Inc.: Boston, MA, USA, 1997.
2. Ronald, F.G. A review of recent research on mechanics of multifunctional composite materials and structures. *Compos. Struct.* **2010**, *92*, 2793–2810.
3. Iijima, S. Helical microtubules of graphitic carbon. *Nature* **1991**, *354*, 56–58.
4. Chandra, R.; Singh, S.P.; Gupta, K. Damping studies in fiber-reinforced composites—A review. *Compos. Struct.* **1999**, *46*, 41–51.
5. Sinnott, S.B.; Andrews, R. Carbon nanotubes: Synthesis, properties, and applications. *Crit. Rev. Solid State Mater. Sci.* **2001**, *26*, 145–249.
6. Li, Y.L.; Kinloch, I.A.; Windle, A.H. Direct spinning of carbon nanotube fibers from chemical vapor deposition synthesis. *Science* **2004**, *304*, 276–278.
7. Garmestani, H.; Al-Haik, M.S.; Dahmen, K.; Tannenbaum, R.; Li, D.S.; Sablin, S.S.; Hussaini, M.Y. Polymer mediated alignment of carbon nanotubes under high magnetic fields. *Adv. Mater.* **2003**, *15*, 1918–1921.
8. Zeineldin, R.; al-Haik, M.; Hudson, L.G. Role of polyethylene glycol integrity in specific receptor targeting of carbon nanotubes to cancer cells. *Nano Lett.* **2009**, *9*, 751–757.
9. García, E.J.; Hart, A.J.; Wardl, B.L. Electrical and thermal properties of hybrid woven composites reinforced with aligned carbon nanotubes. *AIAA J.* **2008**, *46*, 1405–1412.
10. Otsuka, K.; Abe, Y.; Kanai, N.; Kobayashi, Y.; Takenaka, S.; Tanabe, E. Synthesis of carbon nanotubes on Ni/carbon-fiber catalysts under mild conditions. *Carbon* **2004**, *42*, 727–736.
11. Zhu, S.; Su, C.-H.; Lehoczky, S.L.; Muntele, I.; Ila, D. Carbon nanotube growth on carbon fibers. *Diam. Relat. Mater.* **2003**, *12*, 1825–1828.
12. Makris, T.D.; Giorgi, R.; Lisi, N.; Pilloni, L.; Salernitano, E.; de Riccardis, M.F.; Carbone, D. Carbon nanotube growth on PAN- and pitch-based carbon fibres by HFCVD. *Fuller. Nanotub. Carbon Nanostruct.* **2005**, *13*, 383–392.
13. Boskovic, B.O.; Golovko, V.B.; Cantoro, M. Low temperature synthesis of carbon nanofibres on carbon fibre matrices. *Carbon* **2005**, *43*, 2643–2648.
14. Qu, L.; Zhao, Y.; Dai, L. Carbon microfibers sheathed with aligned carbon nanotubes: Towards multidimensional, multicomponent, and multifunctional nanomaterials. *Small* **2006**, *2*, 1052–1059.

15. Phillips, J.; Shiina, T.; Nemer, M.; Lester, K. Graphitic structures by design. *Langmuir* **2006**, *22*, 9694–9703.
16. Wu, N.L.; Phillips, J. Carbon deposition on platinum during ethylene oxidation. *J. Catal.* **1988**, *113*, 383–397.
17. Zhang, Q.; Liu, J.; Sager, R.; Dai, L.; Baur, J. Hierarchical composites of carbon nanotubes on carbon fiber: Influence of growth condition on fiber tensile properties. *Compos. Sci. Technol.* **2009**, *69*, 594–601.
18. Phillips, J.; Luhrs, C.; Leseman, Z.C.; al-Haik, M. Novel graphitic structures by design. In Proceedings of the ASME International Mechanical Engineering Congress and Exposition, Seattle, WA, USA, 11–15 November 2007.
19. Keszler, A.M.; Nemes, L.; Ahmad, S.R.; Fang, X. Characterization of carbon nanotube materials by Raman spectroscopy and microscopy—A case study of multiwalled and singlewalled samples. *J. Optoelectron. Adv. Mater.* **2004**, *6*, 1269–1274.
20. Fitzer, E. PAN-based carbon fibers-present state and trend of the technology from the viewpoint of possibilities and limits to influence and to control the fiber properties by the process parameters. *Carbon* **1989**, *27*, 621–645.
21. Jorio, A.; Pimenta, M.A.; Filho, A.G.S.; Saito, R.; Dresselhaus, G.; Dresselhaus, M.S. Characterizing carbon nanotube samples with resonance Raman scattering. *New J. Phys.* **2003**, *5*, doi:10.1088/1367-2630/5/1/139.
22. Qian, H.; Bismarck, A.; Greenhalgh, E.S.; Shaffer, M.S.P. Carbon nanotube grafted carbon fibres: A study of wetting and fibre fragmentation. *Compos. A Appl. Sci. Manuf.* **2010**, *41*, 1107–1114.
23. Westwood, M.E.; Webster, J.D.; Day, R.J.; Hayes, F.H.; Taylor, R. Oxidation protection for carbon fibre composites. *J. Mater. Sci.* **1996**, *31*, 1389–1397.
24. Luhrs, C.C.; Garcia, D.; Tehrani, M.; al-Haik, M.; Taha, M.R.; Phillips, J. Generation of carbon nanofilaments on carbon fibers at 550 degrees C. *Carbon* **2009**, *47*, 3071–3078.
25. Dupuis, A. The catalyst in the CCVD of carbon nanotubes: A review. *Prog. Mater. Sci.* **2005**, *50*, 929–961.
26. Al-Haik, M.S.; Garmestani, H.; Savran, A. Explicit and implicit viscoplastic models for polymeric composite. *Int. J. Plast.* **2004**, *20*, 1875–1907.
27. Al-Haik, M.S.; Hussaini, M.Y.; Garmestani, H. Prediction of nonlinear viscoelastic behavior of polymeric composites using an artificial neural network. *Int. J. Plast.* **2006**, *22*, 1367–1392.
28. Tehrani, M.; Safdari, M.; al-Haik, M.S. Nanocharacterization of creep behavior of multiwall carbon nanotubes/epoxy nanocomposite. *Int. J. Plast.* **2011**, *27*, 887–901.
29. *Standard Test Method for Tensile Properties of Polymer Matrix Composite Materials*; ASTM D3039/D3039M-08; ASTM International: West Conshohocken, PA, USA, 2008.

Static and Dynamic Characteristics of a Long-Span Cable-Stayed Bridge with CFRP Cables

Xu Xie, Xiaozhang Li and Yonggang Shen

Abstract: In this study, the scope of CFRP cables in cable-stayed bridges is studied by establishing a numerical model of a 1400-m span of the same. The mechanical properties and characteristics of CFRP stay cables and of a cable-stayed bridge with CFRP cables are here subjected to comprehensive analysis. The anomalies in the damping properties of free vibration, nonlinear parametric vibration and wind fluctuating vibration between steel cables and CFRP cables are determined. The structural stiffness, wind resistance and traffic vibration of the cable-stayed bridge with CFRP cables are also analyzed. It was found that the static performances of a cable-stayed bridge with CFRP cables and steel cables are basically the same. The natural frequencies of CFRP cables do not coincide with the major natural frequencies of the cable-stayed bridge, so the likelihood of CFRP cable-bridge coupling vibration is minuscule. For CFRP cables, the response amplitudes of both parametric vibration and wind fluctuating vibration are smaller than those of steel cables. It can be concluded from the research that the use of CFRP cables does not change the dynamic characteristics of the vehicle-bridge coupling vibration. Therefore, they can be used in long-span cable-stayed bridges with an excellent mechanical performance.

Reprinted from *Materials*. Cite as: Xie, X.; Li, X.-Z.; Shen, Y.G. Static and Dynamic Characteristics of a Long-Span Cable-Stayed Bridge with CFRP Cables. *Materials* **2014**, *7*, 4854ï 4877.

1. Introduction

Cable-supported bridges have undergone rapid development over the last century since high-strength steel cables were first made available. Cable-stayed bridges can reach spans of over 1000 m, which makes them practical alternatives to suspension bridges. The cables, which transmit most of the force, are key to the structural stability and safety of cable-stayed bridges. However, cables are very vulnerable to corrosion and fatigue damage, which affect their service lifespan, necessitating their replacement. In China alone, the cables of more than twenty bridges have been replaced over the past twenty years for safety reasons [1]. Cable replacement not only requires a huge financial investment, but also disrupts transportation and causes problems in the maintenance and management of the bridge.

Carbon fiber-reinforced plastic (CFRP) has been widely used in civil engineering, because of its light weight, great strength, considerable flexibility and resistance to corrosion and fatigue. In spite of the disadvantages, like the lack of ductility, high cost, contractor unfamiliarity, susceptibility to impact damage and difficulty in forming connections, CFRP cables are superior to steel cables in some critical mechanical aspects, such as creep and relaxation. The possibility of using CFRP in long-span bridges has received considerable attention for this reason. Meier *et al*. [2] evaluated the applicability of CFRP materials in long-span cable-supported bridges. Later, other scholars made

more comprehensive studies on the possibility of applying CFRP in long-span bridges [3–14]. The mechanical properties of long-span cable-supported bridges built with CFRP cables have been gradually explained. Better ways of manufacturing CFRP cables and anchoring systems have been developed, and these have already seen use in some real-world bridges [15–19]. The increase in knowledge of CFRP materials has decreased the manufacturing costs, and the use of CFRP cables in long-span bridges will upsurge in the near future.

So far, most studies of CFRP cables have been limited in scientific premise. Some problems are still at the probing stage. The impact of CFRP cables on the mechanical properties of long-span cable-stayed bridges has not yet been subjected to systematic research. In this research, a series of studies have been carried out on CFRP cables in bridges of different sizes. Herein, a CFRP cable-stayed bridge is compared to a steel cable-stayed bridge with respect to material, element and structural characteristics. These results provide evidence supporting the use of CFRP cables in long-span cable-stayed bridges.

2. Mechanical Properties of CFRP Cables

2.1. Material Properties of CFRP Cables

At present, there is no uniform production standard for CFRP cables, so the material parameters of CFRP cables produced by different manufacturers differ considerably. Table 1 shows the material properties of four types of CFRP cables, marked as A, B, C and D. In the table, γ, E, σ_u, ε_u, R_e and ρ represent the unit weight, Young's modulus, tensile strength, ultimate strain, relaxation ratio for 1000 h and linear expansion coefficient, respectively. It was here observed that the material characteristics of CFRP cables produced by different manufacturers are typically similar. The Young's modulus is about 140 GPa, which is about 70% of steel cables. The tensile strength is 2.02–2.55 GPa, which is 1.3–1.6 times that of high-strength steel cables. The linear expansion coefficient is 0.6×10^{-6}/°C, and the temperature deformation is only 1/20 that of steel cables. The unit weight is 1/5 that of steel cables, and the relaxation rate is lower than that of steel cables. In addition, the ultimate strain of CFRP cable is so small that the stress-strain curve remains mostly linear before fissure, which indicates that CFRP cables are brittle.

Table 1. Material properties of CFRP and steel cables.

Cable types	γ (kN/mm^3)	σ_u (MPa)	E (GPa)	σ_u/E	R_e (%)	ε_u (%)	a_l ($\times 10^{-6}$/°C)
A	16	2,140	137	0.016	0.3	1.6	0.6
B	16	2,550	147	0.017	0.3	1.6	0.68
C	16	2,022	137	0.015	0.3	2	0.6
D	16	2,421	159	0.015	0.3	1.7	0.6
steel	77	1,570	196	0.008	<2.5	>4	12

2.2. Damping Properties of CFRP Cables

Cable damping is mainly associated with energy dissipation caused by material strain and air friction. There is so little air damping that it can usually be ignored during calculation. This paper focuses on the material damping characteristics of CFRP cables. According to the strain energy proportional damping theory of a single-degree-of-freedom vibration system, the damping ratio ξ can be calculated using the following expression:

$$\xi = \frac{1}{4\pi} \cdot \frac{\Delta W}{W} \tag{5}$$

Here, ΔW is the energy absorbed due to the strain deformation during the vibration cycle, and W is the modal potential energy. Assuming ΔW is proportional to the strain energy $\Delta W \propto V$, replacing the proportionality sign with a constant [20–22]:

$$\Delta W = 2\pi\eta V \tag{6}$$

Here, η is the energy loss factor, and V is the strain energy. Substitution of the equation above into Equation (1) produces the following:

$$\xi = \frac{1}{2}\eta\frac{V}{W} \tag{7}$$

Because there is a large initial tension T_0 in the cable, therefore the modal potential energy W of Formula (3) includes two parts, initial tension potential energy W_0 and strain energy V, hence:

$$W = W_0 + V \tag{8}$$

Because the flexible cable only bears axial tension, as indicated by the relationship of strain and tension shown in Figure 1, the initial potential energy due to tension, W_0 and strain energy V can be calculated as follows:

$$\left.\begin{aligned} W_{0i} &= \sum_{k=1}^{n} T_{k0} S_k \varepsilon_{ki}, \\ V_i &= \sum_{k=1}^{n} \frac{EAS_k}{2} \varepsilon_{ki}^2. \end{aligned}\right\} \tag{9}$$

Figure 1. Potential energy and strain energy in initial tension.

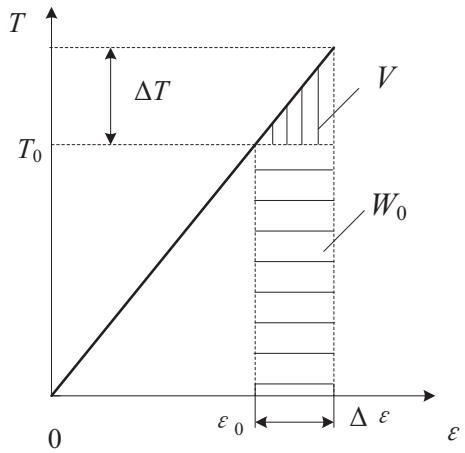

Here, ε_{ki} and S_k are the strain and length of element k generated by the i-th vibration mode.

T_{k0} is the initial tension in element k, and n is the total number of cable elements. Substitution of Equations (4) and (5) into (1) results in the following expression:

$$\xi_i = \frac{1}{2}\eta \frac{V_i}{W_{0i} + V_i} \tag{10}$$

In order to compare the damping characteristics of steel and CFRP cables, a cable vibration test was carried out in Tokyo Metropolitan University [22]. The test steel and CFRP cables were made at Rope Corporation Tokyo, Japan, wherein the steel cable, PCSϕ12.7 (ϕ refers to diameter of the cable), was composed of seven 5.16-mm diameter steel wires, PCSϕ5.16, and the CFRP cable, CFCCϕ12.5, was composed of seven 5.0 mm-diameter CFRP wires, CFCCϕ5.0 (Figure 2). Table 2 lists the material parameters of cables and wires. E, w, D, A and σ_u represent Young's modulus, the unit weight, the diameter, the cross-sectional area and the tensile strength of cables and wires, respectively.

Figure 2. Cross-section of cable CFCCϕ12.5.

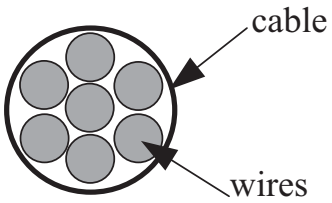

Table 2. Material properties of cables and wires.

Cable and Wire Type	E (GPa)	w (g/m)	D (mm)	A (mm^2)	σ_u (MPa)
CFCCϕ12.5	159	145	12.50	76.0	2,421
PCSϕ12.7	197	774	12.70	98.7	1,854
CFCCϕ5.0	152	29.9	5.00	15.2	2,980
PCSϕ5.16	204	163.8	5.16	20.9	1,999

Figure 3a,b provides details of the cable damping test equipment. The test cable was 20 m-long with an initial tension of 30 kN. The resulting initial stresses in CFRP cables and steel cables were 395 and 304 MPa, respectively, which were equal to half of the service stresses. Here, the design safety factor of the test cable was 2.5. Continuous excitation force was applied at the midpoint of the cable to render the vibrations stable.

Once the excitation force ceased, the cable entered free decay vibration, which was measured by a non-contact laser displacement meter at a sampling rate of 500 Hz. Figure 3b shows the relationship between the cable damping and vibration amplitude. It can be found that, for steel and CFRP cables, damping increases with vibration amplitude, but the trend was more obvious for steel cables than CFRP cables. This indicted that the influence of vibration amplitude on cable damping is not as pronounced for CFRP cable as it is for the steel cable. In addition, the energy loss factor of cables shown in Equation (3) can be calculated from Figure 3b. Here, the damping constant was 0.05 for both steel and CFRP cables, consistent with the test results reported by Kady *et al.* [23].

In order to determine the energy loss factors of wires comprising the cables, the bending deformation experiment of steel and CFRP wires under free vibration was conducted (Figure 4a). A heavy block was hung on by a string on the fixed test wire at a distance of *l* from the fixed end. An initial imposed displacement was used to place the wire in decay free vibration. The strain readings were recorded by the dynamic strain gauges fixed on the wire, at a sampling of 500 Hz. During the test, the distance *l* and the mass of the heavy block were varied multiple times to obtain additional experimental data.

Figure 3. (**a**) Cable damping test; (**b**) cable damping log decrement *vs*. vibration amplitude.

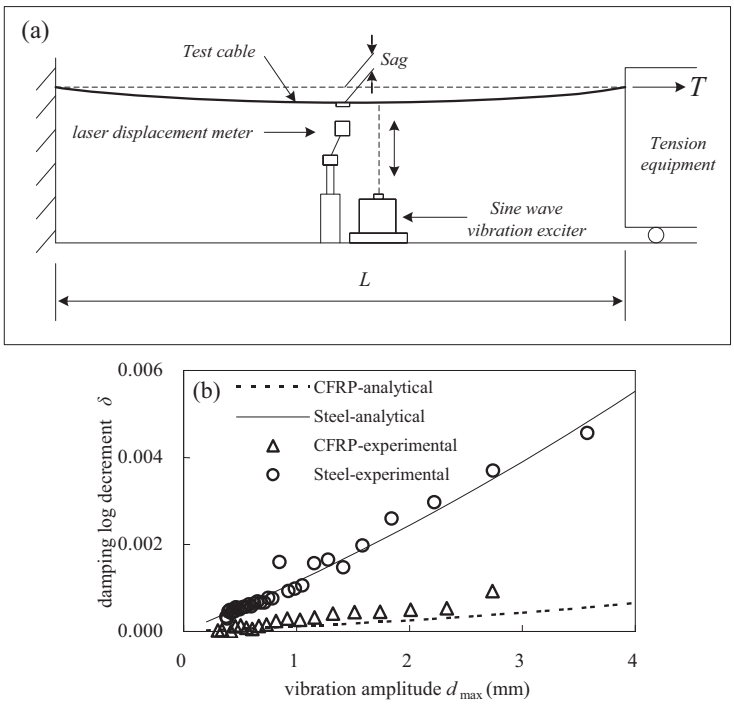

Figure 4. (**a**) Bending deformation experiments of steel and CFRP wires; (**b**) distribution of energy loss coefficient for steel wires; (**c**) distribution of energy loss coefficient for CFRP wires.

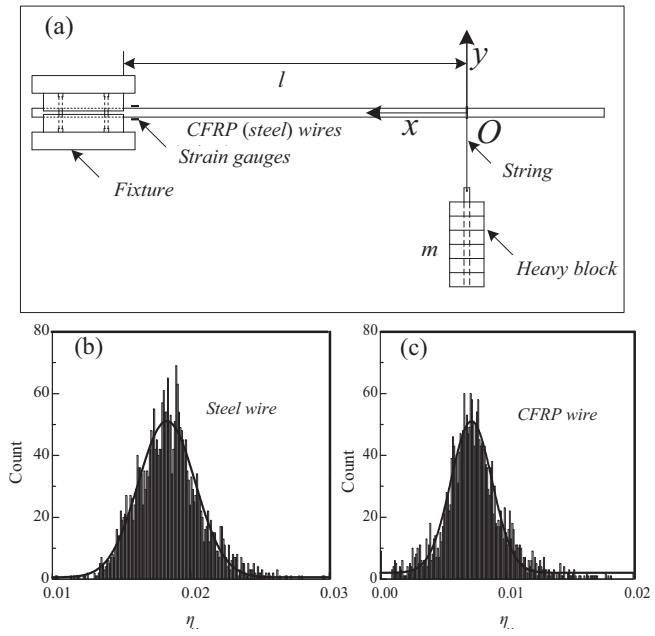

Figure 4b shows the distribution results of energy loss factors for steel and CFRP wires. As shown, the average energy loss factors for steel and CFRP wires are about 0.018 and 0.008, respectively, which is much smaller than the damping constant of steel and CFRP cables, 0.05. This indicates that the damping of the material strain ratio is only a part of the total cable damping, and other damping is relative to the friction among the wires of the cable.

3. Structural Description of the Cable-Stayed Bridge

In this paper, the mechanical characteristics of a cable-stayed bridge with CFRP cables are discussed, and the feasibility of using CFRP cables on long-span cable-stayed bridges is evaluated. The finite element method (FEM) is used to establish a numerical model of the 1400-m span of a cable-stayed bridge. Although the bridge model is not an actual structure, the geometric parameters were chosen by a conceptual design procedure according to some basic parameters of the existing long-span cable-stayed bridges [22]. Figure 5 shows the layout of the bridge model (in meters). This bridge's mid-span is 1400 m, which is about two times its side-span. Thirty-four cables are installed at a horizontal spacing of 20 m on each side of towers to hold the main beam, which is a uniform multi-cell flat steel box girder. The width of the box girder is 30 m, and the height is 4.5 m, which indicates a relatively larger height-to-span ratio as compared to many other cable-stayed bridges. The equivalent thicknesses of the orthotropic top and bottom plates of the girder are 20 mm (derived as 12 mm of steel plate and an 8-mm equivalent thickness of the stiffener). The equivalent thickness of the web is 15 mm. The height of the pylon is 280 m, which is 0.2-times the mid-span, and the tower cross-section is a single cell box composed of walls with an equivalent thickness of 40 mm. Table 3 lists the cross-sectional parameters of the girder and the tower. Along the side-span, there are three middle auxiliary piers at a horizontal spacing of 100 m to support the girder. Constraint springs were set

between the girder and the pylon along the bridge longitudinal axis. Cables of C1, C2 and C3, shown in Figure 5, represent long, medium and short cables of Type C, mentioned in Table 1. The cables here have a relatively low tensile strength of 2022 MPa and an elastic modulus of 137 kN/mm^2. In the numerical model, the tower and box girder are 1111 spatial beam elements with 6 DOF, and the cables are 272 isoparametric elements with 3 DOF. The bridge is fixed at the bottom of the tower and supported by piers. The bridge can move along the longitudinal axis. The geometric nonlinear method and material nonlinear method are used to solve the problem.

The unit weight of the structure is calculated as follows:

$$W_{\mathrm{D}} = k_{\mathrm{D}} \gamma A + W_0 \tag{11}$$

Here, k_{D} is the load factor, chosen by conceptual design considering the self-weight of the stiffener plate of the box girder. [22]. For girders k_{D} = 1.4, and for pylons, k_{D} = 1.2. γ is the unit weight of steel. A is the cross-sectional area of box girder. W_0 is the secondary load, which mainly consists of pavement load, *etc.*, taken as, W_0 = 70 kN/m. The secondary load of the pylon is relatively so small, that it can be ignored.

Table 3. Cross-sectional properties.

Cross-Section	A (m^2)	I_x (m^4)	I_y (m^4)	Torsion Constant (m^4)
Girder	1.607	5.503	120.43	10.352 *
Tower	1.760	30.667	40.320	39.273 *

* Without considering the stiffening rib.

Figure 5. (**a**) 3D model of the bridge; (**b**) layout of half of the bridge; (**c**) typical cross-section of the box girder; (**d**) layout of the pylon and cross-section of the tower.

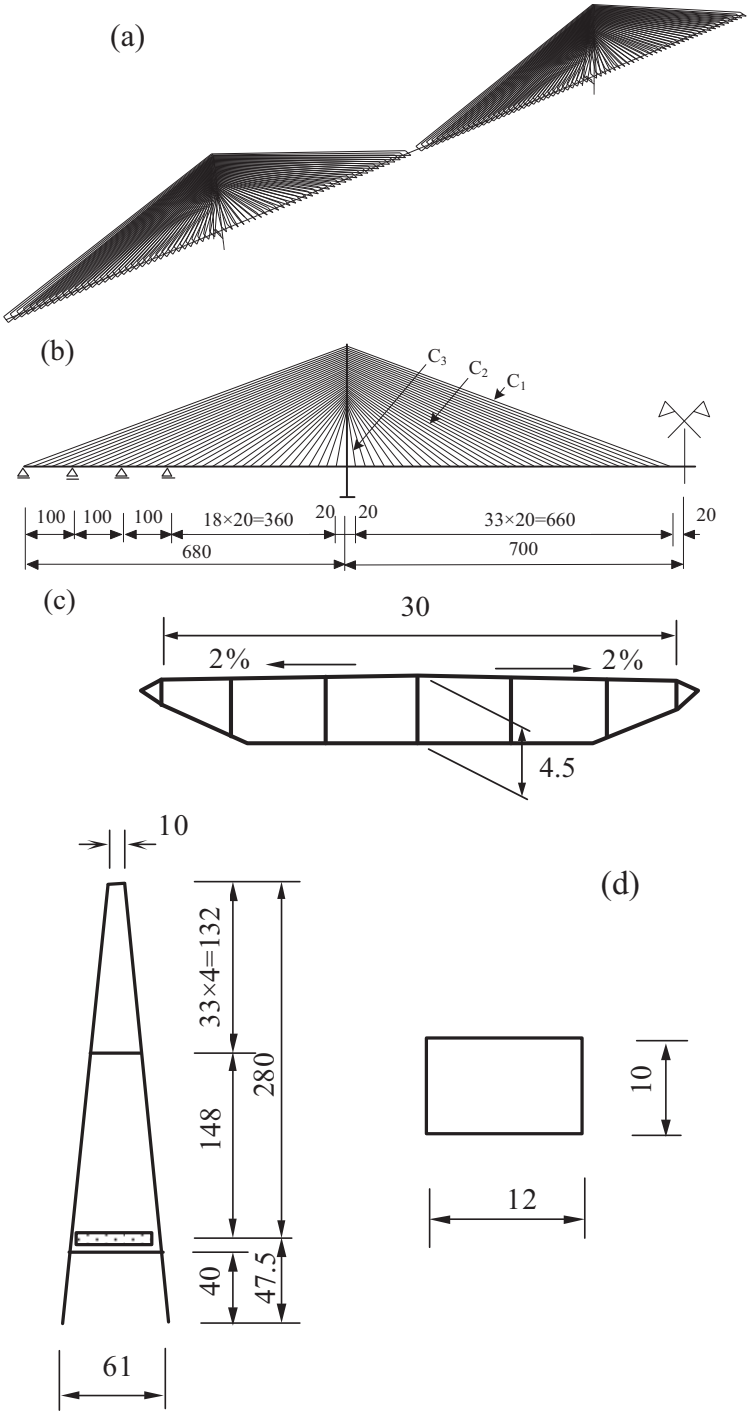

The cross-sectional area of the cable is calculated using the maximum cable tension T_0 and the allowable stress σ. The formula is as follows:

$$A_c = \frac{(1+\alpha)T_0}{[\sigma]} = \frac{\mu(1+\alpha)T_0}{\sigma^b} \tag{12}$$

Here, α is the factor of proportionality. It indicates how much cable tension is produced by the live load in response to the maximum tension produced by the dead load in the long-span cable-stayed bridge. Because the factor of proportionality for long-span cable-stayed bridges is usually not more

than 0.2, it is here assumed that $\alpha = 0.2$. σ is the allowable cable stress, and σ^b is the standard value of tensile strength; μ is the safety factor for the cable, which is generally 2.5 for steel cables. It is here assumed that $\mu = 3.0$ for CFRP cables, because CFRP is a strong, but brittle, material.

Table 4 shows the cable self-weight for steel cable-stayed bridges and CFRP cable-stayed bridges of the same span. Results show that the self-weight of the CFRP cable is only about 1/7 that of steel cable, which is less than the unit weight ratio of CFRP to steel, which is about 1/5. This means that fewer CFRP than steel cables would be needed for a cable-stayed bridge. This is because CFRP cables sag less, giving them greater working efficiency. This may substantiate the cost disadvantage of CFRP cables.

Table 4. Weight of steel and CFRP cables on a whole bridge.

Material	Weight (kN)	Weight Ratio of Steel to CFRP
Steel	115,133	6.8
CFRP	17,056.7	

4. Dynamic Characteristics of CFRP Stay Cables

4.1. Natural Vibration Characteristics

Figure 6 gives the first two order natural frequencies of cables on one side of the half bridge shown in Figure 5. Because there is little difference between the in-plane and out-of-plane vibration, these results only demonstrate the in-plane vibration results. In the figure, the vertical axis *f* is the natural frequency, and the cable numbers on the horizontal axis represent the position of the cable anchor on the girder expressed in terms of the number of markers from the start of the side-span to the midpoint of the bridge. The results show that, due to the large self-weight, the natural frequencies of steel cables are about 0.5-times those of CFRP cables.

The material properties and natural frequencies of stay cables of three different lengths (marked C1, C2 and C3 in Figure 5) are compared in Tables 5 and 6. *S* represents the steel cable, *C* the CFRP cable, *EA* the axial stiffness and *w* the unit weight. The Irvine parameter λ, a dimensionless parameter reflecting the dynamic characteristics, is defined as follows [24]:

$$\lambda = \frac{wL}{H}\sqrt{\frac{LEA}{HL_e}} \tag{13}$$

Here, H represents the horizontal component of cable tension and L_e represents cable length. Expression (9) indicates that the Irvine parameter is related to the geometric and material properties of the cable, the smaller the sag and the tensile stiffness of the cable, the smaller the Irvine parameter. Table 5 shows that, for the same span cables, the Irvine parameters of steel cables are much larger than those of CFRP cables. For cables made of the same material, the Irvine parameters for long cables are larger than that for short cables. Table 6 shows that, for the same cable span, the natural frequencies of CFRP cables are about two-times those of steel cables.

Figure 6. Natural frequencies of steel and CFRP cables.

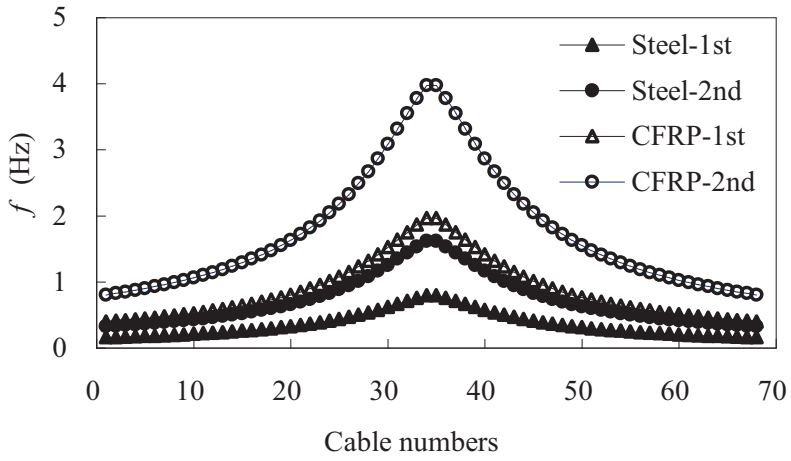

Table 5. Material properties of stay cables.

Cables	*L* (m)	*Y* (m)	*EA* (kN)	*W* (kN/m)	λ
S-C1	660	275.5	3,045,840	1.3114	0.01750
S-C2	460	235.5	2,516,640	1.0835	0.01306
S-C3	260	195.5	1,795,360	0.7730	0.00912
C-C1	660	275.5	1,557,416	0.1840	0.002863
C-C2	460	235.5	1,377,507	0.1630	0.002144
C-C3	260	195.5	1,033,802	0.1220	0.001501

Table 6. Natural frequencies of stay cables (units: Hz).

Cables	Out-of-Plane		In-Plane	
	1st	2nd	1st	2nd
S-C1	0.1652	0.3343	0.1998	0.3341
S-C2	0.2289	0.4635	0.2532	0.4633
S-C3	0.3645	0.7379	0.3771	0.7378
C-C1	0.4083	0.8267	0.4098	0.8266
C-C2	0.5662	1.1443	0.5652	1.1443
C-C3	0.8986	1.8194	0.8991	1.8194

In order to analyze the relationship between the cables and the dynamics of the bridge itself with respect to natural frequencies, the major frequencies of the bridge were calculated taking the influence of local vibrations of the cable into account (Table 7). The results show that the natural frequencies of steel cable-stayed bridges are basically the same as those of CFRP cable-stayed bridges.

Table 7. Major natural frequencies of cable-stayed bridge (units: Hz).

Cable Type	First Lateral Bending	Longitudinal Drifting	First Vertical Bending
Steel cables	0.0319	0.0330	0.1440
CFRP cables	0.0324	0.0340	0.1370

It can be found from Table 6 and Table 7 that the natural frequencies of steel cables overlap those of the first vertical bending frequencies of steel cable-stayed bridge. However, the natural frequencies of CFRP cables differ from the low natural frequencies of the CFRP cable-stayed bridge. That is why the steel cable-bridge coupling vibrations occur so easily. Therefore, using CFRP cables can significantly reduce the possibility of coupling vibrations in the cable bridge. Some major vibration modes of steel cable-stayed bridges and CFRP cable-stayed bridges are shown in Figure 7. It was found that the local vibrations of the cables in steel cable-stayed bridges were dominant for the first vertical bending vibration.

Figure 7. (**a**) Vibration modes of cable-stayed bridges with steel cables; (**b**) vibration modes of cable-stayed bridges with CFRP cables.

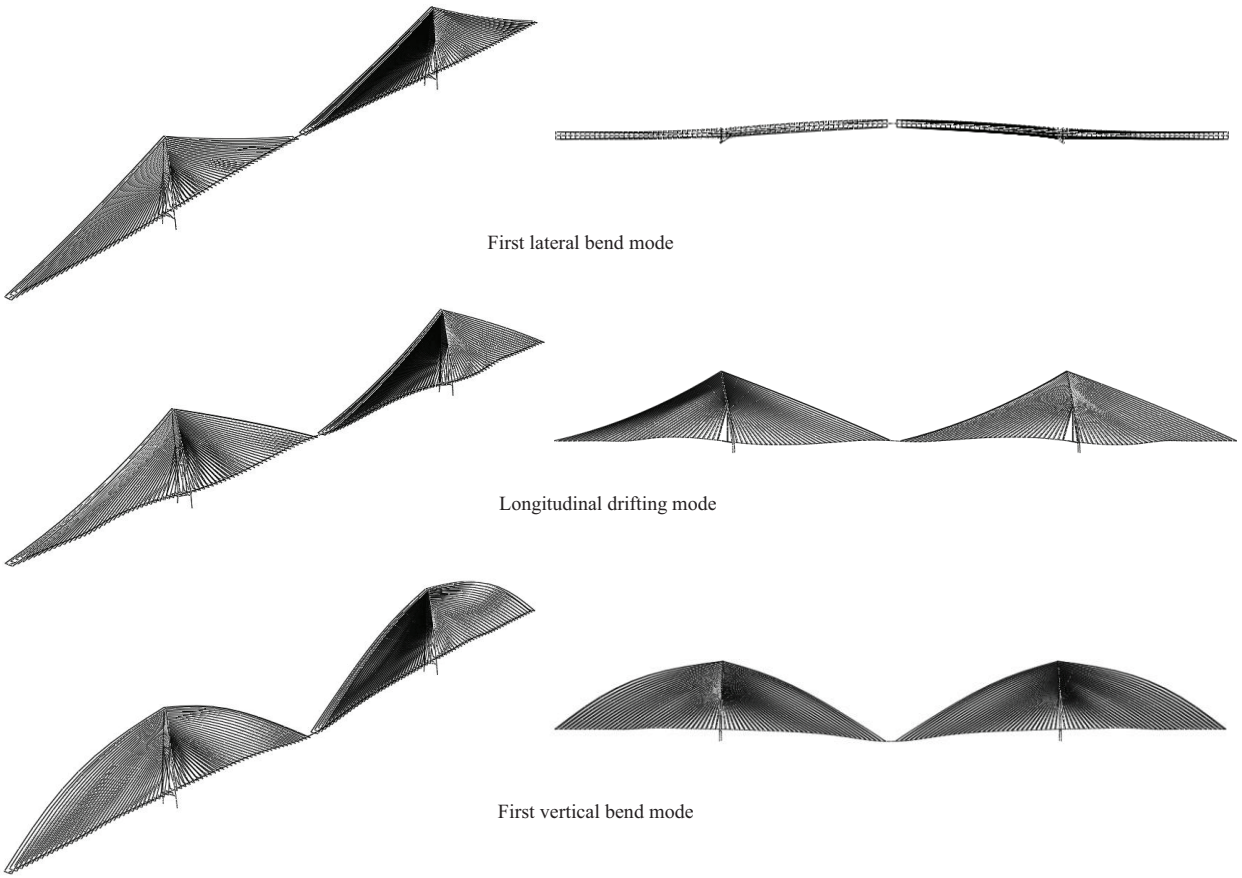

(**a**)

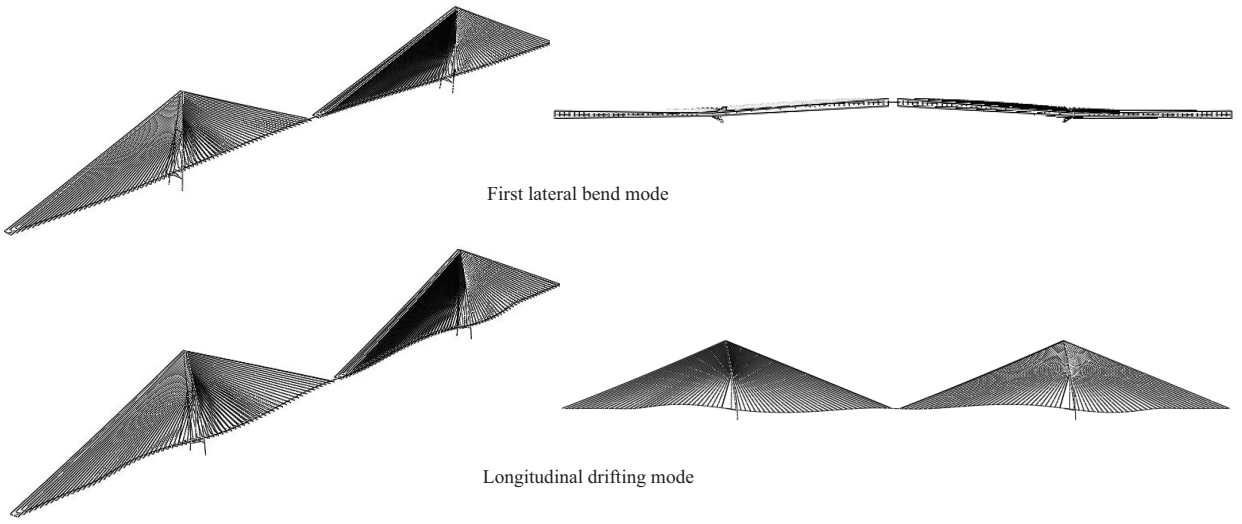

(**b**)

Figure 7. *Cont.*

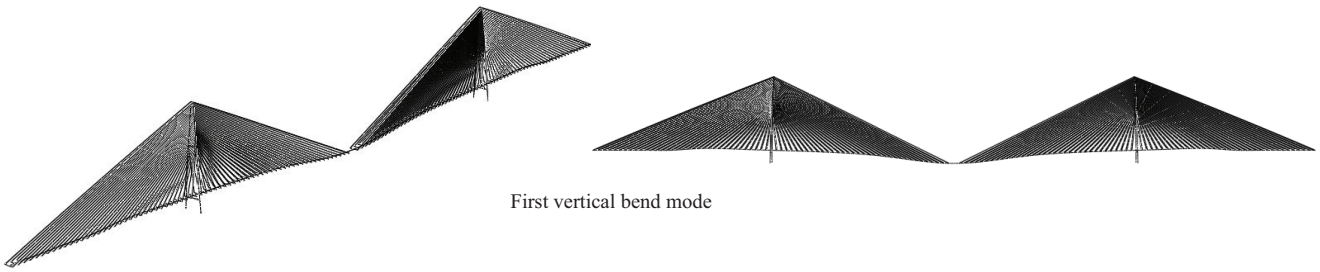

(b)

4.2. Damping Characteristics

Because the strain energy ratios of different lengths of cables are similar, only cable C2 is analyzed in this paper. Figure 8 shows the relationship between the first two vibration modal strain energy ratios calculated using Formulas (5) and (6) and the cable lateral in-plane and out-of-plane amplitudes. In the figure, S represents the steel cable, C represents the CFRP cable, -1st and -2nd represent the first and the second vibration modes and -out and -in represent the in-plane and out-of-plane vibration modes. The results show that the modal strain energy ratios of two materials are on the same order of magnitude. CFRP cables showed lower strain energy ratios than steel cables. If the vibration amplitude is around 1 m, Formula (6) can be used to calculate the structural damping ratios of both steel and CFRP cables, which were here around 1%.

Figure 8. Strain energy ratios of steel and CFRP cables.

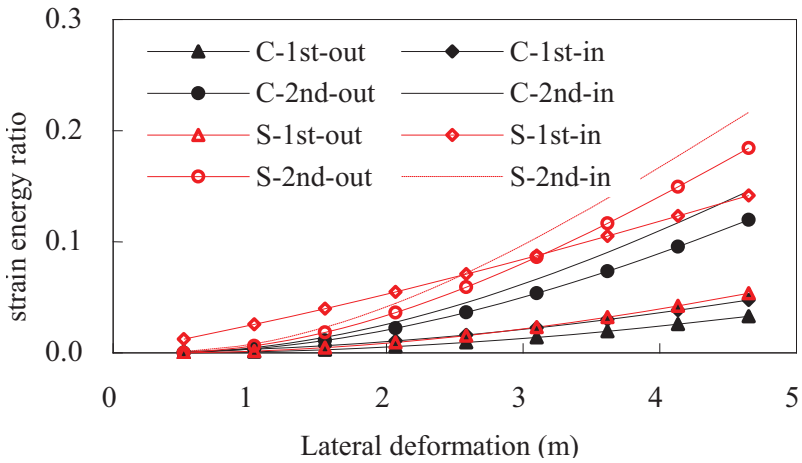

The external viscous damper is usually arranged at the lower end of the cable in order to prevent large vibration. Figure 9 shows the layout of the cable with the external viscous damper. x_c is the horizontal distance between the lower end of the cable and the damper. In this paper, x_c = 0.02 L. The non-proportional damping calculation theory (complex eigenvalue method) was used to calculate the damping value.

Figure 9. Stay cable with viscous damper.

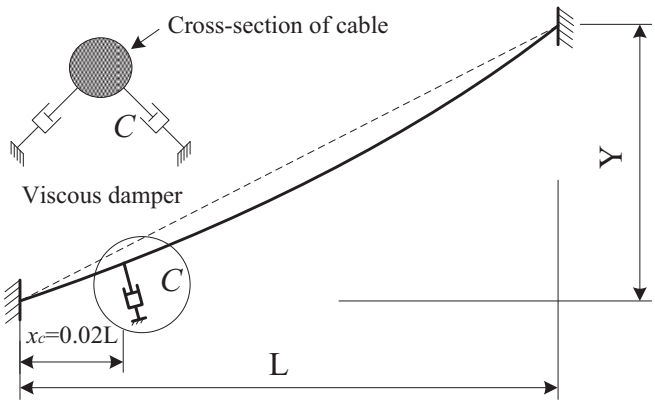

The calculation results show that the damping coefficients *C* have little impact on the natural frequencies of the steel and CFRP cables. Figure 10 shows the relationship between the first in-plane modal damping ratios and the damping coefficients. The damping coefficients significantly affected the modal damping ratios. As the damping coefficients increase, the modal damping ratios also increase significantly, peak and then drop quickly. There is an optimal range within which the damping coefficients produce desirable effects. The optimal damping coefficient can be found using the following formula [25].

$$C = 0.1 \times \frac{m\omega_1 L^2}{x_c} \tag{14}$$

Here, *m* represents the unit mass and ω_1 represents the in-plane damped natural circular frequency of the first mode of the stay cable. Comparisons showed that the optimal viscous damping coefficients of CFRP cables were smaller than that of steel cables. This shows that only smaller dampers can produce the similar effects on CFRP cables that have been seen on steel cables.

Figure 10. Effects of external dampers on modal damping.

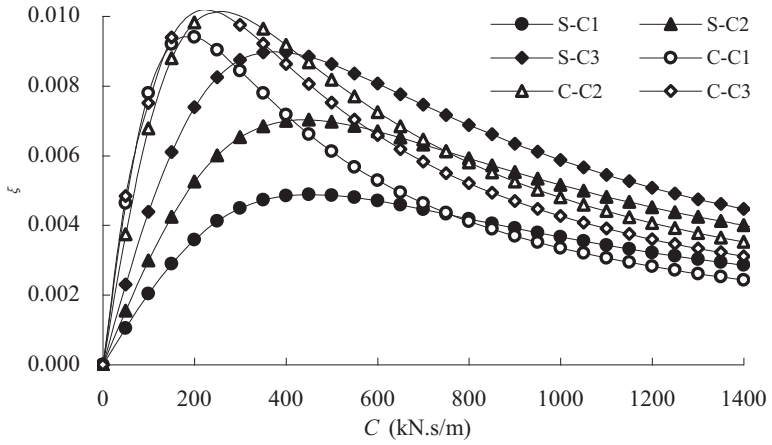

4.3. Parametric Vibration Characteristics of CFRP Stay Cables

4.3.1. Calculation Model and Method

Parametric vibrations are serious hindrances for stay cables, and analyzing this aspect has drawn considerable attention [26–34]. Three steel and three CFRP cables were used to compare the differences in parametric vibration characteristics (Table 5). The impact of the external viscous damper on parametric vibration was also studied. The nonlinear finite element method was used to calculate the parametric vibration of the stay cables [35,36]. The structural damping was ignored in the calculation process.

Figure 11 gives the model of stay cable parametric vibration analysis. A harmonic excitation vibration in the chord direction is given at the lower end of the cable. The vibration amplitude is 1/50,000 of the cable span. The excitation frequency is taken as $f = f_1$ and $f = 2f_1$. Here, f_1 is the in-plane natural frequency of the first mode.

Figure 11. Parametric vibration analysis model of the stay cable.

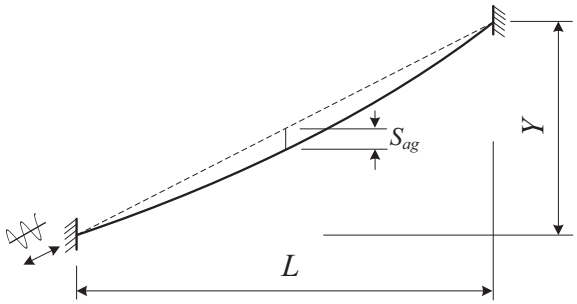

4.3.2. Parametric Vibration of Stay Cables Undamped

Figure 12 gives the time history curves of vibration responses at the midpoint of the stay cable C1 when the excitation frequencies are $f = f_1$ and $f = f_2$, respectively. As shown, the parametric vibration response of the CFRP cable is weaker than that of the steel cable. It also requires more time to excite a larger amplitude for the CFRP cable. This indicates that, to some extent, the use of CFRP cables involves lesser parametric vibration than that of steel cables.

Table 8 gives the parametric vibration response amplitudes of stay cables C1, C2 and C3. It shows that, regardless of the length of the cable, the response amplitude of CFRP cables is weaker than that of steel cables.

Table 8. Response amplitudes of parametric vibration (units: m).

Cable	Steel		CFRP	
	f_1	$2f_1$	f_1	$2f_1$
C1	28.460	10.670	7.059	7.410
C2	11.590	11.150	4.270	4.946
C3	4.007	3.680	1.961	1.961

Figure 12. Parametric vibration response of stay cable C1 (undamped): (**a**) steel cable under excitation frequency $f = f_1$; (**b**) steel cable under excitation frequency $f = 2f_1$; (**c**) CFRP cable under excitation frequency $f = f_1$; (**d**) CFRP cable under excitation frequency $f = 2f_1$.

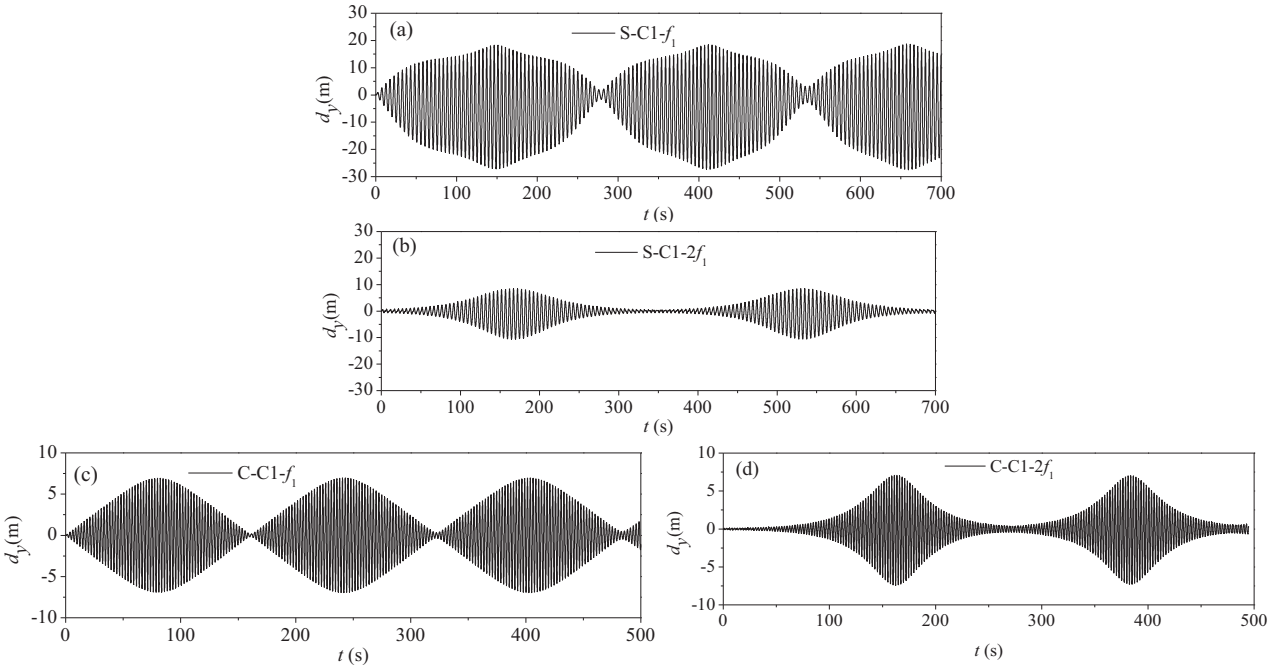

4.3.3. Parametric Vibration of Damped Stay Cables

To study the difference in the damping effect on the parametric vibration of CFRP and steel cables, the viscous dampers shown in Figure 9 were arranged at the lower end of cable C1. Assuming that x_c = 10 m, two viscous dampers were arranged symmetrically at either side of the cable, and the angle between the two dampers was 60°. The optimal damping coefficient for CFRP cable single damper obtained using Equation (10) is 448.86 kN·s/m, is much smaller than that of the steel cable, 127.35 kN·s/m.

Figure 13 gives the time history curves of vibration responses at the midpoint of stay cable C1 damped when the excitation frequencies were $f = f_1$ and $f = 2f_1$, respectively. Figures 12 and 13 show that, although the damper is effective for the cable vibration, it cannot lower the response amplitude after the parametric vibration comes into picture.

Figure 13. Parametric vibration response of stay cable C1 (damped): (**a**) steel cable under excitation frequency $f = f_1$; (**b**) steel cable under excitation frequency $f = 2f_1$; (**c**) CFRP cable under excitation frequency $f = f_1$; (**d**) CFRP cable under excitation frequency $f = 2f_1$.

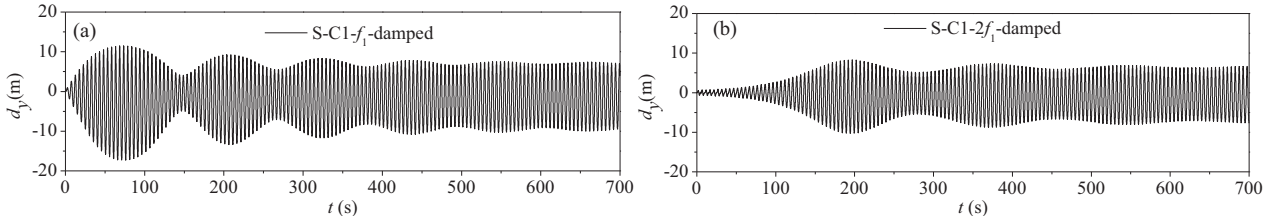

Figure 13. *Cont.*

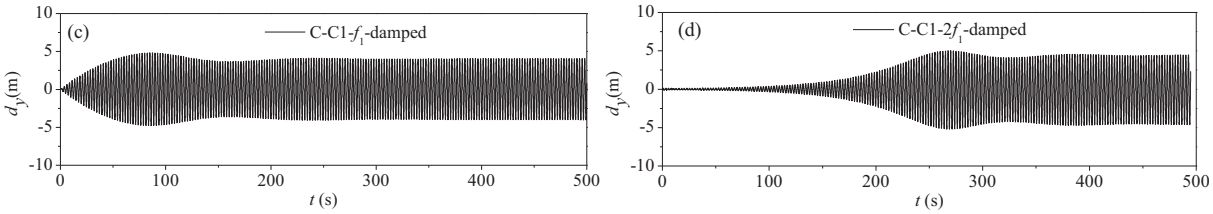

4.4. Fluctuating Vibration Characteristics of CFRP Stay Cables under Wind Load

4.4.1. Calculation

The analysis of wind loads to which the cables are subjected is very complex. The fluctuating wind load can cause them to vibrate. The turbulence power spectral density function of fluctuating wind is as follows [37]:

$$S_u(f) = \frac{4I_u^2 U^2 (L_x/U)}{\left[1 + 70.8(f \cdot L_x/U)^2\right]^{\frac{5}{6}}} \tag{15}$$

$$L_x = 100(Z/30)^{0.5} \tag{16}$$

Here, $S_u(f)$ represents the turbulence power spectral density function; L_x represents the scale of turbulence; I_u represents turbulence intensity, which is related to wind speed, and the ground roughness coefficient $I_u = 0.1$ in this paper. Z is the distance of the girder from the surface of the water surface. Here, $Z = 50$ m.

The random velocity of fluctuating wind is as follows [38]:

$$\Delta U(t) = \sum_{k=1}^{n} a_k \cos(\omega_k t + \phi_k) \tag{17}$$

Here, ϕ_k is the randomly-generated phase angle, and other parameters are calculated as follows:

$$\begin{cases} \Delta f = \dfrac{f_u - f_l}{n} \\ a_k = 2\sqrt{S(f_k)\Delta f} \\ f_k = f_l + \left(k - \dfrac{1}{2}\right)\Delta f \qquad (k = 1, 2, \cdots, n) \\ \omega_k = 2\pi f_k \end{cases} \tag{18}$$

Here, f_u and f_l are the upper and lower bounds of cable frequencies and n is an integer. The power spectral density of fluctuating wind sample with an average speed of 30 m/s was generated using Equation (11).

For the cable laden by lateral wind load shown in Figure 14, the relative wind attack angle θ can be determined as follows:

$$\tan\theta = \frac{U_y + \dot{y}}{U_z - \dot{z}} \tag{19}$$

Here, U_y and U_z are vertical and horizontal components of fluctuating wind speed, which are calculated as follows:

$$\begin{cases} U_y = \bar{U}\sin\beta \\ U_y = \bar{U}\cos\beta \end{cases} \tag{20}$$

Here, β is the wind attack angle shown in Figure 14; $\dot{y}$ and $\dot{z}$ are the vertical and horizontal vibration components, respectively. $\overline{U}$ is the sum of average wind speed and fluctuating wind speed.

Figure 14. Cross-section of cable under lateral wind load.

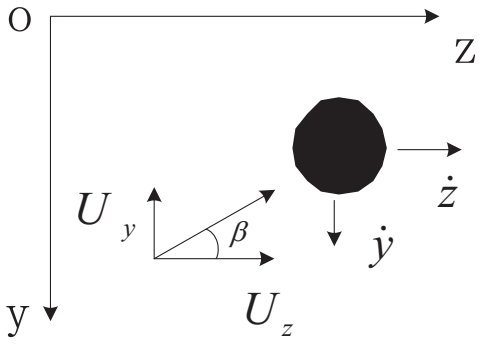

The relative wind speed experienced by the cable U_r is as follows:

$$U_r = \sqrt{(U_y + \dot{y})^2 + (U_z - \dot{z})^2} \tag{21}$$

The drag force D and lift force L acting on the cable along the relative wind direction are as follows:

$$\begin{cases} D = \dfrac{1}{2}\rho C_D \varphi U_r^2 \\ L = \dfrac{1}{2}\rho C_L \varphi U_r^2 \end{cases} \tag{22}$$

Here, C_D and C_L are the drag and lift coefficients of the cable. C_D = 0.7 and C_L = 0 for the round cross-section of the cable. φ is the outside diameter of the cable. ρ is the air density. The vertical and horizontal wind loads can be compounded by drag and lift force:

$$\begin{cases} q_z = D\cos\theta - L\sin\theta \\ q_y = -D\sin\theta - L\cos\theta \end{cases} \tag{23}$$

4.4.2. Wind Fluctuating Vibration of Stay Cables

Figure 15 gives the fluctuating vibration responses of stay cables C1, C2 and C3 under lateral wind load. As shown, the wind fluctuating vibration responses of CFRP cables are smaller than those of steel cables. The vertical vibration amplitudes of CFRP cables are about half those of steel cables of the same length. This also indicates that bridges built with CFRP cables are less subjected to wind fluctuating vibrations.

Figure 15. Wind fluctuating vibration responses of stay cables: (**a**) steel cable C1; (**b**) CFRP cable C1; (**c**) steel cable C2; (**d**) CFRP cable C2; (**e**) steel cable C3; (**f**) CFRP cable C3.

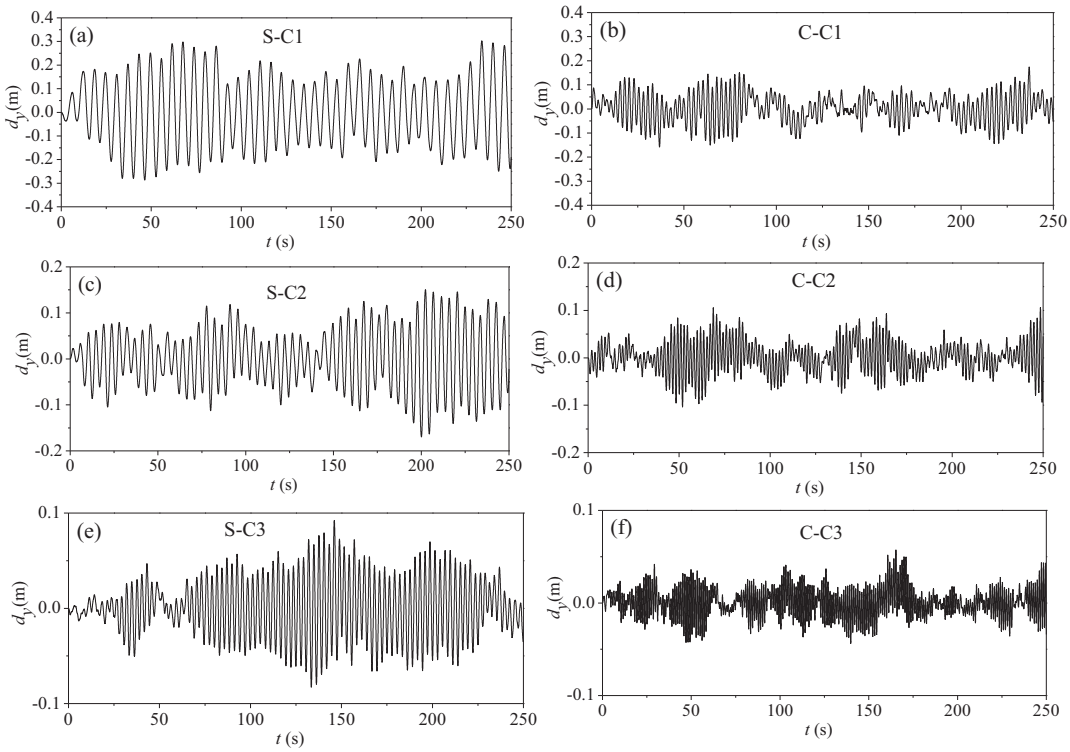

5. Static and Dynamic Characteristics of Cable-Stayed Bridge with CFRP Cables

5.1. Static Characteristics and Stability of Bridge under Live Load

To study the influence of CFRP cables on the mechanical properties of the bridge, the nonlinear finite element method is used to analyze the static characteristics of the girder. The designed distribution load is 43 kN/m, and the designed concentrate load is 1000 kN [39]. The nonlinear equation is as follows:

$$\mathbf{K}(\mathbf{u})\mathbf{u} = \mathbf{F} \tag{24}$$

Here, $\mathbf{u}$ is the displacement vector; $\mathbf{K}(\mathbf{u})$ is the stiffness matrix considering the initial internal force and geometrical nonlinearity; and $\mathbf{F}$ is the live load vector. To determine the most unfavorable loading position of the live load, the tangent stiffness at the finished state of the bridge is used to identify the influence line. The reduction of the live load with the span is neglected.

Figure 16 gives the maximum and minimum deflection values of a half box girder. The minimum deflection of the CFRP cable-stayed bridge was nearly same as that of the steel cable-stayed bridge. However, because steel-cable-stayed bridges have greater structural rigidity, the maximum girder deflection is 0.000119 of the span, but for CFRP cable-stayed bridges, it is 0.000146 of the span, which is 1.22-times the former. This indicates that the material properties of the cable have little impact on the minimum girder deflection and considerable impact on the maximum deflection. The critical girder deflection of cable-stayed bridge is 0.001 of the span, meaning that replacing steel cables with CFRP cables might give the bridge a large margin of safety, with respect to structural rigidity.

Under dead and live loads, the maximum compressive stress in the girders of steel-cable-stayed bridges is 189.3 MPa; that of CFRP-cable-stayed bridges it is 9% lower, at 173.9 MPa. This means that CFRP cables may be suitable for long-span cable-stayed bridges.

Structural stability is very important for long-span cable-stayed bridges, because there is a large amount of axial pressure in girders and pylons. The stability safety factor can be obtained using the following complex eigenvalue equation [40]:

$$\det\left(\mathbf{K}_{ep} + \lambda\mathbf{K}_{G}\right) = 0 \tag{25}$$

Here, $\mathbf{K}_{ep}$ is the stiffness matrix, which takes material nonlinearity into consideration; $\mathbf{K}_{G}$ is the geometric stiffness matrix; and λ is the stability safety factor. Unlike the linear elastic eigenvalue method, the elastic modulus in Equation (21) was obtained based on the law that the buckling strength is equal to the experimental strength, *i.e.*, the effective elastic modulus was adopted for the stiffness matrix, which considers the influence of initial defect and elasto-plastic stress of the structural member.

Figure 16. Maximum and minimum girder deflections under live load.

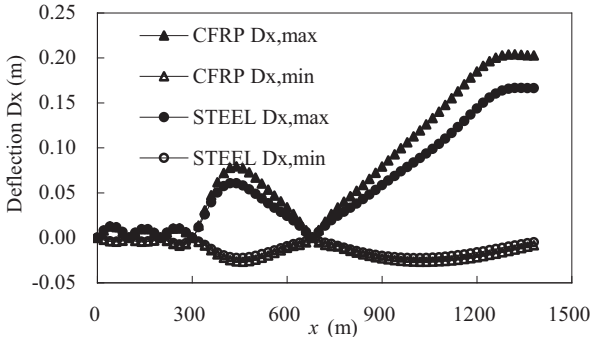

Elasto-plastic branch instability analysis showed that the minimum stability factor is 3.03 for CFRP cable-stayed bridges and 2.88 for steel cable-stayed bridges. The difference is attributed to the buckling caused primarily by the pylon. The self-weight of the steel cables is greater than that of CFRP cables, so the axial force in the pylon for steel-cable-stayed bridge is greater than that for a CFRP-cable-stayed bridge. Figure 17 gives an example of the elasto-plastic buckling mode for cable-stayed bridge with CFRP cables.

Figure 17. Elasto-plastic buckling mode of cable-stayed bridge.

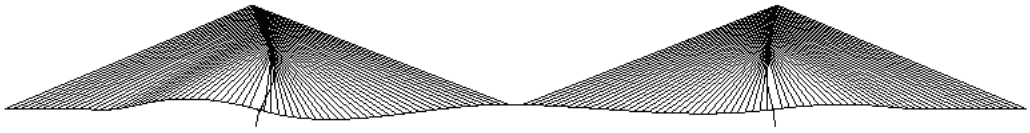

5.2. Aerostatic Characteristics of Bridges under Wind Load

Wind load is an important factor in the design of long-span cable-stayed bridges. It has two effects on the structure: aerostatic and aerodynamic. Fluttering causes the greatest damage amongst all other aerodynamic effects. Cable-stayed bridges with streamlined, flat steel box girders are more aerodynamic resistant, giving the bridge a relatively high critical wind speed. Therefore, the present paper focuses mainly on the transverse deformation of the structure under static wind load.

The aerostatic effect on the structure is related to the structure shape and wind attack angle. In this paper, the static wind load is calculated using three aerostatic coefficients based on the wind tunnel test results of scale model. The aerostatic actions on the box girder are as follows:

$$\begin{cases} D(\alpha) = 0.5\rho U^2 A_n C_D(\alpha) \\ L(\alpha) = 0.5\rho U^2 B C_L(\alpha) \\ M(\alpha) = 0.5\rho U^2 B^2 C_M(\alpha) \end{cases} \tag{26}$$

Here, α is the wind attack angle; ρ is air density; B is girder width; A_n is girder height in the windward side; and U is wind speed. Here, U = 40 m/s. D, L and M are the drag force, the lift force and the torque action on unit length of the box girder in relation to the drag coefficient C_D, the lift coefficient C_L and the torque coefficient C_M, respectively. Figure 18 gives the relation curves between the three aerostatic coefficients and the wind attack angles.

Figure 18. Correlation between aerostatic coefficients and the wind attack angles.

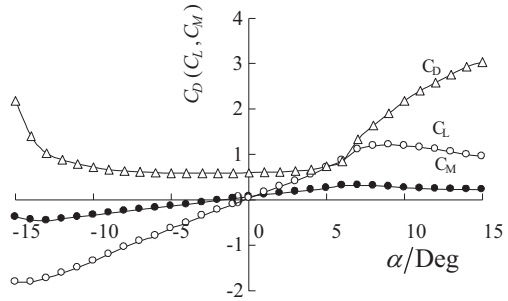

Figure 19 gives the transverse bending moment and deformation of the half-bridge girder under the design wind load. Due to the constraints imposed by the middle piers, the bending moment and deformation of the side span girders are very small, but that of the mid-span girder is considerably high. The transverse bending moment and deformation of mid-span girders is slightly larger for steel cable-stayed bridges than that for CFRP cable-stayed bridges. The logic behind this is that the out-of-plane deformation of the girder is related to the windward area of the cable, and steel cables have more windward area than CFRP cables.

The analysis of the instability of cable-stayed bridges under static wind load showed that when the wind speed reaches 60 m/s for a complete bridge or 50 m/s for a bridge still under construction, bridges built with CFRP cables showed no buckling failure. This indicates that CFRP cable-stayed bridges have better wind resistance than steel cable-stayed bridges.

Figure 19. (**a**) Transverse bending moment of girder under wind load; (**b**) transverse deformation of girder under wind load.

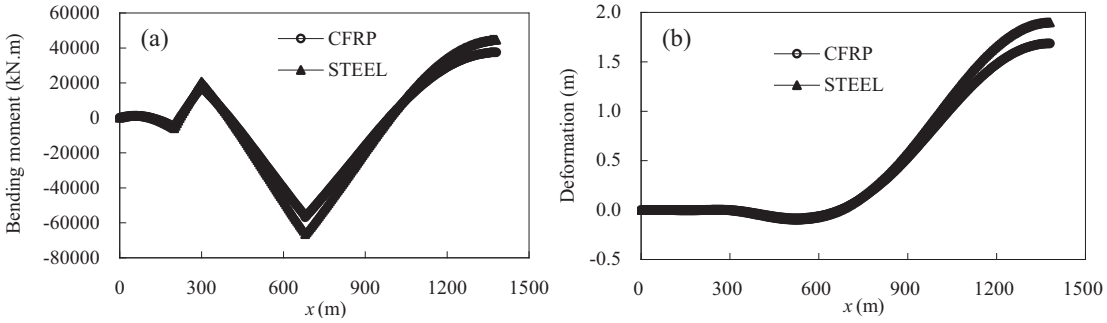

5.3. Dynamic Response of Bridge under Traffic Load

Dynamic response due to traffic loads has a major impact on the safety and durability of a cable-stayed bridge. A vehicle-bridge coupling model was established to study the load impact factor and the cable response of CFRP cable-stayed bridges under traffic load. The girder deflection and cable tension response of the bridge were evaluated for different vehicle speeds and levels of road roughness. Because some of the first natural frequencies of long-span cable-stayed bridges are relatively small, the calculated results of vehicle-bridge coupling using sophisticated vehicle models show little difference from those produced using simplified vehicle models. For this reason, the four-degree vehicle model shown in Figure 20a was used to facilitate calculation. Figure 20b shows the power spectral density of a sample wave that represents the relatively smooth road surface [41].

Figure 20. (**a**) Four-degree vehicle model; (**b**) power spectral density of sample wave.

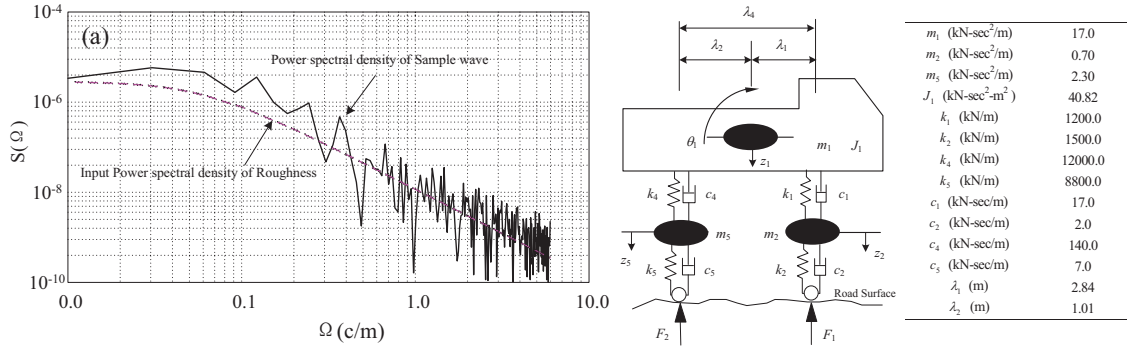

m_1 (kN-sec^2/m)	17.0
m_2 (kN-sec^2/m)	0.70
m_5 (kN-sec^2/m)	2.30
J_1 (kN-sec^2-m^2)	40.82
k_1 (kN/m)	1200.0
k_2 (kN/m)	1500.0
k_4 (kN/m)	12000.0
k_5 (kN/m)	8800.0
c_1 (kN-sec/m)	17.0
c_2 (kN-sec/m)	2.0
c_4 (kN-sec/m)	140.0
c_5 (kN-sec/m)	7.0
λ_1 (m)	2.84
λ_2 (m)	1.01

Figure 21 gives the flexural deflection responses of the bridge girder under moving traffic at speeds of 60 km/m, 80 km/m and 100 km/h. The horizontal axis represents the location of the vehicle, and the vertical axis represents the girder deflection. For both a CFRP cable-stayed bridge and a steel cable-stayed bridge, the deflection responses at mid-span are dominated by static deflection and a long-period vibration response, and the short-period vibration response is insignificant. The influence of traffic speeds was found to be very limited. Figure 21 shows that the flexural deflection of CFRP cable-stayed bridge is greater than that of the steel-cable-stayed bridge. This is because the CFRP cable-stayed bridge has relatively less structural rigidity, and the deflection response is mainly caused by static deformation.

Figure 21. (**a**) Deflection response of CFRP cable-stayed bridge; (**b**) deflection response of steel-cable-stayed bridge.

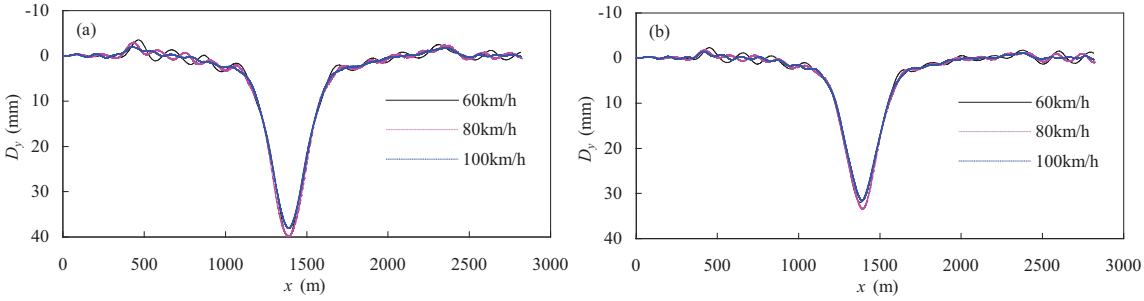

Figure 22 shows the static and dynamic tension responses of cable C1 of a cable-stayed bridge with moving traffic. The tension response of the CFRP cable was generally similar to that of the steel cable, even though the natural frequencies of CFRP cable and steel cable are different. This indicates that the longitudinal vibration of the cable is mainly caused by the vibrations of the support structure, *i.e.*, the anchorage points at the girder and the pylon. The local vibration of the cable does not influence this response.

Figure 22. Static and dynamic tension responses of cables: (**a**) CFRP cable under vehicles moving at 60 km/h; (**b**) steel cable under vehicles moving at 60 km/h; (**c**) CFRP cable under vehicles moving at 80 km/h; (**d**) steel cable under vehicles moving at 80 km/h; (**e**) CFRP cable under vehicles moving at 100 km/h; (**f**) steel cable under vehicles moving at 100 km/h.

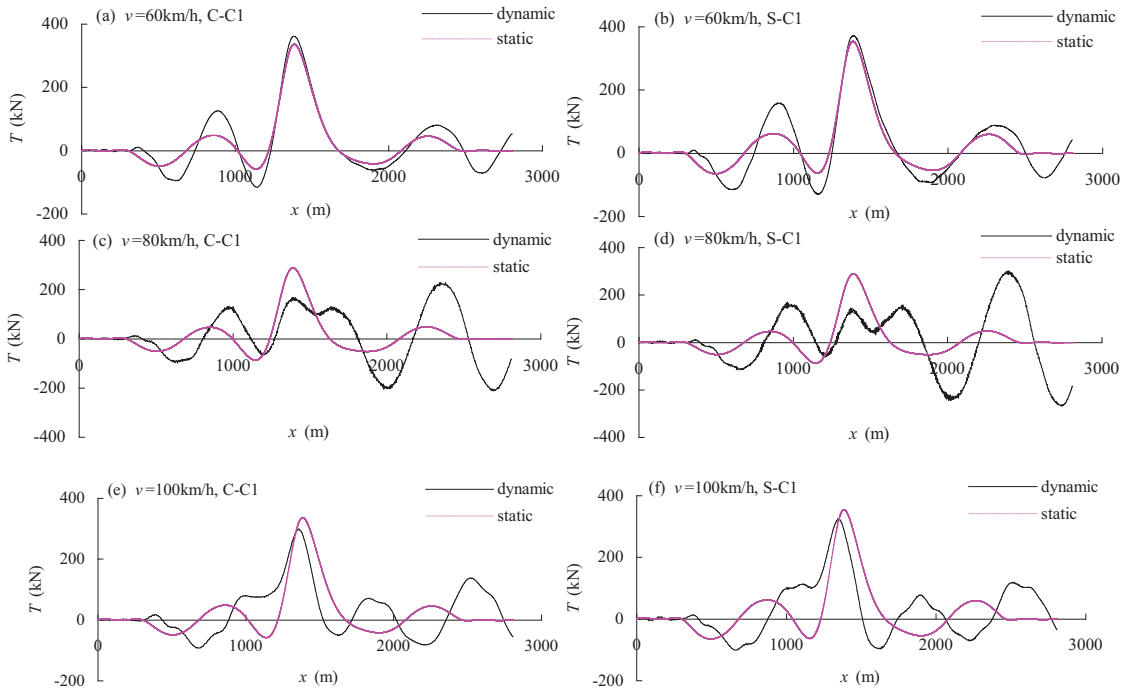

6. Conclusions

To explore the feasibility of using CFRP cables in long-span cable-stayed bridges, this paper establishes a finite element model of a cable-stayed bridge with an ultimate span of 1400 m. The static and dynamic characteristics of cable-stayed bridges with CFRP cables are studied here. By comparing CFRP cables with steel cables in terms of mechanical behavior, some conclusions are drawn:

(1) For the same span cables in a 1400 m span cable-stayed bridge, the self-weight of CFRP cable was only about 1/7 that of steel cable. Additionally, the Irvine parameters of CFRP cables are only about 1/6 that of steel cables. Therefore, the CFRP cable performance in tension is better than that of steel cables.

(2) For the same cable span, the natural frequencies of CFRP cables are about two times those of steel cables. Additionally, the optimal viscous damping coefficients of CFRP cables are about half those of steel cables. Therefore, the CFRP cables can help prevent the cable-bridge coupling vibration caused in lower modes of the cables. The attenuation of the parametric and wind fluctuating vibrations is better for CFRP as compared to the steel cables as suggested by the response amplitudes of the cables. The vibration amplitudes of CFRP cables are less than half those of steel cables.

(3) CFRP cable-stayed bridge has relatively less structural rigidity, so the maximum girder deflection of CFRP cable-stayed bridge is about 1.22-times the steel-cable-stayed bridge.

However, the maximum compressive stress in the girders of CFRP-cable-stayed bridges is 9% lower than that of steel cable-stayed bridges. Additionally, the minimum stability factor of CFRP cable-stayed bridges is 5% larger than that of steel cable-stayed bridges.

(4) The CFRP cables have a lesser windward area than steel cables. Therefore, the transverse bending moment and out-of-plane deformation of mid-span girders is slightly larger for steel cable-stayed bridges than that for CFRP cable-stayed bridges.

(5) An analysis of vehicle-bridge coupling vibrations showed that replacing steel cables with CFRP cables has little impact on the vibration response of a cable-stayed bridge.

Using CFRP cables on long-span cable-stayed bridges is facilitatory in terms of mechanical properties. As the manufacturing process matures and the cost decreases, CFRP cables will see more use in long-span cable-stayed bridges.

Acknowledgments

We gratefully acknowledge the support from the National Natural Science Foundation of China (No. 50578141), without whom the research would not have taken the present shape.

Author Contributions

In this paper, Xu Xie finished the static calculation of CFRP cables and the cable-stayed bridge, and wrote the abstract, introduction, conclusions, structural description of the cable-stayed bridge, static and dynamic characteristics of cable-stayed bridge with CFRP cables. Yonggang Shen finished the dynamic calculation of CFRP cables and the cable-stayed bridge, and wrote the dynamic characteristics of CFRP cables and cable-stayed bridge. Xiaozhang Li finished the damping test of cables, and wrote mechanical properties of CFRP cables.

Conflicts of Interest

The authors declare no conflict of interest.

References

1. Lan, C.M. Study on Life-cycle Safety Assessment Methods for Parallel Wire Stay Cable. Ph.D. Thesis, Harbin Institute of Technology, Harbin, China, February 2009.
2. Meier, U. Carbon Fiber-Reinforced Polymers: Modern Materials in Bridge Engineering. *Struct. Eng. Int.* **1992**, *2*, 7–12.
3. Meier, U.; Meier, M. CFRP Finds Use in Cable Support for Bridges. *Modern Plast. Int.* **1996**, *4*, 87–88.
4. Meier, U. Structural Tensile Elements Made of Advanced Composite Materials. *Struct. Eng. Int.* **1999**, *4*, 281–285.
5. Konno, S.; Noro, T.; Yamazaki, S. Material Properties of Carbon Fiber Cables for Cable Supported Bridges. *Bridge Found. Eng.* **1999**, *9*, 29–32. (In Japanese)
6. Take, N.; Higashino, T.; Mastsumura, T.; Nishimura, N. Study on Aerodynamic Stability and Preliminary Design of Dual Cable Suspension Bridges Using Advanced Composites. *Trans.*

Jpn. Soc. Comput. Eng. Sci. **1999**, *1*, 89–94. (In Japanese)

7. Mei, K.; Lu, Z. Application Prospect of CFRP to Super Length Suspension Bridge and Cable-Stayed Bridge. *Bridge Constr.* **2002**, *2*, 75–78. (In Chinese)
8. Kou, C.; Xie, X.; Kao, C.; Huang, J.Y. Static Behavior of Long-span Cable-stayed Bridges Using Carbon Fiber Composite Cable. *J. Zhejiang Univ. Eng. Sci.* **2005**, *39*, 137–142. (in Chinese).
9. Cheng, S.H.; Lau, D.T. Impact of Using CFRP Cables on the Dynamic Behavior of Cable-stayed Bridges. Reported at the IABSE Symposium, Budapest, Hungary, 11–15 September 2006.
10. Wu, Z.S.; Wang, X. Investigation on a thousand meter scale cable-stayed bridge with fiber composite cables. In Proceedings of the 4th International Conference on FRP Composites in Civil Engineering, Zurich, Switzerland, 22–24 July 2008.
11. Wen, X.; Cai, C.S.; Xiao, R.C.; Lu, D. Study of Super Long Span Cable-stayed Bridges with CFRP Components. *Struct. Eng.* **2011**, *33*, 330–343.
12. Li, H.; Huang, Y.; Chen, W.L.; Ma, M.L.; Tao, D.W.; Ou, J.P. Estimation and Warning of Fatigue Damage of FRP Stay Cables Based on Acoustic Emission Techniques and Fractal Theory. *Comput. Aided Civil Infrastruct. Eng.* **2011**, *26*, 500–512.
13. Wen, X.; Cai, C.S.; Xiao, R.C.; Lu, D. Concept and Analysis of Stay Cables with a CFRP and Steel Composite Section. *Struct. Eng.* **2012**, *16*, 107–117.
14. Meier, U. Carbon Fiber Reinforced Polymer Cables: Why? Why Not? What If? *Arabian J. Sci. Eng.* **2012**, *37*, 399–411.
15. Seible, F.; Karbhari, V.M.; Burgueno, R. Kings Stormwater Channel and I-5/Gilman Bridge, USA. *Struct. Eng. Int.* **1999**, *9*, 250–253.
16. Karbhari, V.M.; Seible, F. Fiber-Reinforced Polymer Composites for Civil Infrastructure in the USA. *Struct. Eng. Int.* **1999**, *4*, 274–277.
17. Burgoyne, C.J. Advanced Composites in Civil Engineering in Europe. *Struct. Eng. Int.* **1999**, *4*, 267–273.
18. Christoffersen, J.; Hauge, L.; Bjerrum, J. Footbridge with Carbon-fibre-reinforced Polymers, Denmark. *Struct. Eng. Int.* **1999**, *9*, 254–256.
19. Lu, Z.T.; Mei, K.H. First Application of CFRP Cables for a Cable-stayed Bridge in China. *China Civil Eng. J.* **2007**, *40*, 50–59. (In Chinese)
20. Yamgauchi, H.; Ito, M. Mode-dependence of Structural Damping in Cable-stayed Bridges. *J. Wind Eng. Ind. Aerodyn.* **1997**, *72*, 289–300.
21. Zhang, H.; Xie, X.; Zhao, J. Parametric Vibration of Carbon Fiber Reinforced Plastic Cables with Damping Effects in Long-span Cable-stayed Bridges. *J. Vib. Control* **2011**, *17*, 2117–2130.
22. Xie, X.; Nakamura, H.; Maeda, K.; Zhang, Z.; Enomoto, T. Theoretical Analysis and Experimental Test on Damping Characteristics of CFRP Stay Cables. *Eng. Mech.* **2010**, *27*, 205–216. (In Chinese)
23. Kady, H.M.; Arockiasamy, M.; Samaan, S. Damping Characteristics of Carbon Fiber Composite Cables for Application in Cable-stayed Bridges. In Proceedings of IABSE Conference on Cable-stayed Bridges- Past, Present and Future, Malmo, Sweden, 2–4 June 1999.

24. Irvine, H.M. *Cable Structures*; MIT Press: Cambridge, MA, USA, 1981.
25. Caetano, E.d.S. *Cable Vibrations in Cable-Stayed Bridges*; Structural engineering documents 9. IABSE-AIPC-IVBH: Zurich, Switzerland, 2007.
26. Takahashi, K. Dynamic Stability of Cables Subjected to An Axial Periodic Load. *J. Sound Vib.* **1991**, *144*, 323–330.
27. Uhrig, R. On Kinetic Response of Cables of Cable-stayed Bridges due to Combined Parametric and Forced Excitation. *J. Sound Vib.* **1993**, *165*, 182–192.
28. Lilien, J.L.; Da Costa, A.P. Vibration Amplitudes Caused by Parametric Excitation of Cable Stayed Structures. *J. Sound Vib.* **1994**, *174*, 69–90.
29. Kang, Z.; Zhong, W.X. Numerical Study on Parametric Resonance of Cable in Cable Stayed Bridge. *China Civil Eng. J.* **1998**, *31*, 14–22. (In Chinese)
30. Sun, B.N.; Wang, Z.G.; Ko, J.M.; Ni, Y.Q. Parametrically Excited Oscillation of Stay Cable and Its Control in Cable-stayed Bridges. *J. Zhejiang Univ. Sci.* **2003**, *4*, 13–20.
31. Yang, S.Z.; Chen, A.R. Parametric Oscillation of Super Long Stay Cables. *J. Tongji Univ. Nat. Sci.* **2005**, *33*, 1303–1307. (In Chinese)
32. Georgakis, C.T.; Taylor, C.A. Nonlinear Dynamics of Cable Stays. Part 1: Sinusoidal Cable Support Excitation. *J. Sound Vib.* **2005**, *281*, 537–564.
33. Georgakis, C.T.; Taylor, C.A. Nonlinear Dynamics of Cable Stays. Part 2: Stochastic Cable Support Excitation. *J. Sound Vib.* **2005**, *281*, 565–591.
34. EI Ouni, M.H.; Kahla, N.B.; Preumont, A. Numerical and Experimental Dynamic Analysis and Control of a Cable Stayed Bridge under Parametric Excitation. *Eng. Struct.* **2012**, *45*, 244–256.
35. Takahashi, K.; Konishi, Y. Non-linear Vibrations of Cables in Three Dimensions, Part I: Non-linear Free Vibrations. *J. Sound Vib.* **1987**, *118*, 69–84.
36. Takahashi, K.; Konishi, Y. Non-linear Vibrations of Cables in Three Dimensions, Part II: Out-of-plane Vibrations under Inplane Sinusoidally Time-varying Load. *J. Sound Vib.* **1987**, *118*, 85–97.
37. Esaka, Y.; Matsui, T.; Qiao, F.; Moribe, Y.; Sugiyama, E. *A Study on Response of Seismically Isolated Large Span Domes to Fluctuating Wind Loads. Part 1: Wind Response of Base Isolation System*; Architectural Institute of Japan: Tokyo, Japan, 2001. (In Japanese)
38. Xie, X.; Zhang, Z.C.; Nakamura, H.; Maeda, K. Nonlinear vibration of stay cables under fluctuating wind load and support excitation. *China Civil Eng. J.* **2008**, *41*, 66–72. (In Chinese)
39. Xie, X.; Zhu, Y.F. Study on Behavior of Long-span CFRP Cable-stayed Bridges. *Eng. Mech.* **2007**, *24*, 113–120. (In Chinese)
40. Nagai, M.; Asano, K.; Watanabe, K. Applicability of the Ef method and design method for evaluating the load-carrying capacity of girders in cable-stayed bridges. *J. Struct. Eng. JSCE* **1995**, *41A*, 221–228. (In Japanese)
41. Xie, X.; Zhu, Y.F.; Shen, Y.G. Study on vibration of long-span cable-stayed bridge with steel and CFRP cables due to moving vehicles. *Eng. Mech.* **2007**, *24*, 53–61. (In Chinese)

Flash Thermography to Evaluate Porosity in Carbon Fiber Reinforced Polymer (CFRPs)

Carosena Meola and Cinzia Toscano

Abstract: It is a fact that the presence of porosity in composites has detrimental effects on their mechanical properties. Then, due to the high probability of void formation during manufacturing processes, it is necessary to have the availability of non-destructive evaluation techniques, which may be able to discover the presence and the distribution of porosity in the final parts. In recent years, flash thermography has emerged as the most valuable method, but it is still not adequately enclosed in the industrial enterprise. The main reason of this is the lack of sufficient quantitative data for a full validation of such a technique. The intention of the present work is to supply an overview on the current state-of-the-art regarding the use of flash thermography to evaluate the porosity percentage in fiber reinforced composite materials and to present the latest results, which are gathered by the authors, on porous carbon fiber reinforced polymer laminates. To this end, several coupons of two different stacking sequences and including a different amount of porosity are fabricated and inspected with both non-destructive and destructive testing techniques. Data coming from non-destructive testing with either flash thermography or ultrasonics are plotted against the porosity percentage, which was previously estimated with the volumetric method. The new obtained results are a witness to the efficacy of flash thermography. Some key points that need further consideration are also highlighted.

Reprinted from *Materials*. Cite as: Meola, C.; Toscano, C. Flash Thermography to Evaluate Porosity in Carbon Fiber Reinforced Polymer (CFRPs). *Materials* **2014**, *7*, 1483ï 1501.

1. Introduction

Composite materials are nowadays ever more massively employed in advanced engineering structures with their use in the transport industry, in civil infrastructures, in chemical equipment, *etc.* This success is justified by the many advantages they offer, amongst others, the possibility to choose both the raw materials and the manufacturing process to obtain a final product of desired characteristics. In civil aviation, composites are highly appreciated especially for their favorable stiffness-to-weight ratio, which involves a significant reduction in fuel burnt per seat per mile with a consequent significant decrease in the emission of CO_2.

Carbon fiber reinforced polymers (CFRPs) are mostly employed in the construction of aircraft [1]. Within the mostly used hand lay-up manufacturing method, plies of fibers impregnated with resin (generally named prepregs) are overlaid, following a fixed stacking sequence, and cured in autoclave. The autoclave cycle involves the combined effects of temperature and pressure. Temperature is needed to activate and to control the chemical reactions in the resin, while pressure is used to squeeze off the excess resin, to consolidate the stacked plies and to minimize the amount of entrapped gas between the plies and within the resin [2]. Therefore, the action of temperature and

pressure, as well as the cycle length are the main parameters to care for in order to assure the effectiveness of the curing process and, consequently, the overall quality of the final part.

Generally, the best curing temperature value is found through specific thermo-physical tests aimed at monitoring the dependence of the resin viscosity on the temperature and through the measure of the glass transition temperature. The determination of the optimum vacuum pressure value with its application time represents a difficult task to deal with [3]. Indeed, if both pressure value and application time are not optimized, voids could rise in the laminate [2]. As a main effect, the presence of voids reduces the interlaminar shear strength causing delamination (inter-lamina debonding) [4]. Besides, the presence of regions of fibers unsupported by the matrix can induce local stress concentration, with consequent severe degradation of strength and stiffness in-service. That is why the porosity level and its distribution within the whole final part must be known and taken into account.

Since the presence of a certain amount of voids is unavoidable [4]; it is important to know the level of voids that is acceptable in the specific application field. In fact, in many composite applications, the void content is quite critical, and levels above about 1% are not tolerable, such as in advanced composite dynamic aerospace structures, while in other applications, levels of 5% and higher can be tolerated [4]. Of course, lower void content means higher production costs, whereas loosening the quality control standards translates to a lower cost of the end products. Often, establishing the acceptable level of voids is a critical issue in designing composite structures, and then, the use of effective evaluation techniques is compulsory.

The intention of this paper is to present an overview of some of the most used methods, with particular attention devoted to the state-of-the-art on the use of flash thermography, which actually seems to be the most effective and advantageous method to assess the porosity percentage in composites. In particular, the overview involves data available in the literature integrated with the latest results, which were gathered by the authors, on porous CFRP laminates. At last, some key points that need further consideration are highlighted.

2. Results and Discussion

Basically, the porosity percentage can be determined through two approaches: destructive and non-destructive. Of course, destructive methods involve small proper samples and supply information only by statistical inference. On the contrary, the use of non-destructive techniques allows for the inspection of the whole part.

2.1. Destructive Methods

The porosity percentage can be estimated through three methods: volumetric, microscopy and acid digestion.

Measurements with the volumetric method are carried out on small samples, which may be cut either from a large laminate or prepared ad hoc, to be representative of a production lot. Basically, the method supplies measurements of density through weight in air and in water; then, the resulting porosity is calculated from the law of mixtures by knowing the average density [5]. In more details,

each small piece, of known volume, is weighted (by a precision digital balance) to allow the calculation of the density, ρ, through the Archimedes' principle. The law of mixtures gives:

$$\rho = \frac{\rho_f V_f + \rho_r V_r}{V_f + V_r} \tag{27}$$

where V_f and V_r respectively represent the volume of fibers and of resin; whereas ρ_f and ρ_r, are the density of the fibers and of the resin (ρ_f and ρ_r are provided by the prepreg lamina supplier). Equation (1) may be rewritten by introducing the volume of voids, V_v:

$$\rho = \frac{\rho_f V_f + \rho_r V_r}{V_f + V_r + V_v} \tag{28}$$

Being $V_f + V_r + V_v = V_T$ the actual total volume of the piece, from Equations (1) and (2), it is easy to calculate V_f/V_T and V_r/V_T and, so, the porosity volume fraction, V_v/V_T.

Small samples are also used for observation through optical microscopy; it is possible to measure the total space occupied by the pores and, by knowing the lens magnification, to infer the porosity distribution percentage. The sample surface requires previous metallurgical polishing.

For both methods, nothing can be said in terms of accuracy and reliability, since the real void content is unknown. However, in consideration of the errors involved in the measurements and owing to data present in the literature [6], it can be inferred that the void fraction obtained with the volumetric method (Archimedes) is affected by a larger deviation in comparison with optical microscopy. Of course, to minimize the section-bias errors, at least three adjacent cross-sections must be taken. Actually, the results of both volumetric and microscopy methods are strongly related to very small portions of the laminate; this, of course, makes the results unlikely to be a depiction of the whole piece.

A more reliable method may be acid digestion, since it involves the testing of the whole part [7]. However, two considerations should be made against this method. On one side, it requires the use of dangerous acids that, in turn, involves severe safety at work measures with additional costs in terms of personnel training and of specific protection devices. On the other side, the obtained porosity value can be assumed to be representative of a manufacturing process, but it cannot account for the real amount of porosity within each final part. Conversely, mainly in the aeronautical field, there is the need to assess the porosity percentage on each part of the entire production; this is the reason for the ever increasing interest on the development of non-destructive testing (NDT) methods.

2.2. Non-Destructive Methods

Brit and Smith [8], in a review on non-destructive evaluation (NDE) methods for porosity assessment in fiber reinforced polymers, stated that none of the current NDE techniques can be considered as a reference technique, due to the dependence of the instrument response on the pore morphology, as well as on the intrinsic nature of the fiber and matrix themselves.

Nevertheless, ultrasonic testing (UT) [9] is actually the most commonly used technique, especially in the industrial environment, in which the production processes are well consolidated, as in the aerospace sector. However, the detection of porosity in resin-starved areas of polymer matrix composites is very difficult and generally not reliable with the ultrasonic method, and so, the

attention has been given also towards other methods, such as computed tomography (CT) [10] and infrared thermography (IRT) [11]. CT [10] may be used to overcome some of the UT limitations regarding size, shape and position of all individual pores. Adversely, it involves difficulties in testing real parts (it is mainly suitable for small samples), as well as safety at work concerns. Industrial production is demanding for proper inline control.

A methodology that acts in a non-destructive and completely non-invasive way and that does not involve any specific surface prerequisites, nor safety at work concerns, is flash thermography (FT). It has proven its suitability, through the evaluation of porosity percentages linked to measurements of thermal diffusivity [11]. The attention of the present work is to trace the actual state-of-the-art on the use of FT and to illustrate its suitability in comparison to the most widely used UT.

2.2.1. Ultrasonic Testing

Porosity can be determined with UT by creating ecographic images (c-scans), through correlation with either a single ultrasonic frequency (narrowband approach) or the ultrasonic frequency slope (broadband approach) [12].

Amongst the empirical techniques developed, the measure of the variation of the signal attenuation is massively used, since it accounts for the scattering effect induced by voids [13]. The decrease of the intensity, I, of the ultrasonic signal [14] while propagating within the path length, z, of an attenuating medium, is well described by the classical Beer–Lambert law:

$$I(z) = I_0 e^{-\beta z} \tag{29}$$

with β being the attenuation coefficient, which, providing an estimation of the bulk attenuation, is a good marker of porosity.

Further, the correlation between the signal attenuation and the amount of porosity has been demonstrated [14], as well as the dependency of the attenuation on the ultrasonic wave frequency [15]. In particular, Hsu [16] used the through-transmission (TT) technique to assess the amount of porosity as volume percentage in CFRP, and successively, Steiner [17] demonstrated that the ultrasonic pulse-echo (PE) technique is effective, too. More recently, researchers at the Italian Aerospace Research Centre (CIRA) [5] demonstrated, via PE, that the amount of porosity that forms during the curing cycle depends also on the fibers' orientation.

The ecographic approach is very effective in the presence of spherical pores that have a diameter exceeding the instrument resolution and that are homogeneously disseminated within an isotropic medium; conversely, a quantitative determination of porosity is very difficult or not reliable. Recently, a correlation model to account for the random presence of voids in an anisotropic medium was proposed [18]. However, at the current state-of-the-art, a quantitative assessment of porosity in rather complex composite structures is not feasible.

2.2.2. Flash Thermography

Flash thermography can be used to evaluate porosity from measurements of thermal diffusivity.

It derives from the flash method, which was proposed by Parker in 1961 [19] and which became an American Society for Testing and Materials (ASTM) standard in 1992 [20]. Parker's method is based

on the analytical solution of the Fourier equation with adiabatic boundary conditions for an infinite slab subjected to a thermal Dirac pulse [21]. The test is performed according to the transmission scheme, with an energy pulse being deposited on the sample front surface, while the temperature evolution is measured on the rear surface. Thermal diffusivity is linked to the sample thickness, L, and to the half-maximum rise time through the equation [19]:

$$\alpha = \frac{0.139L^2}{t_{1/2}} \tag{30}$$

$t_{1/2}$ is the time in seconds needed to reach half of the maximum temperature value, $T_{M/2}$. A typical temperature (T) plot against the number of images (frames) is shown in Figure 1; from the frame rate, it is easy to revert to time in seconds. Of course, the frame rate is chosen according to the infrared camera performance used and the characteristics of the coupon under measure.

Figure 1. Typical temperature (T) plot against the number of images (frames) in a point on the specimen backside. The dotted red line shows the link between $t_{1/2}$ and $T_{M/2}$.

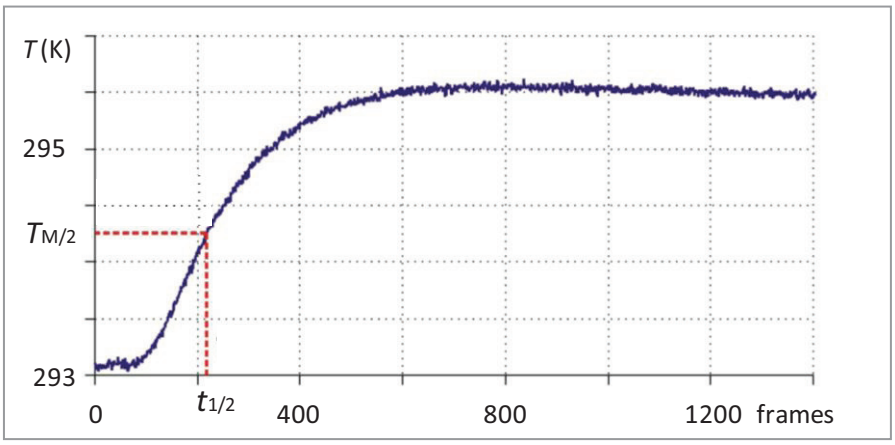

Thermal diffusivity is defined as:

$$\alpha = \frac{k}{\rho c_p} \tag{31}$$

where k is the thermal conductivity, ρ is the density and c_p is the specific heat at constant pressure. Thermal diffusivity, being dependent on density and specific heat, is a good parameter for the indirect estimation of the amount of embedded porosity within the material.

Of course, this method was first conceived [19] for temperature measurements with contact transducers (e.g., leaf thermocouples); while now, it is being used in combination with infrared thermography. The usefulness of the infrared camera is obvious, since it allows for fast monitoring, in a remote way, of temperature variations and for the evaluation of the thermal diffusivity pixel-by-pixel over a given, ever large, area. The possibility to map the thermal diffusivity is an advantage in view of accounting for local variations due to the presence of local material inhomogeneities.

2.3 Some Historical Hints into the Use of Flash Thermography

An early attempt to monitor porosity in thermoplastic composites was done by Steiner *et al*. [22] through the use of thermography and laser-based ultrasonics, but much interest was raised starting

from 2000. In particular, in 2001, Chu *et al.* [23], through finite element analysis (FEA) and experimental tests, demonstrated that there is a good correlation between thermal diffusivity and porosity in composite materials. A series of finite element models were built, and thermal responses for isotropic and orthotropic materials with various thermal diffusivities subjected to different heating conditions were investigated. Experimental tests are useful to validate the numerical models and to estimate the unknown parameters, like the amount of heat flux. They also show that both laser and flash heating can be used to effectively obtain thermal diffusivity.

Later, Grinzato *et al.* [24] carried out tests, with flash thermography, on a real aeronautic CFRP part to evaluate both thermal diffusivity and thermal effusivity. The latter were compared to results obtained with ultrasonics c-scans, and it was found that thermal effusivity is much more sensitive than thermal diffusivity to porosity variations, but it is also more affected by heating non-uniformities.

One of the main problems encountered when testing complex structures is to differentiate between porosity (micro-voids) and resin-starved areas. It has been observed that a high porosity level decreases the thermal diffusivity much more than it does an area rich in resin; but for a better discrimination, good data filtration through mathematical procedures is necessary [25]. An investigation, aimed at discovering porosity in a real aircraft part [26], raised the problem of non-uniform heating within pulse thermography; the approach of the source distribution image (SDI) was proposed as a reference for discriminating between sound and defective zones.

A linear relation between diffusivity and porosity was obtained experimentally through flash thermography, by Hendorfer *et al.* [11]. Measurements were performed on CFRP samples 2 mm-thick with simulated porosity between 1% and 5%; the average nominal porosity being estimated through ultrasonic testing. Flash thermography offers some advantages over ultrasonics in terms of detailed information supplied within a reduced testing time. Mayr and Hendorfer [27] investigated also the possibility to apply flash thermography in reflection mode and found a higher data spread with respect to the use in the transmission mode. In particular, they observed a decrease in sensitivity for both modes (transmission and reflection) when porosity increased up to 10%; this was ascribed to the tendency of pores to interlink, as verified through measurements with computed tomography. Later, Mayr *et al.* [28] carried out tests on CFRP involving prepregs woven in a twill weave pattern at a ratio of 3/1 and found active thermography comparable to ultrasonic testing in terms of the ability to determine porosity. As a main finding, they observed, through a comparison with CT data, that the thermal diffusivity is strongly affected, not only by the porosity content, but also by the pore shape.

Most recently, flash thermography proved suitable for porosity measurements also in flax/epoxy composites [29].

The usefulness of flash thermography within the evaluation of porosity in composites seems extensively demonstrated. However, many papers deal with qualitative estimation of porosity, and some refer to composites of given characteristics, not always completely specified, which make a general data correlation difficult. On the other side, before a full acceptance of a method, lots of tests are needed, as well as comparison of data coming from different laboratories worldwide and carried out on similar test articles. The latter point is very difficult to achieve, due to the variability associated with composites. In fact, composites are made of two basic ingredients: the matrix and the fibers; but each of them has different thermal properties, and then, it is their mutual percentage that drives the thermal diffusivity of the final part [28]. For example, in carbon/epoxy, carbon fibers have

a thermal diffusivity much higher than the resin epoxy; then, the thermal diffusivity of a CFRP part strongly depends on the volume of carbon fibers.

Wrobel *et al.* [30], through flash thermography measurements, found a variation of thermal diffusivity in the range 1.5–2.2 × 10^{-7} m^2/s for a variation of fiber content between 13% and 28%. The fibers' orientation also plays a fundamental role, since, as stated in [31], the direction of the heat flow coincides with the direction of the fibers. In addition, the manufacturing process involves many parameters, making it difficult and almost impossible to replicate a product of completely equal characteristics.

A more extensive investigation, involving a large number of CFRP samples of several different stacking sequences and with different percentages of porosity, was recently carried out by Toscano *et al.* [32,33]. Some samples similar to those used by Toscano *et al.* [32–34] are herein considered to better investigate the influence of the fibers' orientation coupled with a variation of porosity percentage. Such specimens are tested with both flash thermography and ultrasonics with the purpose of a data comparison.

3. Experimental Section

In this section, several specimens of two stacking sequences, which were fabricated following the procedure already used by Toscano *et al.* [32–34], are considered. Data obtained with flash thermography are compared to those obtained with destructive methods and with ultrasonic testing. The intention is to check the ability of flash thermography to discriminate differences of porosity induced by a different orientation of fibers and to get quantitative data that may serve as a basis for a full assessment of flash thermography as an alternative to ultrasonics and in view of its introduction for in-line post-production inspection of composite parts.

3.1. Description of Specimens

Several coupons, involving a polymer (resin epoxy) as a matrix and carbon fibers as a reinforcement, were manufactured that enclosed a certain percentage of porosity and a slag inclusion [32]. More specifically, CFRP specimens include prepreg laminas M21/IM7, provided by Hexcel®, which were superimposed (hand lay-up technique) following two stacking sequences (Table 1). More specifically, a unidirectional and a symmetrical orientation of fibers were considered with coupons named Pu and Ps respectively. Groups of them were separately cured in an autoclave at a different pressure percentage, P_c, being, respectively, P_c = 100%, 75%, 50%, 25% and 0% of the prescribed one (7 bar gauge) to induce the formation of a different percentage of porosity.

Table 1. Specimen characteristics.

Coupon Type	Stacking Sequence	No. of Plies
Pu	$[0°]$	24
Ps	$[45°/-45°]_s$	24

Each specimen is 10 cm-long and 5 cm-wide and has an overall thickness of about 5 mm. A Kapton disk 20 mm in diameter and 0.06 mm thick was inserted on one half (Figure 2a) in the middle of the stacking sequence (Figure 2b) in order to account also for the presence of local delamination. The

photo in Figure 2a shows the position of the Kapton disk over unidirectional fibers; such laminas are overlapped, as the sketch on the left (Figure 2b) shows. More specifically, long fiber laminas are simply overlapped to obtain Pu-type specimens or overlapped after they were cut and rotated by +45°, −45° to obtain Ps type specimens. Indeed, a slag insert acts as a zone of lower thermal diffusivity, which may serve also as a reference for quantitative thermal diffusivity measurements. Three specimens for each stacking sequence and curing pressure were manufactured, resulting in a total of 30 specimens.

Figure 2. Prepreg laminas and the position of the Kapton disk. The photo on the **(a)** shows the position of the Kapton disk over unidirectional fibers. The sketch on the **(b)** shows the position of the insert on one half of the lamina in the middle of the stacking sequence.

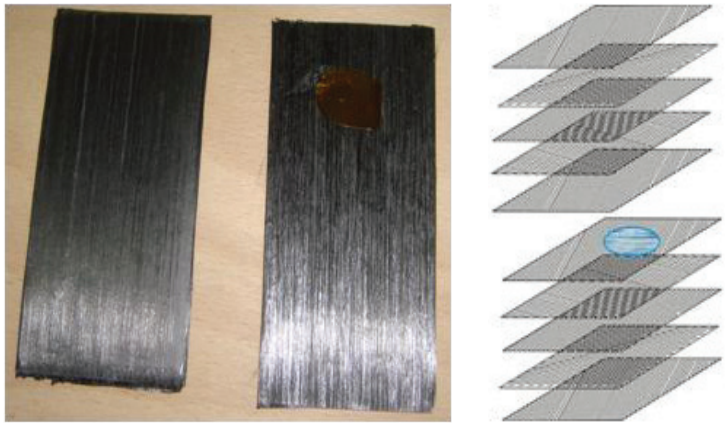

(a) **(b)**

3.2. Porosity Assessment by Destructive Methods

First of all, an estimation of the porosity percentage was performed in a destructive way by measuring the coupons' average density. This was done by weighting in water and in air [3] small pieces that were extracted from each coupon type. Then, through the law of mixtures (properly modified introducing the volume occupied by the voids) [5], the volume fraction of the voids was obtained, V_V%.

Values of V_V%, normalized with respect to the value obtained when P_c = 100%, are plotted against P_c in Figure 3 for specimens Pu and Ps. These specimens were chosen to be, respectively, representative of the variation of the stacking sequence from a unidirectional direction of fibers to an oblique one. As expected, for both specimen types, the percentage of porosity introduced depends almost linearly on the curing pressure following the equation:

$$y = a + bx \tag{32}$$

with coefficients collected in Table 2.

Table 2. Coefficients of Equation (6) for plots shown in Figure 3.

Coupon Type	*a*	*b*	R^2
Pu	9.061	0.080	0.968
Ps	7.276	0.062	0.994

In particular, the higher the applied pressure, the lower the amount of porosity induced in the coupons. The largest data spread lies within ±2% in the Pu-type coupons.

Figure 3. Normalized volume fraction of voids, VV%, versus the curing pressure, Pc%, for Pu and Ps specimens.

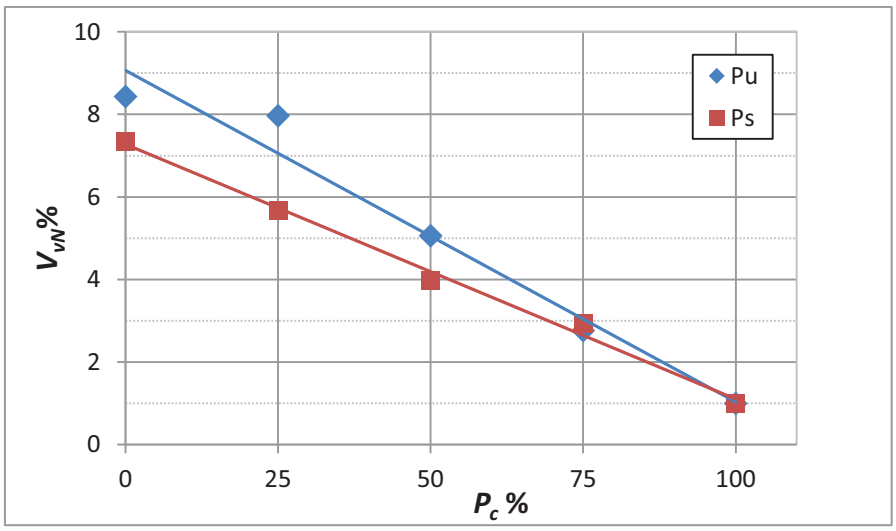

3.3. Measurements with UT

PE in immersion was chosen to perform ultrasonic testing. To prevent water infiltration, each coupon was sealed around the edge with a silicon layer. The inspection of all coupons was carried out using a flat 4–20 MHz probe (by Panametrics®) with a diameter of 0.25 inches (6.35 mm), tuned at 5 MHz and with a spatial resolution of 0.5 mm. The ultrasonic set-up includes a pulser-receiver unit (by Nukem®) and an automated system that allows the probe movements to be synchronized with the signal acquisition. The output of the inspection consists of the attenuation coefficient, β (decibels), and of the time-of-flight (ToF) (microseconds) c-scans.

As already pointed out, β is a good marker of porosity. Therefore, from each attenuation c-scan, the average attenuation β value was measured over an area of almost 20,000 points [5,34] (excluding the area within the Kapton insert). For both coupon types, results are presented in terms of attenuation c-scans (with decibel units) in Figure 4a,b and of ToF c-scans (with microsecond units) in Figure 5a,b; an arrow indicates the position of the Kapton disk in each map.

The local variation in the attenuation of c-scans, principally due to the different amount of porosity in the coupons, is expressed by the different grey levels (Figure 4). In particular, it is easy to notice that coupons cured with P_c = 0% are the darkest ones, because the massive presence of

porosity strongly reduces the signal amplitude. To quantify these observations, total average attenuation values are collected in Table 3.

As can be seen, both attenuation and ToF c-scans are not always effective in outlining the Kapton disk. However, it seems that the probability of detection increases with increasing the amount of porosity in the material; or better, when the curing pressure is much less than the prescribed one. This is probably due to the fact that the Kapton disk, being very thin (s = 0.06 mm), does not affect the passage of the ultrasonic signal in a well-consolidated material.

On the contrary, when the amount of porosity increases ($V_{vN\%} > 2$), a disbonding between the Kapton disk and the surrounding prepreg laminas is promoted, involving the presence of a gas layer that affects the passage of the ultrasonic signal. In this case, the Kapton disk becomes visible in the ToF c-scan because it affects the travel time of the direct reflection.

Figure 4. Attenuation c-scans for different P_c values. (**a**) Pu coupons; (**b**) Ps coupons. An arrow indicates the position of the Kapton disk in each map.

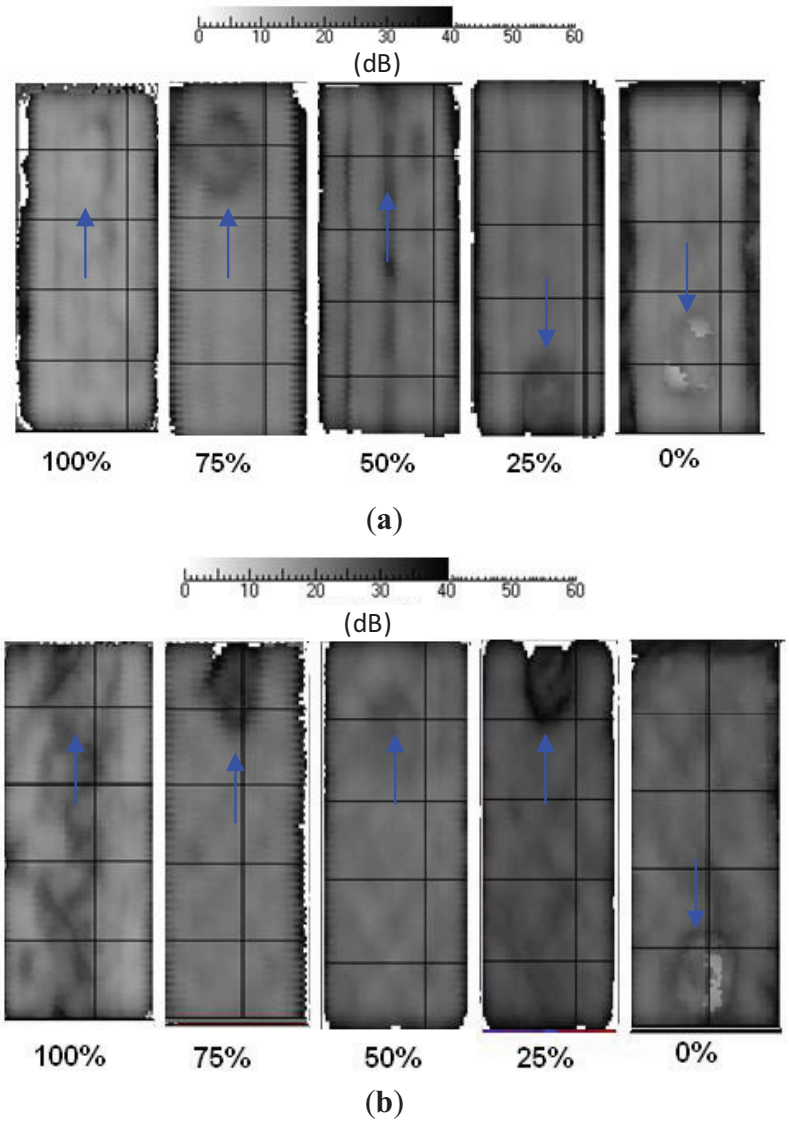

At last, to better account for the fibers' orientation, the average β value was normalized with respect to the value obtained when P_c = 100%; the so obtained values, which are named β_N are

plotted against V_{vN}% in Figure 6. As can be seen, the Ps coupons display a larger variation of the β_N value; instead, the Pu specimens show a lower variation of β_N, but a larger data spread. For Ps and Pu coupons, data are fitted by a polynomial regression:

$$y = a + bx + cx^2 \tag{33}$$

with correlation coefficients collected in Table 4. The plots in Figure 6 display also the error bars to account for the variability of data with respect to the correlation curve. For both coupon types, the data spread increases with increasing the void percentage.

Figure 5. Time-of-flight (ToF) c-scan for different P_c values. (**a**) Pu coupons; (**b**) Ps coupons. An arrow indicates the position of the Kapton disk in each map.

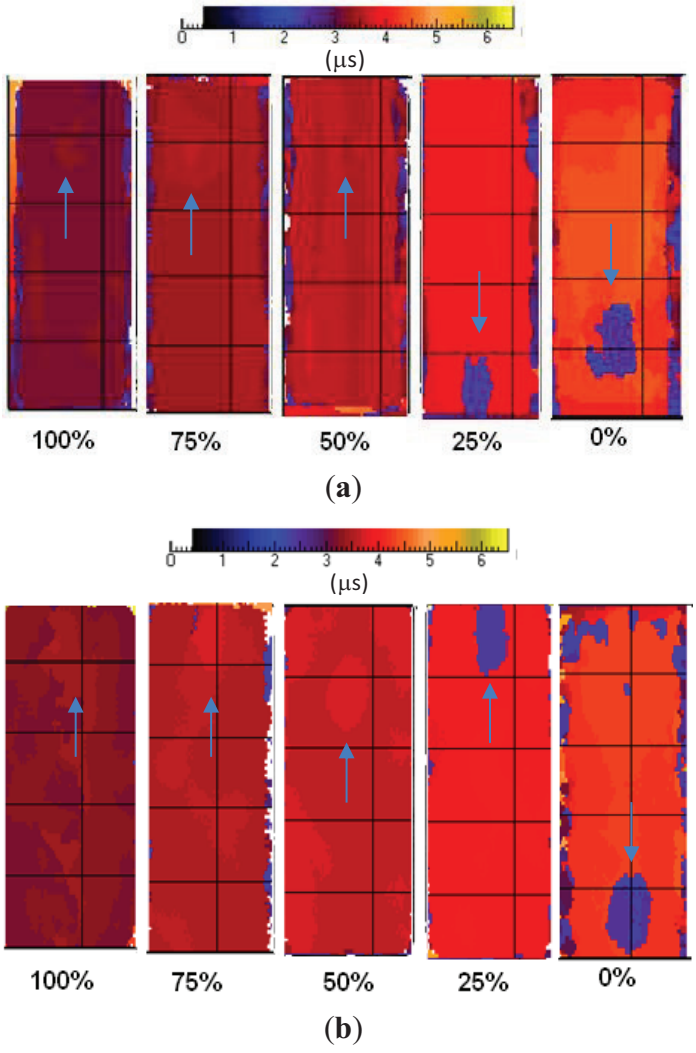

Table 3. Attenuation values and standard deviation for both (Pu and Ps) types of specimens.

P_c%	Pu Total Attenuation (dB)	SD	Ps Total Attenuation (dB)	SD
100	22.5	1.2	20.7	3.4
75	22.1	0.9	22.5	0.7
50	25.0	2.2	25.6	0.9
25	25.6	1.1	29.1	1.1
0	33.5	1.7	38.3	1.2

Table 4. Coefficients of Equation (7) for β_N to Vv_N correlation (Figure 6).

Coupon Type	*a*	*b*	*c*	R^2
Pu	1.067	−0.084	0.018	0.665
Ps	1.016	−0.034	0.026	0.987

Figure 6. Normalized β_N values against V_{VN}% for Pu and Ps coupons.

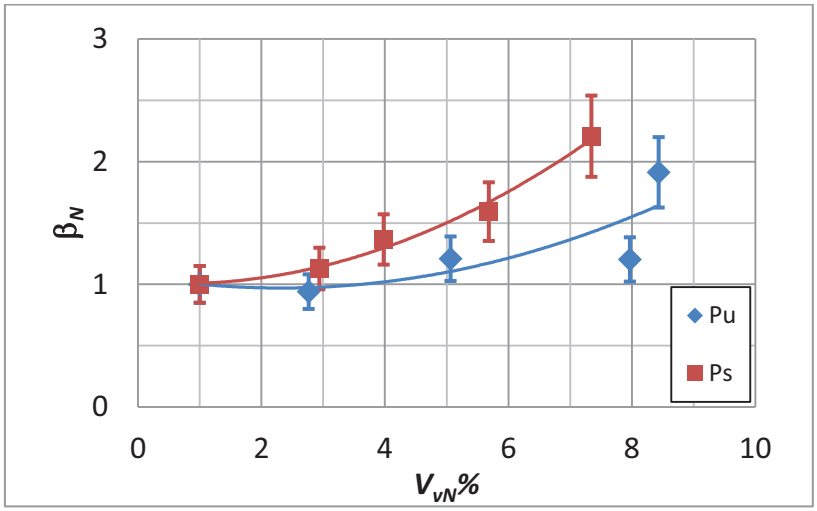

3.4. Measurements with Flash Thermography

A Hensel® flash head and power supply, able to emit 6000 Joules in 1/400 s, was used to instantaneously heat up the inspected specimen [32]. The temperature-time variation on the opposite side of the specimen was monitored by the infrared camera, SC5000 (Flir Systems, Paris, France). This camera is equipped with 320 × 256 InSb focal plane array Stirling cooled detector working in the 3.7–5.1 μm infrared wavelength band and of a thermal resolution of 25 mK. The spatial resolution, in the present tests, was 3 pixels/mm, and the frame rate was 5 Hz.

Through the analysis of the image sequence with an *ad hoc* developed MATLAB tool and by applying Equation (4), thermal diffusivity maps were obtained. They display thermal diffusivity values that were evaluated point-by-point over the entire surface of each coupon as average values through the specimen thickness. Two thermal diffusivity maps for coupon types Pu and Ps are reported in Figure 7a,b with α expressed in 10^{-3} cm^2/s.

As can be immediately noticed from the variation of color, for each map, low values (see the color bar on the right) of thermal diffusivity are attained in correspondence with the location of the Kapton disk, which is visible in almost all the coupons, although in some cases, it is not clearly outlined; to facilitate readability, an arrow indicates the position of the Kapton disk. For coupons cured with P_c = 0%, the relevant amount and distribution of porosity has caused a sort of blurring effect, which makes ambiguous the discrimination of the Kapton disk contour. In addition, assuming α values over the Kapton disk as the lowest ones, it is possible to clearly see, as the distribution of the thermal diffusivity is driven by the fibers' orientation. In particular, a pack-threads effect of fibers is observed mainly for Pu specimens cured at P_c = 50% and 25%. On the other side, this effect was already

visualized [34] within unidirectional fibers as mainly pronounced for the shorter fibers oriented at 90° (along the shorter side). For the plots in Figures 8 and 9, the error bars are visualized to account for the variability of data with respect to the correlation curve. On average, the larger data spread is attained by the Pu coupon type.

Figure 7. Thermal diffusivity maps. (**a**) Pu-type coupons; (**b**) Ps-type coupons. An arrow indicates the position of the Kapton disk in each map.

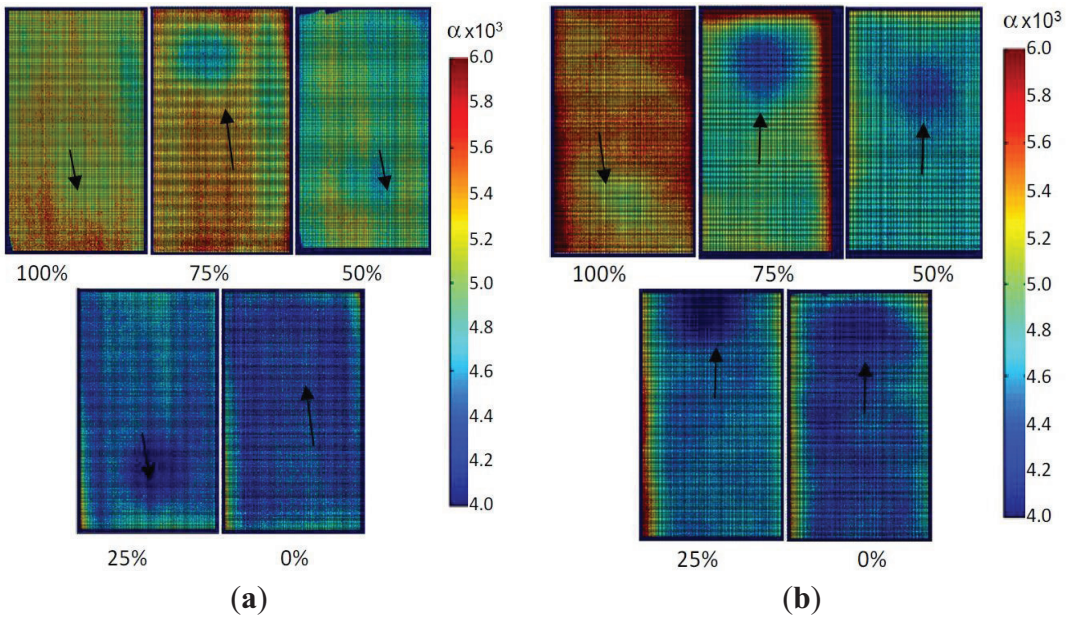

Figure 8. Normalized average thermal diffusivity, α_N, *versus* P_c% for both Pu and Ps coupon types.

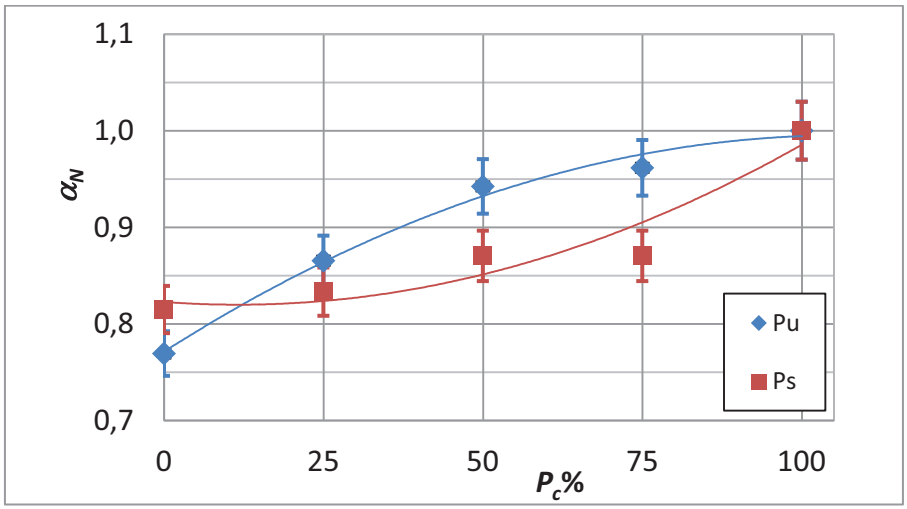

For each coupon, an average thermal diffusivity value was calculated over the sound material (excluding the area containing the Kapton disk); such values were then normalized with respect to the thermal diffusivity value of the coupon with P_c = 100%. The so obtained values, which are named α_N, are plotted against P_c and against the normalized volume of voids V_{vN}%, respectively, in Figures 8 and 9.

From Figures 7–9, it is possible to notice that:

- the thermal diffusivity tends to decrease with decreasing P_c (*i.e.*, increased embedded porosity);
- the largest reduction with decreasing P_c of about 23% is registered for the coupon type, Pu;
- the average value, as well as the distribution of the thermal diffusivity is affected by the fibers' direction.

Figure 9. Normalized average thermal diffusivity, α_N, *versus* V_{vN}% for both Pu and Ps coupon type plots.

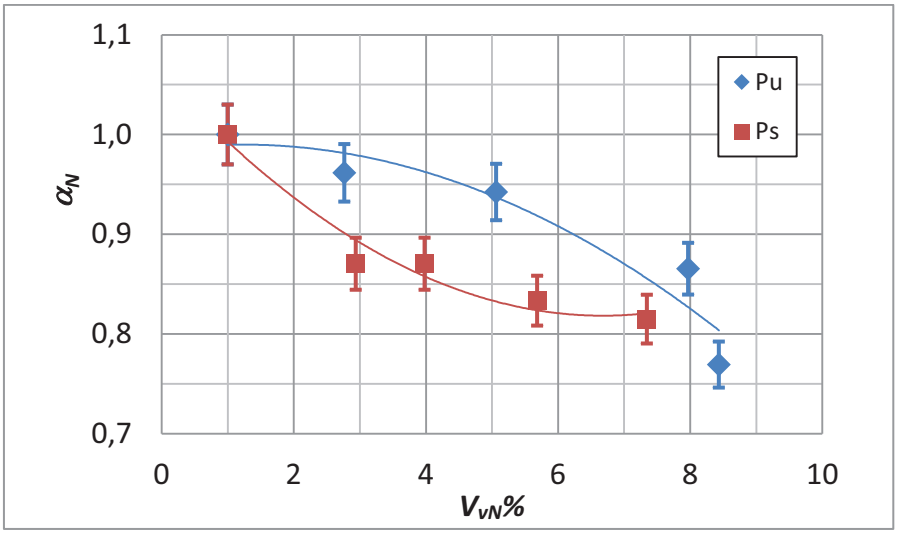

It is known that thermal diffusivity depends on the fibers' direction [31,35]. The curing pressure plays a fundamental role in the formation of voids, but this pressure-dependent effect is also found to be dependent on the stacking sequence. Probably, gases can, under pressure, more easily escape from a unidirectional laminate, than from a more complex stacking sequence in which they may remain entrapped within the labyrinth of fibers; this may explain the larger increase of the thermal diffusivity with increasing the curing pressure for specimens with unidirectional fibers (Figure 8).

Data in both Figures 8 and 9 are well fitted by a second-order polynomial, like Equation (7), with coefficients collected in Table 5 for the α_N to P_c correlation (Figure 8) and in Table 6 for the α_N to V_{vN} correlation (Figure 9). As a main finding, a change of slope is observed for the two different specimen types. This feature, which may appear almost strange at first sight, is surely to be ascribed to the fibers' orientation and will be better discussed in the next section.

Table 5. Coefficients of Equation (7) for α_N to P_c correlation (Figure 8).

Coupon Type	*a*	*b*	*c*	R^2
Pu	0.771	0.0042	-2×10^{-5}	0.989
Ps	0.823	−0.0005	2×10^{-5}	0.907

Table 6. Coefficients of Equation (7) for α_N to V_{vN} correlation (Figure 9).

Coupon Type	*a*	*b*	*c*	R^2
Pu	0.984	0.009	−0.004	0.905
Ps	1.059	−0.072	0.005	0.957

3.5. Comparison between Thermographic and Ultrasonic Data

For a comparison between FT and UT, α_N and β_N are plotted together against V_{vN}% in Figures 10 and 11, respectively, for the Ps and the Pu coupon types. As already shown, the functional relation can be fitted, for every dataset, by a second-order polynomial [Equation (7)] in a least squares sense. Thermal diffusivity decreases, while the ultrasonic attenuation increases with increasing the porosity content; β_N displays larger variations with V_{vN}%, but it displays also a larger data spread, as the error bars show. This observation is in general agreement with the literature [28].

Figure 10. Comparison between ultrasonic attenuation and thermal diffusivity for the Ps coupons type. The results related to ultrasonic attenuation, β_N, are in blue with the scale on the left axis, and the ones related to thermal diffusivity, α_N, are in red with the scale on the right axis.

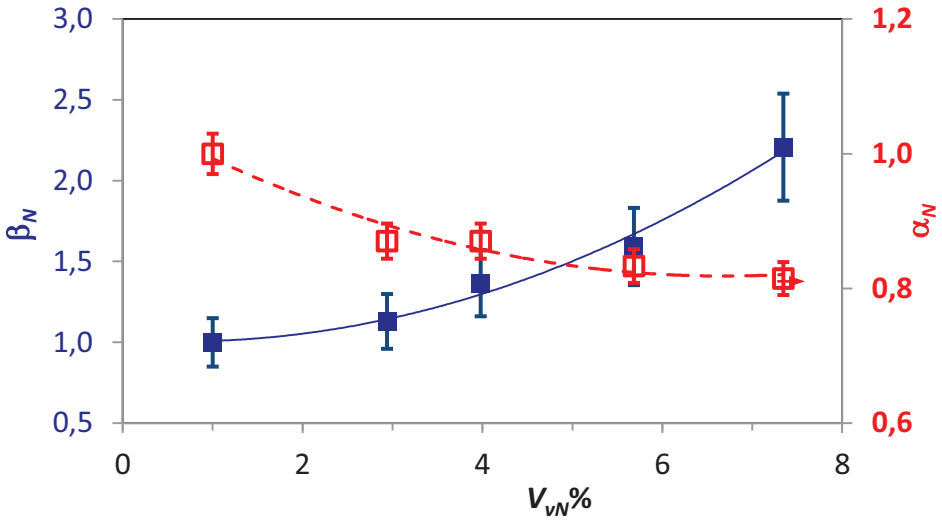

Figure 11. Comparison between ultrasonic attenuation and thermal diffusivity for the Pu coupons type. The results related to ultrasonic attenuation, β_N, are in blue with the scale on the left axis, and the ones related to thermal diffusivity, α_N, are in red with the scale on the right axis.

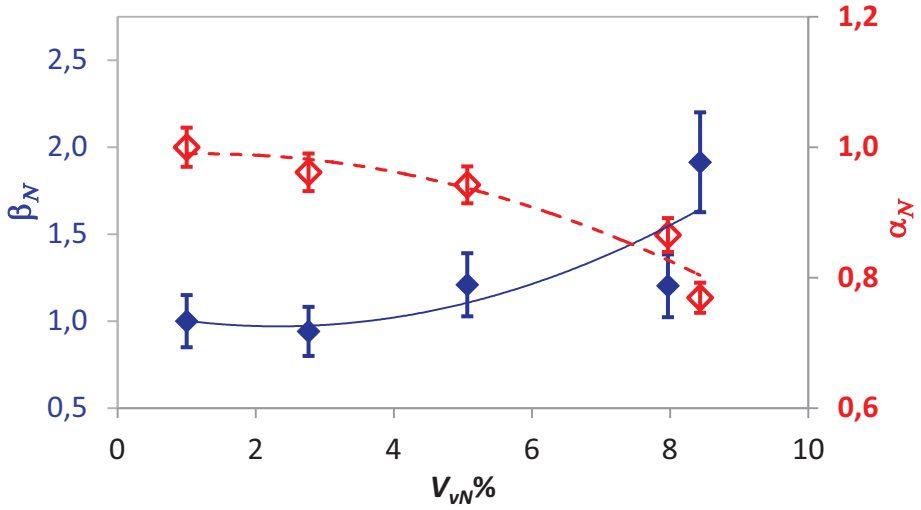

Within the data comparison, it is also worth noting that for each specimen, due to the manufacturing process, one surface is perfectly smooth, while the other one is almost rough. In general, the rough side is characterized by a higher emissivity, making it the preferred one to be viewed by the infrared camera for tests with FT. Indeed, some specimens were tested twice by considering one time the smooth side and, after, the rough one, or *vice versa*; on the whole, no differences were found. On the contrary, ultrasonic tests were carried out on the smooth side, since, as is well known, the surface finishing is of great concern for UT.

Thus, due to the many advantages offered and in agreement with previous literature, amongst others' reference [28], flash thermography can be preferred to ultrasonic for porosity assessment in composites.

Going more in depth into a comparison of Figure 10 to Figure 11, a change of slope in the curve fitting α_N data for both specimen types can be noted. More specifically, the curve fitting β_N (ultrasonic) data displays always, for both specimen types, Pu and Ps, the same concavity, which is also in agreement with [28]. Conversely, a change of concavity is observed for α_N data by changing the type of specimen. This effect is certainly to be ascribed to the different type of material in the sense that the distribution and orientation of fibers, as well as their mutual position play a fundamental role in porosity formation. Mayr *et al.* [28] already observed an abrupt drop of thermal diffusivity at a porosity of about 0.5%; they ascribed such a non-linear correlation between thermal diffusivity and porosity to the variation of the pore shape. In particular, they stated that the pores tend to flatten with increasing the porosity percentage and have a degradation effect on the heat flux, decreasing, in turn, the thermal diffusivity. From Figure 10, which refers to the Ps specimen type, there is first an abrupt drop of the thermal diffusivity with increasing porosity, followed by a much milder decrease; the contrary happens for specimen type Pu in Figure 11. Of course, the space allowing pores to assume either a spherical or a flattened shape is different for fibers aligned in a unidirectional way (Pu) or fastened in a cross-fashion (Ps). Unfortunately, there is no possibility to

compare data with the literature, the materials used being different; in particular, the material used in [28] is a plain weave one. Even if the behavior of the Ps type may be assumed to be similar to that of the plain weave for certain porosity percentages, which may explain the initial abrupt drop of α_N with V_{vN}%, the change of slope with the stacking sequence deserves further attention.

4. Conclusions

The use of flash thermography to assess the amount and distribution of porosity in composites has been investigated. In particular, the most relevant literature has been reviewed, and some new experimental data have been shown to complete the actual state-of-the-art in the use of flash thermography.

The new data come from a set of specimens, including a different amount of porosity, two different stacking sequences and, also, slag inserts, to simulate local delamination. The results obtained with flash thermography were compared with those coming from ultrasonic testing; the percentage of porosity was determined by the destructive volumetric method. A comparison with data present in the literature was attempted, but it was not at all possible, the involved materials being different.

To sum up, it has been demonstrated, in agreement with the literature, that the measure of thermal diffusivity by flash thermography, as a parameter for porosity evaluation, is a high quality alternative to the typical ultrasonic attenuation estimation, which is commonly used, especially, in the aeronautical field. Flash thermography offers some advantages, since it is effective, non-contact (no coupling media are necessary), fast and is also not affected by the surface finishing, meaning that, unlike
UT, a part can be inspected viewing the smooth or the rough side indifferently. In addition, flash thermography allows one to contemporaneously detect manufacturing defects and assess the porosity amount within only one test with, of course, economic advantages. The test setup can be easily incorporated in the industrial enterprise for the in-line inspection of parts. In addition, as an important remark, non-destructive testing with IRT is carried out using a simple and safe (for the personnel) set-up arrangement without any further issues in terms of safety at work concerns.

As a final point, an important outcome regards the influence of the stacking sequence on the correlation between thermal diffusivity and porosity. This feature deserves further attention for a full assessment of the validity of flash thermography.

Author Contributions

This paper includes some results obtained during the PhD work by Cinzia Toscano under the supervision of Carosena Meola. The main contribution of Cinzia Toscano was to carry out the experimental tests and to process data. The main contribution of Carosena Meola was to organize, write and revise the paper.

Conflicts of Interest

The authors declare no conflict of interest.

References

1. Soutis, C. Fiber reinforced composite in aircraft construction. *Progr. Aerosp. Sci.* **2005**, *41*, 143–151.
2. Loos, A.C.; Springer, G.S. *Composite Materials, Quality Assurance and Processing*; Browning, C.E., Ed.; ASTM International: West Conshohocken, PA, USA, 1983; pp. 110–118.
3. Boey, F.Y.C.; Lye, S.W. Void reduction in autoclave processing of thermoset composites. *Composites* **1992**, *23*, 261–265.
4. Liu, L.; Zhang, B.M.; Wang, D.F.; Wu, Z.J. Effects of cure cycles on void content and mechanical properties of composite laminates. *Compos. Struct.* **2006**, *73*, 303–309.
5. Toscano, C.; Vitiello, C. Study of the influence of the staking sequence on porosity formation in carbon fibre composites. *J. Appl. Polym. Sci.* **2011**, *122*, 3583–3589.
6. Little, J.E.; Yuan, X.; Jones, M.I. Characterisation of voids in fibre reinforced composite materials. *NDT & E Int.* **2012**, *46*, 122–127.
7. British Standards Institution. *Carbon Fibre Laminates. Determination of the Fibre, Resin and Void Contents*; EN 2564; British Standards Institution: London, UK, 1998.
8. Brit, E.A.; Smith, R.A. A review of NDE methods for porosity measurement in fibre reinforced polymer composites. *Insight* **2004**, *46*, 681–686.
9. Krautkrämer, J.; Krautkrämer, H. *Ultrasonic Testing of Materials*, 4th ed.; Springer-Verlag: Heidelberg, Germany, 1990.
10. Kastner, J.; Plank, B.; Salaberger, D.; Sekelja, J. Defect and porosity determination of fibre reinforced polymers by X-ray computed tomography. In Proceedings of the NDT in Aerospace, Hamburg, Germany, 22–24 November 2010.
11. Hendorfer, G.; Mayr, G.; Zauner, G.; Haslhofer, M.; Pree, R. Quantitative determination of porosity by active thermography. In Proceedings of the Review of Quantitative Nondestructive Evaluation, Portland, OR, USA, 30 July–4 August 2007; pp. 702–708.
12. Yolken, H.T.; Matzkanin, G.A. *Nondestructive Evaluation of Advanced Fiber Reinforced Polymer Matrix Composites*; NASA Report CR-2009-215566; NASA Langley Research Center: Hampton, VA, USA, 2009.
13. Stone, D.E.W.; Clarke, B. Ultrasonic attenuation as a measure of void content in carbon-fiber reinforced plastics. *Non-Destr. Test.* **1975**, *8*, 137–145.
14. Daniel, I.M.; Wooh, S.C.; Komsky, I. Quantitative porosity characterization of composite materials by means of ultrasonic attenuation measurements. *J. Nondestr. Eval.* **1992**, *11*, 1–8.
15. Nair, S.M.; Hsu, D.K.; Rose, J.H. Porosity estimation using the frequency dependence of the ultrasonic attenuation. *J. Nondestr. Eval.* **1989**, *8*, 13–26.
16. Hsu, D.K. Ultrasonic nondestructive evaluation of void content in CFRP. In Proceedings of the 46th Annual Technical Conference (ANTEC), Atlanta, GA, USA, 18–21 April 1988; pp. 1273–1275.
17. Steiner, K.V. Defect Classifications in Composites Using Ultrasonic Nondestructive Evaluation Techniques. In *Damage Detection in Composite Materials*; ASTM STP 1128;

John, E., Ed.; American Society for Testing and Materials (ASTM): West Conshohocken, PA, USA, 1992; pp. 72–84.

18. Lin, L.; Chen, J.; Zhang, X.; Li, X. A novel 2-D random void model and its application in ultrasonically determined void content for composite materials. *NDT & E Int.* **2011**, *44*, 254–260.
19. Parker, W.J.; Jenkins, R.J.; Butler, C.P.; Abbott, G.L. Flash method of determining thermal diffusivity, heat capacity, and thermal conductivity. *J. Appl. Phys*. **1961**, *32*, 1679–1684.
20. *Standard Test Method for Thermal Diffusivity of Solids by the Flash Method*; ASTM E1461-01; ASTM International: West Conshohocken, PA, USA, 2001.
21. Carslaw, H.S.; Jaeger, J.C. *Conduction of Heat in Solids*; Clarendon Press: Oxford, UK, 1959.
22. Steiner, K.V.; Krieger, K.; Mehl, J.B.; Caron, J.N.; Yang, Y. Infrared thermography and laser-based ultrasonic methods for on-line porosity sensing during thermoplastic composite fabrication. In Proceedings of the 2nd Conference on NDE Applied to Process Control of Composite Fabrication, NTIAC, Houston, TX, USA, 30 January–1 February 1996; pp. 115–122.
23. Chu, T.P.; Russell, S.S.; Walker, J.L. Porosity Measurement in laminate composites by thermography and FEA. In Proceedings of 2001 Society for Experimental Stress Analysis Spring Conference, Portland, OR, USA, 6 June 2001.
24. Grinzato, E.; Marinetti, S.; Bison, P.G. NDE of porosity in CFRP by multiple thermographic techniques. In Proceedings of SPIE 4710, Thermosense XXIV, 588, Orlando, FL, USA, 1 April 2002; pp. 588–598.
25. Ciliberto, A.; Cavaccini, G.; Salvetti, O.; Chimenti, M.; Azzarelli, L.; Bison, P.G.; Marinetti, S.; Freda, A.; Grinzato, E. Porosity detection in composite aeronautical structures. *Infrared Phys. Technol.* **2002**, *43*, 139–143.
26. Susa, M.; Maldague, X.; Boras, I. Application of the source distribution image (SDI) procedure for porosity detection in honeycomb structures. In Proceedings of the 10th International Conference on Quantitative InfraRed Thermography, Québec, Canada, 27–30 July 2010.
27. Mayr, G.; Handorfer, G. Porosity determination by pulsed thermography in reflection mode. In Proceedings of the 10th International Conference on Quantitative InfraRed Thermography, Québec, QC, Canada, 27–30 July 2010.
28. Mayr, G.; Plank, B.; Sekelja, J.; Hendorfer, G. Active thermography as a quantitative method for non-destructive evaluation of porous carbon fiber reinforced polymers. *NDT & E Int.* **2011**, *44*, 537–543.
29. Feuillet, V.; Dujardin, N.; Fois, M.; Ibos, L.; Poilâne, C.; Candau, Y. Pulsed thermography: A useful tool to determine porosity in composite materials? In Proceedings of the 11th International Conference on Quantitative InfraRed Thermography, Naples, Italy, 11–14 June 2012; p. 9.
30. Wrobel, G.; Rdzawski, Z.; Muzia, G.; Pawlak, S. Determination of thermal diffusivity of carbon/epoxy composites with different fiber content using transient thermography. *J. Achiev. Mater. Manuf. Eng.* **2009**, *37*, 518–525.
31. Bhatt, H.; Donaldson, K.Y.; Hasselman, D.P.H.; Chyung, K.; Taylor, M.P. Effect of fibre orientation on the thermal conductivity of a uniaxial carbon fibre-reinforced

aluminoborosilicate glass-matrix composite for various specimen geometries. *J. Mater. Sci. Lett.* **1991**, *10*, 1267–1270.

32. Toscano, C.; Meola, C.; Iorio, M.C.; Carlomagno, G.M. Porosity and inclusion detection in CFRP by infrared thermography. *Adv. Opt. Technol.* **2012**, *2012*, 765953:1–765953:6.
33. Toscano, C.; Meola, C.; Carlomagno, G.M. A comparison between ultrasonic testing and lockin thermography in non-destructive evaluation of porous CFRP plates. In Proceedings of the 9th International Conference (ICCST/9), Sorrento, Italy, 24–26 April 2013.
34. Toscano, C.; Meola, C.; Carlomagno, G.M. Porosity distribution in composite structures with infrared thermography. *J. Compos.* **2013**, *2013*, 140127:1–140127:8.
35. Meola, C.; Carlomagno, G.M.; Squillace, A.; Giorleo, G. Non-destructive control of industrial materials by means of lock-in thermography. *Meas. Sci. Technol.* **2002**, *13*, 1583–1590.

Mechanical, Microstructure and Surface Characterizations of Carbon Fibers Prepared from Cellulose after Liquefying and Curing

Xiaojun Ma, Cheng Yuan and Xinyan Liu

Abstract: In this study, Cellulose-based carbon fibers (CBCFs) were prepared from cellulose after phenol liquefaction and curing. The characteristics and properties of CBCFs were examined by scanning electron microscopy (SEM), Fourier transform infrared spectroscopy (FTIR), X-ray diffraction (XRD), Raman spectroscopy and X-ray photoelectron spectroscopy (XPS). The results showed that, with increasing carbonization temperature, the L_a, L_c, and $L_c/d_{(002)}$ of CBCFs increased gradually, whereas the degree of disorder R decreased. The –OH, $–CH_2–$, –O–C– and phenyl group characteristic absorption peaks of CBCFs reduced gradually. The cross-linked structure of CBCFs was converted into a graphite structure with a six-ring carbon network during carbonization.
The surface of CBCFs were mainly comprised of C–C, C–O, and C=O. The tensile strength, carbonization yield and carbon content of CBCFs obtained at 1000 °C were 1015 MPa, 52%, and 95.04%, respectively.

Reprinted from *Materials*. Cite as: Ma, X.; Yuan, C.; Liu, X. Mechanical, Microstructure and Surface Characterizations of Carbon Fibers Prepared from Cellulose after Liquefying and Curing. *Materials* **2014**, *7*, 75ï 84.

1. Introduction

Carbon fibers (CFs), a type of lightweight and high performance fibrous carbon material, are generally processed as reinforcement materials utilized in area where lightweight and high strength are required [1]. Because of their superior mechanical properties, they have potential application for reducing automobile weight and are receiving increasing attention as an important advancement in solving the urgent problem of reducing carbon dioxide. Cellulose-based carbon fibers were developed first in the 1950s and 1960s, and cellulose is the third largest source of carbon fibers after polyacrylonitrile (PAN) and pitch. Due to their low strength and low yield, cellulose-based fibers have been abandoned for high-strength applications in favor of PAN and pitch-based carbon fibers [2–6]. However, they are still widely used in ablative technology, as carbon fibers and other carbon textile products.

To meet the challenges posed by the rapid development of aerospace, transportation, and medical industries, serious research on cellulose-based fibers has focused on improving their mechanical properties and yield, and eliminating pollution problems [7–9]. Recently, biomass materials are almost completely converted into useful liquid chemical raw by liquefaction technique, which greatly improves the application of biomass materials [10]. It is reasonable to propose that liquefied cellulose is an excellent candidate for making high performance carbon fibers.

In this paper, cellulose-based carbon fibers were prepared successfully by liquefied cellulose, melt spinning, curing treatment, and carbonization. In order to create a comprehensive understanding

of cellulose-based carbon fibers, the molecular structure change, crystal structure transition, and surface functional groups of cellulose-based carbon fibers during carbonization were all investigated in detailed. At the same time, the mechanical properties, modulus and yield of cellulose-based carbon fibers at various temperatures were compared.

2. Experimental

2.1. Samples

The mixture of 20 g of cellulose prepared by nitrate ethanol method [11] and 120 g of phenol as well as 9.6 g of H_3PO_4, loading in a round bottom flask, was heated in an oil bath at 160 °C for 150 min. until the compound including cellulose and phenol is obtained. Subsequently, hexamethylenetetramine as synthetic agent was added to liquefied cellulose by 5 wt% (on the weight of liquefied cellulose) and was held for 5 min after heating to 180 °C in 40 min to prepare a spinning solution. The spinning solution was placed into a spinning machine [12], and the spun filaments were prepared by melt-spinning. The spun filaments were cured by soaking in an acid solution HCHO and HCl (1:1 by volume) as main components at 95 °C for 4 h, washed with distilled water and finally dried at 90 °C for 45 min. The carbon fiber precursors from liquefied cellulose were prepared. The carbonization was carried out in a tubular furnace and the samples were heated from room temperature to the final carbonization temperature (400–1000 °C) with a heating rate of 3 °C/min in a 100 mL/min stream of N_2. The samples were held for 60 min under the carbonization temperature, and then naturally cooled to room temperature. Cellulose-based carbon fibers (CBCFs) from liquefied cellulose were prepared.

2.2. Measurements

The cross-section of CBCFs was observed with a scanning electron microscope (S-4800, Hitachi Co., Tokyo, Japan).

The chemical structures of treated carbon fibers were detected at ambient temperature by a Fourier transform infrared spectrometer (FTIR) of TENSOR37 (BRUKER Co., Karlsruhe, Germany). The fibers were pulverized (150–200 mesh) and mixed with KBr before being pressed into a disk. The concentration of the sample in KBr was 2.5%, and 0.2 g of KBr was used in the preparation of the reference and sample disks.

The crystal structures were measured by scanning the fiber samples in the range of 5°–60° (2θ) by a Powder X-ray Diffractometer (D/MAX2500, Rigaku Co., Tokyo, Japan). The apparent crystallite thickness (L_c), the apparent layer-plane length parallel to the fiber axis (L_a), and the average interlayer spacing d were calculated using the Bragg and Scherrer formula. The formulas can be expressed as:

$$d = \frac{\lambda}{2\sin\theta} \tag{34}$$

$$L = \frac{K\lambda}{\beta\cos\theta} \tag{35}$$

where θ is the Bragg angle of peaks (°), λ is the wavelength of X-ray used (0.154 nm), and β is half-height width of peak (rad). The form factor K is 0.89 for L_c, and 1.84 for L_a, respectively.

The Raman scattering measurements were performed in a Raman spectrometer (Invia, Renishaw Co., Derbyshire, UK) at room temperature under a nitrogen atmosphere, using a 473 nm line of an argon ion laser as the incident radiation. The Raman spectrometer was operated in the continuous scanning mode with laser beam powers of 4 mW and exposure times of 25 s.

XPS measurements of the samples at various temperatures were carried out on a Kratos Axis UltraDLD multi-technique X-ray photoelectron spectroscopy (K-alpha, ThermoFisher Co., East Grinstead, UK) with a monochromated Al Kα X-ray source (hv = 1486.6 eV).

Tensile strength was measured by electrical tensile strength apparatus (YG004N, Hongda Co., Shanghai, China) under a span distance of 10 mm and a crosshead speed of 2 mm·min^{-1}. The data shown are average value for 30 fibers.

3. Results and Discussion

3.1. Morphological Characteristics

As can be seen from Figure 1a,b, the surface of CBCFs is smooth. The cross section shown in Figure 1c is elliptical pattern due to the square bobbin during melt-spinning process. Many fine pores are observed in the cross section, mainly around the center of the cross section (Figure 1d). This is due to the residual gas in the spinning solution and the low crosslinkage degree of the inner of the carbon fiber precursors during curing treatment [13].

Figure 1. Scanning electron microscopy (SEM) micrographs of Cellulose-based carbon fibers (CBCFs): (**a**) and (**b**) side surface; (**c**) and (**d**) crossing section.

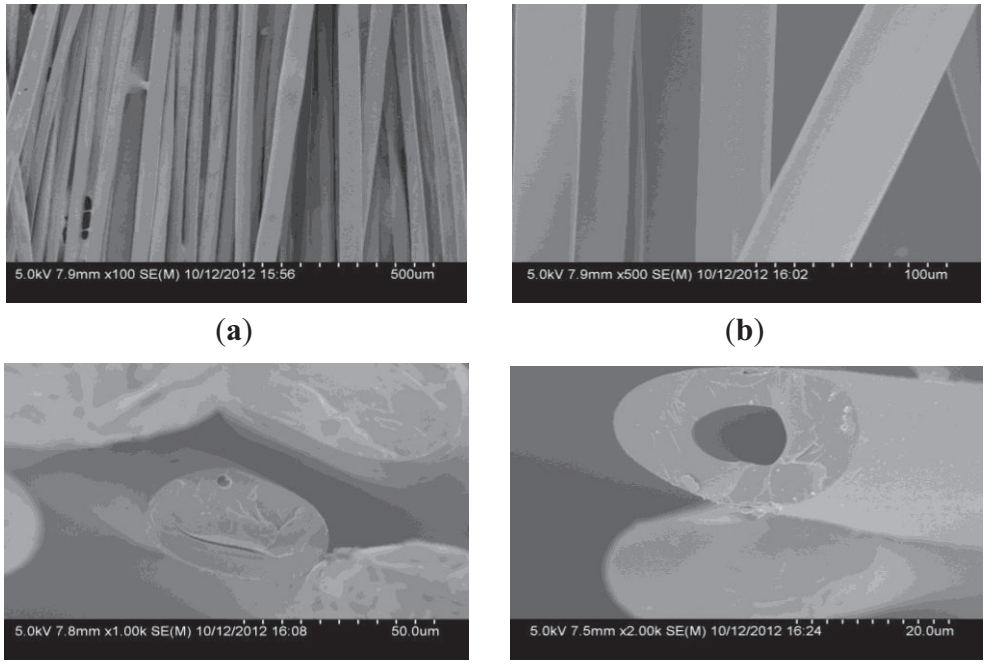

(**a**) (**b**)

(**c**) (**d**)

3.2. Mechanical Properties

The relationship between carbonization temperature and mechanical properties of CBCFs are reported in Figure 2. With carbonization temperature increasing, tensile strength and modulus of CBCFs obviously improve, while elongation at break rapidly reduces. Carbonization temperature increases from 600 to 1000 °C, tensile strength and modulus of CBCFs increase from 650 to 1015 MPa and from 62 to 116 GPa, respectively. At the same time, elongation at break decreases 54.9% from 600 to 1000 °C. From Figure 2a, it can also be seen that the mechanical properties of CBCFs are slightly better than those previously reported for carbon fibers produced from cellulose (tensile strength 0.8 GPa, modulus 70 GPa) [14].

Higher weight losses, or lower yield result in higher production costs [15]. Figure 2b shows the yields of carbon fibers are 61%~52% from 600 to 1100 °C. It is clear that the yield of CBCFs is higher than that of carbon fibers produced from cellulose.

Figure 2. The mechanical properties of CBCFs: (**a**) Tensile strength; (**b**) Elongation at break and Carbon fiber yield.

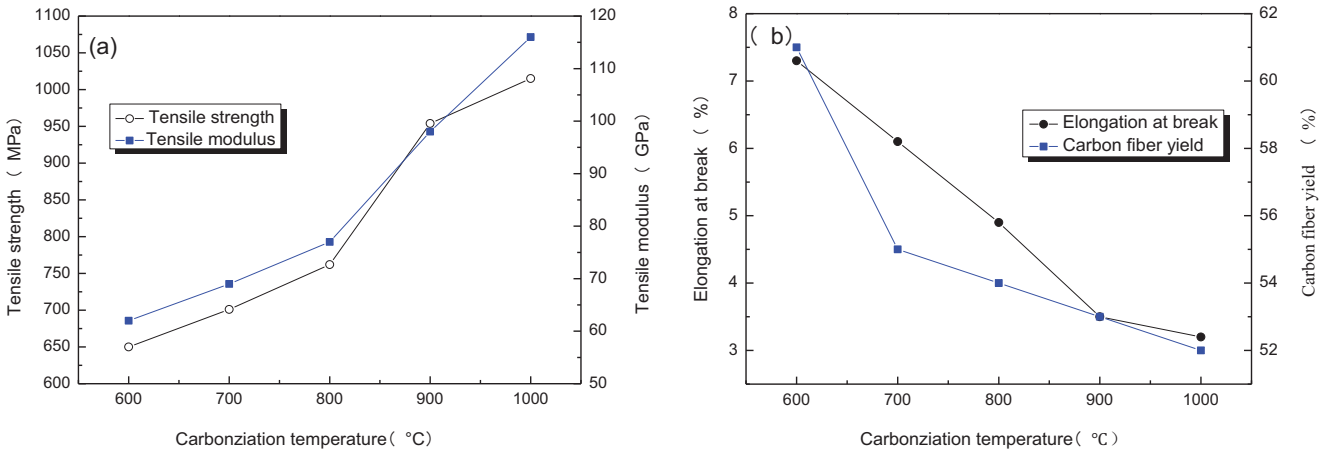

3.3. Structure Transitions

Figure 3 shows Fourier Transform Infrared Spectroscopy (FTIR) spectra of CBCFs under different carbonization temperatures. As temperature increases, the wide-band absorption intensity of the associated hydroxyl group of CBCFs at 3427 to 3429 cm^{-1} is reduced, The absorption peaks at 2925 to 2850 cm^{-1} (mainly methylene bridge) and the absorption peak for the vibration of the benzene ring skeleton at 1631 to 1639 cm^{-1} weaken gradually. Moreover, the absorption peak of the stretching vibration at the C=C bond in the benzene ring skeleton at 1610 to 1504 cm^{-1} and the absorption peak of the C–O–C stretching vibration at 1124 to 1112 cm^{-1} are not changed after 500 °C. In addition, the two characteristic absorption peaks at 821 and 752 cm^{-1} almost disappear. This indicates that, due to the decrease of the –OH, $–CH_2$, –O–C– and phenyl group during carbonization, the benzene rings of the sample get closer to each other, the benzene fused-ring structure is formed, and the cross-linked structure of the sample is changed into the six-member ring carbon network [16,17]. When carbonization temperature reaches 1000 °C, the absorption peak of the C=C bond (1610–1504 cm^{-1}) of CBCFs do not disappear, indicating that the sample is difficult to graphitize [18].

3.4. Crystal Structure Transition

Figure 4 shows X-ray diffraction patterns of CBCFs at various temperatures. As can be seen from Figure 4, the samples carbonized above 600 °C appear (002) and (100) peaks. As carbonization temperature increases, (002) peaks shift from 18.98° to 21.9°, thus approaching the graphite (002) peak position, and the (100) diffraction peakis enhanced. This result indicates that carbon atoms of CBCFs are rearranged from disorderly to orderly and the crystalline structure improves remarkably with increasing carbonization temperature.

Figure 3. FTIR spectra of CBCFs at various temperatures.

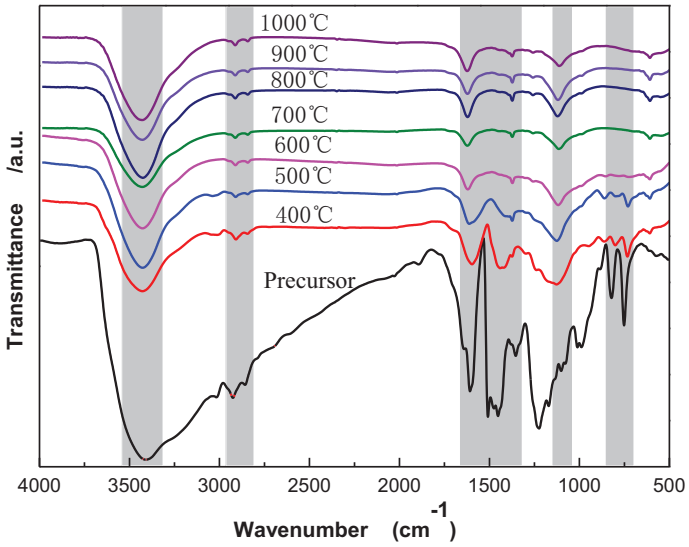

Figure 4. X-ray diffraction patterns of CBCFs at various temperatures.

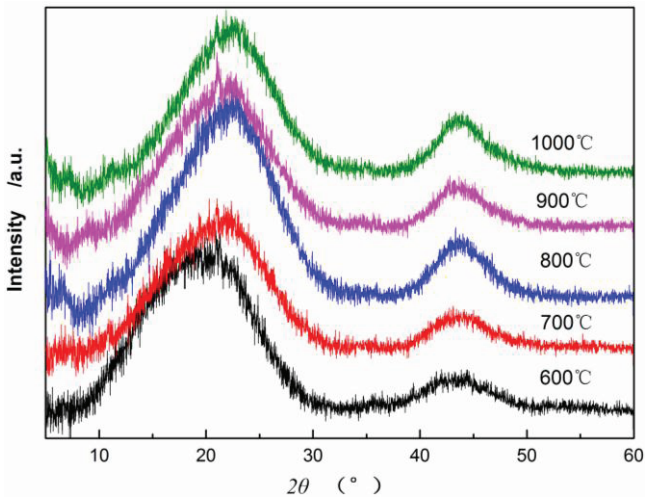

Table 1 shows that as carbonization temperature increases, the value of $d_{(002)}$ decreases from 0.4670 to 0.4053 nm, and that of $d_{(100)}$ decreases from 0.2073 to 0.2066 nm. The numerical variation of $d_{(002)}$ is greater than that of $d_{(100)}$, which is similar to the results of common carbon materials. However, the $d_{(002)}$ of CBCFs is significantly greater than the $d_{(002)}$ of graphite (0.3354 nm) and that of coke (0.3440 nm) at 1000–1350 °C [19,20]. This observation also indicates that, with increasing carbonization temperature, CBCFs is difficult to graphitize. In addition, the carbonization of CBCFs is more complicated than the general carbon materials due to higher complexity of cellulose liquefaction. Meanwhile, L_c, $L_c/d_{(002)}$, and g values (degree of graphitization) increase gradually as carbonization temperature increases, which indicates that the number of graphene sheets and the graphitization degree of CBCFs increase as temperature increases.

Table 1. Structure parameters of X-ray diffraction for CBCFs.

Temperature (°C)	$d_{(002)}$ (nm)	$d_{(100)}$ (nm)	L_c (nm)	$L_c/d_{(002)}$	g (%)
600	0.4670	0.2073	0.6687	1.4318	−14.30
700	0.4237	0.2060	0.7090	1.6732	−9.27
800	0.4075	0.2062	0.7607	1.8665	−7.39
900	0.4193	0.2061	0.7265	1.7323	−8.76
1000	0.4053	0.2066	0.7937	1.9581	−7.13

Figure 5 displays Raman spectra of cellulose carbon fibers under different carbonization temperature. It is found that cellulose-based carbon fibers obtained above 600 °C exhibit D-peak at 1350 cm^{-1} (Figure 5a), which characterizes the disorderly structure of the carbon materials, and G-peak at 1597 cm^{-1}, which characterizes the graphite crystallite structure of the carbon materials [21]. Peaks D and G are strengthened gradually as carbonization temperature increases, indicating thus that higher carbonization temperature could facilitate the arrangement of carbon from a disorderly to an orderly state [22,23]. Meanwhile, the existence of several oxygen-bearing functional groups affects the change in the mechanical constant of the C–C bond, resulting in the shift of curves D and G of the sample during the low-temperature carbonization stage.

Figure 5b shows the graphite crystalline size L_a and R values of disorder calculated using the Matthews' formula and the Tuinstra-Koenig formula. With carbonization temperature increase, the R of the cellulose carbon fibers decreases, whereas L_a increases, thus further indicating that the high carbonization temperature increases the order of the crystalline structure of the sample.

Figure 5. (**a**) Raman spectra of CBCFs at various temperatures; (**b**) the graphite crystalline size L_a and R values of disorder.

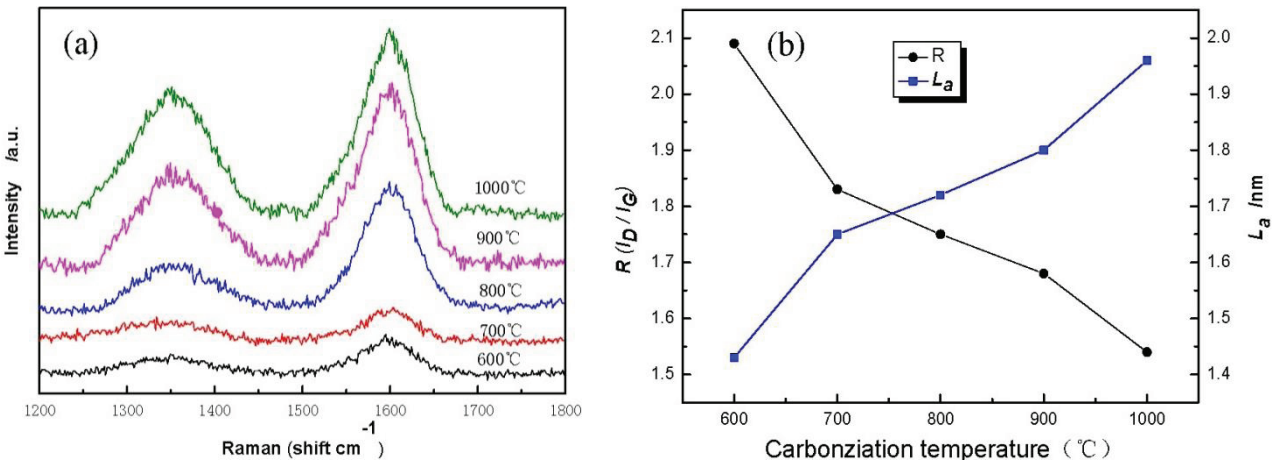

3.5. Surface Characterizations

Figure 6a shows the XPS spectra of CBCFs at various temperatures. As shown in the figure, the elements C and O are the basic elements of CBCFs. The main elemental composition of the surface of CBCFs is shown in Table 2. As seen from Table 2, element C is the most abundant constituent of all CBCFs. With increasing carbonization temperature, elements C of CBCFs increases while

elements O and N reduce. The elements C content of CBCFs have achieved more than 95% above 1000 °C.

Figure 6. X-ray photoelectron spectroscopy (XPS) curve of CBCFs at various temperatures: (**a**) XPS survey spectra; (**b**) XPS spectra of the C1s region.

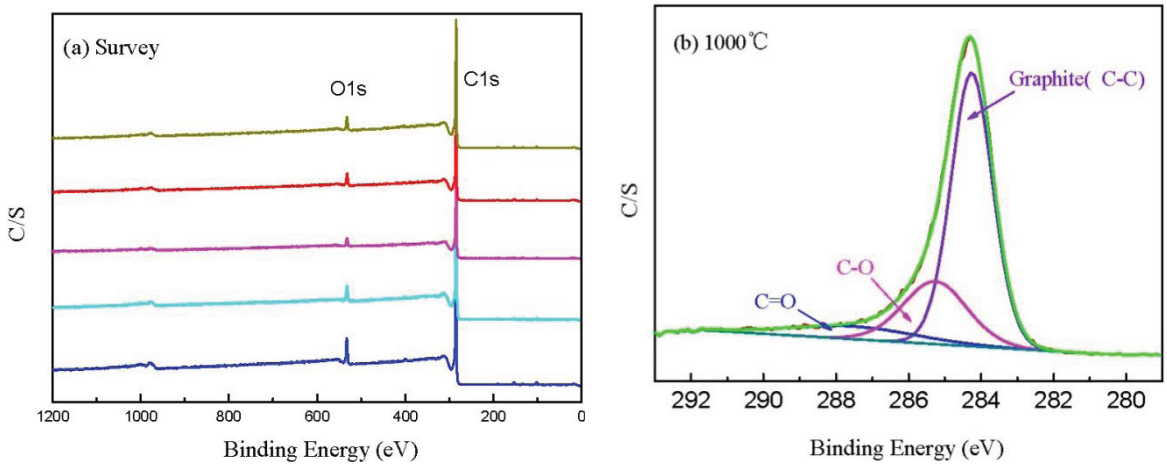

Table 2. C, O, N contents of CBCFs at various temperatures.

Temperature (°C)	C (at%)	O (at%)	N (at%)
600	91.03	7.71	1.26
700	93.77	5.48	0.74
800	94.78	4.71	0.51
900	94.15	4.65	1.20
1000	95.04	4.58	0.38

In order to obtain information about the chemical composition of the fiber surface and the binding characteristics of the elements at the surface, measurements of the XPS spectra of the C1s region were analyzed. The C1s spectra of the five samples are almost the same, thus only the sample is shown in Figure 6b as an example. Figure 6b indicates that the C1s curve fitting is optimized into three independent peaks: the graphitic carbon (C–C, Binding Energy (BE) = 284.0–284.3 eV), either or hydroxy group (C–O, BE = 284.7–285.7 eV), and carbonyl or quinine groups (C=O, BE = 286.5–288.2 eV) [24,25]. The results of the fits of the C1s regions are listed in Table 3. It can be seen that the main peak of C1s corresponds to graphite carbon. With increased carbonization temperature, the fraction of C–C bond increase and then decrease, while that of C–O and C=O bonds first decrease then increase. This is probably due to the partial removal of elements C and O during carbonization at less than 700 C, and some surface oxidation at higher temeprature..

Table 3. The surface functional groups content of CBCFs at various temperatures.

Temperature (°C)	Graphite(C–C)		C–O		C=O	
	BE (eV)	M (%)	BE (eV)	M (%)	BE (eV)	M (%)
600	284.0	56.62	284.7	29.59	287.5	13.79
700	284.2	73.47	285.7	8.59	286.5	17.94
800	284.2	72.07	285.4	25.19	288.2	2.75
900	284.3	68.46	285.3	23.21	287.3	8.23
1000	284.3	66.90	285.3	23.69	287.5	9.40

4. Conclusions

Although cellulose is the third largest source of carbon fibers, the poor strength and yield of cellulose-based carbon fibers has limited its applications. From the results reported in this study, cellulose-based carbon fibers with excellent performance and high yield were prepared after phenol liquefaction and curing. The high carbonization temperature could improve the orderly state of the crystalline structure of carbon fibers from liquefied cellulose, but carbon fibers from liquefied cellulose are difficult to graphitize. The results suggested that other wooden materials after liquefaction could become excellent raw materials for carbon fibers.

Acknowledgments

This research was financially supported by the National Natural Science Foundation of PR China (No. 30901133, 31270607).

Conflicts of Interest

The authors declare no conflict of interest.

References

1. Johnson, D.J.; Frank, C. Recent advances in studies of carbon fibre structure. *Phil. Trans. R. Soc. Lond. A* **1980**, *294*, 443–449.
2. Tse-Hao, K.; Tzyy-Chin, D. The effect of pre-carbonization on the properties of PAN-based carbon fibers. *Polym. Compos.* **1994**, *15*, 401–407.
3. Rearick, B.K.; Harrison, I.R. Modification of pitch-based carbon fibers using a nickel-catalyzed oxidation treatment: Effect of treatment on fiber-matrix interfacial shear strength. *Polym. Compos.* **1995**, *16*, 180–188.
4. Ming, H.; Julien, R.; Shuhei, F.; Nagy, L.T.; Qingmin, J.; Pavuluri, S.; Katsuhiko, A.; Susumu, K.; Yusuke, Y. Direct carbonization of Al-based porous coordination polymer for synthesis of nanoporous carbon. *J. Am. Chem. Soc.* **2012**, *134*, 2864–2867.
5. Ming, H.; Julien, R.; Shuhei, F.; Logudurai, R.; Yuanjian, Z.; Pavuluri, S.; Hideo, I.; Hongjing, W.; Yoshihiro, N.; Norihiro, S.; *et al*. Direct synthesis of nanoporous carbon nitride fibers using Al-based porous coordination polymers (Al-PCPs). *Chem. Commun.* **2011**, *47*, 8124–8126.

6. Logudural, R.; Julien, R.; Shuhei, F.; Pavuluri, S.; Susumu, K.; Yusuke, Y. Preparation of microporous carbon fibers through carbonization of Al-based porous coordination polymer (Al-PCP) with furfuryl alchol. *Chem. Mater.* **2011**, *23*, 1225–1231.
7. Peng, S.; Shao, H.; Hu, X. Lyocell fibers as the precursor of carbon fibers. *J. Appl. Polym. Sci.* **2003**, *90*, 1941–1947.
8. Narendra, R.; Yiqi, Y. Properties of High-Quality Long Natural Cellulose Fibers from Rice Straw. *J. Agric. Food Chem.* **2006**, *54*, 8077–8081.
9. Plaisantin, H.; Pailler, R.; Guette, A.; Biot, M.; Pilot, J.P.; Daude, G.; Olry, P. Ex-cellulose carbon fibers with improved mechanical properties. *J. Mater. Sci.* **2006**, *41*, 1959–1964.
10. Alma, M.H.; Yoshioka, M.; Yao, Y.; Shiraishi, N. Preparation of sulfuric acid-catalyzed phenolated wood resin. *Wood Sci. Technol.* **1998**, *32*, 297–308.
11. Yu, L.L.; Cao, J.Z.; Paul, C.; Tang, Z.Z. Comparison of copper leaching from alkaline copper quat type-D treated Chinese fir and Mongolinan Scots pine after different posttreatments. *Wood Fibers Sci.* **2010**, *42*, 444–449.
12. Ma, X.J.; Zhao, G.J. Structure and performance of fibers prepared from liquefied wood in phenol. *Fibers Polym.* **2008**, *9*, 405–409.
13. Liu, C.L.; Guo, Q.G.; Shi, J.L.; Liu, L. A study on crosslinking of phenolic fibers. *Mater. Chem. Phys.* **2005**, *90*, 315–321.
14. Wu, Q.; Pan, D. An new cellulose based carbon fiber from a lyocell precursor. *Text. Res. J.* **2002**, *72*, 405–410.
15. Kubo, S.; Kadla, J.F. Lignin-based carbon fibers: Effect of synthetic polymer blending on fiber properties. *J. Polym. Environ.* **2005**, *13*, 97–105.
16. Lin, L.; Yoshioka, M.; Yao, Y.; Shiraishi, N. Physical properties of moldings from liquefied wood resins. *J. Appl. Polym. Sci.* **1995**, *55*, 1563–1571.
17. Edie, D.D. The effect of processing on the structure and properties of carbon fibers. *Carbon* **1998**, *36*, 345–362.
18. Donnet, J.B.; Qin, R.Y. Study of carbon fiber surfaces by scanning tunneling microscopy, part II—PAN-based high strength carbon fibers. *Carbon* **1993**, *31*, 7–12.
19. Richards, B.P. Relationships between interlayer spacing, stacking order and crystallinity in carbon materials. *J. Appl. Cryst.* **1968**, *1*, 35–48.
20. Huiming, C.; Hiroyuki, E.; Toshihiro, O.; Kouji, S.; Guobin, Z. Graphitization behavior of wood ceramic and bamboo ceramics as determined by X-ray diffraction. *J. Porous Mater.* **1999**, *6*, 233–237.
21. Tuinstra, F.; Koenig, J.L. Raman spectrum of graphite. *J. Chem. Phys.* **1970**, *53*, 1126–1130.
22. Melanitis, N.; Tetlow, P.L.; Galiotis, C. Characterization of PAN-based carbon fibers with laser Raman spectroscopy. *J. Mater. Sci.* **1996**, *31*, 851–860.
23. Fauteux, C.; Pegna, J. Radial characterization of 3D-LVCD carbon fibers by Raman spectroscopy. *Appl. Phys. A* **2004**, *78*, 883–888.
24. Paiva, M.C.; Bernardo, C.A.; Nardin, M. Mechanical, surface and interfacial characterisation of pitch and PAN-based carbon fibres. *Carbon* **2000**, *38*, 1323–1337.
25. Park, S.; Seo, M.; Lee, Y. Surface characteristics of fluorine-modified PAN-based carbon fibers. *Carbon* **2003**, *41*, 723–730.

Mechanical and Electrical Characterization of Entangled Networks of Carbon Nanofibers

Arash K. Mousavi, Mark A. Atwater, Behnam K. Mousavi, Mohammad Jalalpour, Mahmoud Reda Taha and Zayd C. Leseman

Abstract: Entangled networks of carbon nanofibers are characterized both mechanically and electrically. Results for both tensile and compressive loadings of the entangled networks are presented for various densities. Mechanically, the nanofiber ensembles follow the micromechanical model originally proposed by van Wyk nearly 70 years ago. Interpretations are given on the mechanisms occurring during loading and unloading of the carbon nanofiber components.

Reprinted from *Materials*. Cite as: Mousavi, A.K.; Atwater, M.A.; Mousavi, B.K.; Jalalpour, M.; Taha, M.R.; Leseman, Z.C. Mechanical and Electrical Characterization of Entangled Networks of Carbon Nanofibers. *Materials* **2014**, *7*, 4845ï 4853.

1. Introduction

One-dimensional carbon materials are available in many high-end commercial products [1,2] and continue to be a source of ongoing research [3–5]. This is due to their remarkable material properties. The two main instances of this type of material are carbon nanotubes and carbon nanofibers. Carbon micro- and nanofibers are a common component in high-strength, lightweight fiber-reinforced composites [6–9]. Less studied are the properties of an interwoven assemblage of the nanofibers, which behaves as a coherent, nonwoven component.

Synthesis methods for creating carbon nanotubes [10] and nanofibers [10–12] commonly produce random networks of tangled fibers. These entangled fibers do not have fixed connections with adjoining fibers (*i.e*., they are not cross-linked). Thus, the entangled fibers comprise a random network similar in nature to a nonwoven mass of fibers found in common textile processes. Random networks of textile fibers are commonly modeled using a micromechanical model originally developed by van Wyk in 1946. In 2009 an effort was undertaken to mechanically test a “tangle” of carbon nanotubes [3]. This effort demonstrated that the van Wyk model [13] matched the stress *vs*. change in fiber volume fraction for the loading portion of the curve. It also showed that the van Wyk model did not match the unloading portion of the curve. Allaoui *et al*. [3] surmise that this is due to the dissipation of adhesive energy as contacts break.

The van Wyk model was proposed in 1946 [13] and incorporates fiber bending at contact points in the random network and the creation of new fiber-to-fiber contacts, but ignores other effects such as friction and fiber sliding. Functionally, van Wyk’s model proportionally relates the stress applied to the random fiber network, σ, to the fiber volume fraction, μ, to the third power:

$$\sigma = k_{\mathrm{p}}(\mu^3 - \mu_0^3) \tag{36}$$

where k_{p} is a constant that contains information on fiber characteristics and μ_0 is the initial fiber volume fraction before compression. This model describes the behavior of a large entangled network

of randomly oriented fibers. This amazingly simplistic model has been found to be applicable to many different types of random fiber networks such as short hollow pulp fiber networks [14] and textile reinforcements for composites manufacturing [15].

The electrical response of a random fiber network to an applied stress is not commonly studied, because most types of fibers in the textile industry are not conductive. Thus, there is a lack of studies and modeling addressing this topic. In this paper, the electrical properties are measured in both tension and compression. Sudden changes in electrical resistance seen in tension tests can be used as a method of evaluating the mechanical situation and integrity of the material. For compression tests, the electrical resistance is shown to approach the conductance of amorphous carbon when the carbon nanofibers are under their highest compressive loads. Additionally, the mechanical response of the entangled networks of carbon nanofibers is studied in tension and compression. A discussion of the tensile response is qualitative while the compressive response is modeled using the van Wyk Model. The compression tests reported here are performed in an open die configuration under high stresses (~10 MPa). During loading, it was verified that the sample kept its integrity even at the highest loads. Furthermore, it is shown that the van Wyk Model Equation (1) for a random entanglement of fibers is capable of describing the response of the material with considerable accuracy.

2. Experimental Section

2.1. Carbon Nanofiber Synthesis

Bulk, nonwoven components comprised of carbon nanofibers were synthesized using a method previously developed by Atwater *et al*. [10]. Briefly, Pd nanoparticles are dispersed in a rectangular steel mold and then heated in a furnace in an inert environment. Once heated to 550 °C, a mixture of ethylene and oxygen flows over the catalyst. By varying the Pd particle loading in the mold and the time of gas flow differing densities of carbon nanofiber entanglements were synthesized. Sample densities were determined geometrically by weighing samples of a known volume.

An example of the as-grown samples is shown in Figure 1. Here it can be seen that a relatively large (many centimeters) component can be easily attained with this process. When examined using SEM, it can be seen that the larger structure is actually comprised of much smaller (*ca*. 100 nm diameter), carbon nanofibers, e.g., Figure 1d. Additional characterization of the fibers' properties is contained in References [11,12]. The process, then, creates a multi-scale material with the ability to control both nanoscale and macroscale features.

2.2. Mechanical and Electrical Characterization Setups

Mechanical and electrical characterization was conducted simultaneously for samples of differing densities. In order to accomplish this, a custom setup was required for both the tensile and compressive tests. Tensile samples were tested under relatively low loads, <45 N, while compression tests were to a load as high as 200 N.

Figure 1. Carbon Nanofiber Network at increasing magnification, boxes indicate section in next image (**a**) 1×; (**b**) 1000×; (**c**) 10,000×; (**d**) 20,000×.

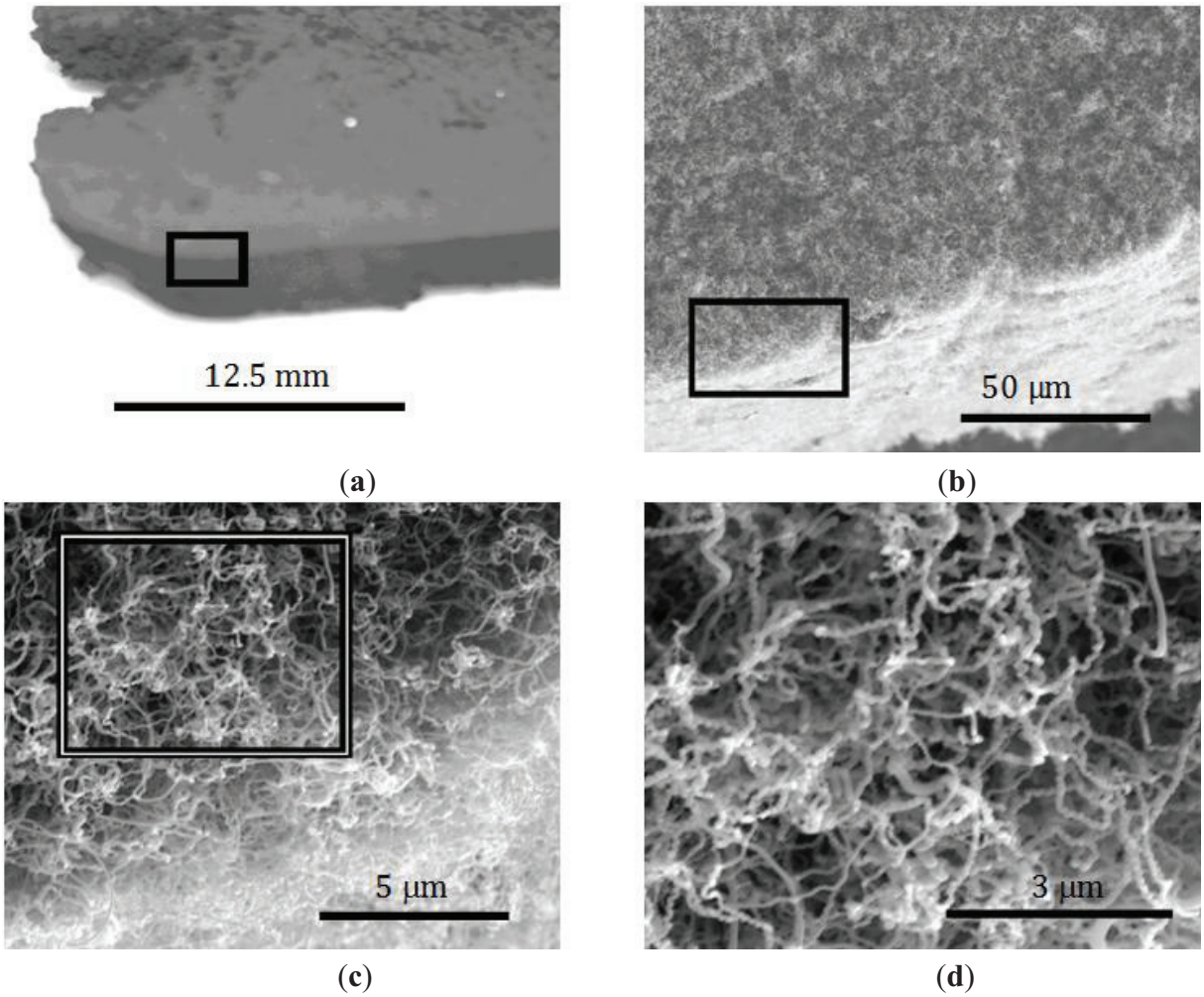

Tensile tests were conducted on an Instron 1101 with a 45 N load cell using a constant displacement of 1.27 mm/min. Sample densities tested were 0.125 and 0.131 g/cc. Carbon nanofiber samples with a cross sectional area of 5 mm × 25 mm were clamped between two electrically isolated grips at a distance of 20 mm apart. A constant current of 250 mA was applied to the samples and the voltage was recorded in order to determine the resistance of the sample as a function of load.

Compression tests were performed on a larger capacity Instron with a 44.5 kN load cell with a constant crosshead displacement of 0.252 mm/min. The 0.40 g/cc cylindrical sample was tested in an open die configuration with a diameter of 4.7 mm and thickness of 5 mm. Electrical measurements were made in the same manner as for the tensile experiments.

3. Mechanical Properties

3.1. Tensile Tests

Tensile loading curves for two different densities of nanofibrous nonwoven carbon are shown in Figure 2. The stress-strain curves are accompanied by their corresponding resistance measurements. Judging from SEM characterization (e.g., see Figure 1), no fiber is expected to span the gage length

of the sample, and therefore no fibers are considered rigidly held by both grips. On that assumption, loading of the samples must be a result of friction between the fibers and mechanical interlocking.

Figure 2. Tensile behavior of carbon nanofiber network under tension, accompanied by resistance measurements as a function of strain (mm/mm). (**a**) Low density network; (**b**) High density network.

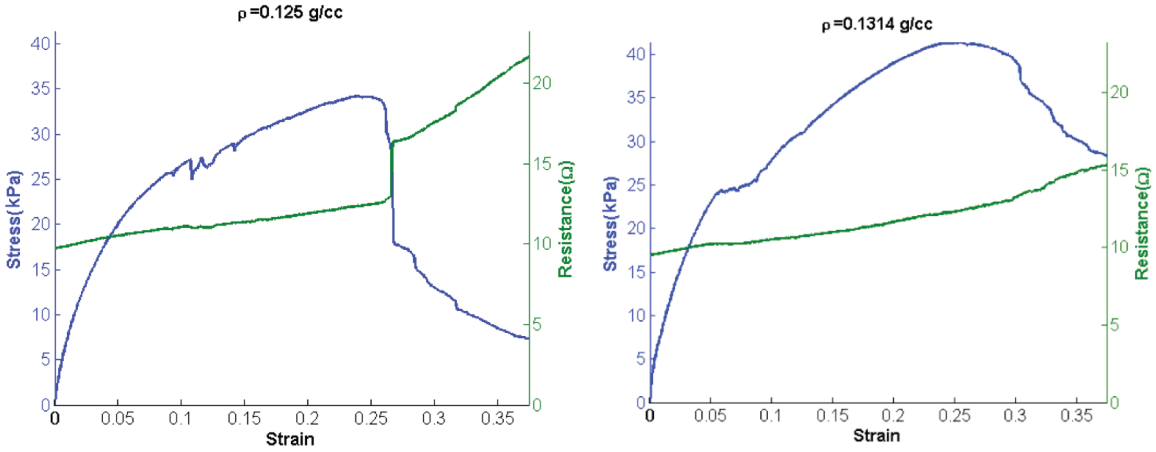

(**a**) (**b**)

Tensile loading of the samples diplays several interesting behaviors. For both samples, a smooth monotonic increase is seen during loading initially. This smooth portion of the loading curves is then followed by data that is generally increasing, but contains several discontinuities. These discontinuities are attributed to avalanches of fiber pullouts. After a critical number of fibers have pulled out, a maximum load is reached, and any increase in displacement results in nothing but decreases in load.

In order to more succinctly compare the behavior of these two samples five material properties are examined: (1) tangent modulus; (2) maximum stress; (3) maximum strain; (4) failure stress and (5) failure strain. Failure is defined as a decrease in the load sustained by the sample. Table 1 compares the compressive moduli and tangent moduli attained from tensile tests. Though the two samples have nearly identical densities and remarkably similar material properties, as listed in Table 1, there is a marked difference in the failure of the two samples. The 0.125 g/cc sample has a massive avalanche of pulled out fibers as is evidenced by a sudden drop in load after reaching σ_u; this is also accompanied by a large jump in resistance of the sample. The 0.131 g/cc sample appears to have a fairly gradual pullout of fibers as it continues to fail after having reached its σ_u.

Table 1. Mechanical Properties of entangled network of carbon nanofibers.

ρ (g/cm^3)	*E*(kPa)	σ_y (kPa)	σ_u (kPa)	Linear Range Percentage (% of σ_u)
0.125	600	13.4	34.2	39.2%
0.131	627	16.9	41.3	40.8%

The resistance of the entangled network of the carbon nanofibers increases almost linearly with increasing tensile load until there is a sudden drop in the load (stress). This is a clear indication that fibers are pulling out from one another. This reduces the number of fibers in contact as well as the

number of contacts per fiber. Once a threshold limit is met, then many fibers separate from one another simultaneously—an avalanche of fiber pullouts. Again, this is most noticeable for the 0.125 g/cc sample near its σ_u.

3.2. Compression Tests

Five compressive loading cycles are shown for a sample with a of density 0.40 g/cc in Figure 3. Cycle 6 and subsequent cycles display the similar hysteresis between the loading and unloading portion of each cycle, but nearly fall on top of one another. The stress *versus* percent fiber volume fraction (μ%) are accompanied by their corresponding resistance measurements. The resistance *vs*. μ% curves follow similar trends, as seen by Atwater *et al*. [10]. Additionally, the loading portions of the curves in Figure 3 are fit with the van Wyk model, Equation (1). The agreement between the experimental data and model demonstrate the utility of the model and also show that the mechanisms modeled in the van Wyk interpretation are responsible for the defromation behavior of the entanglement of the carbon nanofibers.

van Wyk's model describes the bending and creation of new contacts in a random network of fibers. This is appropriate for the compressive loading of the fibers as evidenced by the fit of van Wyk's model to the data in Figure 4. Unloading of the fiber shows a considerable amount of hysteresis and is not modeled well by van Wyk's model (and is not displayed). For unloading, it is likely that adhesion and friction are the main contributors to this hysteresis, as is the case with carbon nanotubes [3].

Even within the loading event, it appears that bending and the creation of contacts contribute different amounts to the loading history of the sample as the fiber volume fraction increases. For lower values of μ (and load) the samples are more porous, *i.e*., there are more air gaps between the carbon nanofibers. Thus, as the sample is compressed, the fibers bend into the empty spaces more readily—bending is more dominant at lower values of load and μ. Thus, the model does not work as well for lower values of load and μ. As the compression continues, new contacts are made at an increasing rate. In fact, it has been recently shown that the rate of increase of the number of contacts is linearly proportional to μ [16]. Thus for higher values of load and μ the van Wyk model is more applicable and therefore more accurate. A considerable amount of hysteresis exists between the loading and unloading cycles in Figure 3. Adhesion (friction) is attributed to this hysteresis. Adhesive forces are commonly known to cause sticking between individual micro and nanodevices, commonly referred to as 'stiction failure' in the literature [17–19]. Because of the small scale of the fibers (*i.e*., *ca*. 100 nm diameter), van der Waals forces, hydrogen bonding, *etc*. may have an appreciable adhesive effect. Allaoui *et al*. [3] also consider this to be the source of adhesion between fibers and the culprit for hysteresis in carbon nanotube tangles.

Figure 3. Five compression cycles (continuous loading and unloading) of a 0.40 g/cc carbon nanofiber tangle sample. Data is displayed as pressure *vs*. percent fiber volume fraction (μ).

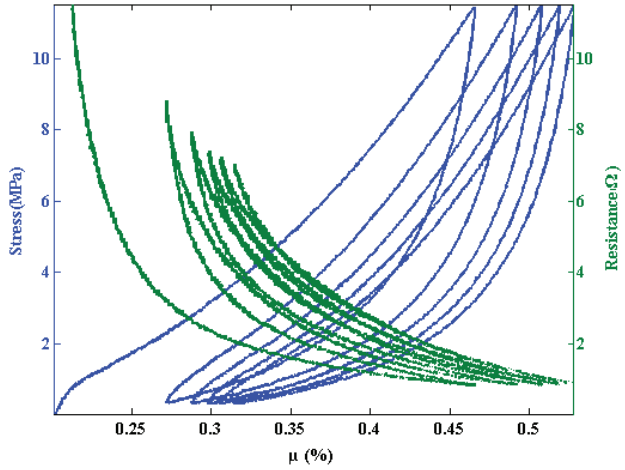

Figure 4. Loading portions of the curves in Figure 3 with fits to the van Wyk model.

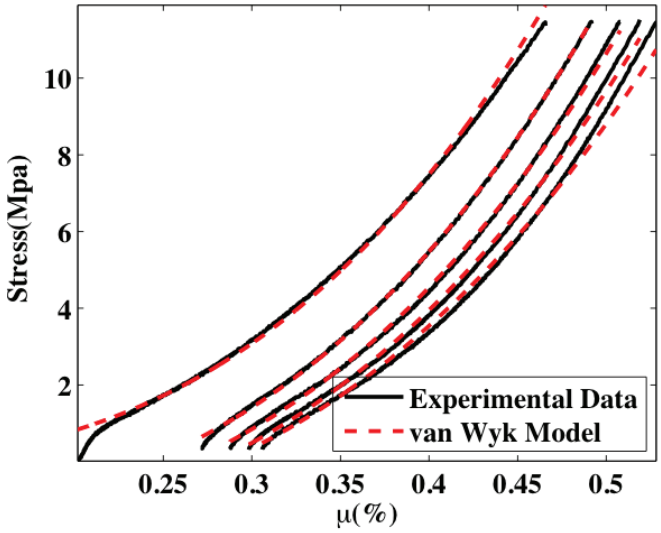

Adhesion between fibers leads to hysteresis while the bending of individual fibers is the main source of elastic energy storage. As the load increases more fibers are being influenced to move, but their motion is impeded due to restrictions from adjacent fibers. For the highest loads, energy is dissipated by irreversible friction and sliding [20]. However, when unloading occurs, only the elastically stored energy can be recovered. Thus a small reverse movement in the compression platen results in a large drop in load as seen in all unloading curves. For lower values of μ (strain) the elastic energy in the fibers becomes considerable and pushes back on the compression platen and a large movement of the platen results in a smaller change in load.

The resistance of the entangled network decreases nonlinearly as the compressive load is applied in Figure 3. An asymptotic value is approached for the highest loads. Considering the sample size, the resistivity of the sample approaches 2.7×10^{-3} Ω·m, which is approximately three to five times that of amorphous carbon (5×10^{-4}–8×10^{-4} Ω·m) [21,22]. Physically, the sample is being compressed and the sizes of the pores filled with air are beginning to decrease while, simultaneously,

more physical connections are being made between fibers. Had all pores been eliminated, it would be expected that the value for the resistivity of the material should approach that of amorphous carbon. However, it can never truly reach this value because the pores never fully disappear and also the surfaces of the carbon nanofibers have adsorbed gases that never allow the entangled network of carbon nanofibers to turn into a continuous piece of amorphous carbon. These interfaces cause additional scattering of electrons over what would be expected in amorphous carbon.

4. Conclusions

The results of this work indicate that bulk collections of carbon nanofibers can behave as traditional nonwoven materials. This understanding was reached through simultaneous mechanical and electrical analyses. Under tensile load, these nanofibrous nonwovens tend to fail by fiber pullout. During elongation there is no significant enhancement of fiber-to-fiber contact (*i.e.*, reduction of cross-sectional area), which would be indicated through a reduction in electrical resistance. Under compression, the material behaves elastically, but with significant hysteresis during unloading. Electrical resistance decreases substantially as the material is compressed. The mechanical properties and the reduction in electrical resistance are consistent with the van Wyk model of fiber interaction. The hysteresis during unloading is attributable to small-scale friction and adhesive affects found in fibrous materials. Based on these data, the material is expected to be suitable for applications where cyclic compressive forces are encountered or in applications where an electrical response to deformation may be valuable.

Author Contributions

The contributions to this article fall into five main categories: synthesis, characterization, modeling, analysis, and preparation of the manuscript. Mark A. Atwater synthesized the samples. Arash K. Mousavi characterized the samples, analyzed the data, developed and applied the models as well as prepared the manuscript. Behnam K. Mousavi contributed to the modeling and studied the electrical response of the sample. Mohammad Jalalpour and Mahmoud R. Taha contributed to the characterization of the samples, in particular the mechanical testing. Zayd C. Leseman conceived the idea for the paper and oversaw: synthesis, characterization, modeling, analysis and preparation of the manuscript.

Conflicts of Interest

The authors declare no conflict of interest.

References

1. Bachtold, A.; Hadley, P.; Nakanishi, T.; Dekker, C. Logic circuits with carbon nanotube transistors. *Science* **2001**, *294*, 1317–1320.
2. Baughman, R.H.; Zakhidov, A.A.; de Heer, W.A. Carbon nanotubes—The route toward applications. *Science* **2002**, *297*, doi:10.1126/science.1060928.

3. Allaoui, A.; Toll, S.; Evesque, P.; Bai, J. On the compressive response of carbon nanotube tangles. *Phys*. *Lett*. *A* **2009**, *373*, 3169–3173.
4. Thostenson, E.T.; Chou, T.-W. Carbon nanotube networks: Sensing of distributed strain and damage for life prediction and self healing. *Adv*. *Mater*. **2006**, *18*, 2837–2841.
5. Rahatekar, S.S.; Koziol, K.K.; Kline, S.R.; Hobbie, E.K.; Gilman, J.W.; Windle, A.H. Length-dependent mechanics of carbon-nanotube networks. *Adv*. *Mater*. **2009**, *21*, 874–878.
6. Skandani, A.A.; Masghouni, N.; Case, S.W.; Leo, D.J.; al-Haik, M. Enhanced vibration damping of carbon fibers-ZnO nanorods hybrid composites. *Appl*. *Phys*. *Lett*. **2012**, *101*, doi:10.1063/1.4746398.
7. Bryning, M.B.; Islam, M.F.; Kikkawa, J.M.; Yodh, A.G. Very low conductivity threshold in bulk isotropic single-walled carbon nanotube-epoxy composites. *Adv*. *Mater*. **2005**, *17*, 1186–1191.
8. Li, W.; Zhang, H.; Xiong, X. Properties of multi-walled carbon nanotube reinforced carbon foam composites. *J*. *Mater*. *Sci*. **2011**, *46*, 1143–1146.
9. Tehrani, M.; Luhrs, C.C.; al-Haik, M.S.; Trevino, J.; Zea, H. Synthesis of WS2 nanostructures from the reaction of WO3 with CS2 and mechanical characterization of WS2 nanotube composites. *Nanotechnology* **2011**, *22*, doi:10.1088/0957-4484/22/28/285714.
10. Atwater, M.A.; Mousavi, A.K.; Leseman, Z.C.; Phillips, J. Direct synthesis and characterization of a nonwoven structure comprised of carbon nanofibers. *Carbon N.Y*. **2013**, *57*, 363–370.
11. Atwater, M.A.; Phillips, J.; Doorn, S.K.; Luhrs, C.C.; Fernández, Y.; Menéndez, J.A.; Leseman, Z.C. The production of carbon nanofibers and thin films on palladium catalysts from ethylene–oxygen mixtures. *Carbon N.Y*. **2009**, *47*, 2269–2280.
12. Atwater, M.; Leseman, Z.C.; Phillips, J. Controlling carbon nanofibres morphology for improved composite reinforcement. *Int. J. Mater. Struct. Integr.* **2009**, *3*, 179–186.
13. Van Wyk, C.M. A study of the compressibility of wool, with special reference to South African merino wool. *Onderstepoort J*. *Vet*. *Sci*. *Anim*. *Ind*. **1946**, *21*, 99–226.
14. Lundquist, L.; Willi, F.; Leterrier, Y.; Månson, J.E. Compression behavior of pulp fiber networks. **2004**, *44*, 45–55.
15. Robitaille, F.; Gauvin, R. Compaction of textile reinforcements for composites manufacturing. III: Reorganization of the fiber network. *Polym*. *Compos*. **1999**, *20*, 48–61.
16. Rodney, D.; Fivel, M.; Dendievel, R. Discrete modeling of the mechanics of entangled materials. *Phys*. *Rev*. *Lett*. **2005**, *95*, doi:10.1103/PhysRevLett.95.108004.
17. Mousavi, A.K.; Kashamolla, M.R.; Leseman, Z.C. Improved model for the adhesion of μcantilevers: Theory and experiments. *J*. *Micromech*. *Microeng*. **2013**, *23*, doi:10.1088/0960-1317/23/11/115011.
18. Leseman, Z.C.; Carlson, S.P.; Mackin, T.J. Experimental measurements of the strain energy release rate for stiction-failed microcantilevers using a single-cantilever beam peel test. *J*. *Microelectromech*. *Syst*. **2007**, *16*, 38–43.
19. De Boer, M.P.; Michalske, T.A. Accurate method for determining adhesion of cantilever beams. *J*. *Appl*. *Phys*. **1999**, *86*, 817–827.
20. Subramanian, G.; Picu, C.R. Mechanics of three-dimensional, nonbonded random fiber networks. *Phys*. *Rev*. *E* **2011**, *83*, doi:10.1103/PhysRevE.83.056120.

21. Serway, R.A.; Jewett, J.W. *Principles of Physics*, 2nd ed.; Saunders College Pub: Philadelphia, PA, USA, 1998.
22. Pauleau, Y.; Barna, P.B.; Barna, P.B. *Protective Coatings and Thin Films: Synthesis*, *Characterization*, *and Applications*; Springer: Alvor, Portugal, 1997.

Fabrication of a Low Density Carbon Fiber Foam and Its Characterization as a Strain Gauge

Claudia C. Luhrs, D. Chris Daskam, Edwin Gonzalez and Jonathan Phillips

Abstract: Samples of carbon nano-fiber foam (CFF), essentially a 3D solid mat of intertwined nanofibers of pure carbon, were grown using the Constrained Formation of Fibrous Nanostructures (CoFFiN) process in a steel mold at 550 °C from a palladium particle catalysts exposed to fuel rich mixtures of ethylene and oxygen. The resulting material was studied using Scanning Electron Microscopy (SEM), Energy Dispersive Spectroscopy (EDX), Surface area analysis (BET), and Thermogravimetric Analysis (TGA). Transient and dynamic mechanical tests clearly demonstrated that the material is viscoelastic. Concomitant mechanical and electrical testing of samples revealed the material to have electrical properties appropriate for application as the sensing element of a strain gauge. The sample resistance *versus* strain values stabilize after a few compression cycles to show a perfectly linear relationship. Study of microstructure, mechanical and electrical properties of the low density samples confirm the uniqueness of the material: It is formed entirely of independent fibers of diverse diameters that interlock forming a tridimensional body that can be grown into different shapes and sizes at moderate temperatures. It regains its shape after loads are removed, is light weight, presents viscoelastic behavior, thermal stability up to 550 °C, hydrophobicity, and is electrically conductive.

Reprinted from *Materials.* Cite as: Luhrs, C.C.; Daskam, C.D.; Gonzalez, E.; Phillips, J. Fabrication of a Low Density Carbon Fiber Foam and Its Characterization as a Strain Gauge. *Materials* **2014**, *7*, 3699ï 3714.

1. Introduction

Carbon nanotubes, in particular, as single wall tubes (SWCNT), have been demonstrated to present remarkable response as piezoresistive elements [1–4]. Individual tube gauge factors, which can be described as the sensitivity of the sensor, have been reported to reach values up to 1000 [5]. However, the sensors based on CNT assemblies have much lower sensitivities than those of the individual tubes mentioned above, typical ensemble piezoresistive sensor have gauge factors up to 22 [6]. Obtaining the maximum possible gauge factor is limited by the features that dominate large assemblies of tubes: defects and difficulties controlling the orientation and position of the tubes to produce homogenous large samples. Thus far, efforts in this direction have opted for using random assemblies of individual tubes, both as single and multiwall tubes [7–10]. Thus, new materials that can attain the expected electrical and mechanical characteristics, or novel approaches to develop such materials with high yields and repeatable results, are still needed.

Other issues limiting the application of carbon structures for pressure/strain gauges are the unresolved engineering challenges. Earlier reported strategies to develop pressure/strain sensors using carbon nanotubes or carbon fibers are quite complex, difficult to reproduce and expensive. Control over the macroscopic object geometry, density, and means to create an interface with other

components has turned to be a titanic effort. Some examples found in recent publications to generate three-dimensional carbon tube/fiber based architectures involve the association of carbon structures with polymeric matrices [11–13], strategies to assemble them during synthesis [14–16] and attempts to create the connections post-synthesis [17–23]. From the former category, the combination with polymers imprints undesired characteristics in the product such as reduced conductivity and low thermal stability due to the use of polymeric matrices. From the second approach: despite the products presenting the desired electrical properties, there has been no reported success in creating highly porous mechanically robust tridimensional architectures. The third approach, post-synthetic routes to generate low density structures, is dominated by techniques that use solvents to align nanotube forests, foams or cellular structures aided by the capillary forces that are present as the solvent evaporates [17,18]. Other post-synthesis efforts include low temperature soldering [19], use of monolayer and multilayered silica templates [20], high frequency pulses of electrical discharge to machine targeted shapes, and radical initiated thermal crosslinking of CNT [21,22], focused laser beam used to locally burn regions of a dense forest [23] and chemical processes to stitch CNTs together [17]. Thus, there is still a necessity for a simple, reproducible way to create mechanically robust 3D structures to be used as sensing elements.

Recently it was established that macroscopic carbon foam could be fabricated in virtually any shape using the constrained formation of fibrous nanostructures process (CoFFiN) [24]. These foams consist of a solid mat of intertwined nanoscale carbon fibers, the shape of the same defined by the shape of the mold in which it is grown. The constrained formation of fibrous nanostructures process was developed as a variation on graphitic structures by design (GSD) technology [25,26]. The key to GSD, as shown in earlier work, is the catalyzed growth of solid carbon structures from radical species formed homogenously during a fuel rich combustion process. In practice, it has been clearly demonstrated that a variety of carbon structures (e.g., fibers, solid mats, graphite encapsulated catalyst, *etc.*) can be grown from combustion mixtures, and that the nature of the structure that grows is a function of catalyst, composition of the fuel rich combustion mixture, temperature, and even gas flow rate.

The CoFFiN process followed to generate the carbon fiber foam studied herein is a natural extension of those previous discoveries: the catalysts, the gas mixtures, and temperatures employed, are selected to be those that lead to the most rapid growth of carbon fibers as revealed in earlier studies. Moreover; by confining growth to a mold the fibers become entangled, leading to the growth of cohesive macroscopic fiber structures that have the same shape as the mold.

In those earlier publications it was demonstrated, for CoFFiN materials, that there is a relationship between applied stress and electrical resistance, but the data was insufficient to fully characterize all features or even to clearly identify the class of material according to its mechanical behavior. The data from the present work permits the following points to be elucidated: (i) CFF on the macroscopic scale behaves precisely as a viscoelastic, and is not simply elastic; (ii) Only after repeated cyclic compression, that is “mechanical aging”, do mechanical and electrical properties stabilize; (iii) the material is not, despite earlier suggestion, particularly suited for use in a pressure gauge, instead the material is suitable for use as the sensing element in a strain gauge; and (iv) other key characteristics of the structure, such as relative density, surface area, contact angle and thermal stability are now

accurately measured. Finally, it is clear that the CFF microstructure, totally composed of conductive fibers, makes it an unusual viscoelastic.

2. Results and Discussion

2.1. Results

After growth and removal from the mold, a single block of carbonaceous material was obtained. The sample roughly had the shape of the mold, although the material tended to twist modestly due to some internal stresses upon removal from the mold. Macroscopically, the product of the synthesis had the texture and consistency of foam. Examination of the sample by SEM revealed that the microstructure is dominated by intertwined fibers of diverse diameters but most of the volume is void space. Analysis of fiber diameters from electron micrographs revealed that the diameters range from approximately 30 nm to 400 nm. Within that distribution the plurality of the fibers have between 60 and 90 nm in width (Figure 1a,b). Given that the fibers grow in random directions while intertwining into each other, the length of individual fibers was not measured. Backscattered electron images of the sample showed a homogeneous distribution of the palladium particles used as catalyst. EDS analysis of the sample showed no evidence of oxygen in regions where Pd was present, indicating that despite the small amounts of oxygen used during the synthesis the palladium remains the metallic state throughout the fiber growth step.

Figure 1. Microstructural analysis by SEM. (**a**) The sample consists of fibers which diameters vary between 30 and 400 nm and regions of empty space; (**b**) The plurality of fibers are between 60 and 90 nm in width; (**c**) During compression the empty spaces between fibers disappear with no evidence of fiber delamination or fracture.

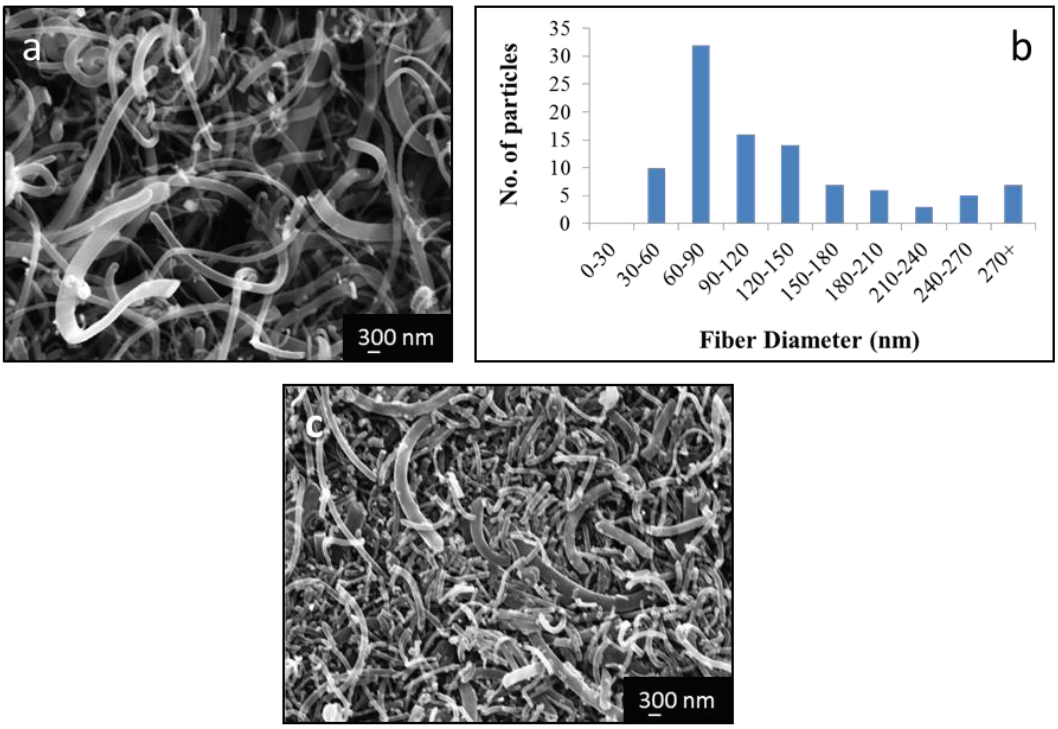

As described in the previous section, a sample of the fiber 3D architecture was compressed inside the SEM using a SEM tester using loads up to 350 N. Micrographs taken during the experiment show that the gaps and empty spaces between the fibers decreased while under load; however, no evidence of fiber failure was detected. After the 350 N were applied the sample compressed to a point that the instrument could not place the platens any closer. Under such circumstances the sample bulged in the directions perpendicular to the applied load but regained its shape and volume after removal of the load. Indeed, even after multiple compressive cycles no breakage, delamination or cracking signatures in individual fibers were seen (Figure 1c). Study of the microstructure of the sample by SEM after mechanical cycling tests showed the same initial characteristics: intertwined fibers with gaps and void space in between them.

According to our measurements the entangled fiber structure as prepared has a relative density of 0.24, similar to cork [27] and aluminum foams [28]. Given that the density of carbon fibers is generally estimated to be the same as graphite, approximately 2.26 g/cm^3, this indicates that approximately 90% of the volume of an uncompressed sample is void space. The BET surface area was relatively high, 118 m^2/g. For comparison, most reported specific surface areas of graphene measured by BET range between 600 and 1000 m^2/g [29–32], although the theoretical specific surface area has been computed to be 2630 m^2/g [33].

The strain that resulted from the application of diverse loads to the fiber structure when using an Instron mechanical tester in compression mode is presented in Figure 2. Under deformation the material presents both viscous and elastic characteristics, with evidence of time-dependent values. The stress *vs.* strain curves of the constrained specimen (using the Plexiglas fixture) show the typical profile of a viscoelastic material; the first section follows a linear—elastic behavior, which is followed by an unloading cycle that does not reproduce the original stress *versus* strain path but presents instead a hysteresis loop typical of viscous materials. When cyclic loading is applied this phase lag is more evident, showing dependence with the loading or strain rate (Figure 2a,b). As other viscoelastic materials, the CFF seems stiffer when loaded fast than when subject to loading at lower rates. Each consecutive cycle performed between 10 and 90 N shows a shift in the corresponding strain to higher strain values during the first 15–17 cycles. Once conditioned the next cycles showed stable behavior, with stress strain profiles that perfectly overlap for higher number of cycles, as shown in Figure 2c. Estimation of the elastic modulus of the linear region for experiments performed at diverse strain rates demonstrate that higher frequencies produce higher values (above 4 MPa), while slower frequencies reach lower values (close to 3 MPa). The area inside the curve usually correlated to the energy absorption at a particular frequency, changes as well: the higher the cycling frequency, the lower the energy absorption capability.

A stress relaxation test was performed by compressing the sample with an initial force of 50 N, which reduced the structure dimension by 2.5 mm, at room temperature. The sample was allowed then to relax while the position was maintained, thereby maintaining a constant strain of 0.63 on the sample. The stress on the sample was then allowed to vary and recorded. As denoted in the stress *versus* time graph upon the imposition of a constant deformation the force necessary to maintain the deformation decreases with time (Figure 3), as is typical in viscoelastic materials like biofilms and gels [34,35].

Figure 2. Stress *vs.* strain curves for the constrained sample. Cycles performed between 10 and 90 N loads using Plexiglas fixture to maintain constant area. The first loading cycle from 0 to 90 N has been removed. (**a**) Cycling behavior at a rate of 0.05 mm/s; (**b**) Cycling at frequencies of 0.01 mm/s; and (**c**) Values reach a reproducible and stable profile after the first conditioning 15–17 cycles.

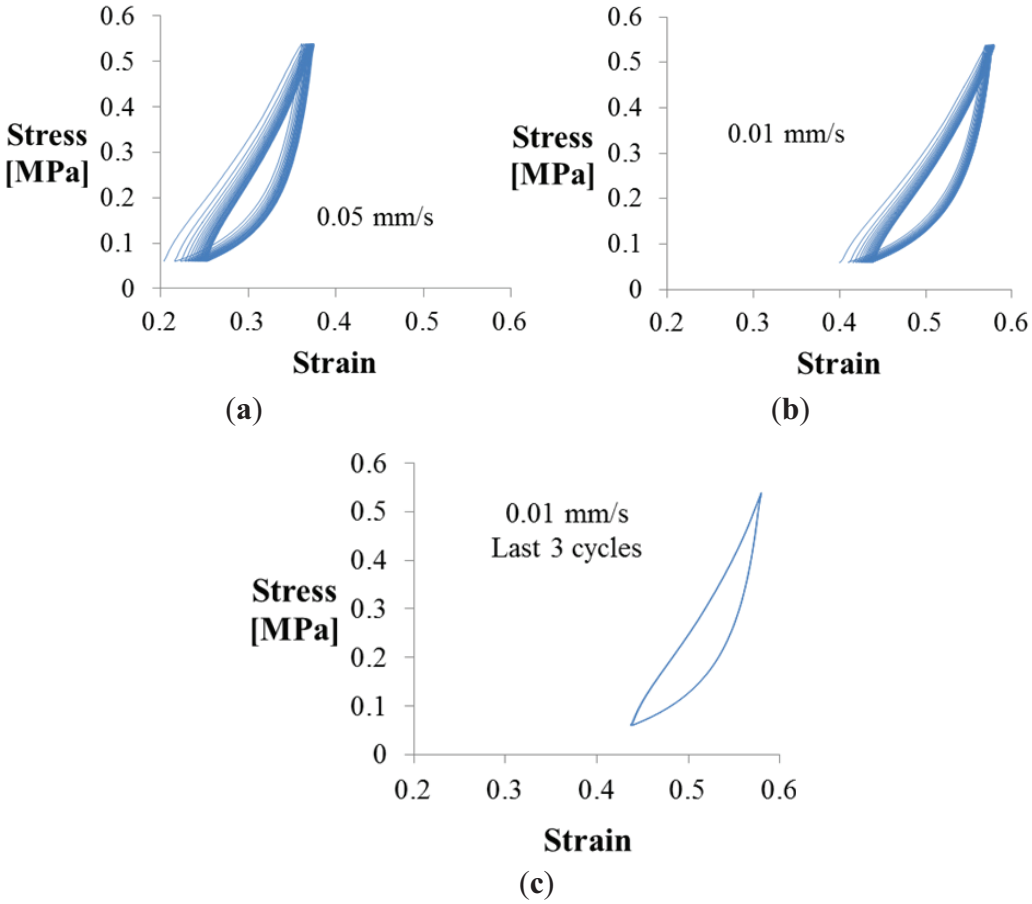

Figure 3. Sample relaxation. A constrained sample was maintained at a constant strain of 0.63 at room temperature. Initially 50 N were applied; the program was adjusted to maintain such strain level and stress over time recorded.

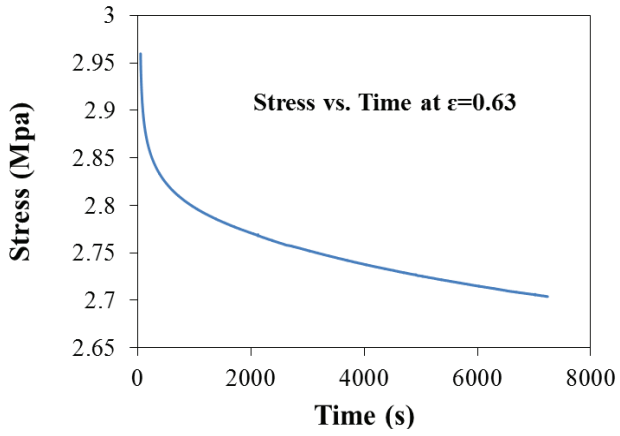

The resistance of the sample can be related to the values of load and strain imposed in the 3D fiber architecture, the higher the level of load/strain the lower the sample resistance. However, the initial

resistance values recorded during cyclic tests seem not to be reproducible, in the same way that mechanical tests showed with the hysteresis loop behavior, the sample requires a conditioning stage of about 15–17 cycles before the resistance values can be correlated to a particular value of strain. Figure 4 exemplifies such behavior. If resistance is plotted against load or stress, a phase lag is observed and a perfect linear correlation is never reached. However, if the correlation of resistance is made with respect to the values of strain, then a perfect line is obtained for multiple cycles. Such linear relationship between strain and resistance suggests the material could be employed as a strain gauge.

Figure 4. Resistance *vs.* time cyclic behavior. Cycles performed between 10 and 90 N loads using Plexiglas fixture illustrate that after some initial the conditioning cycles the Carbon Fiber Foam electrical behavior stabilizes.

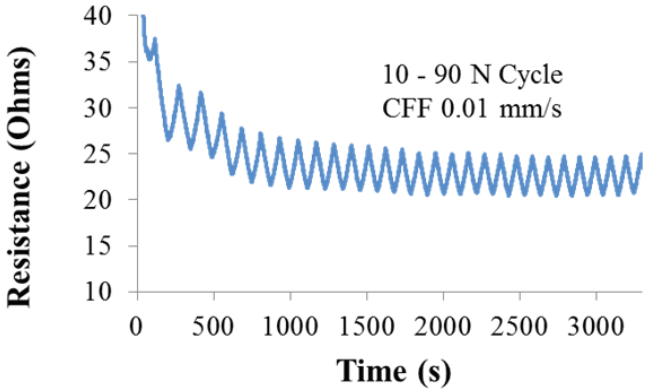

In order to test this proposition the resistance as a function of strain for the final six legs of the process were plotted (Figure 5a) along the $\Delta R/R_0$ *versus* strain (Figure 5b). The slope of the later, 0.43, is related to the sensitivity of the strain gauge or gauge factor. Despite this low value, the material does appear to have potential as sensing element of a strain gauge when high levels of strain are present.

Figure 5. Strain Gauge. The resistance *vs.* strain values taken from the final six segments of cycling experiment show the "aged material" displays a linear relationship between resistance and strain (**a**). The slope of the $(\Delta R - R_o)/R_o$ *vs.* strain, taken from the 3rd to last cycle, has been used to calculate the strain gauge factor (**b**).

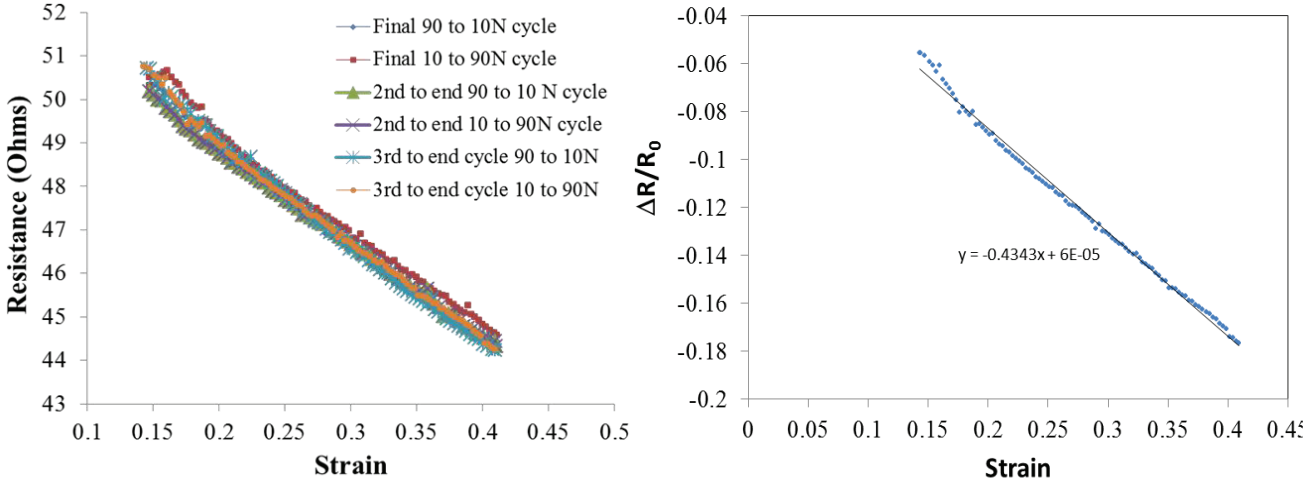

(**a**) (**b**)

Temperature programmed oxidation analysis of the sample using 20% oxygen/80% inert gas atmospheres indicated that the sample does not suffer any weight changes until nearly 550 °C. From 550 to 750 °C the sample reacts with the oxygen to undergo a combustion reaction producing CO_2 as volatile byproduct while losing weight until most of the sample is consumed. At 1000 °C, less than 1% of the original weight remains, associated with leftover Pd catalyst that reacted to produce PdO as single solid byproduct (Figure 6). In comparison, commercial viscoelastic polymers begin to decompose in air at above ~200 °C and are dramatically and irreversibly modified by 300 °C [36]. The CFF under study is completely stable to 550 °C during heating in air.

The hydrophobicity of the samples was demonstrated by placing a water droplet on the surface of the as prepared 3D fiber structure (Figure 7a). The water droplet does not wet the foam and tends to roll off the surface at low angles of inclination. Measurement of the contact angle using the Young-Laplace method, as described in the experimental section, returned a value of 145°. In contrast, a non-polar liquid, mineral oil, did not form a drop at all, being instantly absorbed by the fiber foam (Figure 7b).

Finally, an effort was made to determine if carbon, aluminum and stainless steel could generate a similar signal than the one observed for the CFF employed. In all cases the measured resistance was in the order of 0.1 Ω. Grafoil, a form of commercial carbon created from compressed naturally occurring graphite, of approximately the same thickness as the CFF was placed in the same Plexiglas constraint system and tested using the same constant changing strain rate as that employed for the CFF, 0.01 mm/s, over the same compression limits. The general trend of resistance was the same as that observed for the CFF: resistance decreased with increased strain. However; at least for the number of cycle tests conducted herein, Grafoil resistance and strain values are extremely erratic, and do not present a linear correlation. Moreover, the material never regains its original dimension.

Figure 6. Thermal stability determined by TPO analysis. The sample maintains its weight up to at least 550 °C under an oxygen containing atmosphere, after such the carbon starts to burn off until only the weight of the original palladium catalyst particles, now oxidized, remains.

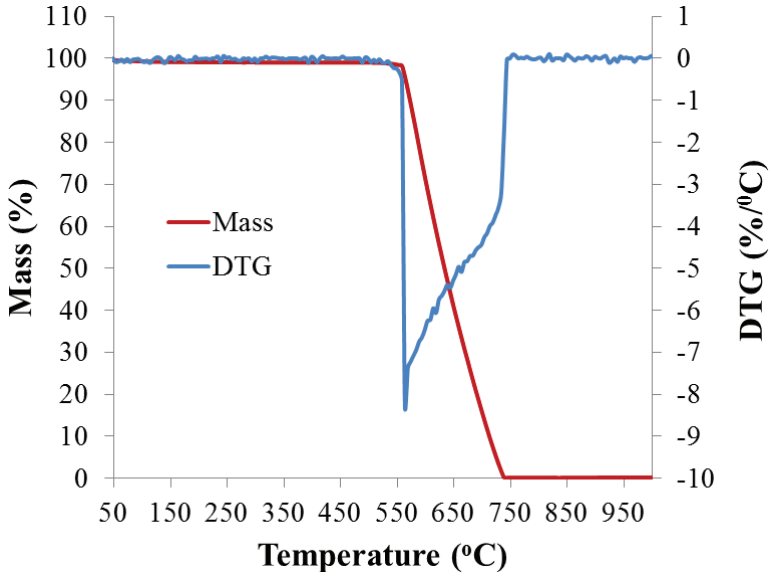

Figure 7. Hydrophobicity. (**a**) Drop of water suspended in the foam surface; (**b**) A drop of oil gets readily absorbed within the foam structure, showing no evidence of oil on the surface, as it is absorbed immediately.

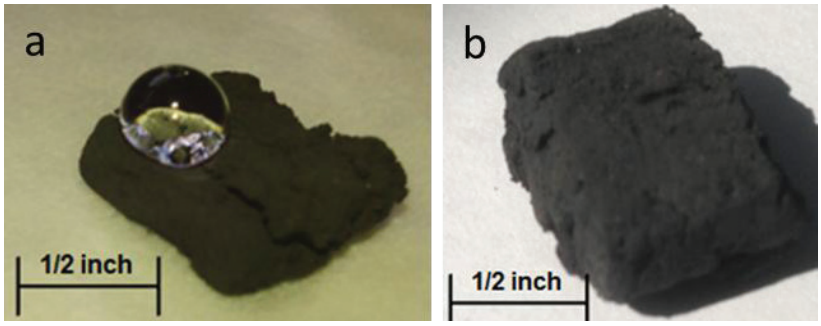

The primary results are briefly summarized as follows. First, mechanically stable samples of CFF clearly behave as viscoelastic material as shown by the fact that after appropriate conditioning, a repeatable hysteresis loop is observed in the stress-strain relationship. Second, there is a linear relationship between electrical resistance and strain that becomes remarkably stable after only a few cycles. The strain range over which this linear relationship is observed is very large, up to 60%. Third, relative to carbon in another form, Grafoil, CFF showed far more regularity with regard to stress/strain and resistance. Fourth, the rest of the characteristics of the sample; light-weight, high surface area, hydrophobicity, conductivity, and possible energy absorption open the opportunity for using it in multiple applications.

2.2. Discussion

The discovery in succession over the last two decades of carbon fullerenes, carbon nanotubes [37] and the special properties of graphene [38], dramatically increased the interest in possible applications of carbon nanostructures, both on the basis of electrical and mechanical properties. For example, carbon nanotubes are under consideration for use in "molecular scale" logic circuits. That is, carbon nanotubes are seriously considered as the active elements for logic circuits, possibly replacing silicon [39–41]. There is also an enormous effort focused on using nanotubes to strengthen composite materials [42–44]. Currently there is widespread interest in employing graphene in supercapacitors due to its high surface area [32,45]. Graphene is also believed to have great potential as a component in corrosion resistant paint, light-strong plastics for cars, sports equipment, aerospace and military applications [46–48].

The present work suggests that another novel carbon material, carbon fiber foam (CFF), also has unique electrical and mechanical properties, which may lead to widespread applications. In particular, the present work provided a variety of data that help define the properties of this material, a proof of concept in evaluation of potential applications. First, application requires repeatability. We were able to duplicate the generation of the material, previously only generated in a single lab [49], and were also able to better define the optimal production conditions. Second, the results suggest this material can be used in place of the current generation of viscoelastic materials. Indeed, after a few cycles (*ca.* 15) the material becomes a viscoelastic with stable mechanical properties. Moreover, it is clearly unusual among viscoelastic materials in that it has high electrical and thermal conductivity, as well as stability at high temperatures. Third, we were able to show that the material has potential for use as the sensing material in a strain sensor since it presents a linear relationship between resistance and strain. However, the gauge factor value is small (0.43) and efforts to increase it should be considered in future work. These applications are discussed in more detail below.

The material has several advantages for possible use as viscoelastic foam. One drawback to the current generation of polymeric foams is the difficulty of temperature control. For these applications relatively complex composite material foams are now employed to create a pathway for thermal conductivity. Given the far higher electrical and thermal conductivity of CFF relative to polymer-based foams, it should be relatively easy to modify its temperature. For example, the foams can be heated electrically, or temperature maintained simply by contacting the material over only a fraction of the surface area with a heat sink maintained at a constant temperature. Moreover, the range of temperatures at which carbon foams are stable is likely to be far greater than that observed for polymer based viscoelastics, although more study is required to quantify the temperature range at which CFF remain stable while retaining its mechanical properties.

The results of this work indicate that the distinct electrical conductivity of CFF will make it an excellent sensing material in a strain gauge. The key feature of a stain gauge is the availability of a single value electrical signal as a function of strain, a value that reports strain as a "state property", and is not a function of the history of stress/strain of the material. As shown in Figure 5, the relationship between strain and measured resistance of CFF in simple single axis compression remains linear over many cycles. Resistance is shown to have a single value, within ~2 percent, as a function of strain. Moreover, a linear relationship is observed up to 40% strain, probably because of

the large void space fraction (~90%) present in the uncompressed material. That is, as the material is compressed the "void" is squeezed out before the solid fibers are deformed by fiber-to-fiber compression. Thus, resistance can serve as the single value electrical signal required to determine strain over an exceptional range of strain.

Our work shows the CFF performs in a linear fashion at least to a 40% strain. Other carbon-based materials have also been evaluated for use in strain gauges, and these do have relatively high gauge factors, on the order of 20. However, CFF in contrast to carbon tubes and fibers need no binders, polymeric matrices or linking additives to form 3D structures of selected shape. Evaluation of the potential use of CFF in multi-axis strain gauges would be appropriate for future studies.

One outcome of this work is the finding that, contrary to an earlier suggestion [49] this material cannot be employed as a pressure gauge. There is a hysteresis clearly observed in the stress-strain curve. This indicates that energy of mechanical deformation observed during the compression leg of a cycle relaxes during the decompression leg and is dissipated as heat.

The hysteresis in stress/strain, but not in stress/resistance provides some insight into the behavior on the microscale. In earlier work it was postulated that resistance changed as a function of strain because the number of contacts between fibers increased with increasing strain, and this would lead to more electrical paths, hence lower resistance. The present work suggests this may not be correct. Indeed, it is generally understood that mechanical relaxation is associated with physical re-arrangement. In the case of fiber foam, that implies that the individual fibers change shape to reduce their mechanical potential energy during relaxation. Certainly this relaxation of many fibers would change the number of fiber-fiber junctions, thus changing resistance. Hence, a change in resistance that matched the magnitude of the change in stress might be expected during transient experiments. This is not observed. Their resistance change, relatively, is much smaller than the stress relaxation. An alternative suggests itself: The conductivity of the individual fibers is changed by strain. That is, there is a relationship between fiber strain and fiber resistance. Specifically, the resistance of each individual fiber decreases as the fiber is shortened. Integrated over a large ensemble of fibers, of many orientations, geometries and sizes, such as that found in a CFF, this leads, on a macroscopic level, to a linear relationship between strain and resistance.

The above suggestion of a relationship between strain and the resistance of individual fibers is in fact consistent with the theory of conductor type strain gauges. Indeed, it is generally understood that single "wires" change resistance because of shape changes, during strain. Broader and shorter wires have lower resistance. In fact, this is the basic physical fact exploited in the design of most strain gauges. Hence, it is a reasonable extension of current understanding of the impact of strain on metal resistance, to apply the same logic to carbon fiber resistance. Moreover, all findings in this work are consistent with this postulate. Finally, there are studies that show the resistances of individual carbon fibers are a function of strain [12]. It is noted this is a reasonable topic for future study.

3. Experimental Section

3.1. Fiber Growth

The growth process employed was a variation on the CoFFiN process described elsewhere in which catalyst is arranged in a steel mold and then exposed to a fuel rich mixture of ethylene and oxygen at 550 °C. Previous studies by our team showed that when comparing to other metal catalysts, the most robust fiber structure, grown as a single macroscopic object containing high levels of porosity, are generated from palladium particle catalysts [26]. Thus, in the present work a simple four-step process was followed. First, 20 mg of palladium (Aldrich submicron >99.9%) particles were spread evenly in three equally spaced, 5.72 cm long columns in the bottom of a 304 Stainless Steel mold of dimensions 5.72 cm long × 2.5 cm wide × 0.89 cm height (Figure 8a). This mold chamber was connected to gas flow system (0.64 cm OD stainless steel tubing) capable of simultaneous control of the four gases using an MKS 647a flow controller. The mold chamber itself was positioned at the center of a 45.72 cm long × 5.08 cm diameter single zone Lindberg/Blue Mini-Mite furnace tube furnace with a maximum temperature capability of 1200 °C. Second, the mold/catalyst was thoroughly flushed with UHP Nitrogen. Third, the temperature was raised (25 °C/min) to 550 °C, and the reactive gas mixture, composed of ethylene, oxygen and nitrogen diluent, introduced. As earlier work showed that gas residence time and composition strongly impacted the growth rate, the flow rates were carefully adjusted to be ethylene 15 SCCM/oxygen 15 SCCM and nitrogen 100 SCCM. Finally, after two hours and forty five minutes ethylene, oxygen and the furnace were turned off, and the system allowed to cool. The single block of CFF (Figure 8b) was then removed from the mold, and cut into smaller pieces for mechanical/electrical testing, observation using SEM or thermal testing in a TGA/DSC.

Figure 8. Steel mold and catalyst geometry. Arranging Pd catalyst particles in the mold as shown (**a**), was found to be a necessary part of the protocol required to create, based on visual inspection, homogenous CFF (**b**).

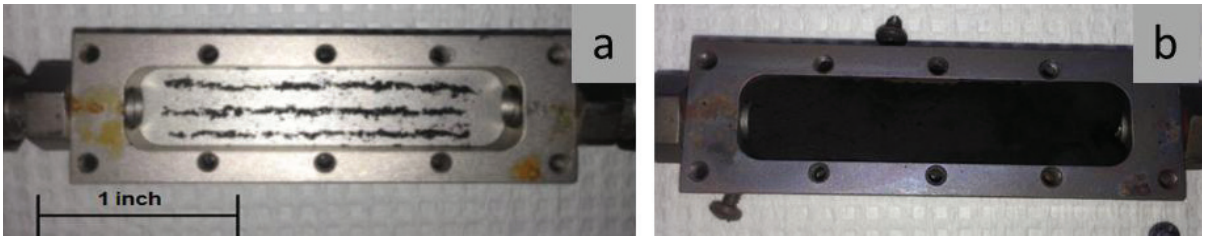

3.2. Samples Characterization

In order to examine the microstructure of the carbonaceous specimens the samples were attached to a standard aluminum holder using carbon tape, placed in vacuum overnight and introduced in the chamber of a Zeiss Neon 40 High Resolution Scanning Electron Microscope (SEM) (Zeiss, Oberkochen, Germany). Images were acquired at diverse magnifications while microscope was operated at 10 or 20 kV. Energy Dispersive Spectroscopy (EDS) experiments were conducted

in conjunction with the SEM using the EDAX equipment with an Apollo 10 silicon drift detector (SDD). Data was collected and analyzed using Genesis Spectrum software.

A MTI Instruments MTII/Fullam SEM tester (MTI Instruments, Albany, New York, NY, USA), with a maximum load capability of 4500 N was used to apply diverse compressive loads to the samples inside the SEM chamber and observe microstructural changes *in situ*.

A Netzsch STA 449 FE Jupiter (Netzsch, Gerätebau, Germany), operated in a TPO mode, was used to study the thermal stability of the samples. The samples were exposed to an Ar/O_2, 80%/20% atmosphere, total flow of 120 mL/min, from RT to 1000 °C at a heating rate of 10 °C/min.

Brunauer Emmet Teller (BET) surface area analysis was performed employing a Quantachrome Nova 4200 (Quantachrome, Boynton Beach, FL, USA). A 300 °C degas step was conducted prior to the analysis; samples were then allowed to cool down to room temperature and then transferred to the analysis station. The measurements were done using nitrogen atmosphere.

The relative density of the product was calculated as the ratio of the mass of a portion of the sample with respect of its volume. The volume of the material was measured using a graduated cylinder filled with DI water, immersing the sample on it and determining the volume of water displaced.

The contact angle of a water droplet in the surface of the as prepared solid was measured from images taken with the CCD camera of a digital microscope. The water was dispensed using a micro-syringe and the contact angle evaluated by fitting the drop profile according to the Young-Laplace method using the software Image J for image processing [50]. Mineral oil, Pfeiffer D-35614 Asslar Oil P3 (Pfeiffer, Asslar, Germany), was used to observe the fiber structure interaction with a non-polar substance.

3.3. Mechanical and Electrical Testing

In order to mechanically characterize the carbon fiber samples, several different test conditions were employed: dynamic; with variable loads changing at different rates over time, and transient; with static loads maintained as a function of time. To ensure that the samples only changed dimensions in the direction of applied force and that their top and bottom maintained a constant area during resistivity measurements, the highly porous samples were cut to cylindrical shapes. Those cylindrical shapes were made to match the size and shape of two 13 mm stainless steel anvils that served as platens to compress the sample and as electrical contacts. A Plexiglas mold with a cavity of 1.3 cm diameter was used to maintain the sample cylinder and anvils aligned during tests (Figure 9). The anvils closely fit the mold gap without touching the Plexiglas, therefore creating no friction against it. There was no space for the carbon sample to expand in the lateral direction during compression; hence, tests in this configuration were denominated as constrained.

Figure 9. Anvils and sample placement for simultaneous mechanical and electrical tests. Sections of the carbon fiber based material were cut to the same diameter than the anvils, placed inside a Plexiglas cavity to avoid changes in cross sectional area during measurements.

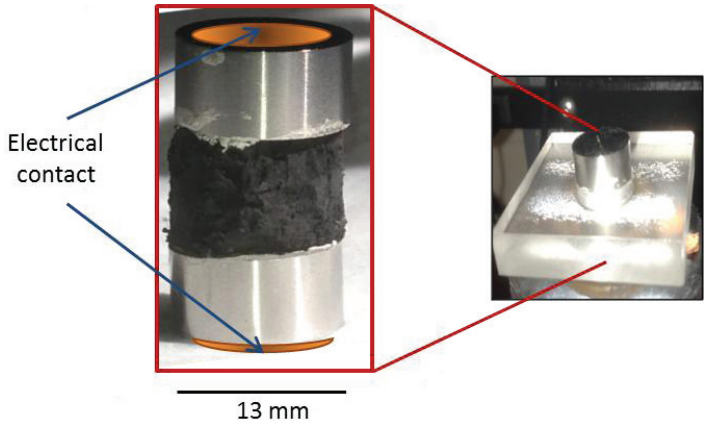

An Instron 5942 with a 100 N load cell (Instron, Norwood, MA, USA), configured to study the material in compression, was employed for all macroscopic tests. The compressive force was selected to remain between 10 and 90 N. The lower limit was selected in order to prevent the carbon nano-fiber from losing contact with the anvil while the upper limit was chosen to prevent reaching the 100 N automatic cutout limit on the load cell used in the test.

The system was organized to allow simultaneous measure of the electrical, specifically resistance, and mechanical properties. This required creating an electrical connection, using copper tape, to each anvil. As control studies showed zero resistance when the anvils touched, the resistance measured was simply that of the CFF between them. The resistance was measured using an Agilent 34410A 6 ½ Digital Multimeter (Agilent, Santa Clara, CA, USA) with software that permitted direct connected to a PC computer and data download directly to a spreadsheet.

Transient tests were performed at diverse levels of constant stress and the change in strain as a function of time recorded. For simplicity only the results for samples held at 90 Newton over 72 h were included in this manuscript. Cyclic tests, generally known as dynamic tests, were performed by linear change in strain as a function of time between two stress limits. Two strain rates were employed: 0.01 and 0.05 mm/s. Load limits for the cycles were within one of the following values: 10 to 40, 40 to 90, or 10 to 90 N.

4. Conclusions

Carbon fiber foams (CFF) were grown using the Constrained Formation of Fibrous Nanostructures process (CoFFin). The outcome of the growth process suggests these foams can be grown to any desired shape in a mold. For the first time the viscoelastic properties of the foam were demonstrated. Moreover, microscopic evaluation showed the foams to have a distinct microstructure, intertwined nano-fibers, for a viscoelastic material. As with many other recently discovered carbon structures, this foam has distinctive properties that imply improved performance for various uses. The high conductivity, low specific gravity, high temperature stability and hydrophobicity also suggest this material would be superior to existing closed cell viscoelastics for many applications: shock absorber

foam, sensing element, electrode material, filter or absorbent membrane, and low drag surface, among others.

Acknowledgments

This work was supported by Research Initiation Program of the Naval Postgraduate School and with funds from the Office of Naval Research, Force Protection Thrust, ONR Code 30.

Author Contributions

This work is largely based on the Engineer Degree thesis of LCDR Chris Daskam, US Navy. He was closely supervised and aided in all aspects of the work by his advisors, Claudia Luhrs and Jonathan Phillips. Edwin Gonzalez, a Hartnell College intern at NPS, helped in many aspects of the laboratory work, particularly synthesis and mechanical data collection. Luhrs and Phillips collaborated writing the manuscript.

Conflicts of Interest

The authors declare no conflict of interest.

References

1. Yang, L.; Anantram, M.; Han, J.; Lu, J. Band-gap change of carbon nanotubes: Effect of small uniaxial and torsional strain. *Phys. Rev. B* **1999**, *60*, 13874–13878.
2. Yang, L.; Han, J. Electronic structure of deformed carbon nanotubes. *Phys. Rev. Lett.* **2000**, *85*, 154–157.
3. Minot, E.; Yaish, Y.; Sazonova, V.; Park, J.; Brink, M.; McEuen, P. Tuning carbon nanotube band gaps with strain. *Phys. Rev. Lett.* **2003**, *90*, 156401:1–156401:4.
4. Cao, J.; Wang, Q.; Dai, H. Electromechanical properties of metallic, quasimetallic, and semiconducting carbon nanotubes under stretching. *Phys. Rev. Lett.* **2003**, *90*, 157601:1–157601:4.
5. Grow, R.; Wang, Q.; Cao, J.; Wang, D.; Dai, H. Piezoresistance of carbon nanotubes on deformable thin-film membranes. *Appl. Phys. Lett.* **2005**, *86*, 093104:1–093104:3.
6. Hu, N.; Karube, Y.; Arai, M.; Watanabe, T.; Yan, C.; Li, Y.; Liu, Y.; Fukunaga, H. Investigation on sensitivity of a polymer/carbon nanotube composite strain sensor. *Carbon* **2010**, *48*, 680–687.
7. Hwang, J.; Jang, J.; Hong, K.; Kim, K.N.; Han, J.H.; Shin, K.; Park, C.E. Poly(3-hexylthiophene) wrapped carbon nanotube/poly(dimethylsiloxane) composites for use in finger-sensing piezoresistive pressure sensors. *Carbon* **2011**, *49*, 106–110.
8. Choi, E.; Jeong, M.; Choi, K.W.; Lim, C.; Lee, S. Flexible and Transparent Touch Sensor Using Single-Wall Carbon Nanotube Thin-Films. In Proceedings of the 3rd International Nanoelectronics Conference (INEC), Hong Kong, China, 3–8 January 2010.
9. Zhang, J.; Liu, J.; Zhuang, R.; Maeder, E.; Heinrich, G.; Gao, S. Single MWNT-Glass Fiber as Strain Sensor and Switch. *Adv. Mater.* **2011**, *23*, 3392–3397.

10. Dau, V.T.; Yamada, T.; Dao, D.V.; Tung, B.T.; Hata, K.; Sugiyama, S. Integrated CNTs thin film for MEMS mechanical sensors. *Microelectron. J.* **2010**, *41*, 860–864.
11. Knite, M.; Teteris, V.; Kiploka, A.; Kaupuzs, J. Polyisoprene-carbon black nanocomposites as tensile strain and pressure sensor materials. *Sens. Actuators A Phys.* **2004**, *110*, 142–149.
12. Karimov, K.S.; Saleem, M.; Karieva, Z.M.; Khan, A.; Qasuria, T.A.; Mateen, A. A carbon nanotube-based pressure sensor. *Phys. Scr.* **2011**, *83*, 065703:1–065703:6.
13. Su, C.; Li, C.; Chang, N.; Gao, F.; Chang, S. Fabrication of High Sensitivity Carbon Microcoil Pressure Sensors. *Sensors* **2012**, *12*, 10034–10041.
14. Rao, C.; Sen, R.; Satishkumar, B.; Govindaraj, A. Large aligned-nanotube bundles from ferrocene pyrolysis. *Chem. Commun.* **1998**, *15*, 1525–1526.
15. Dai, L.; Patil, A.; Gong, X.; Guo, Z.; Liu, L.; Liu, Y.; Zhu, D. Aligned nanotubes. *ChemPhysChem* **2003**, *4*, 1150–1169.
16. Franklin, N.; Dai, H. An enhanced CVD approach to extensive nanotube networks with directionality. *Adv. Mater.* **2000**, *12*, 890–894.
17. Chakrapani, N.; Wei, B.; Carrillo, A.; Ajayan, P.; Kane, R. Capillarity-driven assembly of two-dimensional cellular carbon nanotube foams. *Proc. Natl. Acad. Sci. USA* **2004**, *101*, 4009–4012.
18. Futaba, D.N.; Hata, K.; Yamada, T.; Hiraoka, T.; Hayamizu, Y.; Kakudate, Y.; Tanaike, O.; Hatori, H.; Yumura, M.; Iijima, S. Shape-engineerable and highly densely packed single-walled carbon nanotubes and their application as super-capacitor electrodes. *Nat. Mater.* **2006**, *5*, 987–994.
19. Kumar, A.; Pushparaj, V.L.; Kar, S.; Nalamasu, O.; Ajayan, P.M.; Baskaran, R. Contact transfer of aligned carbon nanotube arrays onto conducting substrates. *Appl. Phys. Lett.* **2006**, *89*, doi:10.1063/1.2356899.
20. Kaur, S.; Ajayan, P.M.; Kane, R.S. Design and characterization of three-dimensional carbon nanotube foams. *J. Phys. Chem. B* **2006**, *110*, 21377–21380.
21. Khalid, W.; Ali, M.S.M.; Dahmardeh, M.; Choi, Y.; Yaghoobi, P.; Nojeh, A.; Takahata, K. High-aspect-ratio, free-form patterning of carbon nanotube forests using micro-electro-discharge machining. *Diam. Relat. Mater.* **2010**, *19*, 1405–1410.
22. Lalwani, G.; Kwaczala, A.T.; Kanakia, S.; Patel, S.C.; Judex, S.; Sitharaman, B. Fabrication and characterization of three-dimensional macroscopic all-carbon scaffolds. *Carbon* **2013**, *53*, 90–100.
23. Hung, W.H.; Kumar, R.; Bushmaker, A.; Cronin, S.B.; Bronikowski, M.J. Rapid prototyping of three-dimensional microstructures from multiwalled carbon nanotubes. *Appl. Phys. Lett.* **2007**, *91*, 093121:1–093121:3.
24. Atwater, M.A.; Mousavi, A.K.; Leseman, Z.C.; Phillips, J. Direct synthesis and characterization of a nonwoven structure comprised of carbon nanofibers. *Carbon* **2013**, *57*, 363–370.
25. Phillips, J.; Shiina, T.; Nemer, M.; Lester, K. Graphitic structures by design. *Langmuir* **2006**, *22*, 9694–9703.
26. Atwater, M.A.; Phillips, J.; Doorn, S.K.; Luhrs, C.C.; Fernandez, Y.; Menendez, J.A.; Leseman, Z.C. The production of carbon nanofibers and thin films on palladium catalysts from ethylene-oxygen mixtures. *Carbon* **2009**, *47*, 2269–2280.

27. Forsythe, W.E. *Smithsonian Physical Tables (9th Revised Edition). Knovel. Table 282. Density of Various Solids*; Smithsonian Institution: Washington, DC, USA, 1954.
28. Shiomi, M.; Tanino, Y. Molding of Aluminum Foams by Using Hot Powder Extrusion. *Metals* **2012**, *2*, 136–142.
29. Lambert, T.N.; Luhrs, C.C.; Chavez, C.A.; Wakeland, S.; Brumbach, M.T.; Alam, T.M. Graphite oxide as a precursor for the synthesis of disordered graphenes using the aerosol-through-plasma method. *Carbon* **2010**, *48*, 4081–4089.
30. Wakeland, S.; Martinez, R.; Grey, J.K.; Luhrs, C.C. Production of graphene from graphite oxide using urea as expansion-reduction agent. *Carbon* **2010**, *48*, 3463–3470.
31. Schedin, F.; Geim, A.K.; Morozov, S.V.; Hill, E.W.; Blake, P.; Katsnelson, M.I.; Novoselov, K.S. Detection of individual gas molecules adsorbed on graphene. *Nat. Mater.* **2007**, *6*, 652–655.
32. Stoller, M.D.; Park, S.; Zhu, Y.; Ruoff, R.S. Graphene-Based Ultracapacitors. *Nano Lett.* **2008**, *8*, 3498–3502.
33. Rao, C.N.R.; Sood, A.K.; Subrahmanyam, K.S.; Govindaraj, A. Graphene: The New Two-Dimensional Nanomaterial. *Angew. Chem. Int. Ed.* **2009**, *48*, 7752–7777.
34. Cuq, B.; Gontard, N.; Cuq, J.; Guilbert, S. Rheological model for the mechanical properties of myofibrillar protein-based films. *J. Agric. Food Chem.* **1996**, *44*, 1116–1122.
35. Stanley, D.; Aguilera, J.; Baker, K.; Jackman, R. *Structure/Property Relationships of Foods as Affected by Processing and Storage*; Marcel Dekker: New York, NY, USA, 1998.
36. Ayres, E.; Vasconcelos, W.L.; Oréfice, R.L. Attachment of inorganic moieties onto aliphatic polyurethanes. *Mater. Res.* **2007**, *10*, 119–125.
37. Dresselhaus, M.S. *Science of Fullerenes and Carbon Nanotubes*; Dresselhaus, M.S., Dresselhaus, G., Eklund, P.C., Eds.; Elsevier: San Diego, CA, USA, 1996.
38. Geim, A.K.; Novoselov, K.S. The rise of graphene. *Nat. Mater.* **2007**, *6*, 183–191.
39. Rueckes, T.; Kim, K.; Joselevich, E.; Tseng, G.; Cheung, C.; Lieber, C. Carbon nanotube-based nonvolatile random access memory for molecular computing. *Science* **2000**, *289*, 94–97.
40. Chen, Z.; Appenzeller, J.; Lin, Y.; Sippel-Oakley, J.; Rinzler, A.; Tang, J.; Wind, S.; Solomon, P.; Avouris, P. An integrated logic circuit assembled on a single carbon nanotube. *Science* **2006**, *311*, 1735–1735.
41. Ding, L.; Zhang, Z.; Liang, S.; Pei, T.; Wang, S.; Li, Y.; Zhou, W.; Liu, J.; Peng, L. CMOS-based carbon nanotube pass-transistor logic integrated circuits. *Nat. Commun.* **2012**, *3*, doi:10.1038/ncomms1682.
42. Song, K.; Zhang, Y.; Meng, J.; Green, E.C.; Tajaddod, N.; Li, H.; Minus, M.L. Structural Polymer-Based Carbon Nanotube Composite Fibers: Understanding the Processing-Structure-Performance Relationship. *Materials* **2013**, *6*, 2543–2577.
43. Kroustalli, A.; Zisimopoulou, A.E.; Koch, S.; Rongen, L.; Deligianni, D.; Diamantouros, S.; Athanassiou, G.; Kokozidou, M.; Mavrilas, D.; Jockenhoevel, S. Carbon nanotubes reinforced chitosan films: Mechanical properties and cell response of a novel biomaterial for cardiovascular tissue engineering. *J. Mater. Sci. Mater. Med.* **2013**, *24*, 2889–2896.
44. Kwon, H.; Leparoux, M. Hot extruded carbon nanotube reinforced aluminum matrix composite materials. *Nanotechnology* **2012**, *23*, 415701:1–415701:41.

45. Wang, Y.; Shi, Z.; Huang, Y.; Ma, Y.; Wang, C.; Chen, M.; Chen, Y. Supercapacitor Devices Based on Graphene Materials. *J. Phys. Chem. C* **2009**, *113*, 13103–13107.
46. Stankovich, S.; Dikin, D.A.; Dommett, G.H.B.; Kohlhaas, K.M.; Zimney, E.J.; Stach, E.A.; Piner, R.D.; Nguyen, S.T.; Ruoff, R.S. Graphene-based composite materials. *Nature* **2006**, *442*, 282–286.
47. Novoselov, K.S.; Fal'ko, V.I.; Colombo, L.; Gellert, P.R.; Schwab, M.G.; Kim, K. A roadmap for graphene. *Nature* **2012**, *490*, 192–200.
48. Wang, H.; Maiyalagan, T.; Wang, X. Review on Recent Progress in Nitrogen-Doped Graphene: Synthesis, Characterization, and Its Potential Applications. *ACS Catal.* **2012**, *2*, 781–794.
49. Atwater, M.A.; Phillips, J.; Leseman, Z.C. The effect of powder sintering on the palladium-catalyzed formation of carbon nanofibers from ethylene-oxygen mixtures. *Carbon* **2010**, *48*, 1932–1938.
50. Image J Homepage. U.S. National Institutes of Health, Bethesda, Maryland, USA, 1997–2012. Available online: http://rsb.info.nih.gov/ij/ (accessed on 7 May 2014).

Titania Nanotubes Grown on Carbon Fibers for Photocatalytic Decomposition of Gas-Phase Aromatic Pollutants

Wan-Kuen Jo, Joon Yeob Lee and Ho-Hwan Chun

Abstract: This study aimed to prepare titania (TiO_2) nanotube (TNT) arrays grown on un-activated carbon fibers (UCFs), with the application of different TiO_2 loadings based on the coating-hydrothermal process, and to evaluate their photocatalytic activity for the degradation of sub-ppm levels of aromatic pollutants (benzene, toluene, ethyl benzene, and o-xylene (BTEX)) using a plug-flow photocatalytic reactor. The characteristics of the prepared photocatalysts were determined by scanning electron microscopy (SEM), energy-dispersive X-ray (EDX), transmission electron microscopy (TEM), UV-visible absorption spectroscopy (UV-Vis) and X-ray diffraction (XRD) analyses. Spectral analysis showed that the prepared photocatalysts were closely associated with the characteristics of one-dimensional nanostructured TiO_2 nanotubes for TNTUCFs and spherical shapes for TiO_2-coated UCF (TUCF). The photocatalytic activities of BTEX obtained from TNTUCFs were higher than those obtained from a reference photocatalyst, TUCF). Specifically, the average degradation efficiencies of BTEX observed for TNTUCF-10 were 81%, 97%, 99%, and 99%, respectively, while those observed for TUCF were 14%, 42%, 52%, and 79%, respectively. Moreover, the photocatalytic activities obtained for TNTUCFs suggested that the degradation efficiencies of BTEX varied with changes in TiO_2 loadings, allowing for the optimization of TiO_2 loading. Another important finding was that input concentrations and air flow rates could be important parameters for the treatment of BTEX, which should be considered for the optimization of TNTUCFs application. Taken together, TNTUCFs can be applied to effectively degrade sub-ppm levels of gas-phase aromatic pollutants through the optimization of operational conditions.

Reprinted from *Materials*. Cite as: Jo, W.-K.; Lee, J.Y.; Chun, H.-H. Titania Nanotubes Grown on Carbon Fibers for Photocatalytic Decomposition of Gas-Phase Aromatic Pollutants. *Materials* **2014**, *7*, 1801ï 1813.

1. Introduction

Specific structural designs of titania (TiO_2) photocatalysts can be applied to enhance TiO_2 oxidation activity for the treatment of a number of environmental pollutants [1]. Especially, one-dimensional structured TiO_2 nanotube (TNT) arrays have unique charge-transport natures, large adsorption capacities, and multiple pathways for the enhanced diffusion of molecules [1–3]. The free movement of charge carriers over the length of TNTs can reduce the recombination rates of photo-induced electron and hole pairs when compared to TiO_2 particles [3,4]. TNTs also contain large amounts of hydroxyl functional groups on the interlayer region of their walls, which are likely responsible for the reduced charge recombination rates [5]. In addition, TNTs are known to possess large surface areas and multiple channels for adsorption, resulting in a high adsorption capacity and improved photocatalytic performance [2]. These characteristics of one-dimensional TNTs have led to

their applications to a number of environmental pollutant treatments. Several studies [4–6] have found that the photocatalytic performance of TNTs was superior to that of anatase phase TiO_2 particles for the photocatalytic decomposition of a range of environmental pollutants such as aqueous phenols, methyl orange, and gaseous acetone.

Application of nanomaterials, including one-dimensional nanostructured TNTs and TiO_2 nanoparticles, for air pollutant treatments requires their combination with a supporting substrate in order to minimize their escapes from photocatalytic reactors with cleaned air. Popular supporting substrates of nano-sized photocatalysts which have been applied to air purification include granular activated carbon [7], activated carbon fiber [8], glass materials [9], polymer materials [10], and un-activated carbon fiber [11,12]. Special attention has been given to un-activated carbon fibers (UCFs) as photocatalyst supporting materials because of their unique properties, such as temperature and corrosion resistance, and high strength and flexibility [12]. The combination of TiO_2 with carbon materials can also retard the recombination rates of photo-generated electron and positive hole pairs, thereby enhancing photocatalytic activity [13]. In addition, UCFs are quite robust, and hence, are resistant to degradation throughout photocatalysis, whereas some other polymers or cotton textiles are less durable [11,14]. Nevertheless, to date, only limited studies of the application of TiO_2 combined with UCFs have been carried out [11,12]. Moreover, the aforementioned studies investigated the photocatalytic activity of TNT or TiO_2 nanosheet arrays grown on UCFs based on the degradation of aqueous-phase dyes such as methyl orange and rhodamine B. The photon absorbance mechanisms and heterogeneous photocatalytic kinetics of chemical species differ between the two different interfaces [15]. As such, there are still a number of relevant yet unanswered questions relating to the photocatalytic performance of TNTs grown on UCFs, and their applications to treatment of polluted air.

In this study, TNT arrays on UCFs (TNTUCFs) with different loadings of the TiO_2 source were prepared using a coating-hydrothermal process, and their photocatalytic activities were investigated for the decomposition of aromatic pollutants at indoor air concentration levels (sub-ppm). A TiO_2-coated UCF (TUCF) was also investigated as a reference photocatalyst for its surface characteristics and photocatalytic decomposition under the same photocatalytic conditions. The target chemicals were four aromatic volatile organic compounds (VOCs) (benzene, toluene, ethyl benzene, and o-xylene, (BTEX)), which were selected based on their prevalence in indoor air [16] and due to their representing both carcinogenic and non-carcinogenic health hazards [17,18].

2. Results and Discussion

2.1. Characteristics of Prepared Photocatalysts

TNTUCFs with different TiO_2 loadings, as well as a reference TUCF photocatalyst, were characterized by SEM, EDX, TEM, and XRD analyses. Figure 1 displays the SEM photographs of TNTUCF-5, TNTUCF-7.5, TNTUCF-10, TNTUCF-12.5, TNTUCF-15 and TUCF. The SEM images of TNTUCFs showed the TNT arrays grown on UCFs, of which the degree of cover was increased with increasing TiO_2 loading, whereas SEM images of TUCF exhibited TiO_2 nanoparticles coated onto UCFs. In addition, the TEM images of TNTUCF-10 revealed the nanotubular structure, whereas those for TUCF showed spherical shapes (Figure 2). Similarly, Fu *et al*. [19] reported that an

N-TiO_2 structure prepared using a solid-state reaction method with NH_4Cl as the nitrogen source revealed a tubular structure in its TEM image. For the present study, the length and outer diameter of the TNTUCF-10 were *ca.* 20–110 nm and *ca.* 6–11 nm, respectively. Consequently, these results demonstrated that the hydrothermal process used in this study could be used to grow TNTs on the surface of the supporting substrate (UCF) to form TNTUCFs. In addition, Guo *et al*. [12] reported that TiO_2 nanosheet arrays could be successfully grown on UCFs via an alternative hydrothermal process.

The EDX spectra of the TNTUCFs displayed peaks of C, Ti, Pt, and O atoms with different peak intensities (Figure 3). The peaks of the Ti and O atoms were assigned to TiO_2, while the C atom peak was attributed to UCF. In addition, Pt atoms were considered to have originated from the Pt coating pretreatment of the TNTUCF samples prior to conducting SEM analysis. Similar to the TNTUCFs, the EDX spectra of the TUCF also revealed peaks of C, Ti, Pt, and O atoms, although their peak intensities differed.

Figure 1. Scanning electron microscopy (SEM) of titania nanotube arrays grown on un-activated carbon fibers (TNTUCFs) with different TiO_2 loadings (TNTUCF-5, TNTUCF-7.5, TNTUCF-10, TNTUCF-12.5, TNTUCF-15) and TiO_2-coated UCF (TUCF).

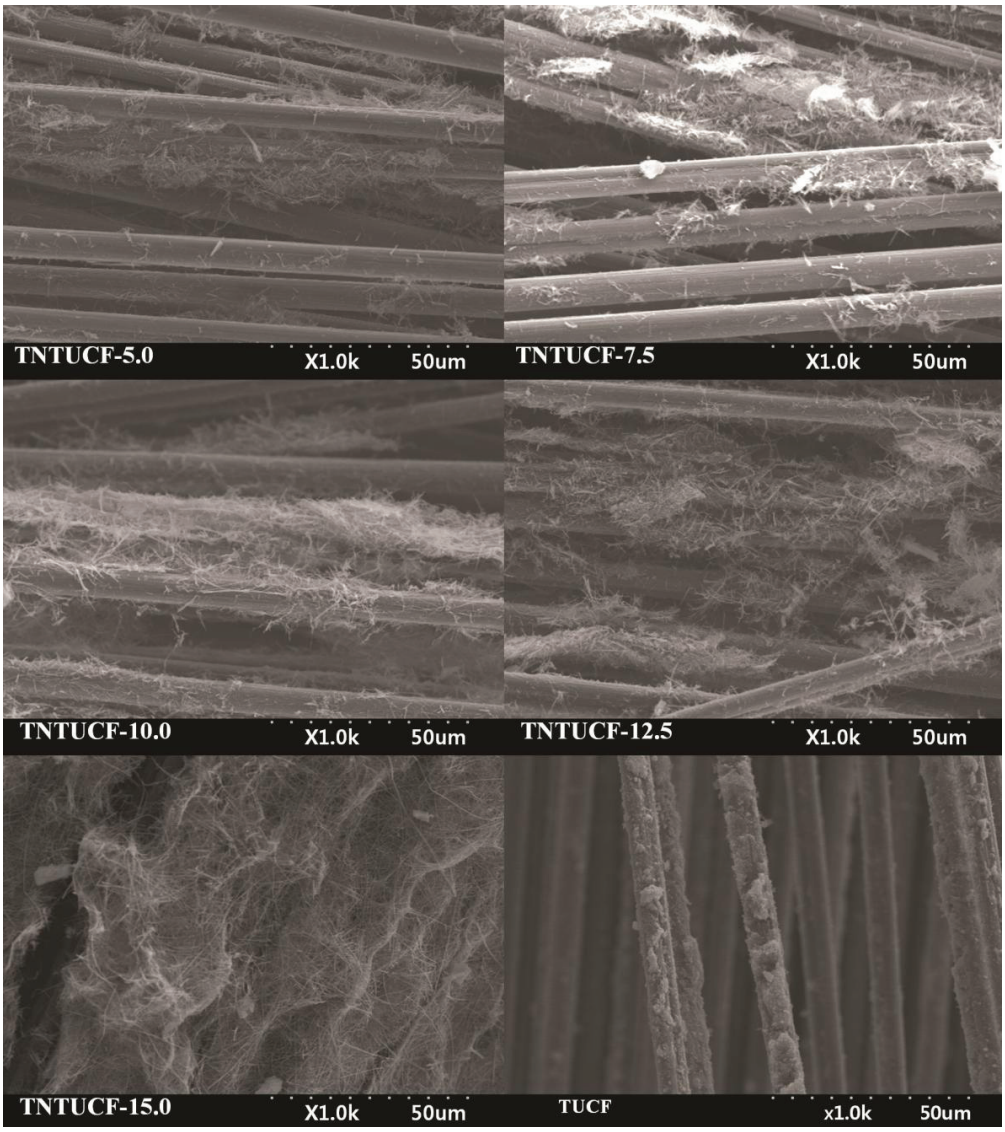

Figure 2. Transmission electron microscopy (TEM) of TNTUCF-10, and TUCF.

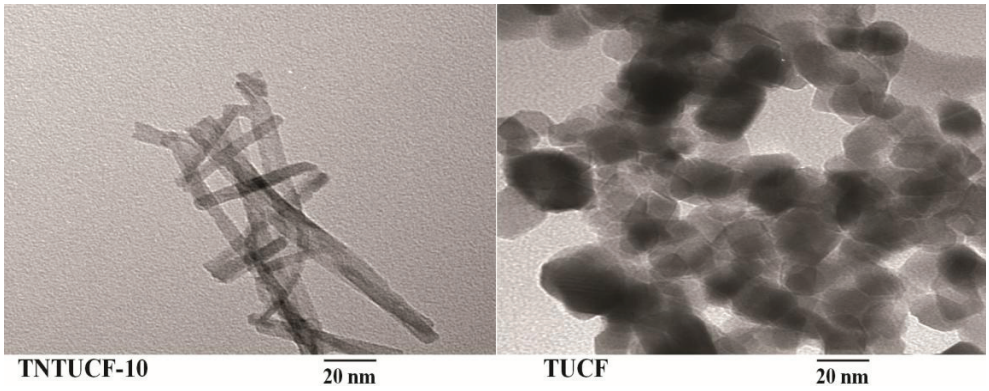

Figure 3. Energy-dispersive X-ray (EDX) of five TNTUCFs with different TiO_2 loadings (TNTUCF-5, TNTUCF-7.5, TNTUCF-10, TNTUCF-12.5, TNTUCF-15) and TUCF.

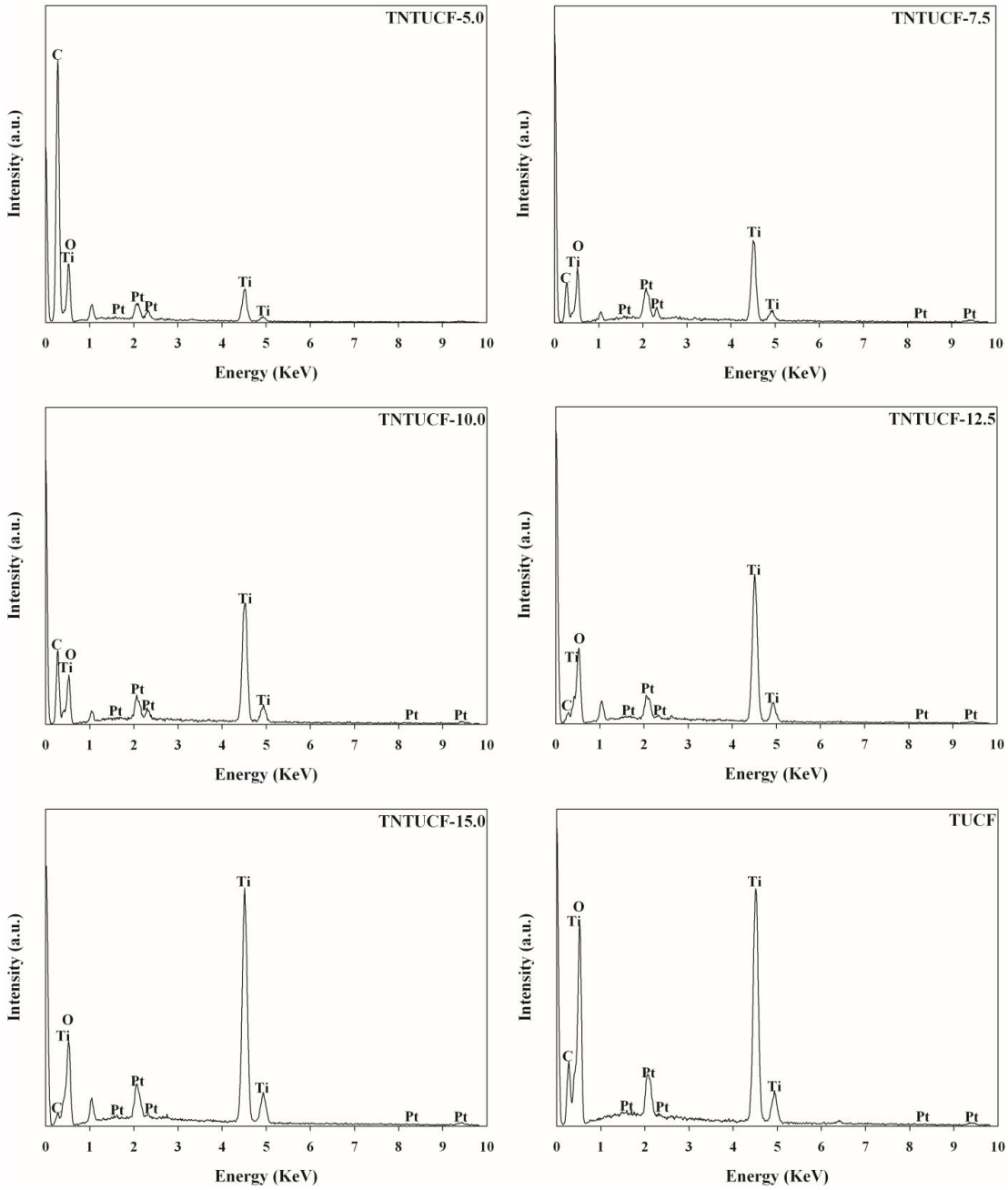

Figure 4 illustrates the XRD images of TNTUCF-10 and TUCF. Both photocatalysts showed a broad C peak at 2θ = 25.3° and a smaller C peak at 2θ = 43.3°. In addition, TNTUCF-10 revealed an anatase crystal phase with a peak at 2θ = 48.2°, while the typical anatase peak at 2θ = 25.3° was thought to be overlapped with the carbon peak of UCFs. These results were similar to those obtained by Chen *et al*. [11]. Accordingly, the prepared one-dimensional structured TNTs had the characteristics of TiO_2 crystals, which have photocatalytic activity for the degradation of environmental pollutants. In contrast, TUCF showed rutile crystal phases with two peaks at 2θ = 37.6° and 53.9°, while the typical anatase peak at 2θ = 25.3° and rutile peak at 2θ = 27.4° were thought to be overlapped with the carbon peak of UCFs. These results were ascribed to the uses of

Degussa P25 TiO_2 for the preparation of TUCF, which is composed of both rutile and anatase phases. Although the UV-Vis spectra of the prepared photocatalysts were not shown in this paper because of limited space, their band gap energies estimated using their UV-Vis absorption spectra were all close to 3.1 eV.

Figure 4. X-ray diffraction (XRD) patterns of a representative TNTUCF (TNTUCF-10) and TUCF.

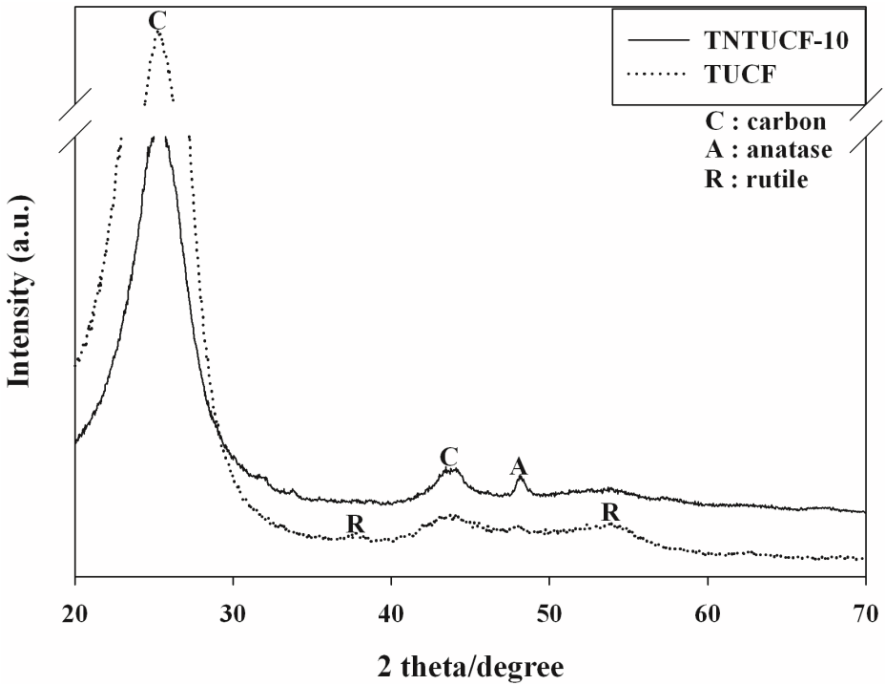

2.2. Photocatalytic Activity of As-Prepared Photocatalysts

The photocatalytic activity of four TNTUCFs, TUCF, and UCF were evaluated based on their ability to decompose four target compounds (BTEX). Figure 5 shows the time-series degradation efficiencies of BTEX observed via the as-prepared photocatalysts. All BTEX degradation efficiencies determined for the TNTUCFs were higher than those of TUCF and UCF, except for those of TNTUCF-15. Specifically, the average degradation efficiencies of BTEX for the TNTUCF-10 were 81%, 97%, 99% and 99%, respectively, while those for TUCF were 14%, 42%, 52% and 79%, respectively. Additionally, the BTEX removal efficiencies determined via the TNTUCF-10 were higher than those obtained via a prototype photocatalyst (P25 TiO_2), which were reported in Jo *et al*. [10]. Specifically, the aforementioned study reported that the average degradation efficiencies of BTEX determined for P25 TiO_2 under similar operational conditions were 28%, 38%, 51%, and 64%, respectively. The higher degradation efficiencies of TNTUCFs were attributed to synergistic effects between their large adsorption capacity and reduced recombination rates of photo-induced electron and hole pairs of one-dimensional nanostructured TNTs [1–3]. Moreover, the BTEX degradation efficiencies determined for the TNTUCFs increased as the TiO_2 loadings increased from 5% to 10%, but then decreased as the TiO_2 loadings increased further from 10% to 15%. Specifically, the average degradation efficiencies of BTEX for the TNTUCF-5 were 19%, 48%, 71%, and 81%, respectively, while those for TNTUCF-15 were 4%, 24%, 42%, and 47%,

respectively. These findings allowed for the optimization of TiO_2 loading during TNTUCFs preparation for BTEX degradation. For high TiO_2 loading conditions, TiO_2 nanoparticles might block some of carbon sites, lowering adsorption capacity of prepared photocatalysts. In a similar study, Chen *et al*. [11] reported that TNTUCF showed a higher photocatalytic efficiency for the degradation of aqueous rhodamine B when compared with pure UCF. In addition, Guo *et al*. [12] showed that TiO_2 nanosheets grown on carbon fibers had higher photocatalytic activities for aqueous methyl orange when compared with pure UCF. Meanwhile, a long-term study is suggested to examine the dependence of the activity of the prepared photocatalysts on application time.

The time-series degradation efficiencies of BTEX obtained via the representative TNTUCF-10 according to air flow rates (AFRs) are shown in Figure 6. The BTEX degradation efficiencies revealed a decreasing trend with increasing AFRs. Specifically, the average degradation efficiencies of BTEX decreased from 81% to 22%, 97% to 37%, 99% to 46%, and 99% to 51%, respectively, as the AFR increased from 1 to 4 $L \cdot min^{-1}$. Similarly, Yu and Brouwers [20] reported a descending trend in NO degradation efficiencies within an AFR range of 1–5 $L \cdot min^{-1}$. These results were attributed to the mass transfer of target compounds to the surface of the catalysts and the reaction kinetics of target compounds, which are two important factors of heterogeneous photocatalytic degradation [21,22].

The mass transfer rate of gas-phase pollutants in a plug-flow reactor is strongly associated with the face velocities of air [23]. Accordingly, the degradation efficiencies of BTEX might have increased as face velocities increased, if the increased mass transfer rate was likely a crucial factor for the photocatalytic degradation kinetics of BTEX. Conversely, for the present study, the degradation efficiencies of BTEX decreased as the face velocities increased. Specifically, the face velocities for AFRs of 1, 2, 3, and 4 $L \cdot min^{-1}$ corresponded to 2.1, 4.2, 6.3, and 8.4 $cm \cdot s^{-1}$, respectively, suggesting that the degradation efficiencies of BTEX obtained from TNTUCF-10 would have been somewhat limited by reaction kinetics on the photocatalyst surface. This suggestion was supported by the finding that the residence times of the target compounds in the plug-flow reactor, which were calculated by dividing the reactor volume by the AFRs, decreased as the AFR increased. Specifically, the residence times for the AFRs of 1, 2, 3 and 4 $L \cdot min^{-1}$ were 16.4, 12.3, 8.2 and 4.1 s, respectively. Consequently, the low degradation efficiencies of BTEX under high AFR conditions were likely due to low reaction rates on the catalyst surface because of insufficient reaction times in the plug-flow reactor.

Figure 5. Degradation efficiencies (DE) of (**a**) benzene; (**b**) toluene; (**c**) ethyl benzene; (**d**) o-xylene, as determined using TNTUCFs with different TiO_2 loadings (TNTUCF-5, TNTUCF-7.5, TNTUCF-10, TNTUCF-12.5, TNTUCF-15), TUCF, and UCF under UV light irradiation.

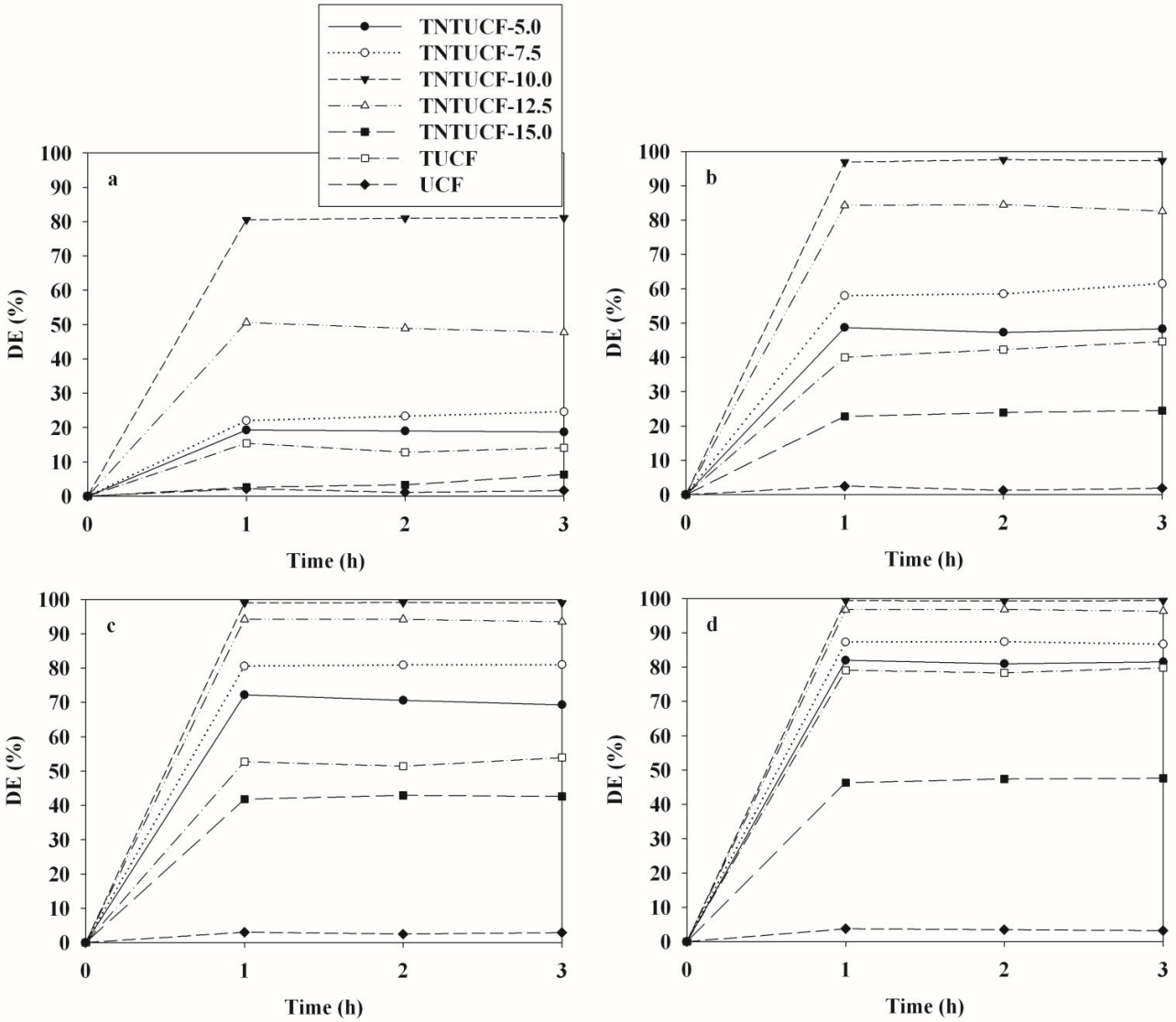

Figure 7 illustrates the time-series degradation efficiencies of BTEX determined via TNTUCF-10 according to input concentrations (ICs) within a range of typical indoor air concentrations. For the target compounds, the degradation efficiencies decreased as ICs increased. Specifically, at the lowest IC of 0.1 ppm the average degradation efficiencies of BTEX were 48%, 83%, 89% and 91%, respectively, whereas those for the highest IC of 0.9 ppm were 32%, 56%, 68% and 75%, respectively. Similarly, Devahasdin *et al*. [24] reported that the NO degradation efficiency determined using UV-activated TiO_2 decreased from 70% to 15% when IC increased from 5 to 60 ppm. Yu and Brouwers [20] also found that the degradation efficiency of NO determined using visible light-activated carbon-impregnated TiO_2 decreased from 61% to 16% when IC increased from 0.1 to 0.9 ppm. Because chemical adsorption onto photocatalyst surfaces is known as a primary factor influencing the degradation efficiency of chemicals [22], the increasing pattern in degradation efficiencies with IC increases was ascribed to adsorption competition of BTEX molecules on the

catalyst surface. Specifically, a small amount of the active adsorption sites on the surface of the TNTUCF-10 under low IC conditions would have been available for BTEX adsorption before the surface reaction was initiated.

Figure 6. Degradation efficiencies (DE) of (**a**) benzene; (**b**) toluene; (**c**) ethyl benzene; (**d**) o-xylene as determined using TNTUCF-10 according to various air flow rates (1, 2, 3, and 4 L·min^{-1}).

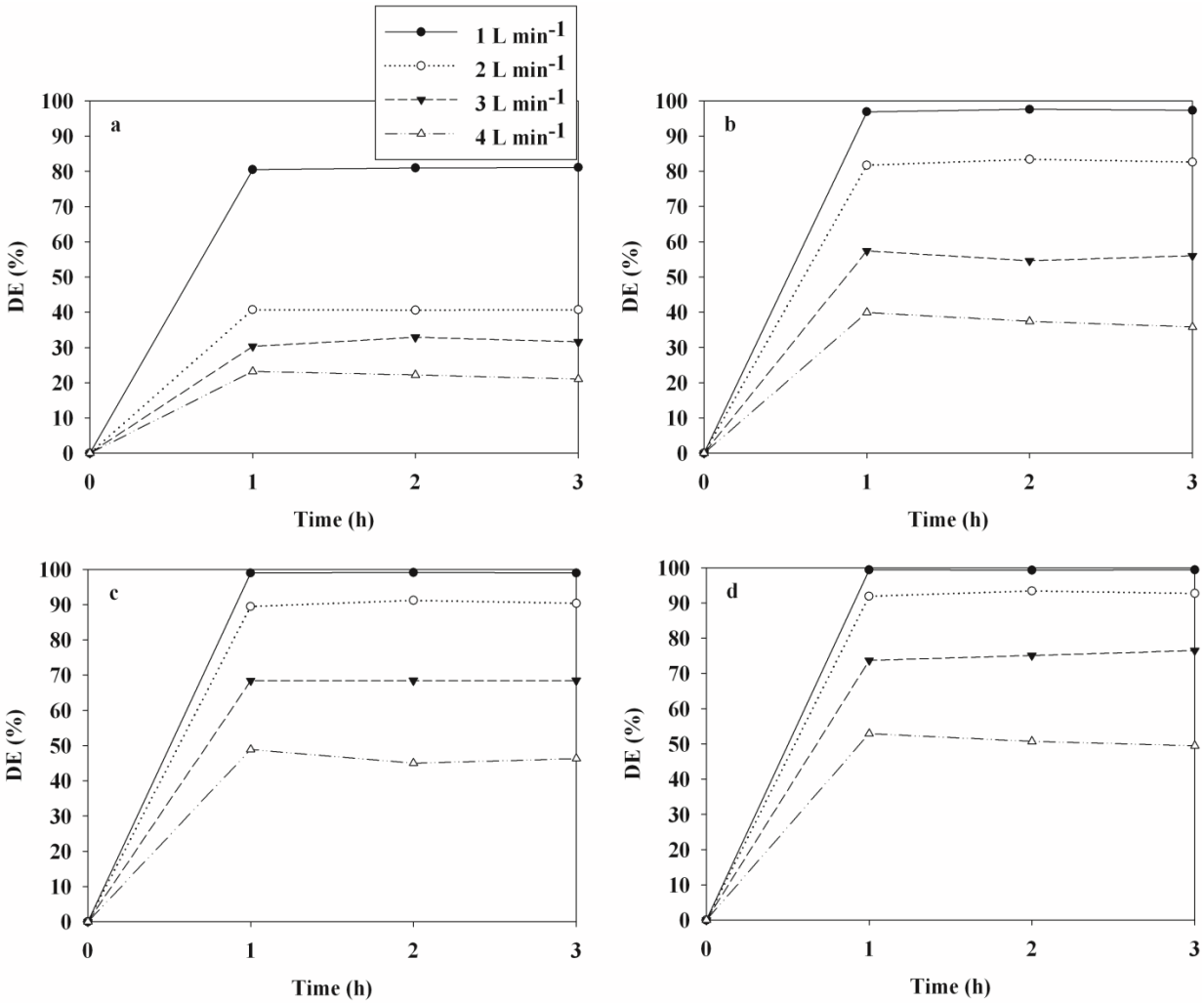

3. Experimental Section

3.1. Synthesis and Characterization of TUCF and TNTUCFs

A TUCF was synthesized using a simple coating process, while TNTUCFs with different TiO_2 loadings were prepared by hydrothermally treating the prepared TUCF. CF sheets (Hyundai Fiber Co., Hanam, Korea) were first washed with NaOH solution (1 M, Sigma-Adrich, St. Louis, MO, USA) and then with distilled water, after which they were dried in an oven at 110 °C. The cleaned CFs were immersed into tetrabutyl titanate (TBT, Sigma-Aldrich, St. Louis, MO, USA)-hexane (Sigma-Aldrich, St. Louis, MO, USA) solution (10 vol% TBT) for 10 min and were then exposed to water-saturated air for the hydrolysis of TBT. These immersion and hydrolysis processes were repeated five times in order to obtain high TiO_2 loaded CFs. The coated CF was calcined in an oven

at 400 °C for 6 h to obtain TUCF. In addition, CF sheets were immersed in TBT-hexane solutions (5%, 7.5%, 10%, 12.5%, or 15%) to prepare TNTUCFs with different TiO_2 loadings (named as TNTUCF-5, TNTUCF-7.5, TNTUCF-10, TNTUCF-12.5, or TNTUCF-15, respectively). To hydrothermally treat the coated CFs, they were rolled up and immersed into NaOH solution (10 M) in a stainless steel autoclave (170 mL) with Teflon-lined inner-walls, after which they were heated at 160 °C for 48 h. The autoclave was then cooled down to room temperature, and the hydrothermally treated samples were washed with acetic acid (0.1 M, Sigma-Aldrich, St. Louis, MO, USA) and distilled water in turn, after which they were calcined in an oven at 400 °C for 6 h to obtain final products, as white powders. The characteristics of the prepared TNTUCFs and TUCF were examined using scanning electron microscopy (FE-SEM, Hitachi S-4300, Tokyo, Japan), energy-dispersive X-ray (EDX, Hitachi EDX-350, Tokyo, Japan), transmission electron microscopy (TEM, Hitachi H-7600, Tokyo, Japan), and X-ray diffraction (XRD, Rigaku D/max-2500 diffractometer, Rigaku, Tokyo, Japan) spectroscopy. In addition, for the calculation of band gaps of the prepared photocatalysts, UV-Vis absorption spectra were obtained for the dry pressed disk samples using a Varian CARY 5G spectrophotometer (Vrian Inc., Cary, NC, USA) in the wavelength range between 200 and 800 nm at a scanning rate of 120 nm/min.

Figure 7. Degradation efficiencies (DE) of (**a**) benzene; (**b**) toluene; (**c**) ethyl benzene; (**d**) o-xylene determined using TNTUCF-10 according to varying input concentrations (0.1, 0.5, 0.7, and 0.9 ppm).

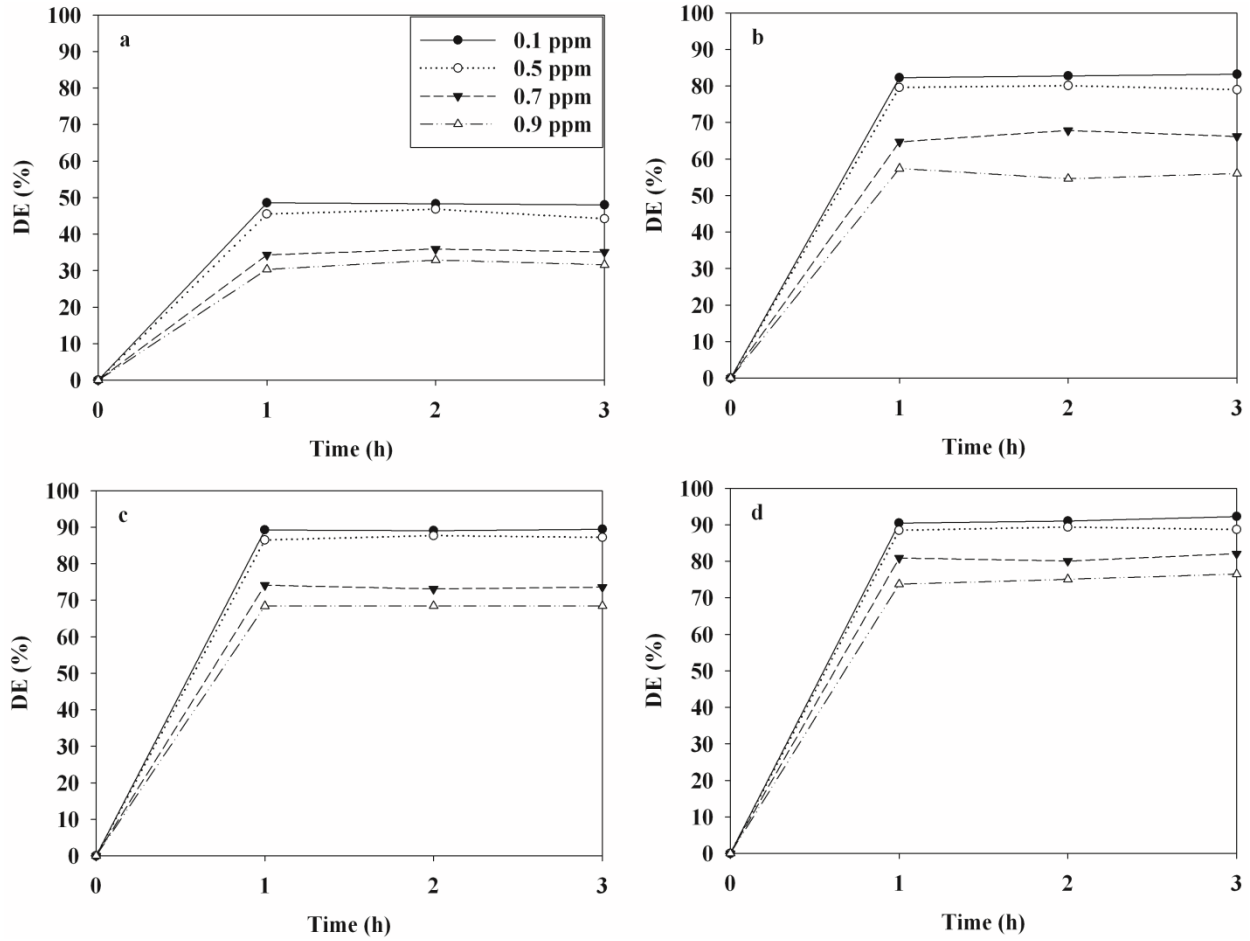

3.2. Photocatalysis of BTEX via TNTUCFs and TUCF

The photocatalytic activity of the TNTUCFs, TUCF, and UCF for the degradation of aromatic VOCs were examined using a continuous-flow Pyrex tubing reactor (4.0 cm inside diameter (i.d.) and 26.5 cm length), the inner wall of which was covered with each of the prepared photocatalysts. A cylindrical UV-light source (8-W fluorescent black light lamp, F8T5BL, Youngwha Lamp Co., Seoul, Korea) was inserted inside the Pyrex reactor, serving as the inside surface boundary layer of the reactor. The high-purity dried air supplied by the air cylinder was further cleaned by passing through an activated carbon filter. Humidified air was generated by passing the cleaned air through a humidification device immersed in a water bath. Standard gases were produced by mixing the humidified air with the target chemicals injected into a heated buffering Pyrex bulb via an auto-controlled syringe pump (Model Legato 100, KdScientific Inc., Holliston, MA, USA). The produced standard gases were allowed to flow into another buffering Pyrex bulb to decrease the fluctuation of input concentration fluctuation prior to being fed into the photocatalytic reactor.

The photocatalytic activity tests of the prepared photocatalysts were conducted under different operational conditions by varying air flow rates (AFRs) and input concentrations (ICs). The AFRs were adjusted to 1.0, 2.0, 3.0, or 4.0 $L \cdot min^{-1}$, while ICs were adjusted to 0.1, 0.5, 0.7, or 0.9 ppm. For each parameter test, the other parameters were fixed to their representative values: AFR, 1.0 $L \cdot min^{-1}$; and IC, 0.9 ppm. The relative humidity (RH) was fixed 45%, which is within the range of comfort (40%–60%) recommended by the American Society of Heating, Refrigerating and Air Conditioning Engineers. The hydraulic diameter (HD, defined as the inner diameter of the Pyrex tubing reactor minus the outside diameter of the light source) of the Pyrex reactor was 1.2 mm. The light intensity supplied by the light source was 0.4 $mW \cdot cm^{-2}$ at a distance from the light source equal to half the HD of the photocatalytic reactor. Each test was repeated three times in order to obtain more reliable results.

Measurements of gaseous chemicals were conducted both upstream and downstream of the Pyrex tubing reactor. Gas samples were collected by drawing air through a stainless steel tube (1/4 in. i.d. and 10 cm length) containing Tenax-TA adsorbent. The gaseous species collected on the Tenax-TA trap were analyzed by combining a thermal desorbing device (ATD 500, Perkin Elmer Co., Shelton, CT, USA) to a gas chromatograph (GC, Perkin Elmer Clarus 680, Shelton, CT, USA)/mass spectrometer (MS, Perkin Elmer Clarus SQ8 T, Shelton, CT, USA) equipped with a capillary column (DB-1, Agilent Co., Santa Clara, CA, USA). The trap was thermally desorbed at 250 °C for 10 min, and the gaseous species were cryofocussed at −30 °C using an internal cryo trap, after which they were rapidly heated to 250 °C and subsequently flushed to transfer the target compounds to the GC/MS system. The initial oven temperature was set to 40 °C for 5 min, and was then ramped to 230 °C at 5 °C min^{-1} for 7 min. The gaseous species were identified based on their reaction times and mass spectra (Wiley 275 software library), while their quantification was carried out using calibration equations based on five different concentrations. The quality control program for gas measurements included blank and spiked sample traps. On each day, a blank sample was analyzed in order to examine the trap for contamination. A spiked sample was analyzed daily to validate the quantitative response of the analytical system. The method detection limits for BTEX ranged from 0.005 to 0.008 ppm, depending on the chemical species.

4. Conclusions

In this study, TNTUCFs with different TiO_2 loadings were prepared using a coating-hydrothermal process and their photocatalytic activities were investigated for the decomposition of sub-ppm levels of aromatic pollutants using a plug-flow photocatalytic reactor. Spectral results of the prepared photocatalysts were closely associated with the characteristics of one-dimensional nanostructured TNTs for TNTUCFs and spherical shapes for TUCF. TNTUCFs exhibited superior photocatalytic degradation of BTEX compared to that of TUCF. Moreover, the photocatalytic activities obtained from TNTUCFs suggested that the degradation efficiencies of BTEX varied with changes in TiO_2 loading, allowing for the optimization of TiO_2 loading. Another important finding was that ICs and AFRs could be important parameters for the treatment of sub-ppm level vapors, which should be considered for the optimum operation of TNTUCFs.

Acknowledgments

This work was supported by the National Research Foundation of Korea (NRF) grant funded by the Korean government (MEST) (2011-0027916) and the Korean government (MSIP) through GCRC-SOP (No. 2011-0030013).

Author Contributions

Wan-Kuen Jo established the research protocol and analyzed the experimental data. Joon Yeob lee performed experimental works, and Ho-Hwan Chun assisted in data analysis.

Conflicts of Interest

The authors declare no conflict of interest.

References

1. Nakata, K.; Fujishima, A. TiO_2 photocatalysis: Design and applications. *J. Photochem. Photobiol. C* **2012**, *13*, 169–189.
2. Toledo-Antonio, J.A.; Capula, S.; Cortés-Jácome, M.A.; Angeles-Chávez, C.; López-Salinas, E.; Ferrat, G.; Navarrete, J.; Escobar, J. Low-temperature FTIR study of CO adsorption on titania nanotubes. *J. Phys. Chem. C* **2007**, *111*, 10799–10805.
3. Yang, H.Y.; Yu, S.F.; Lau, S.P.; Zhang, X.; Sun, D.D.; Jun, G. Direct growth of ZnO nanocrystals onto the surface of porous TiO_2 nanotube arrays for highly efficient and recyclable photocatalysts. *Small* **2009**, *5*, 2260–2264.
4. Tachikawa, T.; Tojo, S.; Fujitsuka, M.; Sekino, T.; Majima, T. Photoinduced charge separation in titania nanotubes. *J. Phys. Chem. B* **2006**, *110*, 14055–14059.
5. Toledo-Antonio, J.A.; Cortes-Jacome, M.A.; Orozco-Cerros, S.L.; Montiel-Palacios, E.; Suarez-Parra, R.; Angeles-Chavez, C.; Navarete, J.; López-Salinas, E. Assessing optimal photoactivity on titania nanotubes using different annealing temperatures. *Appl. Catal. B* **2010**, *100*, 47–54.

6. Górska, P.; Zaleska, A.; Kowalska, E.; Klimczuk, T.; Sobczak, J.W.; Skwarek, E.; Janusz, W.; Hupka, J. TiO_2 photoactivity in vis and UV light: The influence of annealing temperature and surface properties. *Appl. Catal. B* **2008**, *84*, 440–447.
7. Matos, J.; García-López, E.; Palmisano, L.; García, A.; Marci, G. Influence of activated carbon in TiO_2 and ZnO mediated photo-assisted degradation of 2-propanol in gas-solid regime. *Appl. Catal. B* **2010**, *99*, 170–180.
8. Jo, W.K.; Shin, S.H.; Hwang, E.S. Removal of dimethyl sulfide utilizing activated carbon fiber-supported photocatalyst in continuous-flow system. *J. Hazard. Mater.* **2011**, *191*, 234–239.
9. Verbruggen, S.W.; Ribbens, S.; Tytgat, T.; Hauchecorne, B.; Smits, M.; Meynen, V.; Cool, P.; Martens, J.A.; Lenaerts, S. The benefit of glass bead supports for efficient gas phase photocatalysis: Case study of a commercial and a synthesised photocatalyst. *Chem. Eng. J.* **2011**, *174*, 318–325.
10. Chun, H.-H.; Lee, J.Y.; Jo, W.-K. Photocatalysis of low-concentration gaseous organic pollutants over electrospun iron-doped titanium dioxide nanofibers. *Solid State Sci.* **2013**, *25*, 103–109.
11. Chen, P.; Gu, L.; Xue, X.; Li, M.; Cao, X. Engineering the growth of TiO_2 nanotube arrays on flexible carbon fibre sheets. *Chem. Commun*. **2010**, *46*, 5906–5908.
12. Guo, W.; Zhang, F.; Lin, C.; Wang, Z.L. Direct growth of TiO_2 nanosheet arrays on carbon fibers for highly efficient photocatalytic degradation of methyl orange. *Adv. Mater.* **2012**, *24*, 4761–4764.
13. Leary, R.; Westwood, A. Carbonaceous nanomaterials for the enhancement of TiO_2 photocatalysis. *Carbon* **2011**, *49*, 741–772.
14. Bozzi, A.; Yuranova, T.; Guasaquillo, I.; Laub, D.; Kiwi, J. Self-cleaning of modified cotton textiles by TiO_2 at low temperatures under daylight irradiation. *J. Photochem. Photobiol. A* **2005**, *174*, 156–164.
15. Ochiai, T.; Fujishima, A. Photoelectrochemical properties of TiO_2 photocatalyst and its applications for environmental purification. *J. Photochem. Photobiol. C* **2012**, *13*, 247–262.
16. Ohura, T.; Amagai, T.; Shen, X.; Li, S.; Zhang, P.; Zhu, L. Comparative study on indoor air quality in Japan and China: Characteristics of residential indoor and outdoor VOCs. *Atmos. Environ.* **2009**, *43*, 6352–6359.
17. Rumchev, K.; Brown, H.; Spickett, J. Volatile organic compounds: Do they present a risk to our health? *Rev. Environ. Health* **2007**, *22*, 39–55.
18. World Health Organization (WHO). Air quality guidelines for Europe. Regional Office for Europe, Copenhagen. 2000. Available online: http://www.euro.who.int/_data/assets/pdf_file/0005/74732/E71922.pdf (accessed on 11 December 2012).
19. Fu, J.; Tian, Y.; Chang, B.; Xi, F.; Dong, X. Facile fabrication of N-doped TiO_2 nanocatalyst with superior performance under visible light irradiation. *J. Solid State Chem.* **2013**, *199*, 280–286.
20. Yu, Q.L.; Brouwers, H.J.H. Indoor air purification using heterogeneous photocatalytic oxidation. Part I: Experimental study. *Appl. Catal. B* **2009**, *92*, 454–461.

21. Demeestere, K.; Dewulf, J.; van Langenhove, H. Heterogeneous photocatalysis as an advanced oxidation process for the abatement of chlorinated, monocyclic aromatic and sulfurous volatile organic compounds in air: State of the art. *Crit. Rev. Environ. Sci. Technol.* **2007**, *37*, 489–538.
22. Fujishima, A.; Zhang, X.; Tryk, S.A. TiO_2 photocatalysis and related surface phenomena. *Surf. Sci. Rep.* **2008**, *63*, 515–582.
23. Boulinguiez, B.; Bouzaza, A.; Merabet, S.; Wolbert, D. Photocatalytic degradation of ammonia and butyric acid in plug-flow reactor: Degradation kinetic modeling with contribution of mass transfer. *J. Photochem. Photobiol.* **2008**, *200*, 254–261.
24. Devahasdin, S.; Fan, C.; Li, K., Jr.; Chen, D.H. TiO_2 photocatalytic oxidation of nitric oxide: Transient behavior and reaction kinetics. *J. Photochem. Photobiol. A* **2003**, *156*, 161–170.

Theoretical Estimation of Thermal Effects in Drilling of Woven Carbon Fiber Composite

José Díaz-Álvarez, Alvaro Olmedo, Carlos Santiuste and María Henar Miguélez

Abstract: Carbon Fiber Reinforced Polymer (CFRPs) composites are extensively used in structural applications due to their attractive properties. Although the components are usually made near net shape, machining processes are needed to achieve dimensional tolerance and assembly requirements. Drilling is a common operation required for further mechanical joining of the components. CFRPs are vulnerable to processing induced damage; mainly delamination, fiber pull-out, and thermal degradation, drilling induced defects being one of the main causes of component rejection during manufacturing processes. Despite the importance of analyzing thermal phenomena involved in the machining of composites, only few authors have focused their attention on this problem, most of them using an experimental approach. The temperature at the workpiece could affect surface quality of the component and its measurement during processing is difficult. The estimation of the amount of heat generated during drilling is important; however, numerical modeling of drilling processes involves a high computational cost. This paper presents a combined approach to thermal analysis of composite drilling, using both an analytical estimation of heat generated during drilling and numerical modeling for heat propagation. Promising results for indirect detection of risk of thermal damage, through the measurement of thrust force and cutting torque, are obtained.

Reprinted from *Materials*. Cite as: Díaz-Álvarez, J.; Olmedo, A.; Santiuste, C.; Miguélez, M.H. Theoretical Estimation of Thermal Effects in Drilling of Woven Carbon Fiber Composite. *Materials* **2014**, *7*, 4442ï 4454.

1. Introduction

The attractive properties of Carbon Fiber Reinforced Polymer (CFRPs) make this family of materials suitable for a wide range of high responsibility structural applications. CFRPs exhibit fatigue and corrosion resistance combined with lightweight, high specific stiffness, and strength. [1] CFRP components are manufactured to be near net shape, however, dimensional and assembly requirements commonly involve some machining operations. Mainly trimming and drilling are required, being critical operations, since they are performed on high value components susceptible to suffering machining induced damage. Delamination, fiber pull-out, and thermal degradation [2], usually observed when machining with worn tools or inappropriate cutting parameters, could affect the performance of the composite component or the mechanical joint during service life [3–5].

Delamination related to further strength reduction of the component, has received considerable attention in the scientific literature, using experimental and numerical approaches, see for instance recent advances in [6,7]. However, mechanical delamination is not the unique risk for the surface integrity of the component. Thermal damage, related to low glass transition temperatures (around

180 °C for a typical epoxy resin in CFRPs), can cause matrix degradation and, thus, it is also involved in plies separation [8].

Despite of the potential risk of thermal damage when machining CFRPs, it has been analyzed, mostly based on experimental works, and only in a few works in the literature. The measurement of the temperature at the cutting tool has been achieved, using thermocoupling, by several authors. Chen [9] obtained the temperature reached during drilling at the flank surface. A significant influence of the cutting speed was observed, with temperature increasing from 120 to 300 °C when the cutting speed increased from 40 to 200 m/min. Brinksmeier *et al.* [10] embedded a thermocouple at the tool tip for temperature measurement in drilling and orbital milling of hybrid components Ti/CFRP/Al. Drilling operation involved lower surface quality and higher temperatures than orbital milling.

The installation of a thermocouple inside the tool gives indirect information about the temperature level at the workpiece. Direct measurement of workpiece temperature was achieved in [8], also completed with temperature measurement at the cutting tool. Milling of CFRP was conducted with carbide endmill in dry conditions. Two different techniques were used: infrared thermo-graph camera for endmill surface temperature measurement, and embedded K-type thermocouple in the CFRP for measurement of the temperature at the machined surface. The temperature at a depth of 0.3 mm beneath the machined surface reached 104 °C (at cutting a speed equal to 300 m/min), this temperature being much lower than that measured at tool–chip contact point.

The influence of tool wear in temperature induced during trimming was analyzed in [11]. Fresh tools induced temperatures below the glass transition temperature of the composite, while a critical level was reached using worn tools. In addition, machining parameters had significant influence on the variation of the machined surface quality and cutting forces.

Cutting temperature in rotary ultrasonic machining of carbon fiber reinforced plastic has been recently analyzed [12] using two techniques: fiber optic sensor and thermocouples. Relations between input variables (ultrasonic power, tool rotation speed, and feed rate) and cutting temperature were obtained from experiments. The authors found that the maximum cutting temperature decreased as ultrasonic power and feed rate decreased. On the other hand, as tool rotation speed increased, maximum cutting temperature firstly increased, and then decreased. Concerning the method for temperature measurement, the fiber optic sensor gave higher temperatures than those measured by the thermocouple method.

The development of modeling tools, able to predict temperature distribution during composite cutting, is a desirable objective because of its relation with damage. Prediction of mechanical damage in composite cutting has been commonly achieved using finite element analyses. Although this field is not as active as metal cutting, it is possible to find some works focusing on orthogonal cutting of composite, involving two-dimensional (2D) models (see for instance [13–16]), as well as three-dimensional (3D) approaches (see, for example, [17,18] analyzing the validity of 2D hypotheses). Main contributions in the field of modeling of composite machining have been summarized in a recent review [19].

Simulation of real cutting processes, such as drilling, requires a high computational cost because of the need of simulating tool rotation and feed movement using both damage and failure criteria of

the workpiece. These types of complex models for drilling have been recently developed showing good correlation between measured and predicted torque, thrust force, and delamination area [7,20].

Although mechanical effects in composite cutting have been analyzed using simulation tools, thermal effects have been neglected in these models. The first approach to the numerical modeling of thermal phenomena involved in the orthogonal cutting of CFRPs has been presented in a recent work of the authors [21]. The model included heat generation due to friction at the chip/tool interface and it was used for the prediction of intralaminar damage, delamination, and thermal damage accounted in terms of temperature level beneath the machined surface.

The heat generated due to plastic work can be assumed to be negligible in CFRPs because they exhibit elevated elastic modulus with small deformations, even when breakage is initiated. Deformation energy is negligible and, thus, heat generated can be neglected. This behavior is quite different from that observed in metal cutting, involving large amount of plastic work converted into heat, leading to very high temperatures at the primary shear zone and, sometimes, to the formation of adiabatic shear bands (see, for instance, [22]). As deformation energy is neglected, the unique heat source considered in the model was friction at the interface. Thus, the estimation of friction heat at the tool/chip interface is crucial in drilling. Measurement of temperature during industrial drilling is not possible since the thermocouple technique is invasive.

The main objective of this paper is the estimation of heat amount from easy-to-measure, in-process variables: torque and thrust force. A simple analysis, based on energy balance, is presented to obtain the heat generated at the interface, indirectly, from experimental tests. As far as the bibliographic revision has been carried out, this approach has not been applied to the problem of drilling. However, it is possible to find interesting analytical models of composite impact in [23], based on energy balance (impact processes have common characteristics with drilling, mainly the penetration of the projectile/drill into the target/workpiece). Once the frictional heat amount is available, it is possible to establish temperature distribution with a simple numerical model accounting for thermal conductivity in a composite. The detection of critical levels of temperature at certain zones can be used for assessment during the definition of drilling process of structural components, avoiding risk of thermal damage. The establishment of maximum levels of thermal energy, directly related with torque and thrust force evolution registered during cutting, could be used as an indicator of excessive tool wear. The aim of the paper and its practical application are illustrated in Figure 1.

Figure 1. Relationships between experimental, analytical, and numerical steps proposed.

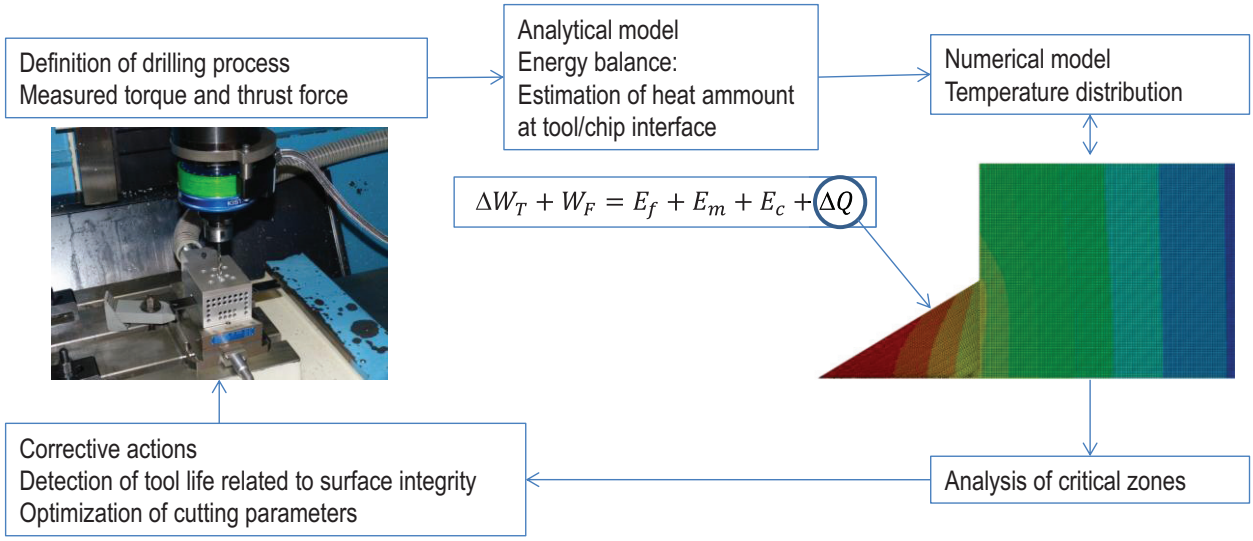

This work is structured firstly in this introduction, followed by the estimation of heat developed in the second section. The third section involves the simulation of heat propagation, analyzing different cases and, finally, discussion and conclusions are presented.

2. Estimation of Frictional Heat

A drilling process is performed at a constant feed and rotary velocity. The control of the machine tool maintains these parameters and the resultant torque and thrust force measured at the spindle are dependent on the cutting parameters, the material properties, and the characteristics of the cutting tool, including contact behavior at the interface. Figure 2 illustrates the entrance of the drill through the composite during cutting. Thus, a simplified method to estimate the heat generated at the interface has been developed assuming constant feed and rotary velocity of the drill. The assumption of axial-symmetry was considered. Although CFRP strength is orientation dependent, a woven laminate was selected to minimize the effect of the anisotropy.

2.1. Energy Balance

The differential work due to torque (dW_T) and thrust force (dW_F) during a differential time increment, dt, involved in a differential of turn angle of the drill, $d\theta$, and is the result of several contributions. These contributions are summarized in Equation (1): the energy required for breakage of composite (dE_f), the kinetic energy transferred to the chip (dE_c), and the amount of heat generated at the interface due to friction (dQ).

$$dW_T + dW_F = dE_f + dE_c + dQ \quad (37)$$

The kinetic energy of the chip, once separated from the workpiece, can be neglected due to the small mass of the chip and the moderated velocity involved in cutting. A first estimation showed that the level was negligible compared to the rest of terms of Equation (1) (around 0.005% of the energy required for breakage of composite (dE_f)). Thus, the heat generated at the interface can be estimated as:

$$dQ = dW_T + dW_F - dE_f \tag{38}$$

The terms corresponding to work developed by torque and thrust force were obtained from experiments. The torque and thrust force recorded at each time increment were derived from the discretization of the evolution with cutting time of both variables, measured during the drilling test.

The term corresponding to energy involved in composite breakage can be calculated considering the differential volume removed by the drill during a differential time, *dt*, corresponding to a differential drill turn, dθ.

$$dE_f(\theta) = w_f dV_f(\theta) \tag{39}$$

where w_f is the specific energy of the woven composite breakage; and dV_f is the differential volume associated to a differential turn of the drill, $d\theta$.

The specific energy can be estimated as $w_f = 2(1/2X\varepsilon_f)$, where X is the strength of the woven composite (the same in direction 1 and 2 because of the woven architecture of the composite); and ε_f is the ultimate strain of the composite. It is worth noting that composite strength is orientation dependent, but the hypothesis of axial-symmetry was necessary to avoid unaffordable computational costs. The approach was similar to that used by Artero-Guerrero *et al.* [24] when modeling impact on a woven composite. Mechanical and thermal problems are uncoupled in the present, simplified model. Thus, mechanical properties are considered temperature independent under 180 °C, and thermal damage is assumed for temperatures above 180 °C.

The differential volume considered is presented in Figure 2. From this figure the volume can be calculated as:

$$dV_f(\theta) = \pi L_{\text{cut}}^2 f_{\text{cut}} \frac{d\theta}{2\pi} \tag{40}$$

where L_{cut} is the effective cutting edge length; and f_{cut} is the feed rate.

It is worth noting that the volume of material removed depends on the stage of the drilling process. It is possible to distinguish three different stages illustrated in Figure 2, the entrance of the conical zone, the cut performed with the complete edge and the exit of the drill.

For the geometry of the drill used in the machining tests (described in the next section) the stages indicated in the figure corresponds with the following values of time and effective length of cutting edge.

-Entrance stage, time 0–t_1: $$L_{\text{cut1}} = \frac{R_{\text{cut}}}{\cos\alpha} \cdot \frac{t}{t_1} \tag{41}$$

-Steady stage, time t_1–t_2: $$L_{\text{cut2}} = \frac{R_{\text{cut}}}{\cos\alpha} \tag{42}$$

-Exit stage, t_2–t_3: $$L_{\text{cut3}} = \frac{R_{\text{cut}}}{\cos\alpha} \cdot \left[1 - \left(\frac{t-t_2}{t_3-t_2}\right)\right] \tag{7}$$

where R_{cut} is the drill radius.

The expression presented in Equation (2) was applied to real experiments involving drilling of woven carbon composite. The specific conditions of the experiments are presented in the next subsection, involving both new and worn tool geometries.

Figure 2. Scheme of drilling process: differential volume removed during the differential time d*t* and effective cutting edge at the different stages of drilling from entrance to drill exit.

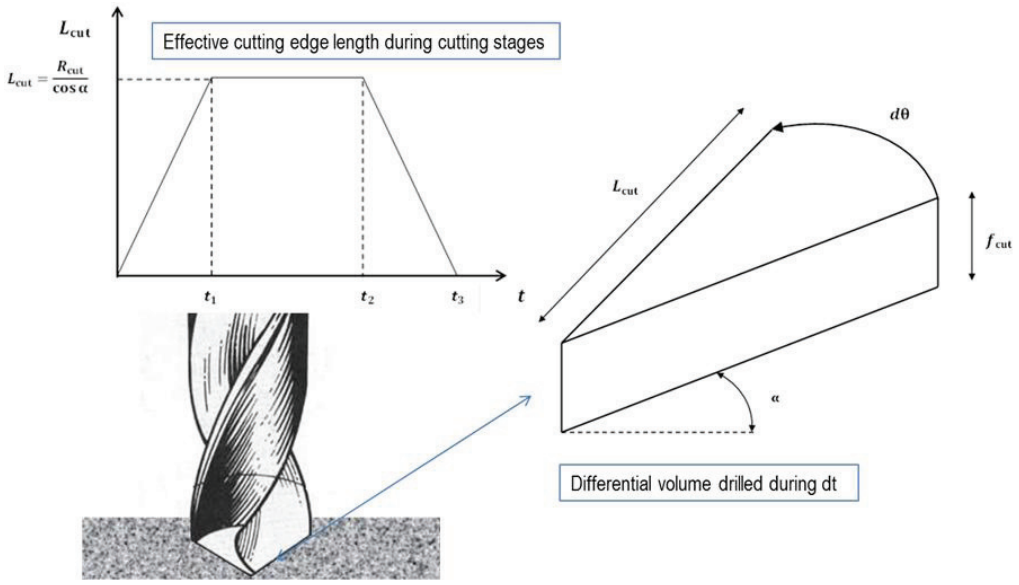

2.2. Application to Experiments

In order to apply the energy balance formulated in Equation (2) to a real case of drilling, experimental tests were performed on woven CFRP composite. Each ply was manufactured by Hexcel Composites consisting of AS-4 carbon fiber and epoxy matrix. The specimens, with a stacking sequence of 10 plies with the same fiber orientation in all of them, and a total thickness of 2.2 mm, were cut in plates. The mechanical properties of this material were obtained from scientific literature [24], see Table 1.

The cutting tests were carried out in a machining center (B500 KONDIA, Kondia, Elgoibar, Spain), shown in Figure 3. The machining center was equipped with a dynamometer (Kistler 9123C, Winterthur, Switzerland) for measurement of cutting forces and torque (see Figure 3).

The drill (diameter, 6 mm; point angle, 118°) was recommended by the manufacturer GUHRING (Albstadt-Ebingen, Germany) for CFRP drilling.

Table 1. Mechanical properties of AGP 193-PW/8552 composite material [24].

Property	Value
Density, ρ (kg/m^3)	1570
Resin content (%)	55.29
Longitudinal modulus, E_1 (GPa)	68
Transverse modulus, E_2 (GPa)	68
Major Poisson's ratio, ν_{21}	0.21
Longitudinal tensile strength, X_T (MPa)	880
Longitudinal compressive strength, X_C (MPa)	880
Transverse tensile strength, Y_T (MPa)	880
Transverse compressive strength, Y_C (MPa)	880
In-plane shear strength, S_T (MPa)	84

Figure 3. Machining center used in the experiments was equipped with the dynamometer, acquisition system and also with a system for chip aspiration.

Drilling tests were performed with new drill and with worn tool exhibiting flank wear (this wear mode is commonly observed to be dominant in the drilling of CFRPs). Fresh tool and severe wear (flank = 0.3 mm [25]) were tested in order to study different conditions for cutting forces and torque, and, in consequence, different levels of generated heat. Obtaining controlled worn geometries directly from wear tests is not easy, thus, the flank at the clearance surface was artificially generated by grinding.

Several drilling experiments were performed in the ranges of cutting speed (25, 50, 100 m/min) and feed (0.05, 0.1, 0.15 mm/rev). From the observation of force and torque evolution, the tests corresponding to cutting speed 50 m/min and feed 0.1 mm/rev, with fresh and worn tool, were selected. In the selected cases, it was possible to identify steady values of force and torque in the different states of the drilling process and levels of energy large enough to consider the possibility of thermal damages in the matrix in the case of worn tool.

The characteristics of the workpiece and drill, stated for the experiments, allowed the calculation of time intervals defined in Equations (5)–(7). Accounting for the drill tip angle equal to 118°, the thickness of the composite plate and the drill radius equal to 6 mm, t_1 = 0.38 s; t_2 = 0.88 s; and t_3 = 1.26 s.

As feed and rotary velocities are known, the evolution of thrust force and torque allowed the calculation of consumed power in penetration and rotation movement. In Figure 4, the total consumed power in both thrust and cutting movement (for cutting speed 50 m/min and feed 0.1 mm/rev) is presented. The curves were obtained with a fresh tool (Figure 4a) and a worn tool (Figure 4b), respectively.

Figure 4. (**a**) Power due to the drilling operation (spindle velocity 2653 rpm and feed 0.1 mm/rev) for a new tool; (**b**) power due to the drilling operation (spindle velocity 2653 rpm and feed 0.1 mm/rev) for a worn tool (with flank = 0.3 mm).

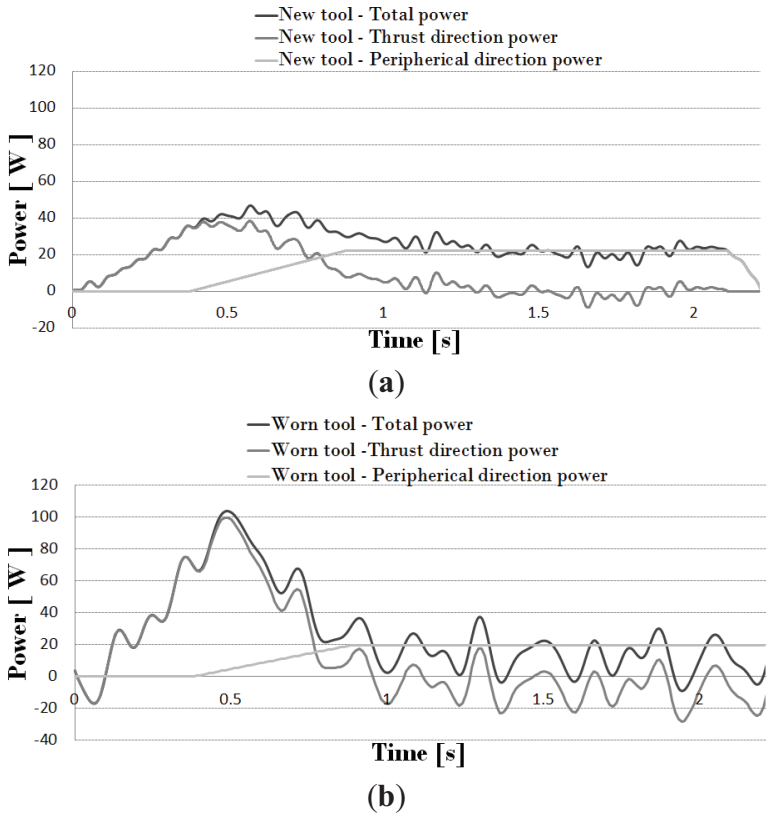

From the recorded signal, the amount of heat generated due to friction was obtained. The power consumed by peripheral friction was calculated as the average value of total power once the exit stage is reached ($t > t_3$). During entrance stage ($t < t_1$) peripheral friction power (due to contact between the drill body and the hole wall) is null while during steady stage ($t_1 < t < t_2$) it varies linearly from 0 to the exit stage value. The power consumed by cutting edge friction was estimated according to Equation (3) as the total power, minus the energy consumed by composite breakage (Equations (5)–(7)), and minus the peripheral friction. Negative values in some points are the result of noise and also due to subtracting the peripheral power from the total power (as it was considered as a constant value when all the drill nose get through the specimen thickness, when this value is subtracted from the total power negative values appear but these values are not applied to the model since there is no material in the nose direction).

The discretization of the curve of power *vs.* cutting time, allows the statement of thermal flux to the workpiece and the analysis of heat propagation in the finite element code.

The heat propagation in the workpiece is analyzed in the next section.

3. Numerical Modeling of Temperature Distribution

The numerical model was developed using the commercial finite element code ABAQUS/Explicit [26]. The aim of the model is the analysis of heat propagation during the drilling process in order to identify critical zones with excessive temperature level.

Simplifying hypotheses have been formulated. First of all, the model does not account for chip removal; in fact, it is an uncoupled thermal model. The assumption of axial-symmetry was considered in order to create a simplified model with reasonably computational cost. It is worth noting that CFRP strength and thermal conductivity is orientation dependent, but the disposal of low computational cost models to evaluate heat generation from experimental data requires the assumption of a strong hypotheses. Unidirectional tape laminates present high anisotropy in mechanical and thermal properties, thus, a woven laminate was selected to minimize the effect of the anisotropy in the axial-symmetrical model.

Complex models of composite drilling recently developed in the literature (see, for instance, [7]) involve elevated computational costs. These models account for chip removal and are able to predict mechanical damage at the machined surface, both intra laminar and delamination. However, up to the present, mechanical analysis has not been coupled with heat generation and propagation. The main objective of the model developed in this paper is the prediction of thermal issues during drilling, however, mechanical damage cannot be predicted.

The model has been divided in zones corresponding to each drill revolution corresponding to penetration equal to the feed (this depth of penetration per revolution will be used as time increment per step to apply the loads).

The frictional heat generated in each time increment was calculated from the analysis explained in the previous section. The proportion of the frictional heat energy allocated to the chip is characterized by the coefficient of heat partition. In the case of composite cutting the chip is highly fragmented as it is not observed the adhesion mechanism at the tool/chip interface found in metal cutting, characterizing the sticking/sliding zones (see for instance [22]). The amount of heat transferred to the chip is neglected and the frictional heat is assumed to be transferred 50%/50% to the workpiece and to the tool. The present paper is one of the earliest works dealing with the thermal effects in composite cutting. Further improvements of the research in this field are desirable and the statement of heat partition in composite cutting should be soundly analyzed. It is worth noting that the nature of both materials in contact (composite and tool material) could cause the increase of the amount of heat transferred to the tool and, thus, the extension of the thermal affected zone of the workpiece would diminish. Simulations with lower level of percentage of heat transferred to the workpiece were carried out (25% and 40%, respectively). In the first case critical temperature were not reached, even in the case of worn tool. For the second case, the thermal damage appeared but the affected zone was smaller than in the case corresponding to 50%. Heat partition, 50%/50%, could be treated as a starting point for the analysis of thermal problems in composite cutting and an upper limit for the generation of damage.

The scheme of the model is shown in Figure 5, including boundary conditions and geometry. The model was meshed with 70,000 linear triangular elements with a size of 25 μm. With the element size used in the model, each simulation takes around 2 h, being a reasonable computational cost. The

element size was stated after several iterations; no change in the temperature distribution was observed when the element size was lower than 25 μm, however the computational cost increased.

The mechanical properties of the workpiece are summarized in Table 1. Thermal properties for CFRPs are given in a wide range in the literature, thus, the values used in this work (thermal conductivity 5 W/mK and specific heat 1100 J/KgK) were averaged from several references covering different applications [4,8,21,27,28].

Figure 5. Scheme of the numerical model.

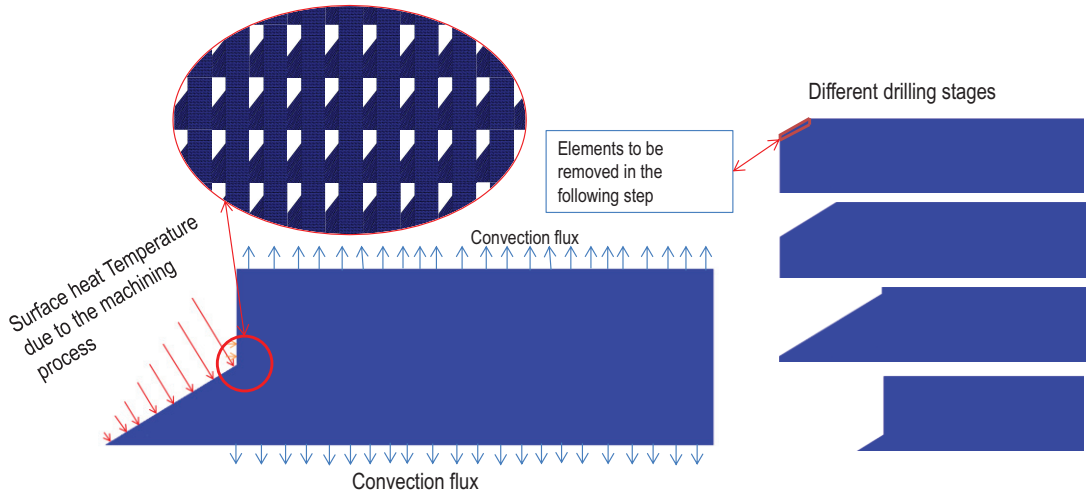

The procedure of the simulation is described in the following. In a generic time step (being the time involved in a drill revolution) the amount of heat along the cutting edge and lateral wall is calculated, applying the analytical model to the measured thrust force and torque, as it was explained in the previous section. At the end of each step, the layer of elements corresponding to the chip area removed in one revolution of the drill is eliminated from the model (thus, the layer become inactive for heat propagation) and the heat corresponding to the subsequent step is applied.

4. Results and Discussion

The numerical model was applied to the analysis of heat propagation. The model developed was used for analysis of the effect of tool wear. The effect of wear on torque and thrust force were included in the estimation of heat generated, and the numerical model allowed the estimation of the temperature distribution and the establishment of critical levels.

Figure 6 shows the evolution of the temperature fields as the entrance of the drill progresses. The cases, shown in Figure 6, correspond to drilling tests performed at cutting speed 50 m/min and feed rate 0.1 mm/rev. Figure 6a,b present, respectively, a fresh drill and a worn tool. It is observed at three stages of the drill entrance, the maximum level of the wall temperature occurred at the exit of the hole. It is worth noting that this zone also experience mechanical delamination [7]. Both effects would superpose inducing combined thermal and mechanical damage.

Figure 6. Predicted temperature (K) for tests developed at cutting speed 50 m/min and feed 0.1 mm/rev (grey zone represents temperature higher than 180 °C, 453 K): (**a**) fresh tool; (**b**) worn tool.

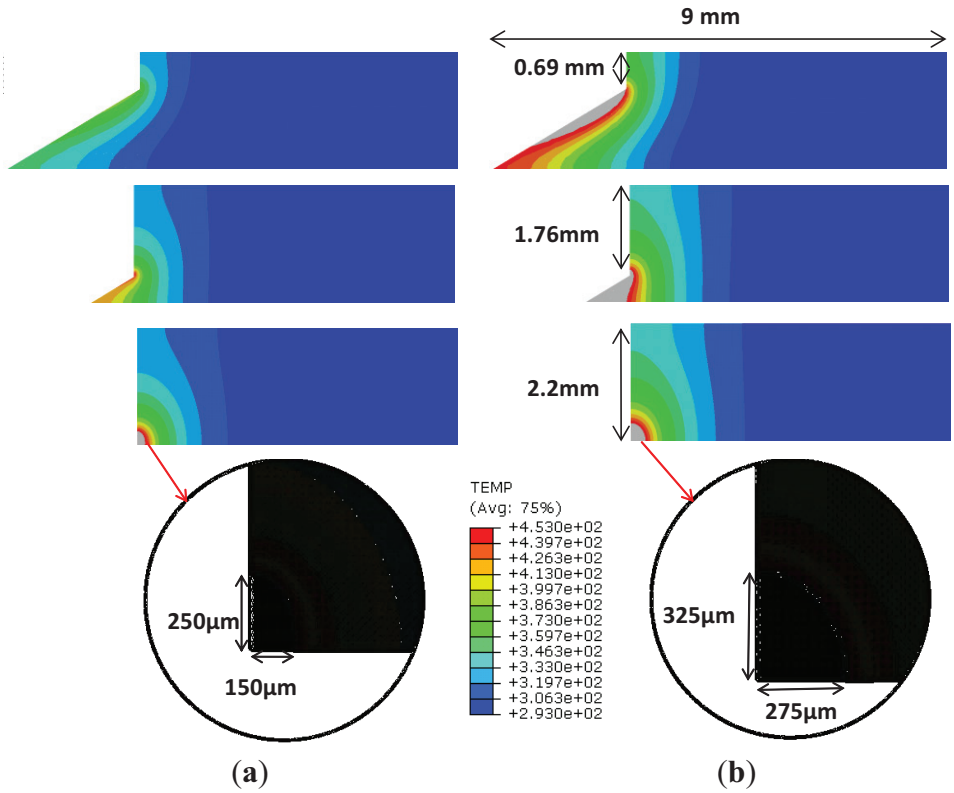

For a typical epoxy-based CFRP material, the initiation of resin degradation can be produced at a temperature of approximately 180 °C. The thermal damage at this temperature can create cracks leading to the onset of delamination and strength reduction [8,29]. The maximum temperature at the wall was significantly higher in the case of worn tool, with a temperature level higher than 180 °C (453 K) in a more extended area (in depth penetration below the machined wall equal to 275 µm). It is clear that this value of wear produces unacceptable level of temperature. In the case of a new tool the area reaching this high value of temperature is also significant (penetration beneath machined surface 150 µm). Although it is not directly comparable, the temperature distribution predicted with

the model is in the order of that measured in milling CFRP [8]. The temperature at 0.3 mm beneath the machined surface reached 104 °C being drilling more critically under the thermal point of view.

5. Conclusions

This work focuses on the prediction of temperature at the workpiece during drilling of woven CFRPs composites. The approach combine experimental testing (to establish the evolution of thrust and torque with cutting time); analytical modeling to estimate the heat flux at the interface tool/workpiece, and numerical simulation to analyze the heat propagation and the maximum level of temperature in the workpiece. The main contribution of the work is the development of the combined approach for the prediction of thermal damage.

The model was applied to two different real cases of drilling: fresh tool and worn tool (significant level of flank wear). The numerical model showed the maximum temperature occurring at the hole wall, close to the exit of the drill, being a zone where mechanical delamination is commonly observed. The occurrence of thermal damage, in the case of excessive wear, enhances the risk of defect at the exit of the hole.

The model is simple and very efficient from the computational point of view. The problem of using realistic models of drilling, including penetration and cutting movement, and elements erosion is the computational cost. The implementation of simulations tools in industry for assistance during manufacturing requires rapid response. The model proposed could be easily implemented to detect excessive levels of thermal power, because of inappropriate cutting parameters or excessive wear of the tool.

Acknowledgments

The authors acknowledge the financial support for the work to the Ministry of Economy and Competitiveness of Spain under the project DPI2011-25999.

Author Contributions

Carlos Santiuste and Alvaro Olmedo have developed the analytical model for the estimation of heat. José Díaz-Álvarez and María Henar Miguélez developed the numerical model and the drilling experiments for real application. All authors have participated in the manuscript writing and figures preparation.

Conflicts of Interest

The authors declare no conflict of interest.

References

1. Huang, X. Fabrication and properties of carbon fibers. *Materials* **2009**, *2*, 2369–2403.
2. Cong, W.L.; Pei, Z.J.; Deines, T.W.; Treadwell, C. Rotary ultrasonic machining of CFRP using cold air as coolant: Feasible regions. *J. Reinf. Plast. Compos.* **2011**, *30*, 899–906.

3. Haddada, M.; Zitoune, R.; Bougherara, H.; Eymac, F.; Castanié, B. Study of trimming damages of CFRP structures in function of the machining processes and their impact on the mechanical behaviour. *Compos. Part B Eng*. **2014**, *57*, 136–143.
4. Santiuste, C.; Barbero, E.; Miguélez, M.H. Computational analysis of temperature effect in composite bolted joints for aeronautical applications. *J. Reinf. Plast. Compos*. **2011**, *30*, 3–11.
5. Isbilir, O.; Ghassemieh, E. Delamination and wear in drilling of carbon-fiber reinforced plastic composites using multilayer TiAlN/TiN PVD-coated tungsten carbide tools. *J. Reinf. Plast. Compos.* **2012**, *31*, 717–727.
6. Liu, D.F.; Tian, Y.J.; Cong, W.L. A review of mechanical drilling for composite laminates. *Compos. Struct*. **2012**, *94*, 1265–1279.
7. Feito, N.; López-Puente, J.; Santiuste, C.; Miguélez, M.H. Numerical prediction of delamination in CFRP drilling. *Compos. Struct*. **2014**, *108*, 677–683.
8. Yashiro, T.; Ogawa, T.; Sasahara, H. Temperature measurement of cutting tool and machined surface layer in milling of CFRP. *Int. J. Mach. Tools. Manuf*. **2013**, *70*, 63–69.
9. Chen, W.-C. Some experimental investigations in the drilling of carbon fiber-reinforced plastic (CFRP) composite laminates. *Int. J. Mach. Tools Manuf*. **1997**, *37*, 1097–1108.
10. Brinksmeier, E.; Fangmann, S.; Rentsch, R. Drilling of composites and resulting surface integrity. *CIRP Ann. Manuf. Technol*. **2011**, *60*, 57–60.
11. Haddad, M.; Zitoune, R.; Eyma, F.; Castanié, B. Machinability and surface quality during high speed trimming of multi directional CFRP. *Int. J. Mach. Mach. Mater.* **2013**, *13*, 289–310.
12. Cong, W.L.; Zou, X.; Deines, T.W.; Wu, N.; Wang, X.; Pei, Z.J. Rotary ultrasonic machining of carbon fiber reinforced plastic composites: An experimental study on cutting temperature. *J. Reinf. Plast. Compos*. **2012**, *31*, 1516–1525.
13. Mahdi, M.; Zhang, L. A finite element model for the orthogonal cutting of fiber reinforced composite materials. *J. Mater. Process. Technol*. **2001**, *113*, 373–377.
14. Iliescu, D.; Gehin, D.; Iordanoff, I.; Girot, F.; Gutiérrez, M.E. A discrete element method for the simulation of CFRP cutting. *Compos. Sci. Technol*. **2010**, *70*, 73–80.
15. Santiuste, C.; Soldani, X.; Miguélez, M.H. Machining FEM model of long fiber composites for aeronautical components. *Compos. Struct*. **2010**, *92*, 691–698.
16. Soldani, X.; Santiuste, C.; Muñoz-Sánchez, A.; Miguélez, M.H. Influence of tool geometry and numerical parameters when modelling orthogonal cutting of LFRP composites. *Compos. Part A Appl. Sci. Manuf*. **2011**, *42*, 1205–1216.
17. Santiuste, C.; Miguélez, H.; Soldani, X. Out-of-plane failure mechanisms in LFRP composite cutting. *Compos. Struct*. **2011**, *93*, 2706–2713.
18. Santiuste, C.; Olmedo, A.; Soldani, X.; Miguélez, H. Delamination prediction in orthogonal machining of carbon long fiber-reinforced polymer composites. *J. Reinf. Plast. Compos.* **2012**, *31*, 875–885.
19. Dandekar, C.R.; Shin, Y.C. Modeling of machining of composite materials: A review. *Int. J. Mach. Tools Manuf*. **2012**, *57*, 102–121.
20. Phadnis, V.A.; Farrukh, M.; Anish, R.; Silberschmidt, V.V. Drilling in carbon/epoxy composites: Experimental investigations and finite element implementation. *Compos. Part A Appl. Sci. Manuf*. **2013**, *47*, 41–51.

21. Santiuste, C.; Díaz-Álvarez, J.; Soldani, X.; Miguélez, H. Modelling thermal effects in machining of carbon fiber reinforced polymer composites. *J. Reinf. Plast. Compos.* **2014**, *33*, 758–766.
22. Miguélez, M.H.; Soldani, X.; Molinari, A. Analysis of adiabatic shear banding in orthogonal cutting of Ti alloy. *Int. J. Mech. Sci*. **2013**, *75*, 212–222.
23. López-Puente, J.; Varas, D.; Loya, J.A.; Zaera, R. Analytical modelling of high velocity impacts of cylindrical projectiles on carbon/epoxy laminates. *Compos. Part A Appl. Sci. Manuf*. **2009**, *40*, 1223–1230.
24. Artero-Guerrero, J.A.; Pernas-Sánchez, J.; López-Puente, J.; Varas, D. On the influence of filling level in CFRP aircraft fuel tank subjected to high velocity impacts. *Compos. Struct.* **2014**, *107*, 570–577.
25. Rawat, S.; Attia, H. Wear mechanisms and tool life management of WC–Co drills during dry high speed drilling of woven carbon fiber composites. *Wear* **2009**, *267*, 1022–1030.
26. *ABAQUS User's Manual 6.4-1*; Hibbit, Karlson & Sorensen Inc.: Pawtucket, USA, 2003.
27. Villière, M.; Lecointe, D.; Sobotka, V.; Boyard, N.; Delaunay, D. Experimental determination and modelling of thermal conductivity tensor of carbon/epoxy composite. *Compos. Part A Appl. Sci. Manuf*. **2013**, *46*, 60–68.
28. Gralewicz, G.; Owczarek, G.; Więcek, B. Investigations of single and multilayer structures using lock-in thermography—Possible applications. *Int. J. Occup. Saf. Ergon.* **2005**, *11*, 211–215.
29. Chatterjee, A. Thermal degradation analysis of thermoset resins. *J. Appl. Polym. Sci.* **2009**, *114*, 1417–1425.

Drilling Damage in Composite Material

Luís Miguel P. Durão, João Manuel R.S. Tavares, Victor Hugo C. de Albuquerque, Jorge Filipe S. Marques and Oscar N.G. Andrade

Abstract: The characteristics of carbon fibre reinforced laminates have widened their use from aerospace to domestic appliances, and new possibilities for their usage emerge almost daily. In many of the possible applications, the laminates need to be drilled for assembly purposes. It is known that a drilling process that reduces the drill thrust force can decrease the risk of delamination. In this work, damage assessment methods based on data extracted from radiographic images are compared and correlated with mechanical test results—bearing test and delamination onset test—and analytical models. The results demonstrate the importance of an adequate selection of drilling tools and machining parameters to extend the life cycle of these laminates as a consequence of enhanced reliability.

Reprinted from *Materials*. Cite as: Durão, L.M.P.; Tavares, J.M.R.S.; de Albuquerque, V.H.C.; Marques, J.F.S.; Andrade, O.N.G. Drilling Damage in Composite Material. *Materials* **2014**, *7*, 3802ï 3819.

1. Introduction

Reinforced composite laminates are one of the most remarkable families of materials of this technological era. Their ability to be tailored for use and endless possibilities provided by the combination of reinforcements together with their alignment and fiber fraction, allow design engineers to have almost total freedom in the design of new parts. Unique properties such as low weight, high strength and stiffness are normally referred to whenever the advantages of these materials are listed. Nevertheless, some problematical issues remain concerning the use of composite laminates, thus providing arguments for the selection of conventional materials instead of composites, mainly in structural parts. Some of these issues are cost-related, but considerations about reliability or fatigue resistance also cause some difficulties for a wider usage of these materials.

However, the importance of composite materials has been growing steadily over the last decade, which can be confirmed by their intensive use in the new Airbus A380 or Boeing 787 airplanes. In the latter, 50% of the weight of its primary structure will be made of composite materials [1], an unprecedented ratio; which was difficult to imagine just some 30 years ago. One can now find composite materials not only in the aeronautical field, but also in other industries such as automotive, railway, marine or sports goods. There is no doubt that the level of confidence and reliability already achieved in metallic materials can also be reached for composites, it is just a question of time.

Taking the main problematic issues related to laminate parts into account, it is possible to find different arguments for the selection of conventional materials. One of them is associated with the relative complexity and cost of the production process. In the later stage of parts production, machining operations like drilling are frequently needed in composite structures, as the use of bolts, rivets or screws is required to join the parts. Generally, machined parts have poor surface appearance and tool wear is higher. One of the problems related with composites' machining is the nature of the fibre

reinforcement, which is usually very abrasive and causes rapid tool wear and deterioration of the machined surfaces [2]. As early as 1983, Koplev, Lystrup and Vorm [3] examined the cutting process of unidirectional carbon fibre reinforced plastics in directions perpendicular and parallel to the fibre orientation. A series of quick-stop experiments was carried out to examine the area near the tool tip. The authors stated that the machining of CFRP consists in a series of fractures, each creating a chip. In the following years there were extensive contributions improving knowledge regarding composites and the most frequent associated problems.

One of the most common problems relates to the need of drilling without delamination. Several studies on this subject have been reported, and it is therefore now possible to envisage a drilling strategy that keeps delamination risk at a minimum. Davim and Reis [4], studied the effect of cutting parameters on specific cutting pressure, delamination and cutting power in carbon fibre reinforced plastics. The authors concluded that feed rate has the greater influence on thrust force, so damage increases with feed. Hocheng and Tsao [5], conducted several practical experiments to support the benefit of using special drills instead of twist drills. In this work, the authors concluded that thrust force varies with drill geometry and with feed rate which allows for the use of higher feed rates if adequate drill geometry is selected. Durão *et al.* [6], confirmed the influence of appropriate drill geometry selection on delamination reduction, as well as the advantage of the use of a pilot hole strategy.

Zitoune *et al*. [7] investigated the influence of the machining performance during drilling of sandwiched composites using various dimensions of double cone drill. In the experimental work presented, the authors concluded that it is possible to reduce the thrust force during drilling by using a double cone drill in a multi-material aeronautic component (copper mesh/CFRP laminate/carbon-epoxy fabric layer).

Another option frequently referred to in order to avoid delamination, is the use of a backup plate. The effects of using a backup plate on delamination are well known in the composites industry. This drilling strategy is always a good option when the opposite side of the plate is accessible, which sometimes is not the case, mainly in field work as those involved in maintenance or repair are well aware. The use of a backup plate allows for drilling with higher feed rates, and consequently with higher thrust forces, as critical thrust force for delamination onset is also higher [8].

Non-conventional machining processes were also addressed in several published papers, see [9,10]. In [9] the authors concluded that although the surface roughness of machined walls was higher when drilling with Abrasive Water Jet, the outcomes for mechanical resistance are dependent not only on the damage extension but also on the type and mode of loading. In [10] the authors used a Thermographic Damage Criterion (TDC) based on heat dissipation to assess the effect of the machining process on the mechanical behavior of CFRP plates, concluding that the choice of the machining process has a paramount impact on the mechanical behavior of CRFP plates.

After the drilling operation is completed, some damage in the region around the hole boundary is present; delamination being the most serious as it can reduce the load carrying capacity of the joint. Sometimes, due to the nature of the material, this damage is not detected by visual inspection, leading to the need of non-destructive testing (NDT) to assess the soundness of the parts. This effect can be diminished by a correct choice of tool geometry and/or cutting parameters. In general, it is

accepted that a drilling process that reduces the thrust force exerted by the drill chisel edge can prevent the delamination risk.

In this work, some of the typical problems associated with drilling operations are studied and discussed. The main focus is the experimental determination of the critical thrust force for the delamination onset and its correlation with the damage extension caused by the drilling operation. For this purpose, delamination onset tests according to the procedure presented by Lachaud *et al.* [11] are performed. Then, similar plates are drilled and delamination around the hole quantified using image processing and analysis algorithms on enhanced radiographic images [12]. Finally, the delamination onset results are compared with existing analytical models such as the Hocheng-Dharan model [13]. The results found in this work show the importance of adequate knowledge of the material properties when establishing a suitable drilling strategy for the machining of composite materials.

This work also intends to contribute towards setting adequate and sound testing standards to assess the mechanical strength loss of assembly joints in composite parts.

2. Results and Discussion

The results of the maximum thrust force variation according to drill geometry and feed rate were largely published and discussed see, for example, [4,5,13–15]. According to that extensive published work, it is possible to say that, as the feed rate rises, the resultant thrust forces get higher too. It is also possible to say that different geometries cause a variation in the thrust force evolution during drilling and, consequently, on the values of the maximum force obtained during drilling, all the other factors remaining constant: plate characteristics and drill diameter. In addition, it is known that higher diameters cause larger thrust forces. However, the main focus in this work was on the damage assessment and mechanical consequences in terms of bearing resistance, so this issue is not discussed herein.

2.1. Double Cantilever Beam (DCB) Test Results

The results of the DCB test are presented in Table 1, and an example of a load-displacement curve can be seen in Figure 1. The values obtained in this test are in accordance with other values found in the published literature [16,17], and were important for the subsequent mechanical testing.

Table 1. Results of the delamination criteria for the three feed rates studied.

Feed Rate (mm/rev)	Delamination Factor (F_d)		Adjusted Delamination Factor (F_{da})	
	Value	Standard deviation	Value	Standard deviation
0.03	1.186	0.05	1.431	0.11
0.10	1.692	0.08	1.959	0.11
0.20	2.196	0.10	2.566	0.16

2.2. Delamination Assessment

The delamination assessment was carried out according to the procedure described in Section 4.2. The average results concerning the unidirectional plates and all the combinations of drills and feed rates are presented in Tables 1 and 2, respectively. From these results, it is possible to conclude that,

as expected, an increase in the feed rate had a direct effect in the delamination extension, for both assessment criteria. Based on these results and on the previous works referred to above, a clear connection between the thrust force results and the delamination extension can be established. The drilling conditions with less damage corresponded to the coupons associated to the lowest feed rate.

Figure 1. Example of a load-displacement curve from a DCB test.

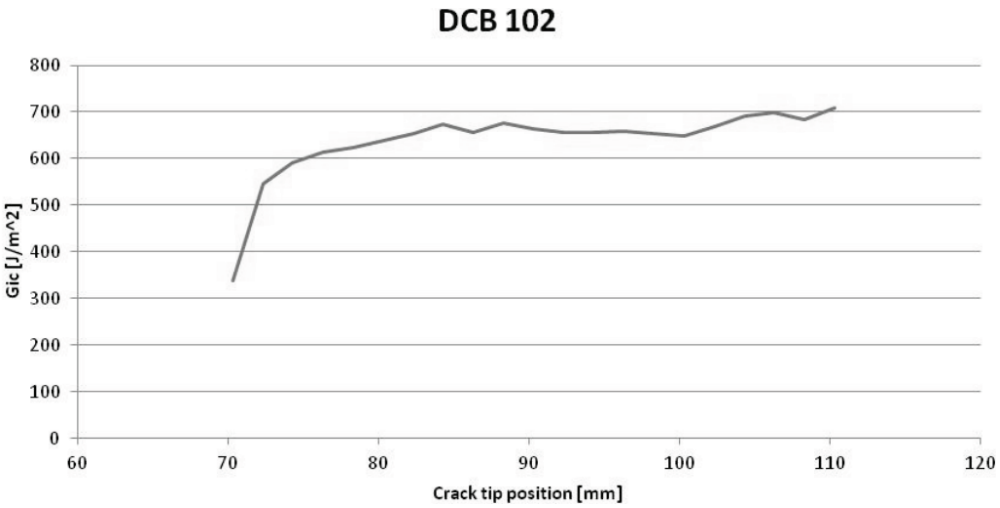

Table 2. Results of the delamination criteria for tool geometry and tool material.

Tool geometry	Delamination Factor (F_d)		Adjusted Delamination Factor (F_{da})	
	Value	Standard deviation	Value	Standard deviation
WC Twist	1.655	0.07	1.858	0.08
HSS Twist	2.034	0.06	2.719	0.08
WC Brad	1.523	0.12	1.695	0.14
WC Step	1.553	0.06	1.670	0.08

The results from the damage extension related with the tool geometry are shown in Table 2. It should be noted that, to reduce the amount of data presented, Table 1 presents average values for the three feed rates used in the experimental work.

Although the stacking sequence was not studied here, it is known that this parameter also had some effect on the delamination extension. The damage in unidirectional plates tends to be higher and extended along the direction of the fibers. This effect is less noticeable in cross-ply or quasi-isotropic plates, where the remaining drilling conditions remain unchanged. Taking into account the tool influence, the lowest values of damage extension were those obtained for the plates drilled with Brad drill. This is a special tool, designed to increase the tension of the fiber before cutting, thus enabling a clean cut and a smooth machined surface. The damage from the step drilled plates was almost equal. The carbide twist drill holes presented a damage extension that is, on the average, 10% higher. Confirming the evidence that HSS drills should not be used for drilling carbon/epoxy composites, the damage extension was always the highest, around 40% more extended damage on the average.

From these results, it is possible to state that the selection of an appropriate combination of tool geometry in relation to the characteristics of the plate is more important than the tool's influence.

This must always be kept in mind when defining the drilling conditions. Unsurprisingly, the feed rate has to be kept as low as possible, to minimize damage extension. The limit on this condition is given by the need to avoid unwanted thermal damages that result from the matrix softening and the need, in industrial terms, to ensure a reasonable number of hourly productions.

2.3. Mechanical Testing

The results of the bearing stress test are shown in Figure 2, including the results for the step drill geometry.

Figure 2. Bearing stress test: (**a**) feed rate effect on the bearing strength; (**b**) drill geometry influence on the bearing strength.

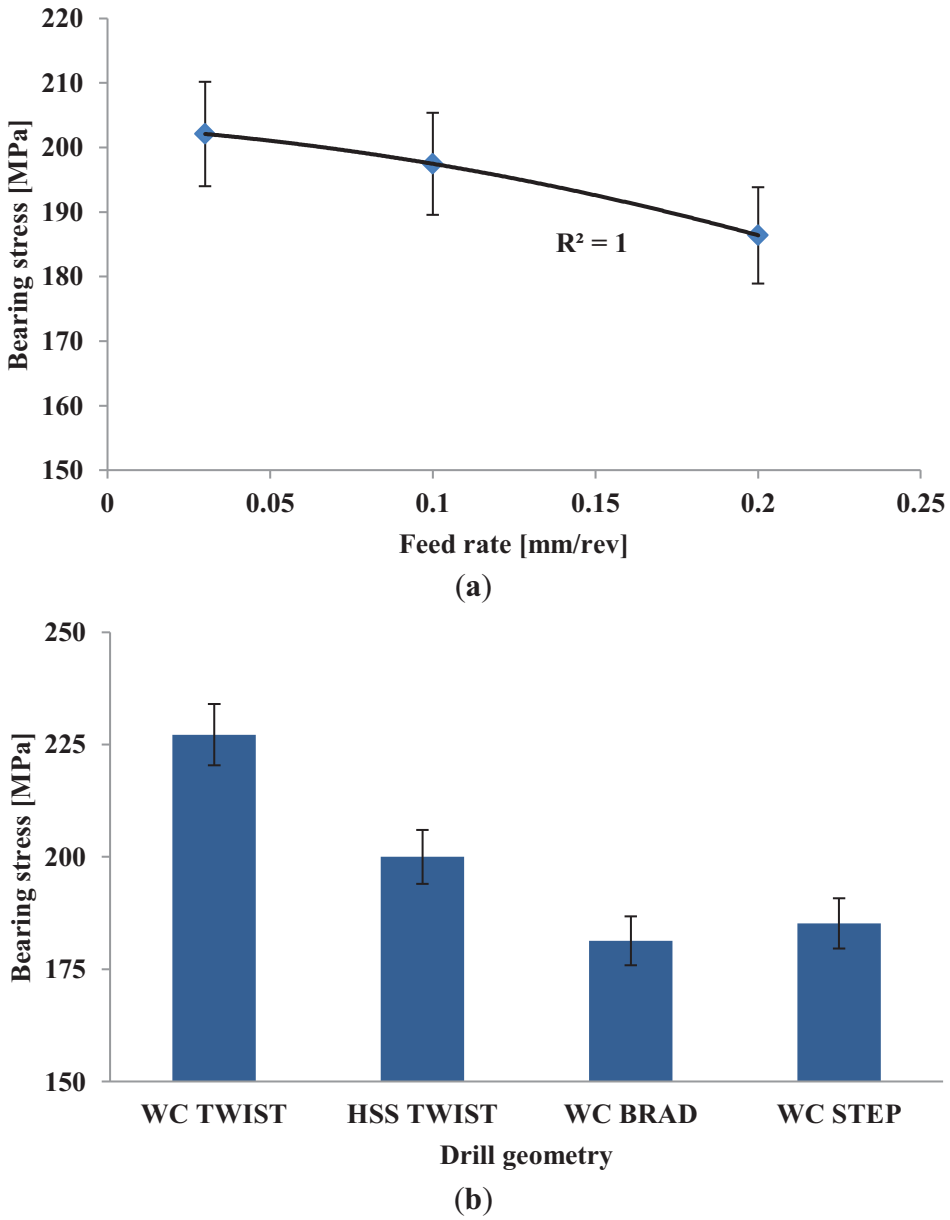

A correlation between feed rate and mechanical loss by the bearing strength can be easily identified in Figure 2a, as one can learn from the polynomial trend line. Larger values of feed, although promoting productivity by higher output of drilled plates per hour, had an adverse effect on

the damage extension, thus leading to mechanical loss. Independently of the tool used, all plates drilled with higher feed rates had lower values of mechanical resistance. From the lowest to the highest feed rate used in this experimental sequence, there was an average loss of 8% on the bearing strength result. This result means that higher feed rates should be avoided when drilling composite plates.

On the other hand, the same correlation could not be identified for the drill geometry. In spite of the larger extension of the damaged area, the plates drilled with the twist drill returned higher values of bearing strength, as observed in Figure 2b. This result suggests that the drill geometry is a key factor in damage onset and propagation. So, a good selection of the tool, combined with the feed rate can reduce the damage extension. Nevertheless, one should keep in mind that the existence of damage, such as delamination, around the hole can sometimes act as a stress relief factor increasing the force-carrying capacity of the plate. Therefore, testing results can sometimes be odd when correlating with damage extension caused by diverse drill geometries.

As to the delamination onset test, the results found are presented in Figure 3. These results correspond to the tests carried out using the tungsten carbide twist drill as a punch. As expected, the delamination onset load increases with the uncut thickness, according to analytical models prediction. Regarding the testing speed, there was a large scattering of the results when using the lowest speed: 1 mm/min. Finally, the experimental work was focused on the two remaining speeds: 3 and 6 mm/min, so more specimens were tested under these two speeds. It seems, from the results presented herein, that the delamination onset load tends to decrease as testing speed increases. This aspect of the testing speed will need further attention as the lower feed rates used in drilling, around 0.01 mm/rev, would correspond to a testing speed of 14 mm/min in a 1400 rpm spindle speed machine, but without the cutting action promoted by the rotating movement of the tool. There is no doubt that it is important to establish a range of acceptable testing speeds to enhance and strengthen the conclusions from this experimental technique.

Figure 3. Delamination onset test results as a function of uncut thickness (*h*) and test speed—experimental values and analytical model Equation (1).

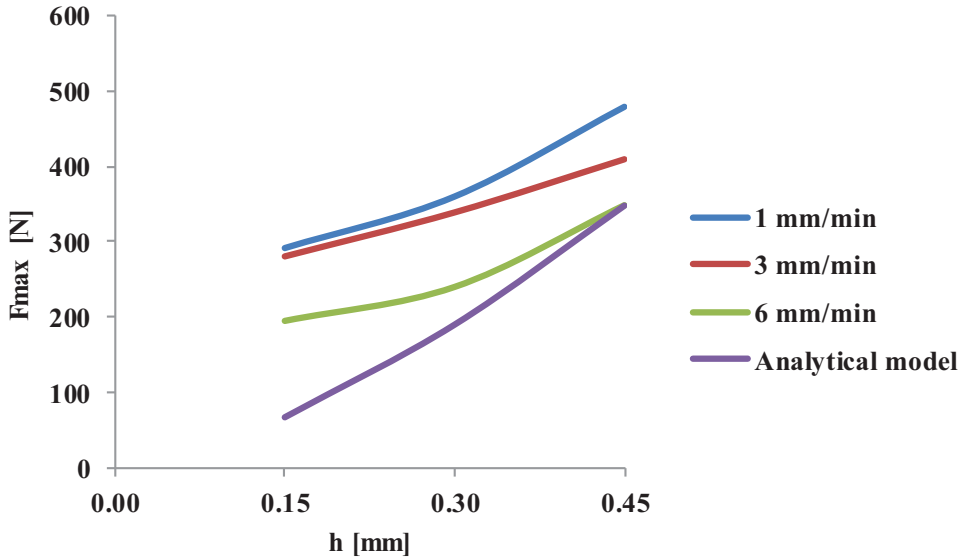

A fourth line was added into the graph of Figure 3, corresponding to the theoretical values obtained when using Equation (1) and the measured properties of the plates. The experimental results are higher than the analytical model values. As the uncut thickness increases, the values tend to be equal. This shows the conservative options of the model, also pointed out by the authors in [13] enabling a cautious selection of parameters and corresponding thrust forces during drilling thus reducing the risk of delamination onset during machining.

Finally, when trying to establish a correlation between the tool geometry and the delamination onset load, no clear trend was found, and some results were surprisingly unstable, giving the general idea of the existence of outlier factors that could influence the results. The dispersion was higher than normally expected when testing composite materials and the trends were not steady when changing from one drill geometry to the other. Some of the factors that could affect this result could be: inadequate testing speed, misalignment of the punch drill axis with the hole axis, friction between the hole walls and the drill or even the evidence that this test will not give any difference regarding the tool geometry. A possible reason is that the piercing action carried out by the drill mainly depends on the plate interlaminar fracture toughness, and not on drill tip geometry and so the shape of the contact zone between drill and plate will not be of any importance.

Further testing is needed to establish some conclusions on the testing speed influence together with a review of the testing device concept and compare the results when using a smaller diameter of the punching tool—or larger diameter of the blind hole—to prevent friction.

3. Delamination in Composite Materials

3.1. Delamination Mechanism

Delamination is a damage that is likely to occur in the interlaminar region, along the contact plan between the adjacent layers in laminate parts. It therefore depends not only on fibre nature but also on resin type and respective properties such as the interlaminar fracture toughness, the elastic modulus or the Poisson ratio. The delamination mechanisms are divided into push-down and peel-up, according to on which laminate side it occurs: drill exit or entrance, respectively.

Peel-up is caused by the cutting force pushing the abraded and cut materials to the flute surface. Initially, the cutting edge of the drill will abrade the laminate. As the drill moves forward, it tends to pull the abraded material along the flute, and the material spirals up before being effectively cut. This action creates a peeling force upwards that tends to separate the upper laminas of the plate (Figure 4a). This peeling force is a function of tool geometry and friction between tool and workpiece [13].

Push-down is a consequence of the compressive thrust force that the chisel edge of the drill always exerts on the workpiece. The laminate under the drill tends to be drawn away from the upper plies, breaking the interlaminar bond in the region around the hole. As the drill approaches the end of the laminate, the uncut thickness becomes smaller and the resistance to deformation decreases. At some point before the laminate is totally penetrated by the drill, the loading exceeds the interlaminar bond strength and delamination occurs (Figure 4b). A suitable tool geometry that lowers the thrust force can reduce the delamination damage [13].

A recent advance on machining strategy was given by Schulze *et al.* [18] minimizing the damage by directing the process forces towards the center of the workpiece. This is achieved through a

combined process of circular and spiral milling on a three-axial machining center. According to the authors, the advantages of this process still require further research.

Figure 4. Delamination mechanisms: (**a**) peel-up delamination at entrance; (**b**) push-down delamination at exit.

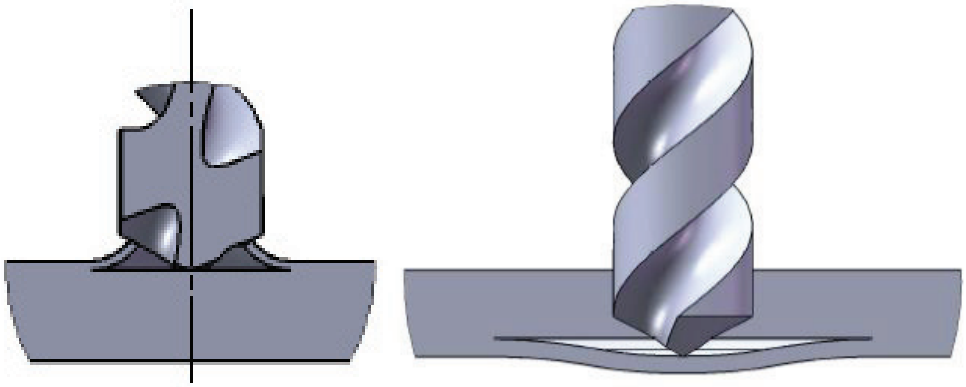

(**a**) (**b**)

The works published by Hocheng and Tsao have contributed to the understanding of the delamination mechanism associated with different drilling conditions, like drill geometry [5,19], the use of a core drill [14] or the influence of using an exit back-up plate on delamination depending on drill geometry [8]. In [5,19], distinct drill bits are compared for drilling-induced delamination. The different drill geometries considered in these works are the twist drill, the saw drill, the candle stick drill, the core drill and the step drill. In [14], only the core drill was studied, showing that grit size and feed rate are the most important parameters for delamination reduction and should be kept low. According to the authors, there are advantages in using special drill bits for composites drilling. The traditional twist drill provides a reduced threshold of the thrust force for delamination onset when compared to other geometries. Concerning these geometries, the higher threshold feed rate at the delamination onset was obtained with the core drill, followed by the candle stick drill, saw drill and step [5].

A comparative study regarding distinct drill geometries and feed rate was presented in [15]. The authors assessed the thrust force, surface roughness and delamination extension for five different drill geometries and two feeds, concluding that the twist drills are well suited for carbon/epoxy plates drilling. However, only one drill diameter was considered. A study on the cutting variables on the thrust force, torque, quality of hole and chip was presented in [20]. A comparative study on the machinability of metallic materials and fiber-reinforced composites and the influence of various factors on the machinablity of these materials was presented in [21].

3.2. Damage Models

The analysis of delamination during drilling in composite materials using fracture mechanics has been developed and different models presented. The models referred to herein are based on the study of carbon/epoxy laminates, although other materials, like glass/epoxy or hybrid composites are also suitable for their application. The main focus on carbon/epoxy laminates can be explained by the fragile nature of the carbon fibers, when compared with glass fibers that are less troublesome in

machining study. The delamination mechanisms are assumed to be modeled by linear-elastic fracture mechanics (LEFM), considering the laminate structure of composites, its high modulus of elasticity in direction 1 and the failure in delamination form.

From known models, the one that is most referred to is the Hocheng and Dharan delamination model [13]. The authors studied the onset of delamination in two different situations: push-down at exit and peel-up at entrance. The first one is the result of the compressive thrust force that the drill exerts on the uncut plies of the laminate, whose thickness is reduced as the drill advances. At some point, the loading exceeds the interlaminar bond strength of the material, and delamination occurs (Figure 4b).

According to the authors, the applicability of LEFM to composite has been previously discussed and confirmed, provided that crack growth is collinear and the crack is in a plan of material symmetry.

In this model, the critical thrust force for delamination onset, F_{crit}, is related to properties of the unidirectional laminate, such as the elastic modulus, E_1, the Poisson ratio, υ_{12}, the interlaminar fracture toughness in mode I, G_{Ic}, and the uncut plate thickness, h:

$$F_{crit} = \pi \frac{8 G_{Ic} E_1 h^{3½}}{3(1-\upsilon_{12}^2)} \tag{1}$$

A comprehensive summary of the steps towards free-delamination holes can be found in [22].

Starting from the model presented in Equation (1), Zitoune and Collombet [23] developed a numerical model and compared the results obtained with the two processes—numerical and analytical. The validation of the numerical model is carried out thanks to quasi-static punching tests in an experimental assembly very similar to the one presented here. A good correlation has been noticed between the numerically calculated efforts and those which were experimentally obtained.

3.3. Damage Extension Assessment

After laminate holes are drilled, it is important to establish criteria to compare the delamination extension caused by different machining processes in an easy way. Damage extension can be evaluated through NDT. Some examples are: the use of a tool maker's microscope [4], ultrasound techniques [24], acoustic emission [25], enhanced radiography [26,27] (Figure 5a), C-Scan [28] (Figure 5b) or Computerized Tomography (CT) [28–30] (Figure 5c). In all these methods, the main goal is to obtain images representing the hole surrounding areas that can be further analyzed and measured, mainly for diameters and areas.

Figure 5. Damage evaluation: (**a**) radiography [26]; (**b**) ultrasonic C-Scan [28]; (**c**) computerized tomography [28].

(**a**) (**b**) (**c**)

Then, it is possible to carry out the quantification of the damaged region to calculate a factor that numerically expresses the damaged region extension and shape. Chen [31] presented a comparing factor that enables the evaluation and analysis of delamination extent in laminated composites. That ratio was called the delamination factor, F_d; and it was defined as the quotient between the maximum delaminated diameter, D_{max}; and the hole nominal diameter, D_0 (Figure 6):

$$F_d = D_{max} / D_0 \quad (2)$$

In the experimental work presented in [31], the author examined the effects of tool geometry and cutting parameters as well as of tool wear on the delamination factor. Two types of drills were used: a carbide drill and a HSS drill. The damage zone was evaluated by using radiographic non-destructive inspection, and the results showed a near-linear relationship between the delamination factor and average thrust forces for both drill materials. The author also concluded that the thrust force increased when the drill point angle increases and that the helix angle did not have a significant effect on this force. Also, the tool flank wear causes an increase of the delamination factor, as the thrust force increases with the tool wear.

Figure 6. Measurement of the maximum delaminated and hole diameters.

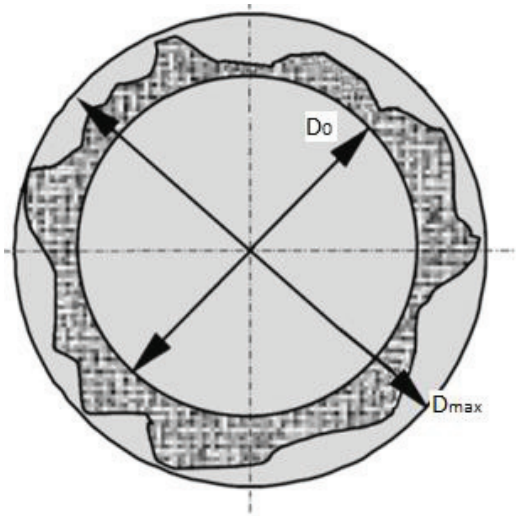

Although the feed rate has a strong influence on the thrust force; the cutting speed has not shown a significant effect on that force. Finally; the author noticed the absence of a built up edge during carbon/epoxy machining.

Mehta *et al.* [32] have suggested a different ratio with the same purpose, named damage ratio, D_{RAT}; defined as the ratio of the hole peripheral damage area, D_{MAR}; to the nominal drilled hole area, A_{AVG}, *i.e.*,:

$$D_{RAT} = D_{MAR}/A_{AVG} \tag{3}$$

This hole damage evaluation method is based on the existence of damage images from C-Scan and pixel counting of the digitized damage area, as described in [32], or from digitized radiographs [33]. In spite of the interesting approach of this criterion, it will not be used in this work.

One limitation of Chen's criterion is related with situations when the delamination involved is not circular, but presents breaks and cracks. In such cases, the values of the delaminated area are more appropriate for the damage quantification. Based on this, Davim *et al.* [34] presented a novel approach known as the Adjusted Delamination Factor, F_{da}:

$$F_{da} = \alpha \frac{D_{max}}{D_0} + \beta \frac{A_{max}}{A} \tag{4}$$

where A_{max} is the area corresponding to the maximum delaminated diameter D_{max}; and A is the hole nominal area. In this new criterion, the first term is the conventional delamination factor and a second term was added to take into account the damaged area contribution, and the parameters α and β are used as weights. Their sum always equal to 1 (one).

4. Experimental Work and Discussion

4.1. Composite Plates Production and Drilling

For the experimental work, a batch of 300 × 300 mm^2 carbon/epoxy plates using prepreg CC160 ET 443, SAATI, Appiano Gentile, Italy, with 24 layers were produced. The unidirectional plates intended for DCB testing had a 70 mm Teflon® insert, Wrightlon, AirTech, Huntington Beach, CA, USA, at the extremities to act as a pre-crack. The plates were then cured for one hour under 300 kPa pressure and 130 °C, followed by cooling. Final plate thickness was equal to 4 mm. Then, the plates were cut into test coupons of 135 × 36 mm^2 for the bearing tests and the delamination onset test experiments and in coupons with dimensions according to the mechanical test specifications—DCB test, tensile test. Calcinations tests according to EN ISO 1172:1988 [35] were performed and the result showed a fiber content of 64%. Tensile tests according to ASTM D3039-08 [36] were also carried out and the plate's properties, presented in Table 3, were found (see Section 2.1).

Table 3. Material properties.

Property	Fiber Content (%)	R_m (MPa)	E_1 (GPa)	E_2 (GPa)	ν	G_{Ic} (N/mm)
Value	64	1700	111	7	0.29	0.419
Standard deviation	–	20	9	1	0.05	0.017

The experimental work initiated with the drilling of the laminate plates for thrust force monitoring, delamination measurement by enhanced radiography and automated computational algorithms of image processing and analysis and mechanical tests. Then, the composite coupons were

tested according to ASTM D5961-10 [37]—Procedure A. Finally, the results of the delamination damage assessment were correlated with the bearing stress and delamination onset tests results.

The drilling operation was carried out in a 3.7 kW DENFORD Triac Centre CNC machine (Denford, West Yorkshire, UK). As it has been previously identified, feed rate is crucial compared to spindle speed in the development of thrust forces [26]. The cutting speed was kept constant and equal to 2800 rpm and the feed rate had three levels: low feed rate of 0.03 mm/rev, intermediate feed rate equal to 0.10 mm/rev and high feed rate of 0.20 mm/rev. These cutting parameters were selected according to previous published works [15,26,33] as well as the tool manufacturer's recommendation. A tool diameter of 6 mm was used combined with the three drill geometries: twist, Brad and step. Details on the drills can be found in [15]. The tool selection is in line with past papers published by the same authors, see [6,12,15,26,33]. Twist drill is still the most common drilling tool used in almost every tool shop, Brad drill is a commercial drill normally available in tool manufacturers' catalogue and step drill is an experimental prototype tool that has been studied and developed by the first author along the last years. Although other geometries are normally referred to in published papers [3–5,7,8,11,14,18–22,28] they are not often found in current tools products.

The experimental sequence described herein does not correspond to a complete factorial or to a Design of Experiment plan as there were some limitations on the tool availability and number of test coupons. Considering HSS tools, there are no Brad or step tools or other geometry for composites material drilling. This option was to highlight the worst possible case in terms of experimental results and to enable us to demonstrate the consequences for mechanical test results when comparing the results of HSS and WC twist drill. So, the main target is the comparison of three different tool geometries.

For the DCB test specimens according to ASTM D5528-13 [38], it was necessary to bond piano hinges at the edge of the Teflon insert. To enable the bonding operation, both the piano hinges and the extremities of the specimens were prepared with sandpaper, carefully cleaned and bonded using industrial adhesive Araldite® 2012 (Everberg, Belgium). Then, one of the sides of each specimen was painted white and marked with vertical lines every 2 mm with a special mark at the end of the Teflon® insert (Everberg, Belgium).

The specimens for the delamination onset test were blind drilled using an end mill and stopping the machining cycle to have different uncut thicknesses according to the height corresponding to one to four plies, that is to say, 0.15 mm, 0.30 mm, 0.45 mm and 0.60 mm.

4.2. Delamination Assessment

After the drilling process, the delaminated region around each drilled hole was evaluated using enhanced digital radiography. To generate a suitable image contrast, the plates were first immersed in di-iodomethane for approximately 15 to 20 min. Then the radiographic images were acquired using a 60 kV, 300 kHz Kodak 2100 X-Ray system associated with a Kodak RVG 5100 digital acquisition system (Kodak Corp., Rochester, NY, USA). The exposition time was set to 0.125 s.

Each radiographic image was computationally processed to identify and characterize the regions of interest: hole region, delaminated and non-delaminated regions. The hole region corresponds to the central area, the delaminated region consists on a dark border around the machined hole, and the non-delaminated regions are lighter areas located outside the damaged region (Figure 7) [26].

The final goal of the image processing and analysis performed was to automatically measure the damaged diameters and areas in each radiographic image. This was achieved by using in the image segmentation step a neuronal network with 1 input layer with 3 neurons, 1 hidden layer with 7 neurons [39], 1 output layer with 3 neurons, and the logistic function [40] as the neurons activation function, which was trained using the back propagation learning algorithm [41]. The inputs of the network were each image pixel's value, and the output was the correspondent segmentation region. Further details of the neuronal network used can be found in [42]. After the identification of the three regions presented in an input image, the related diameter and area values were computed: the diameters were calculated by searching for the longest diagonal within the delaminated region, and the areas by summing up the pixels within the associated regions.

Figure 7. Pipeline of the computational processing of a radiographic image: (**a**) original image; (**b**) image segmented by using a neuronal network; (**c**) identification of the delamination region.

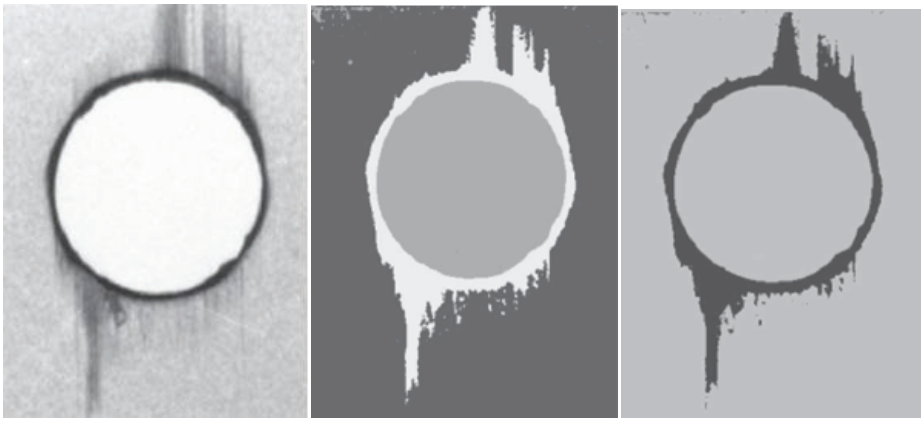

(**a**) (**b**) (**c**)

The values obtained from the radiography images can be used to determine the delamination factor, F_d, [31], the Damage Ratio, [32], and the adjusted delamination factor, F_{da}, [34], according to Equations (2), (3) and (4) (see Section 3.3).

So, taking advantage of the computational techniques of imaging processing and analysis, the adjusted delamination factor was used in this work for damage assessment.

4.3. Mechanical Testing

In all the tests performed in this work, a Shimadzu AG-X/100 kN Universal Testing machine (Shimadzu, Kyoto, Japan) equipped with a Trapezium X software for data registration was used.

The DCB tests according to ASTM D5528 -13 [38] were carried out at a testing speed of 5 mm/min both for pre-crack and final crack opening. The values of time, force and displacement were registered by the Shimadzu machine system, and a synchronization method was developed to ensure data correlation between the force and crack opening. The values of the energy release rate were calculated using the Modified Beam Theory method with a 5% offset for the initiation values of the interlaminar fracture toughness in Mode I, G_{Ic}.

The mechanical test carried out to assess the damage effects on plate resistance in the area of the mechanical joint was the "Bearing test" according to ASTM D5961M-10 [37]. This test was used to assess the effect of the delamination extension on the mechanical properties of the drilled plates in the joint area. Test coupons of 135 × 36 mm^2 were cut and drilled under the same experimental conditions.

Finally, for the delamination onset test, a device based on the work of Lachaud *et al.* [11] was designed and built, see Figure 8. With the purpose of evaluating the several possible effects of test variables, three different testing speeds were used: 1 mm/min, 3 mm/min and 6 mm/min. These testing speeds were combined with the plates previously drilled with blind holes machined using twist, Brad and step drills. Details on these drills can be found in [15]. To carry out the test, a perpendicular load was applied using a drill as a punch (Figure 8). The drill movement was only linear, without rotation.

Figure 8. Delamination onset test: (**a**) device presented in [11]; (**b**) experimental work.

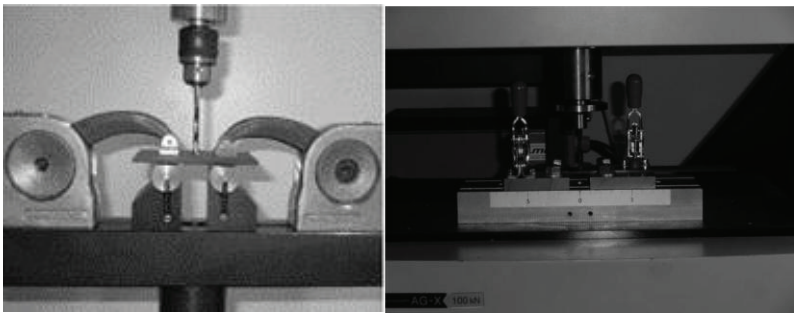

(**a**) (**b**)

5. Conclusions

Carbon fiber reinforced laminates were drilled with the objective of comparing the performance of three different tool geometries regarding the bearing stress and delamination onset load. Relevant results considered for assessment were the delamination extension and the mechanical strength by the bearing stress test and delamination onset test. A batch of plates was prepared to perform DCB tests. According to the experimental findings, it was possible to make the following conclusions:

- As expected, when dealing with composite materials, some dispersion on the results was found;
- The results of the DCB test to determine the interlaminar fracture toughness were within the predicted values;
- The synchronization system developed for the DCB test allows for an easy trace of the load-displacement curve and crack opening measurement, reducing error hazard;
- The feed rate influence is well known and the results confirmed that higher feeds correspond to higher delamination extension and lower values of bearing resistance. So, in conventional drilling, the feed rates should be kept as conservative as possible;
- In the delamination onset test, as the uncut thickness increases, the delamination onset load also increases. This was an expected outcome.

- Also in the delamination onset test, as testing speed increases, the delamination onset result tends to decrease. For this test, there is a need to establish a standardized speed and to enhance the procedure for test results robustness:
- The influence of the punch geometry (drill) has to be thoroughly investigated as no clear trend was found.
- In future works, the effect of alternative stacking sequences, like cross-ply or quasi-isotropic, deserve some attention.
- Future development of the present work will have the purpose of adding analytic and FEM models for the simulation of drilling with delamination onset determination.

Acknowledgments

This work was partially granted by Fundação para a Ciência e a Tecnologia (FCT), in Portugal, in the scope of the strategic funding project PEst-OE/EME/UI0615/2011.

The authors would like to express their acknowledgment to INEGI for the fabrication of the plates, to the Mechanical Workshop of DEM/ISEP for the drilling work and to the Mechanical Test Laboratory of DEM/ISEP for the mechanical test work.

Author contributions

Luís Miguel P. Durão, Jorge Filipe S. Marques and Oscar N.G. Andrade had performed the experimental work regarding coupon preparation and mechanical testing. João Manuel R.S. TavaresVictor Hugo C. de Albuquerque contributed to the delamination assessment work. All authors participated in manuscript writing and in converting data into graphical information.

Nomenclature

A	hole nominal area
A_{AVG}	nominal drilled hole area
A_{max}	area corresponding to the maximum delaminated diameter
D_0	hole nominal diameter
D_{max}	maximum delaminated diameter
D_{RAT}	damage ratio
D_{MAR}	hole peripheral damage area
E_1	elastic modulus in 1-direction
E_2	elastic modulus in 2-direction
F_{crit}	critical thrust force for delamination onset
F_d	delamination factor
F_{da}	adjusted delamination factor
G_{Ic}	interlaminar fracture toughness in mode I
G_{IIc}	interlaminar fracture toughness in mode II
υ_{12}	Poisson ratio

Conflicts of Interest

The authors declare no conflict of interest.

References

1. Gilpin, A. Tools solutions for machining composites. *Reinf. Plast.* **2009**, *53*, 30–33.
2. Abrate, S. Machining of Composite Materials. In *Composites Engineering Handbook*; Mallick, P.K., Ed.; Marcel Dekker: New York, NY, USA, 1997; pp. 777–809.
3. Koplev, A.; Lystrup, A.; Vorm, T. The cutting process, chips, and cutting forces in machining CFRP. *Composites* **1983**, *14*, 371–376.
4. Davim, J.P.; Reis, P. Drilling carbon fibre reinforced plastics manufactured by autoclave—Experimental and statistical study. *Mater. Des.* **2003**, *24*, 315–324.
5. Hocheng, H.; Tsao, C.C. Effects of special drill bits on drilling-induced delamination of composite materials. *Int. J. Mach. Tools Manuf.* **2006**, *46*, 1403–1416.
6. Durão, L.M.P.; Tavares, J.M.R.S.; Marques, A.T.; Baptista, A.M.; Magalhães, A.G. Damage analysis of carbon/epoxy plates after drilling. *Int. J. Mater. Prod. Technol.* **2008**, *32*, 226–242.
7. Zitoune, R.; El-Mansori, M.; Krishnaraj, V. Tribo-functional design of double cone drill implications in tool wear during drilling of copper mesh/CFRP/woven ply. *Wear* **2013**, *302*, 1560–1567.
8. Tsao, C.C.; Hocheng, H. Effects of exit back-up on delamination in drilling composite materials using a saw drill and a core drill. *Int. J. Mach. Tools Manuf.* **2005**, *45*, 1261–1270.
9. Haddad, M.; Zitoune, R.; Bougherara, H.; Eyma, F.; Castanié, B. Study of trimming damages of CFRP structures in function of the machining processes and their impact on the mechanical behaviour. *Compos. Part B Eng.* **2014**, *57*, 136–143.
10. Saleem, M.; Toubal, L.; Zitoune, R.; Bougherara, H. Investigating the effect of machining processes on the mechanical behaviour of composite plates with circular holes. *Compos. Part A Appl. Sci. Manuf.* **2013**, *55*, 169–177.
11. Lachaud, F.; Piquet, R.; Collombet, F.; Surcin, L. Drilling of composite structures. *Compos. Struct.* **2001**, *52*, 511–516.
12. Durão, L.M.P.; Gonçalves, D.J.S.; Tavares, J.M.R.S.; Albuquerque, V.H.C.; Marques, A.T. Comparative analysis of drills for composite laminates. *J. Compos. Mater*. **2012**, *46*, 1649–1659.
13. Hocheng, H.; Dharan, C.K.H. Delamination during drilling in composite laminates. *J. Eng. Ind.* **1990**, *112*, 236–239.
14. Tsao, C.C.; Hocheng, H. Parametric study on thrust force of core drill. *J. Mater. Process. Technol.* **2007**, *192–193*, 37–40.
15. Durão, L.M.P.; Gonçalves, D.J.S.; Tavares, J.M.R.S.; de Albuquerque, V.H.C.; Vieira, A.A.; Marques, A.T. Drilling tool geometry evaluation for reinforced composite laminates. *Compos. Struct.* **2010**, *92*, 1545–1550.
16. Savage, G. Enhancing the exploitation and efficiency of fibre-reinforced composite structures by improvement of interlaminar fracture toughness. *Eng. Fail. Anal*. **2006**, *13*, 198–209.
17. Pereira, A.B.; de Morais, A.B.; de Moura, M.F.S.F.; Magalhães, A.G. Mode I interlaminar fracture of woven glass/epoxy multidirectional laminates. *Compos. Part A* **2005**, *36*, 1119–1127.

18. Schulze, V.; Becke, C.; Weidenmann, K.; Dietrich, S. Machining strategies for hole making in composites with minimal workpiece damage by directing the process forces inwards. *J. Mater. Process. Technol.* **2011**, *211*, 329–338.
19. Hocheng, H.; Tsao, C.C. Comprehensive analysis of delamination in drilling of composite materials with various drill bits. *J. Mater. Process. Technol.* **2003**, *140*, 335–339.
20. Zitoune, R.; Krishnaraj, V.; Collombet, F. Study of drilling of composite material and aluminium stack. *Compos. Struct.* **2010**, *92*, 1246–1255.
21. Krishnaraj, V.; Zitoune, R.; Davim, J.P. Drilling of polymer-matrix composites. In *Springer Briefs in Applied Sciences and Technology*; Davim, J.P., Ed.; Springer: Heidelberg, Germany, 2014.
22. Hocheng, H.; Tsao, C.C. The path towards delamination-free drilling of composite materials. *J. Mater. Process. Technol.* **2005**, *167*, 251–264.
23. Zitoune, R.; Collombet, F. Numerical prediction of the thrust force responsible of delamination during the drilling of the long-fibre composite structures. *Compos. Part A Appl. Sci. Manuf.* **2007**, *38*, 858–866.
24. Hosur, M.V.; Chowdhury, F.; Jeelani, S. Low-velocity impact response and ultrasonic NDE of woven carbon/epoxy—Nanoclay nanocomposites. *J. Compos. Mater.* **2007**, *41*, 2195–2212.
25. Jong, H.J. Transverse cracking in a cross-ply composite laminate—Detection in acoustic emission and source characterization. *J. Compos. Mater.* **2006**, *40*, 37–69.
26. De Albuquerque, V.H.C.; Tavares, J.M.R.S.; Durão, L.M.P. Evaluation of delamination damages on composite plates from radiographic image processing using an artificial neural network. *J. Compos. Mater.* **2010**, *44*, 1139–1159.
27. Johnson, W.S.; Treasurer, P.; Woodruff, G.W. radiographic investigation of the effects of ply modification on damage development in laminates containing circular holes. *J. Compos. Mater.* **2008**, *42*, 2143–2161.
28. Tsao, C.C.; Hocheng, H. Computerized tomography and C-Scan for measuring delamination in the drilling of composite materials using various drills. *Int. J. Mach. Tools Manuf.* **2005**, *45*, 1282–1287.
29. Wang, L.B.; Frost, J.D.; Voyiadjis, G.Z.; Harman, T.P. Quantification of damage parameters using X-ray tomography images, *Mech. Mater.* **2003**, *35*, 777–790.
30. Schilling, P.J.; Karedla, B.P.R.; Tatiparthi, A.K.; Verges, M.A.; Herrington, P.D. X-ray computed microtomography of internal damage in fiber reinforced polymer matrix composites. *Compos. Sci. Technol.* **2005**, *65*, 2071–2078.
31. Chen, W.C. Some experimental investigations in the drilling of carbon fibre-reinforced plastic (CFRP) composite laminates. *Int. J. Mach. Tools Manuf.* **1997**, *37*, 1097–1108.
32. Mehta, M.; Reinhart, T.J.; Soni, A.H. Effect of Fastener Hole Drilling Anomalies on Structural Integrity of PMR-15/Gr Composite Laminates. In Proceedings of the Machining Composite Materials Symposium, ASM Materials Week, Chicago, IL, USA, 1–5 November 1992; pp. 113–126.
33. Durão, L.M.P.; Magalhães, A.G.; Tavares, J.M.R.S.; Marques, A.T. Analyzing objects in images for estimating the delamination influence on load carrying capacity of composite laminates. *Electron. Lett. Comput. Vis. Image Anal.* **2008**, *7*, 11–21.

34. Davim, J.P.; Campos Rubio, J.C.; Abrão, A.M. A novel approach based on digital image analysis to evaluate the delamination factor after drilling composite laminates. *Compos. Sci. Technol.* **2007**, *67*, 1939–1945.
35. International Organization for Standardization. *Textile-Glass-Reinforced Plastics. Prepregs, Moulding Compounds and Laminates. Determination of the Textile Glass and Mineral-Filler Content. Calcination Methods*; EN ISO 1172:1998; ISO (International Organization for Standardization): Geneva, Switzerland, 1998.
36. ASTM D3039–08. *Standard Test Method for Tensile Properties of Polymer Matrix Composite Materials*; ASTM International: West Conshohocken, PA, USA.
37. ASTM D5961/D5961M-10. *Standard Test Method for Bearing Response of Polymer Matrix Composite Laminates*; ASTM International: West Conshohocken, PA, USA, 2010.
38. ASTM D5528-13. *Standard Test Method for Mode I Interlaminar Fracture Toughness of Unidirectional Fiber-Reinforced Polymer Matrix Composites*; ASTM International: West Conshohocken, PA, USA, 2013.
39. Bodyanskiy, Y.; Kolodyazhniy, V.; Otto, P. Neuro-fuzzy Kolmogorov's network for time series prediction and pattern classification. In *KI 2005: Advances in Artificial Intelligence*; Furbach, U., Ed.; Springer LNCS: Berlin, Heidelberg, Germany, 2005; Volume 3698, pp. 191–202.
40. Elliott, D.L.; Better, A. *Activation Function for Artificial Neuronal Network*. ISR Technical Report TR 93–8; Institute for Systems Research, University of Maryland: College Park, MD, USA, 1993.
41. Singh, V.; Rao, S.M. Application of image processing and radial basis neuronal network techniques for ore sorting and ore classification. *Miner. Eng.* **2005**, *18*, 1412–1420.
42. De Albuquerque, V.H.C.; Silva, C.C.; Menezes, T.I.S.; Farias, J.P.; Tavares, J.M.R.S. Automatic evaluation of nickel alloy secondary phases from SEM images. *Microsc. Res. Tech.* **2011**, *74*, 36–46.

Experimental Analysis of the Influence of Drill Point Angle and Wear on the Drilling of Woven CFRPs

Norberto Feito, José Díaz-Álvarez, Antonio Díaz-Álvarez, José Luis Cantero and María Henar Miguélez

Abstract: This paper focuses on the effect of the drill geometry on the drilling of woven Carbon Fiber Reinforced Polymer composite (CFRPs). Although different geometrical effects can be considered in drilling CFRPs, the present work focuses on the influence of point angle and wear because they are the important factors influencing hole quality and machining forces. Surface quality was evaluated in terms of delamination and superficial defects. Three different point angles were tested representative of the geometries commonly used in the industry. Two wear modes were considered, being representative of the wear patterns commonly observed when drilling CFRPs: flank wear and honed cutting edge. It was found that the crossed influence of the point angle and wear were significant to the thrust force. Delamination at the hole entry and exit showed opposite trends with the change of geometry. Also, cutting parameters were checked showing the feed's dominant influence on surface damage.

Reprinted from *Materials*. Cite as: Feito, N.; Díaz-Álvarez, J.; Díaz-Álvarez, A.; Cantero. J.L.; Miguélez, M.H. Experimental Analysis of the Influence of Drill Point Angle and Wear on the Drilling of Woven CFRPs. *Materials* **2014**, *7*, 4258ï 4271.

1. Introduction

Carbon Fiber Reinforced Polymer (CFRP) composites combine fatigue and corrosion resistance, light weight and high specific stiffness and strength. These properties make CFRPs suitable for a wide range of structural applications [1]. Within this family of materials, woven graphite fiber epoxy composites have been extensively used in aerospace, automotive and civil applications. Woven CFRPs exhibit higher strength-to weight ratio and higher fracture toughness than unidirectional composites [2].

Although composite components are manufactured close to the final shape, they usually require machining operations in order to achieve dimensional tolerances and assembly specifications. In most cases the component is drilled previously to mechanical joining [3]. Drilling operations of woven carbon composite CFRPs should be designed to be productive processes ensuring the quality of the resultant component. This operation is performed in a high value component, the susceptibility of the composite to undergo machining-induced damage highlights the importance of controlling the process. The composite is exposed to the generation of damage during processing, mainly delamination. This phenomenon is related to machining parameters and drill geometry. Drilling operations of CFRPs involve strong tool wear due to the presence of hard fibers; wear progression leads to variations of the initial geometry of the drill [4].

Various authors have studied CFRPs drilling, mainly in the case of unidirectional composites. A brief summary of the contributions focusing on woven CFRP drilling is presented in the following paragraphs.

Karpat *et al.* [5] analyzed the drilling performance of the double point angle drill for woven CFRP laminates. Uncoated carbide drill and diamond coated carbide drills with different drill point angles were tested in drilling experiments of thick fabric woven CFRP laminates. The feed was more influential than cutting speed on damage generation. At elevated feed rates, the hole diameter tolerance was observed to be more critical than the hole exit delamination.

The influence of the drill point angle on the machining forces and the drill hole quality (in terms of delamination, fraying and burr formation) was analyzed in [6] for woven CFRPs. Increased point angles resulted in enhanced thrust force; however, the torque remains almost constant. The quality at the hole entrance was enhanced when increasing point angles while it was poorer at the exit. The increment of cutting speed lead to negligible differences in the hole quality but resulted in increased thrust forces and decreased drilling torques. This behavior was also observed when drilling cross-ply composite materials with twist drill bits [7]: point angle equal to 120° produced less delamination at hole entry than point angle equal to 85° even though the thrust force was higher in the former case.

The influence of different types of tool geometry when drilling unidirectional CFRP $[0/90]_{13}$ was analyzed in [8]. "SPUR" drill bit (commonly used for wood materials) gave the best results causing small damage extension in the hole perimeter. On the other hand, a twist drill presented higher delamination located at the hole entrance. Similar tests were carried out on unidirectional CFRPs in [9] showing no advantage for step drill when compared with commercial drill bit, which reduced the surface damage.

On the other hand, wear evolution influences drill geometry. The initial design of the fresh tool is modified because of wear progression and, consequently, the effective cutting geometry is varied.

Mayuet *et al.* [10] carried out drilling tests of woven CFRP with conventional carbide drill geometry. It was demonstrated that the abrasion due to the presence of hard fibers was the dominant wear mechanism. The matrix adhesion had a much lower effect. The influence of wear in hole quality was demonstrated since delamination at the hole exit increased significantly as the number of machined holes increased.

Illiescu *et al.* [11] analyzed the influence of feed rate and tool wear in drilling of woven CFRPs with coated and uncoated drills. The feed rate and tool wear were the most significant factors affecting the thrust force. The torque was much less sensitive to wear than the thrust force. The contact length and the axil force applied at the cutting edge were the main factors involved in wear evolution, in both cases considered (coated and uncoated drills).

Shyha *et al.* [12] analyzed the drilling of small holes (1.5 mm); with two different geometries: conventional twisted and stepped. Delamination at the hole entrance was higher for the stepped drill than for the twisted drill. Increases in the feed rate also lead to delamination enhancement. However, the increment of point angle, from 118° to 140°, lead to decrease of delamination.

Rawat and Attia [13] analyzed the tool wear mechanisms of carbide tools in high speed drilling (10,000–15,000 rpm) of woven CFRPs. Fracture (chipping) at the beginning of drilling process and

subsequent abrasion were the main wear mechanisms. Abrasive wear on the flank face of the primary cutting edge was stronger than the wear at the rake face.

The influence of cutting edge rounding (CER) and its correlation with surface damage in drilling of woven CFRPs was analyzed in [14]. A correlation between delamination, machining forces and cutting edge rounding was found. Numerical analysis of the influence of CER in the elemental case of orthogonal cutting has been developed by the authors in [15]. The interest of analyzing drilling-induced delamination has motivated the recent development of complex models for drilling. These numerical models have shown good correlation between measured and predicted torque and thrust force as well as delamination extension [16,17].

Although drilling operations of woven composite have motivated the development of different studies, it is still a challenge to advance the comprehension of the effect of tool geometry and the level of wear. In fact the analysis of the crossed effect of the tool geometry and the geometrical changes due to wear progression has been poorly developed in the literature.

The objective of this paper is analyzing the effect of the drill point angle combined with the geometrical effect of drill wear evolution. Two different types of wear modes were studied: flank wear (commonly identified in the literature as the dominant wear mode) and cutting edge honing (resulting from the transition from new acute to used cutting edge). The effect of cutting parameters (cutting speed and feed rate) were also studied. Resultant thrust force and torque have been evaluated together with surface integrity, analyzed in terms of delamination at the entrance and exit of the hole.

2. Experimental Work

2.1. Workpiece Material

The material studied in this work is a woven CFRP composite, based on AS-4 carbon fiber and epoxy matrix (55.29% resin content) manufactured by Hexcel Composites (Madrid, Spain). The specimens were cut in plates of 120 mm × 29 mm and 2.2 mm thick, composed of 10 plies with the same fiber orientation. The characteristics and mechanical properties of the workpiece provided by the composite manufacturer are presented in the Table 1, where ρ is density; E_i elastic modulus in the direction i; υ_{ij} Poisson coefficient; G_{ij} elastic modulus in shear directions; X_t, Y_t and S_t maximum tensile stress in longitudinal and shear directions respectively; X_c and Y_c maximum compressive stress in longitudinal directions.

Table 1. Characteristics and mechanical properties of the composite.

ρ	$E_1 = E_2$	E_3	υ_{12}	$\upsilon_{13} = \upsilon_{23}$
1570 Kg/m^3	68 GPa	10 GPa	0.22	0.49
G_{12}	$G_{23} = G_{13}$	$X_t = Y_t$	$X_c = Y_c$	S_t
5 GPa	4.5 GPa	795 MPa	860 MPa	98 MPa

2.2. Drills

Uncoated helicoidal carbide drills recommended by the manufacturer GUHRING for CFRPs drilling were used. Nominal diameter was equal to 6 mm with 30° helix angle. Three different values of the point angle 90°, 118° and 140° were used. Three different stages concerning wear evolution

were tested: fresh drill, flank wear equal to 0.3 mm and honed cutting edge with length equal to 0.05 mm (see Figure 1).

Figure 1. Edge geometry of the drills: (**a**) fresh tool; (**b**) flank wear; and (**c**) honed edge.

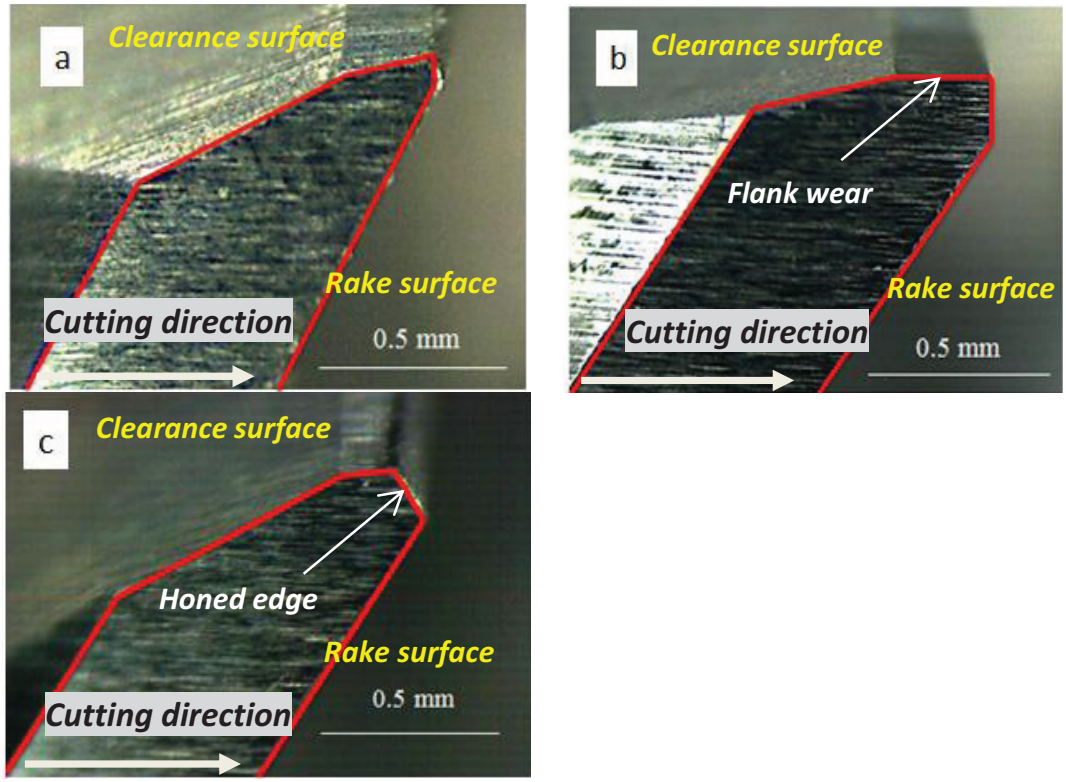

The worn geometries were artificially generated using grinding. The level of wear has been stated according to values corresponding to the end of tool life in the literature. Faraz *et al.* [14] reported a value of flank around 0.25 mm corresponding with advanced wear progression. On the other hand, honed edge is an approximation to chipping wear observed in drilling CFRP. As drilling starts chipping appears because acute cutting edges are not able to tolerate high stress. This phenomenon was reported by Rawat *et al.* [13] with an extension of honed edge zone similar to that considered in the present work.

2.3. Machining Tests

The drilling tests were carried out on a machining center (B500 KONDIA, Kondia, Elgoibar, Spain). The machining center was equipped with a rotating dynamometer (Kistler 9123C, Winterthur, Switzerland) used for the measurement of the three force components F_x, F_y, F_z and the drive moment M_z on the rotating tool. The acquisition system coupled to the machine tool is shown in Figure 2.

Drilling induced damage was quantified in terms of the delamination factor (F_d) being the ratio between the maximum diameter of delaminated area and the nominal diameter of the hole (see Figure 3). Other defects induced during machining were analyzed from observation of images of the machined hole obtained with a stereo microscope (Optika SZR, Ponteranica, Italy).

Figure 2. Experimental device for drilling tests.

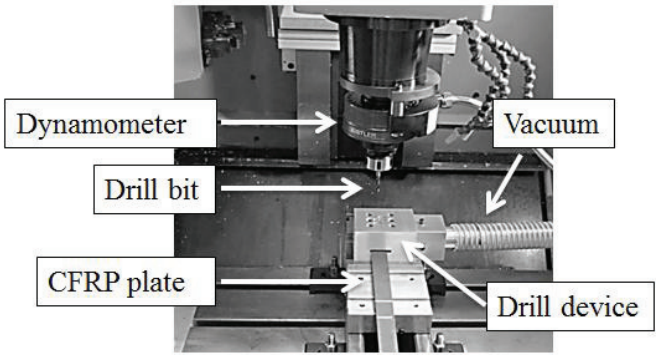

Figure 3. Example of delaminated specimen for calculation of delamination factor F_d.

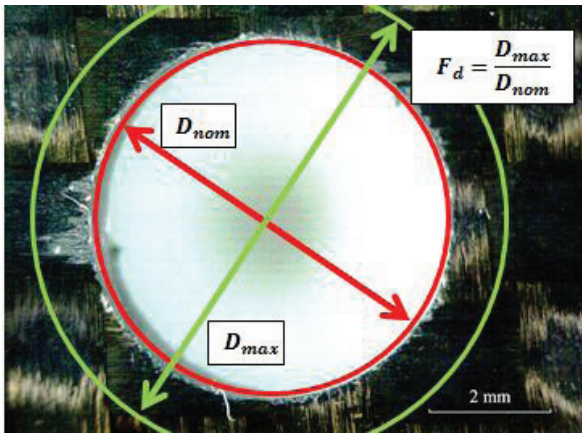

Concerning the cutting conditions, the drilling experiments were conducted without coolant and the cutting parameters summarized in Table 2. Machining operations in composites are commonly carried out in dry conditions because it is required to avoid the composite contamination with the cutting fluid. The machining parameters (cutting speed 25–100 m/min and feed 0.05–0.2 mm/rev) were selected following the recommendations of the drills manufacturer GUHRING for drilling CFRPs.

Table 2. Cutting parameters used in drilling tests: f, feed and V, cutting speed.

Parameter	**Range**		
f [mm/rev]	0.05	0.1	0.15
V [m/min]	25	50	100

Drilling tests were performed using a supporting back plate previously drilled with hole diameter equal to 6.2 mm. The use of back plate is commonly desired in industry when drilling plates of composite in order to diminish delamination. The influence of the position of the drilled hole related to the textile float was not considered in this paper. Although this parameter may influence the delamination, the drilling tests were carried out in random relative positions of the drill to the textile float. Observed delamination did not show significant differences for the tests carried out in the same cutting conditions despite the variations of the relative position drilled hole/float, indicating low influence of this parameter.

3. Results and Discussion

3.1. Thrust Force and Torque

The evolution of thrust force and torque with cutting time was recorded using the dynamometer. The maximum level of thrust force obtained during drilling tests is presented in Figure 4. The maximum thrust force obtained with new and worn drills is presented for the different values of point angle and cutting speed considered. It is possible to observe the negligible influence of the point angle on thrust force when fresh drill is used since the projection of the resultant force in the axial direction is the same for all point angles. The increment of feed lead to thrust force enhancement (the maximum values of thrust force obtained with new tools ranged between 50 and 150 N for all cases tested).

Figure 4. Thrust force for three point angles at different cutting speeds (measurement variations are indicated including error bars): (**a**) cutting speed 25 m/min; (**b**) cutting speed 50 m/min; and (**c**) cutting speed 100 m/min.

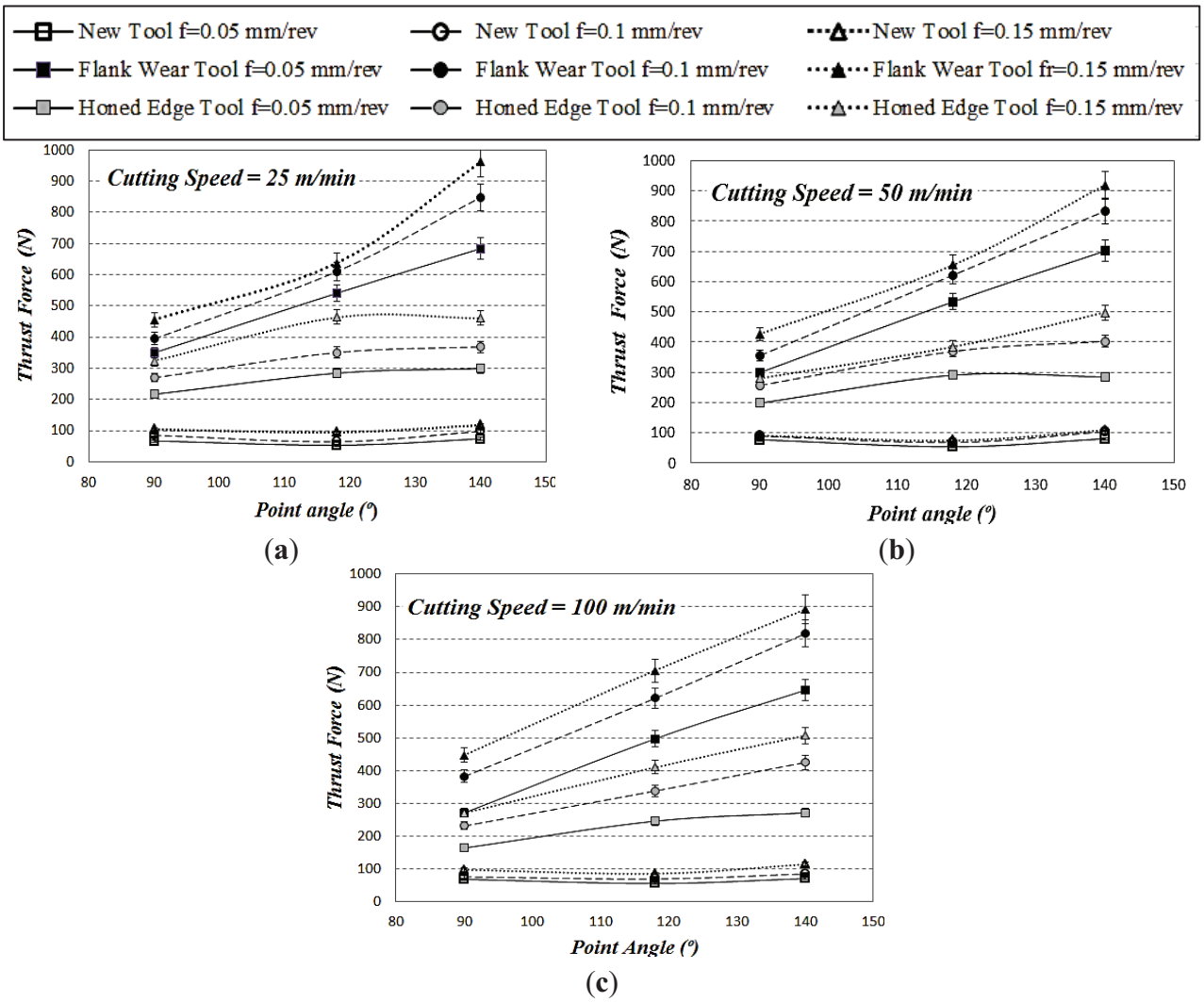

Honed tools showed increasing thrust force (around 50%–65%) with the increment of point angle. The thrust force also increases with the point angle when the flank wear geometry is tested. Relative variations around 100% are observed when the angle ranged from 90° to 140°. This trend is observed for all values of cutting speed analyzed.

The enhancement of the feed also resulted in increased thrust force in all cases analyzed. The variation is small for the fresh geometry. However, the increment of thrust force with feed reached increments around 50% and 70% when drilling with flank and honing wear respectively.

The increased values of thrust force due to the use of worn tools are related to enhanced risk of delamination. This trend is observed in the range of cutting speed tested (25–100 m/min). The progression of wear in both cases analyzed (flank wear and honed edge), increases the effect of the feed and the point angle on the thrust force.

In the case of new tool, torque decreased when the point angle increased from 90° to 118° and increased slightly when the angle changed from 118° to 140°. However, for both worn tools, flank wear and honed edge, maximum values of the torque were observed for the point angle 118°. The influence of feed in torque was much higher than in the thrust force, for all cases. The increment of feed lead to torque enhancement in the range 53%–100%.

Concerning the influence of cutting speed, slight decrease of thrust force and torque were observed when the velocity was increased. This trend has been also reported in other works in the literature for woven [12,14] and unidirectional composites [7].

ANOVA analysis presented in Table 3 showed that the main contributing factors for thrust force were tool geometry, point angle and feed rate. For all cases, p-value < 0.05 and Test F >> Fα = 5%. The cutting velocity factor did not present a statistical significance because p-value > 0.05 and Test F < Fα = 5%. This analysis corroborates the previous discussion concerning the prevalent influence of the worn geometry and the thrust force. On the other hand Davim *et al.* [18] showed the same effect with ANOVA analysis in previous research.

Table 3. ANOVA analysis developed for thrust force.

Factors	SS	DF	MS	F	F *	P *
A: Geometry	3.57×10^6	2	1.79×10^6	242.83	3.12	**0.0000**
B: Point Angle	525385	2	262692	35.71	3.12	**0.0000**
C: Cutting Speed	3023.19	2	1511.59	0.21	3.12	0.8147
D: Feed rate	192734	2	96367.1	13.1	3.12	**0.0000**
Residual	529651	72	7356.26	–	–	–
Total	4.82E+06	80	–	–	–	–

SS: Sum of squares; DF: Degrees of freedom; MS: Mean square; F: F-test value; P *: Probability; * Significant at the 5% level.

3.2. Surface Quality

The hole quality was evaluated in terms of hole diameter, delamination factor at the entrance and exit of the hole and other qualitative defects related to surface damage.

The diameter was measured after each drilling test using a micrometer Mitotuyo model 368-101 (Kawasaki, Japan). The values of diameter measured showed a reasonable quality for a drilling operation with a nominal drill diameter equal to 6 mm.

The delamination factor F_d, was calculated as the ratio between maximum diameter of delaminated area and the nominal diameter of the drill (6 mm). The drilled holes were examined with an optical microscope in order to measure the delaminated area. Examples of delamination at the hole entrance (peel up) and at the exit (push out) are shown in Figures 5 and 6.

Figure 5. Peel up delamination at the hole entrance for new tool (**a**), flank wear tool (**b**) and honed edge tool (**c**) with point angle 118°, V = 50 m/min and f = 0.05 mm/rev.

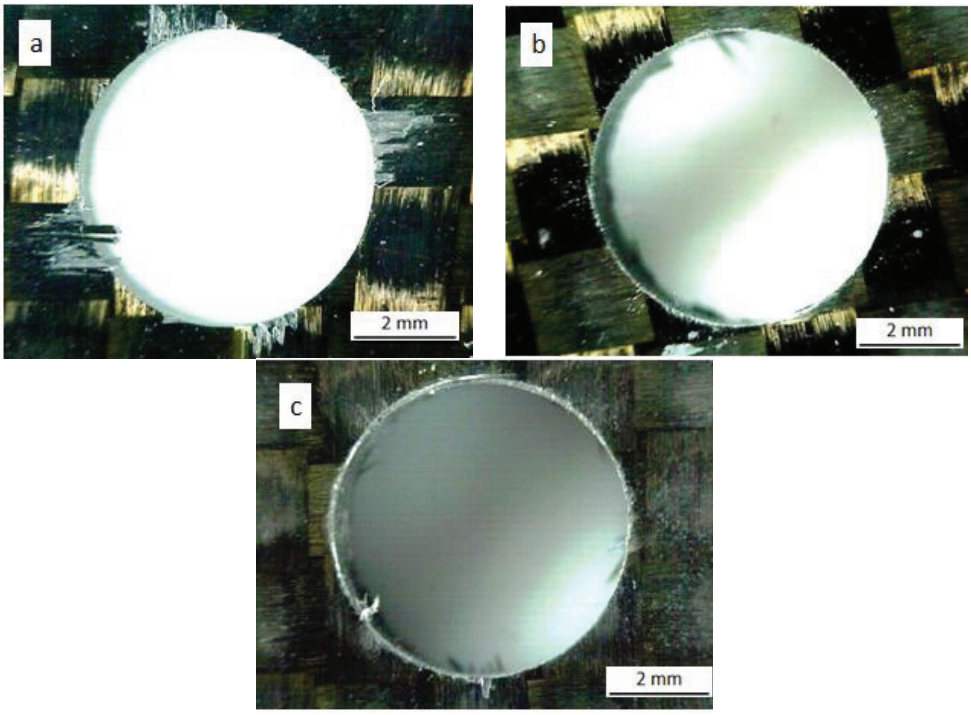

Figure 6. Push out delamination at the hole exit for new tool (**a**), flank wear tool (**b**) and honed edge tool (**c**) with point angle 118°, $V = 50$ m/min and $f = 0.05$ mm/rev.

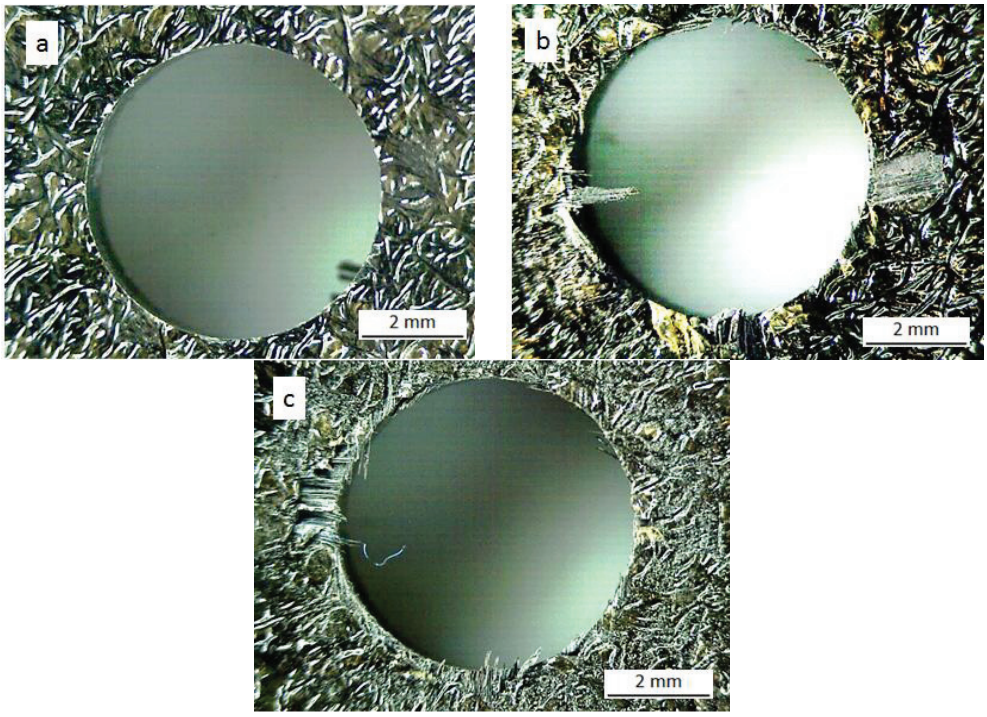

The maximum delamination factor obtained after drilling tests at the hole entry and exit is presented in Figures 7 and 8 respectively.

Figure 7. Maximum delamination at hole entry (measurement variations are indicated including error bars).

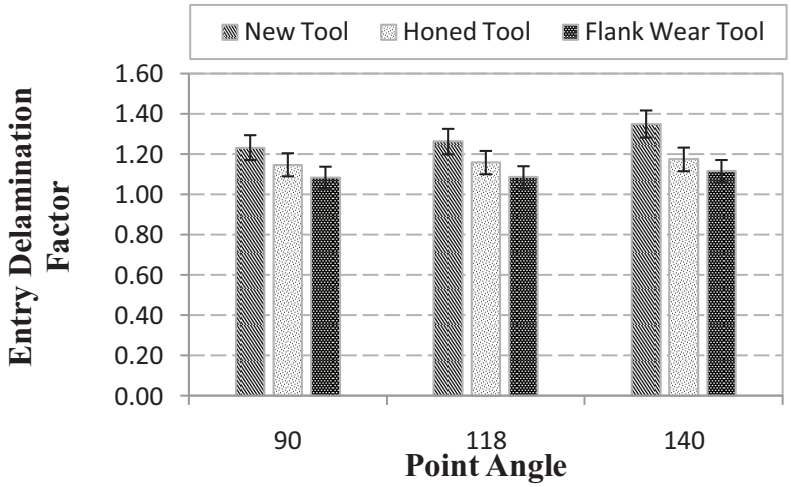

Figure 8. Maximum delamination at the hole exit (measurement variations are indicated including error bars).

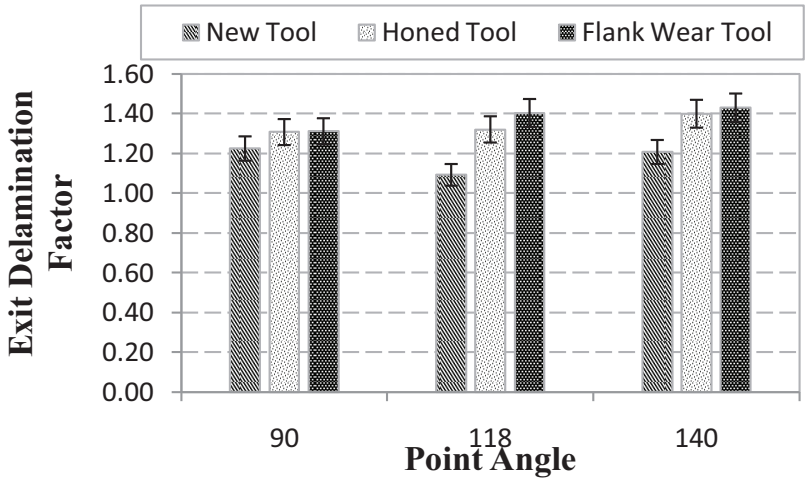

Delamination factor at the hole entry increased with point angle when drilling with a new tool. However, when a worn tool is used the influence of point angle is almost negligible. Concerning the influence of wear in the delamination factor at hole entry it is observed that the worn geometry produces less fraying of the fibers, and thus the extension of delamination is lower than in the case of fresh geometry. This behavior is consistent with the trends reported in [5] where similar effect was observed with angle point higher than 180°. The lowest delamination factor was obtained for drills exhibiting flank wear (in the range 1.14–1.18) while honed drills lead to slightly increased entrance delamination (around 1.3).

The delamination factor at the hole exit increased with wear, showing that the holes machined with flank wear the highest delaminated areas. This fact is related to the increment of the thrust force with wear progression.

The opposite effect of wear in the delamination factor considered at the hole exit and entrance can be explained as follows: when the cutting edges of drill bit make contact with the material, a peeling force through the slope of the drill results in separating the plies from each other. When the edge starts to wear, this force diminishes due to the decreasing sharpness. This fact elevates the thrust force but diminishes the peel force, leading to reduced peel up (related to hole entrance delamination) and elevated push out (corresponding to exit delamination) mechanisms.

Tables 4 and 5 show the results of the ANOVA analysis corresponding to the entry and exit delamination factor. Drill geometry is the main factor with statistical and physical significance on delamination factor (p-value < 0.05 and Test F >> Fα = 5%). Feed rate and point angle might have a low contribution to delamination but not a negligible one (Test F > Fα = 5%). Finally, for both cases cutting speed is not a significant factor (p-value > 0.05 and Test F < Fα = 5%). Shyha *et al.* [12] and Davim *et al.* [18] came to the same conclusion with a similar ANOVA analysis for CFRP woven composites.

Table 4. ANOVA results for entry delamination factor.

Factors	SS	DF	MS	F	F *	P *
A: Geometry	0.485973	2	0.24299	60.58	3.12	**0.0000**
B: Point Angle	0.05018	2	0.02509	6.26	3.12	**0.0031**
C: Cutting Speed	0.020491	2	0.01025	2.55	3.12	0.0848
D: Feed rate	0.118565	2	0.05928	14.78	3.12	**0.0000**
Residual	0.28877	72	0.00401	–	–	–
Total	0.96398	80	–	–	–	–

SS: Sum of squares; DF: Degrees of freedom; MS: Mean square; F: F-test value; P *: Probability; * Significant at the 5% level.

Table 5. ANOVA results for exit delamination factor.

Factors	SS	DF	MS	F	F *	P *
A: Geometry	0.722067	2	0.361033	36.05	3.12	**0.0000**
B: Point Angle	0.108919	2	0.054459	5.44	3.12	**0.0063**
C: Cutting Speed	0.008956	2	0.004478	0.45	3.12	0.6412
D: Feed rate	0.138689	2	0.069344	6.92	3.12	**0.0018**
Residual	0.721059	72	0.010015	–	–	–
Total	1.69969	80	–	–	–	–

SS: Sum of squares; DF: Degrees of freedom; MS: Mean square; F: F-test value; P *: Probability; * Significant at the 5% level.

It was possible to observe other defects related to the hole quality. Normally, fraying (Figure 9) was not observed at hole entrance for all geometries tested. Fraying was observed at the hole exit with both worn geometries. Flank wear produced less fraying than honed edge tool, and in some cases, it could be confused with chipping. It was observed that this defect increases when the point angle is higher, 118° and 140°. This defect showed a negligible dependence on feed.

Figure 9. Hole entry quality variation with feed for different geometries with 180° point angle and V = 50 m/min.

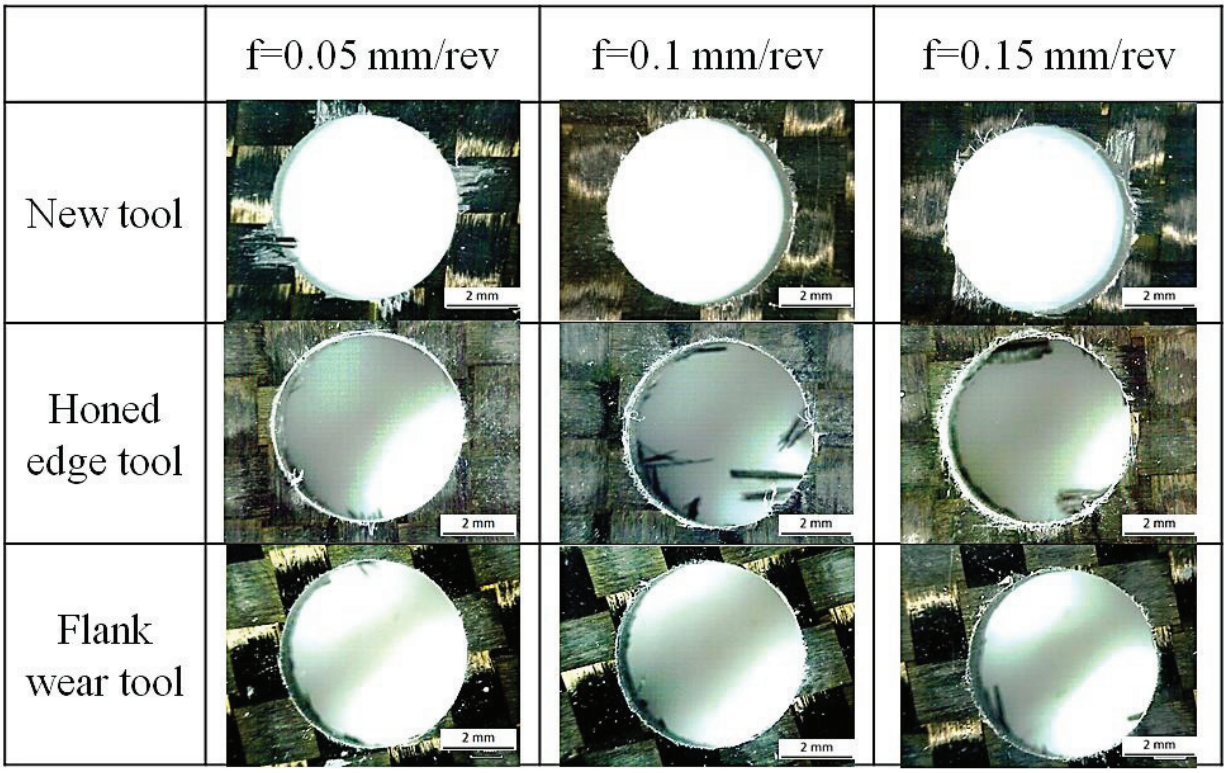

Concerning chipping (Figure 10), all geometries showed this defect both at the hole entry and exit. For worn tools, this defect was observed more frequently than for new tools and was enhanced for high feed. Increasing cutting speed has the same effect but less marked.

Another frequent surface defect was spalling, also observed with all geometries analyzed, but in different ways. For the honing tool, this defect was observed in a homogeneous area surrounding the hole entry, and located at some affected points at exit. Holes machined with flank wear and fresh tool showed this defect in concentrated zones at the hole entry and exit respectively, but it was more severe than that found with honing geometry. It was mainly observed with high feeds (0.15 mm/rev).

Finally, fuzzing (Figure 10) increased with point angle and feed and appeared mainly associated to machining with the honed edge. It was normally found together with spalling.

Figure 10. Different defects related with hole quality found after drilling. (**a**) fraying; (**b**) chipping; (**c**) spalling; and (**d**) fuzzing.

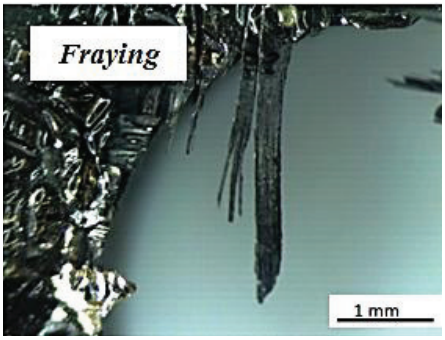

(**a**)

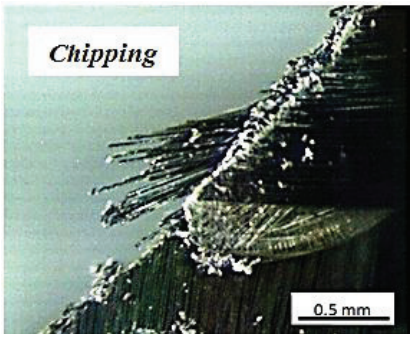

(**b**)

Figure 10. *Cont.*

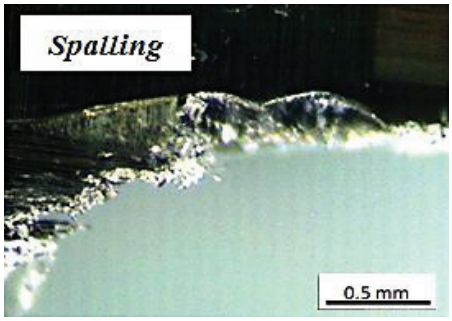

(**c**)

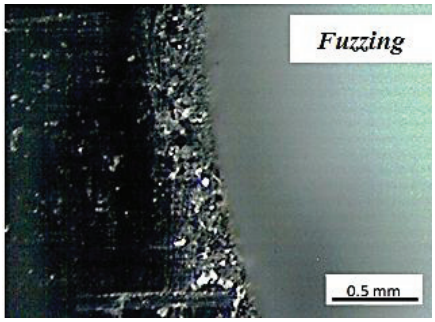

(**d**)

4. Conclusions

In this paper the influence of drill point angle and worn geometry in drilling of woven CFRP composite has been analyzed. The main contribution of the paper is the analysis of the crossed effect of the drill point angle and the geometrical changes due to wear progression. Moreover, the worn geometry was artificially generated ensuring the level and type of wear imposed and avoiding coupled effects of different wear patterns combined in the tool.

The following conclusions can be drawn:

Drill point angle influenced thrust force when it was combined with the effect of wear progression. However, fresh tools showed negligible influence of the drill point angle on thrust force. This fact is important for drill geometry selection since the evolution of wear could lead to inacceptable levels of thrust force.

Wear progression had a different effect on delamination at the entry and exit hole. While entry delamination diminished with wear progression, exit delamination was enhanced. The most favorable results concerning delamination were obtained with the lowest value of the drill point angle: delamination factor at entry and exit hole increased with the drill point angle. This result is important for the workpiece inspection after drilling, establishing critical zones. In addition, during the drill selection, the favorable effect of low drill point should be accounted for.

ANOVA analysis showed that the most influential parameters on thrust force and delamination were tool geometry (wear and point angle) and feed, while cutting speed has negligible influence.

This result is important in order to define productive processes with high removal rates ensuring quality requirements of the workpiece.

Acknowledgments

The authors acknowledge the financial support for the work to the Ministry of Economy and Competitiveness of Spain under the project DPI2011-25999.

Author Contributions

José Díaz-Álvarez, Antonio Díaz-Álvarez and José Luis Cantero developed drilling tests and data treatment. Norberto Feito and María Henar Miguélez analyzed delamination and studied the crossed influence of the parameters involved. All authors collaborated in preparing figures and tables and Norberto Feito and María Henar Miguélez wrote the paper.

Conflicts of Interest

The authors declare no conflict of interest.

References

1. Huang, X. Fabrication and Properties of Carbon Fibers. *Materials* **2009**, *2*, 2369–2403.
2. Teti, R. Machining of composites materials. *Ann. CIRP* **2002**, *51*, 611–634.
3. Santiuste, C.; Barbero, E.; Miguélez, M.H. Computational analysis of temperature effect in composite bolted joints for aeronautical applications. *J. Reinf. Plast. Compos.* **2011**, *30*, 3–11.
4. Liu, D.; Tang, Y.J.; Cong, W.L. A review of mechanical drilling for composite laminates. *Compos. Struct.* **2012**, *94*, 1265–1279.
5. Karpat, Y.; Deger, B.; Bahtiyar, O. Drilling thick fabric woven CFRP laminates with double point angle drills. *J. Mater. Process. Technol.* **2012**, *212*, 2117–2127.
6. Heisel, U.; Pfeifroth, T. Influence of Point Angle on Drill Hole Quality and Machining Forces when Drilling CFRP. *Proc. CIRP* **2012**, *1*, 471–476.
7. Durão, P.; Gonçalves, J.S.; Tavares, R.S.; de Albuquerque, C.; Aguiar, A.; Torres, A. Drilling tool geometry evaluation for reinforced composite laminates. *Compos. Struct.* **2010**, *92*, 1545–1550.
8. Grilo, T.J.; Paulo, R.M.F.; Silva, C.R.M.; Davim, J.P. Experimental delamination analyses of CFRPs using different drill geometries. *Compos. Part B* **2013**, *45*, 1344–1350.
9. Marques, T.; Durão, M.; Magalhães, G.; Silva, J.F.; Tavares, R.S. Delamination analysis of carbon fibre reinforced laminates: Evaluation of a special step drill. *Compos. Sci. Technol.* **2009**, *69*, 2376–2382.
10. Mayuet, P.; Gallo, A.; Portal, A.; Arroyo, P.; Alvarez, M.; Marcos, M. Damaged Area based Study of the Break-IN and Break-OUT defects in the Dry Drilling of Carbon fiber Reinforced Plastics (CFRP). *Proc. Eng.* **2013**, *63*, 743–751.
11. Iliescu, D.; Gehin, D.; Gutierrez, M.E.; Girot, F. Modeling and tool wear in drilling of CFRP. *Int. J. Mach. Tools Manuf.* **2010**, *50*, 204–213.

12. Shyha, I.S.; Aspinwall, D.K.; Soo, S.L.; Bradley, S. Drill geometry and operating effects when cutting small diameter holes in CFRP. *Int. J. Mach. Tools Manuf.* **2009**, *49*, 1008–1014.
13. Rawat, S.; Attia, H. Wear mechanisms and tool life management of WC–Co drills during dry high speed drilling of woven carbon fibre composites. *Wear* **2009**, *267*, 1022–1030.
14. Faraz, A.; Biermann, D.; Weinert, K. Cutting edge rounding: An innovative tool wear criterion in drilling CFRP composite laminates. *Int. J. Mach. Tools Manuf.* **2009**, *49*, 1185–1196.
15. Soldani, X.; Santiuste, C.; Muñoz-Sánchez, A.; Miguélez, M.H. Influence of tool geometry and numerical parameters when modeling orthogonal cutting of LFRP composites. *Compos. Part A* **2011**, *42*, 1205–1216.
16. Feito, N.; López-Puente, J.; Santiuste, C.; Miguélez, M.H. Numerical prediction of delamination in CFRP drilling. *Compos. Struct*. **2014**, *108*, 677–683.
17. Phadnis, V.A.; Farrukh, M.; Anish, R.; Silberschmidt, V.V. Drilling in carbon/epoxy composites: Experimental investigations and finite element implementation. *Compos. Part A Appl. Sci. Manuf*. **2013**, *47*, 41–51.
18. Davim, J.P.; Reis, P. Drilling carbon fiber reinforces plastic manufactures by autoclave experimental and statistical study. *Mater. Des.* **2003**, *24*, 315–324.

MDPI AG
Klybeckstrasse 64
4057 Basel, Switzerland
Tel. +41 61 683 77 34
Fax +41 61 302 89 18
http://www.mdpi.com/

Materials Editorial Office
E-mail: materials@mdpi.com
http://www.mdpi.com/journal/materials

MDPI • Basel • Beijing • Wuhan ÅBarcelona
ISBN 978-3-906980-70-6
www.mdpi.com